Angular Deposition of II-VI Compounds by Thermal Evaporation

BY

TANVIR HUSSAIN

A Dissertation Presented to the

DEANSHIP OF GRADUATE STUDIES

KING FAHD UNIVERSITY OF PETROLEUM & MINERALS

DHAHRAN, SAUDI ARABIA

In Partial Fulfillment of the

Requirements for the Degree of

DOCTOR OF PHILOSOPHY

In

PHYSICS

April 2018

KING FAHD UNIVERSITY OF PETROLEUM & MINERALS

DHAHRAN- 31261, SAUDI ARABIA

DEANSHIP OF GRADUATE STUDIES

This thesis, written by **Tanvir Hussain** under the direction of his thesis advisor and approved by his thesis committee, has been presented and accepted by the Dean of Graduate Studies, in partial fulfillment of the requirements for the degree of **DOCTOR OF PHILOSOPHY IN PHYSICS.**

Dr. Mohammad F. Al-Kuhaili
(Advisor)

Dr. Abdullah A. Al-Sunaidi
Department Chairman

Dr. Sardar Mohammad Ayub
(Co-Advisor)

Dr. Salam A. Zummo
Dean of Graduate Studies

Dr. Khalil A. Ziq
(Member)

2015/12
Date

Dr. Akhtar A. Naqvi
(Member)

Dr. Ahsan Ul Haq Qurashi
(Member)

Dedicated to My Family

ACKNOWLEDGMENTS

All praise and glory to Almighty ALLAH (SubhanahuWaTaalaa), the most Gracious, the most Merciful, and Creator of all Universe, with ideas of beauty, symmetry and Who is supreme authority knowing the ultimate realities underlying all sort of phenomena going on in this universe, Who is our benefactor, Who guides us in darkness and difficulties and Who gave me courage and patience to carry out this work.

On the submission of my thesis "Angular Deposition of II-VI Compounds by Thermal Evaporation", I would like to express my abandoned appreciation to my advisor Prof. Dr. Mohammad F. Al-Kuhaili who encouraged me to take this project and his vast experience, noble guidance, valuable suggestions, tremendous cooperation and profound interest in my studies enabled me to complete my research work successfully.

I would like to thank Prof. Dr. Sardar Mohammad Ayub Durrani for his guidance and assistance during the course of my experimental work.

I would like to thank my committee members Prof. Dr. Khalil A. Ziq, Prof. Dr. Akhtar A. Naqvi, and Dr. Ahsanulhaq Qurashi for their useful response, advice, and the time they spent reviewing this thesis.

I would like to thank the Chairman of the Physics department Dr. Abdullah A. Al-Sunaidi for providing me a continuous support throughout my studies.

I am very obliged to King Fahd University of Petroleum and Minerals (KFUPM) for providing me an opportunity to pursue my degree. I would also like to appreciate all the support that I received from the Physics Department in carrying out my research.

I would like to thank all the faculty members, non-teaching staff, and my friends for the help they provided me at various stages of this work.

TABLE OF CONTENTS

LIST OF TABLES

LIST OF FIGURES

List of Symbols

a, c	Lattice parameters
a_B	Bohr's radius
A	Cross-sectional area of film
B	Full width half maximum
C	specific heat
d	Thickness of film
d_i	Lattice spacing
D_{ij}	Binary diffusion coefficient
E	Energy of incident light
E_1	Exciton binding energy
E_B	Binding energy of photoelectrons
E_e	Electric field
E_g	Band gap
E_k	Kinetic energy of photoelectrons
G	Gibbs free energy
$G(E)$	Green function
G_L	Generation rate of excess carriers
H_0	Perfect crystal Hamiltonian
H^α	Enthalpy of α phase
H^β	Enthalpy of β phase
I_{dark}	Dark current
I_{Photo}	Photocurrent

J Rate of diffusion in moles per unit time per unit area

K_e Equilibrium constant

K_x Sherrer constant

l Bond length

m^*/m_o Effective mass

n Principal quantum number

n_b Refractive index of bulk material

n_c Number of molecules that suffered a collision

n_f Refractive index of the film

n_w Number of molecules that remain without collision at any instant

n^α Number of moles of α phase

n^β Number of moles of β phase

n_0 Electron concentration

N Carrier concentration

p_0 Holes concentration

P_r Photocurrent response

P Pressure

R_{ref} Reflectance of film

R_{rms} Surface roughness

R_y Rydberg energy

S Entropy of system

T Temperature

T_M Melting point

t_s	Crystallite Size
T_{trans}	Transmittance
V	Volume
V_e	Effective impurity potential
z	Power factor of the transition mode
α_c	Absorption coefficient
γ	Deposition angle
δn	Excess electron concentration
δp	Excess hole concentration
ε	Dielectric constant
θ	X-ray diffraction angle
λ	Wavelength of incident light
λ_f	Mean free path
λ_x	Wavelength of x-ray
μ_n	Mobility of electrons
μ_p	Mobility of holes
ρ	Density
ρ_f	Density of film
ρ_b	Density of bulk material
ρ_e	Electrical resistivity
σ	Conductivity of semiconductor
$\Delta\sigma$	Photoconductivity
τ_p	Lifetime of minority carrier

$h\upsilon$	Energy of incident x-ray
ϕ_{spec}	Work function of the spectrometer
φ_{II}	Density of II element
φ_{IV}	Density of IV element
X_{II}	elemental concentration of II element
X_{IV}	elemental concentration of IV element
Ω	Columns tilt angle
ψ	Wave function

List of Abbreviations

AFM	Atomic Force Microscopy
B.E	Binding Energy
FWHM	Full Width at Half Maximum
PL	Photoluminescence
XPS	X-ray Photoelectron Spectroscopy
XRD	X-ray Diffraction

ABSTRACT

Full Name : Tanvir Hussain

Thesis Title : Angular Deposition of II-VI Compounds by Thermal Evaporation

Major Field : Physics

Date of Degree : April 2018

In this work, II-VI compound thin films were deposited at different angles by thermal evaporation to investigate the factors that are responsible for the change of stoichiometry of the films from the source material and the effect of angular deposition on the structural, morphological, electrical, optical, and photocurrent properties of the films. The stoichiometry of the II-VI compound films prepared by evaporation varied from that of the source material. The II-VI compounds dissociate into molecules of II and VI elements during evaporation. The vapor pressure of dissociative elements or collision between them during transport could be responsible for the change of stoichiometry. Energy dispersive spectroscopy and x-ray photoelectron spectroscopy analyses of angular-deposited II-VI compound films revealed that the stoichiometry of the film changed from the source material due to a collision between the molecules of II and VI elements during transport. X-ray diffraction analysis showed that angular-deposited CdSe and CdS films were single crystal while angular-deposited CdTe, ZnTe, ZnSe, and ZnS films were polycrystalline. Atomic force microscopy revealed that the surface morphology of angular deposited II-VI compound films was dependent on deposition angle. It was observed that optical, electrical, and photocurrent properties of II-VI compound films were highly dependent on the stoichiometry of the films.

ملخص الرسالة

الاسم الكامل: تنوير حسين

عنوان الرسالة: الترسيب الزاوي لمركبات II-VI بواسطة التبخير الحراري

التخصص: فيزياء

تاريخ الدرجة العلمية: أبريل ٢٠١٨م

في هذه الدراسة، تم ترسيب أغشية رقيقة من مركبات المجموعة الثانية والسادسة عند زوايا ترسيب مختلفة بواسطة التبخير الحراري، ومن ثم فحص العوامل المسؤولة عن تغير الخصائص الكيميائية (النسب الذرية للعناصر الكيميائية في المركب) لهذه الأغشية الرقيقة مقارنة بالمصادر الأولية (العناصر الكيميائية في المركبات التي تم تبخيرها لتحضير الأغشية الرقيقة) وتأثير الترسيب الزاوي على الخصائص البنيوية، والشكلية، والكهربائية، والبصرية وخواص التيار الكهروضوئي لهذه الأغشية الرقيقة. لقد لوحظ أن النسب الذرية للعناصر الكيميائية في الأغشية الرقيقة تختلف عن تلك النسب الموجودة في المواد الأولية التي استخدمت كمصدر لتحضير الأغشية الرقيقة، وأن مركبات المجموعة الثانية والسادسة التي تم تبخيرها للحصول على الأغشية الرقيقة قد تفككت إلى جزيئات من عناصر المجموعة الثانية وعناصر المجموعة السادسة أثناء التبخير. كذلك يمكن أن يكون ضغط البخار للعناصر المتفككة أو التصادم بينهم أثناء الانتقال من المصدر الأولي للترسب على شكل غشاء رقيق بفعل التبخير مسؤولاً عن تغيير الخصائص الكيميائية. إن التحاليل الكيميائي للأغشية الرقيقة المصنعة والتي تم إجراؤها باستخدام جهاز مطياف الأشعة السينية الالكتروضوئي وجهاز مطياف تشتت الطاقة بالأشعة السينية أثبتت أن تغير الخصائص الكيميائية للأغشية الرقيقة مقارنة بالمركبات الأولية يُعزى للتصادم بين جزيئات عناصر المجموعة الثانية وعناصر المجموعة السادسة أثناء التبخير. من ناحية أخرى أظهرت تحاليل جهاز حيود الأشعة السينية أن الأغشية الرقيقة المصنعة من مركبات سيلينيد الكادميوم وكبريتيد الكادميوم تتسم بأنها ذات بنية أحادي البلورة بينما الأغشية الرقيقة المصنعة من مركبات تيلوريد كادميوم وتيلوريد الزنك وسيلينيد الزنك وكبريتيد الزنك كانت ذات شكل متعدد البلورات. أما الخصائص الشكلية لأسطح الأغشية الرقيقة المصنعة فقد تم فحصها باستخدام جهاز مجهر القوة الذرية حيث أوضحت الدراسة ان الخصائص الشكلية لأسطح الأغشية الرقيقة يعتمد على الترسيب الزاوي. وقد لوحظ أيضا

أن الخصائص البصرية والكهربائية وخواص التيار الكهروضوئي للأغشية الرقيقة المصنعة من مركبات المجموعة الثانية والسادسة تعتمد بشكل واضح على الخواص الكيميائية لهذه الأغشية الرقيقة.

CHAPTER 1

Introduction

Semiconductors are materials which play an important role in the development of science and technology [1-4]. One of the most important characteristics of a semiconductor, which differentiates it from insulators and metals, is its energy band gap [1-4]. Germanium (Ge) and silicon (Si) are the first semiconductors to be used for the fabrication of microelectronic devices. Germanium was widely used in the early days of semiconductor development for the fabrication of diodes and transistors [5-8]. Silicon has been used to fabricate rectifiers, transistors, integrated circuits and solar cells [9-11]. Si and Ge have some inherent limitations, like narrow and indirect band gap [12, 13]. Si has been widely used in solar cells, but crystalline Si is expansive. In the last four decades, a various group of semiconductors like II-VI compounds, III-V compounds, and their alloys has come up to play a role in optoelectronic and microelectronic applications [12-16]. As a result of this, a wide range of lasers, and light emitting diodes can be made with a wide range of the visible and infrared portions of the EM spectrum using compound semiconductors [16-23]. Compound semiconductors are extensively used in high-speed devices and devices requiring the absorption or emission of light, where Si and Ge semiconductors cannot work efficiently. The concentration of impurities, defects, and doping in compound semiconductors also play an important role to control the electronic and optical properties of the semiconductors [24-27]. II-VI compounds such as ZnS, ZnSe, ZnTe, CdS, CdSe and CdTe have direct band gaps and can, in principle, yield

proficient optoelectronic devices [28, 29]. These materials are extensively used in optoelectronic devices, and the efficiency of these devices is hampered due to their poor electronic and optical properties. During the past decades, many scientists have been trying to fabricate the p-n junctions using II-VI compounds by the introduction of shallow donors and acceptors by different deposition techniques as well as control of elemental composition [30, 31]. II-VI compounds show poor electrical properties because of the inability to incorporate suitable dopants that can provide a high concentration of free charge carriers. The difficulty in doping II-VI compounds is due to (i) a lack of control of stoichiometry and its relation with intrinsic and extrinsic defects, and (ii) the presence of unwanted background impurities like Li, Cl, Cu, Na etc. [32, 33]. The incorporation of background impurities in II-VI compounds is much easier as compared to in III-V compounds and VI semiconductors. In recent years, scientists have been trying to prepare II-VI compounds under stoichiometric conditions for getting both p- and n-type conductivities in the same material [33]. The increasing success in fabricating high quality and pure crystals, epilayers and quantum wells out of different II-VI compounds has raised huge interest for their use in device applications in the visible region, which cannot be covered by III-V based compounds. CdS, CdSe, CdTe, ZnS, ZnSe and ZnTe and their multilayer alloys are the best candidates for application in the visible region [34, 35].

1.1 Crystal Structures

II-VI compounds have the form MX, where M donates the metal and X denotes the chalcogen, typically characterized by the presence of four elongated electron clouds around each other [36]. Metals of group II have two electrons (s^2) in the outermost shell;

while chalcogens of group VI have six electrons (s^2p^4) in the outermost shell. The s and p orbitals overlap and form sp^3 orbitals by hybridization [36]. This leads to a crystal where M and X atoms are tetrahedrally coordinated in such a way that each atom is surrounded symmetrically by four atoms of the other element. Two possible structures are possible by such arrangements of atoms; zincblende (cubic) and wurtzite crystal structures [37]. The ground state electronic configuration of some group II and Group VI elements are shown in Table 1.1.

Table 1.1 Ground state electronic configuration (GSEC) of some group II and group VI elements

Group II metals	**GSEC**	**Group IV Chalcogen**	**GSEC**
Cd	$[Kr].4d^{10}.5s^2$	Te	$[Kr].4d^{10}.5s^2.5p^4$
Zn	$[Ar].3d^{10}.4s^2$	Se	$[Ar].3d^{10}.4s^2.4p^4$
---		S	$[Ne].3s^2.3p^4$

Similar to the diamond structure, the zinc blende structure may be viewed as two fcc structures displaced from each other by one-quarter of a body diagonal [38]. However, in the zinc blende structure, one of the fcc sub-lattices is formed by cations (group II metals), while the other sub-lattice is formed by anions (group VI chalcogens). Therefore, unlike the diamond structure, the zinc blende structure does not have inversion symmetry. The stacking sequence along the tetrahedral bonds is repeated every three anion-cation bilayers (ABCABC…..). The dimensions of the unit cell are defined in terms of the lattice constant "*a*". The coordination number of II and VI elements is 4. The space group is F43m [39]. The zincblende structure is shown in fig. 1.1 (a).

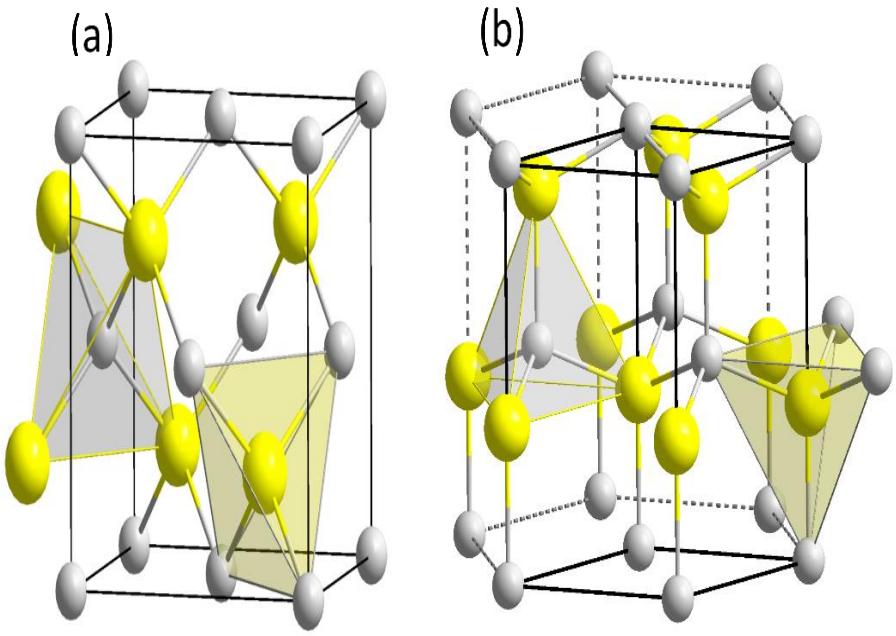

Figure 1.1 (a) Zinc blend and (b) wurtzite structures illustrating their respective tetrahedral sites

Figure 1.1(b) shows the wurtzite structure. It consists of two interpenetrating hexagonal close-packed lattices of lattice constants "*a*" and "*c*". These lattices are relatively displaced along the hexagonal axis *c* by the nearest neighbor distance (3/8)**c* [40]. Ideally, the ratio of (*c/a*) should be 1.633 [40]. However, most of the wurtzite compounds have slightly different (*c/a*) ratios [41]. The crystal structure and lattice parameters of II-VI compounds are shown in Table 1.2.

Table 1.2 Crystal structure, lattice parameters *a*, *c*, *(c/a)*, and bond length *l* of II-VI semiconductors (all dimensions in Å)

Group II-VI compounds	Znic blend		Wurtzite			
	a	*l*	*a*	*c*	*c/a*	*l*
CdTe	6.48	2.80	4.57	7.48	1.64	2.80
CdSe	6.05	2.62	4.30	7.01	1.63	2.63
ZnTe	6.10	2.64	4.31	7.09	1.65	2.65
ZnSe	5.67	2.45	4.00	6.54	1.63	2.45
ZnS	5.41	2.34	3.81	6.23	1.64	2.33

1.2 Chemical bonding

II-VI semiconductor compounds with the tetrahedral coordination of zinc blende or wurtzite structure are formed when group II metals have sufficiently high ionization potentials and do not give up their electrons, but rather share them with neighboring chalcogens [36]. The stronger electronegativity of group VI chalcogens causes the electron clouds to shift from group II metals to group VI chalcogens. As a result, the binding is partly ionic and partly covalent. This would be better understood by considering the effective charge of group II metals in pure ionic and covalent bonds. Pure ionic bonds are formed when the valence electrons are detached from the metal *M* and transferred to the chalcogen *X*. In this case, the group II metal is fully ionized, with an effective charge of +2. However, pure covalent bonds are formed upon an equal distribution of valence electrons between the metal *M* and the chalcogen *X*, with the center of the electron cloud located at the center of the interatomic distance d_{MX} [36]. Consequently, the effective charge of the group II metal is −2. If this center is located at a distance 1/4 d_{MX}, the distribution of valence electrons may be described as $2e^-$ around the metal *M* and $6e^-$ around the chalcogen *X*. The effective charges of the component atoms

of the resultant compound M^0X^0 equal zero. This is the effective covalent bond between neutral atoms [37]. Table 1.3 indicates that the effective charge of the metal atoms is always positive but less than unity, which confirms that the chemical binding is partly ionic and partly covalent. It is worth noting that as the atomic number increases, the inter-atomic distance d_{MX} increases. Consequently, the bond strength decreases, which results in a decrease in the heat of atomization, the optical bandgap, and the melting point. Figure 1.2 shows the melting point (T_M) of some II-VI semiconductor compounds as a function of the lattice constant *a*. The solid line represents the least-squares fit with the relation [42]:

$$T_M = 7159 - 957a \tag{1.1}$$

where T_M was measured in *K* and *a* was measured in ***Å.*** Table 1.3 shows that such dependence on the atomic number is noticeable when the aforementioned properties are compared for different anions (S_2^-, Se_2^-, and Te_2^-) within group II-VI compounds that have the same cation. The same is true when comparing compounds with the same anion and different cations (Zn_2^+, and Cd_2^+). Meanwhile, considering compounds with common cation, the effective charge of the metal telluride is less than that of the metal selenide, which is less than that of the metal sulfide, indicating a decrease in the ionicity of bonds within each group when the atomic number of the chalcogen is increased [42].

Table 1.3 Some physical properties of II-VI compounds

Group II-VI compounds	d_{MX} (Å)	Heat of atomization (Kcal/g-atom)	E_g (eV)	Melting point (˚C)	Difference of electronegativity between II and VI atoms	Effective charge of metal atoms
CdTe	2.79	48.0	1.51	1371	0.4	0.08
CdSe	2.62	52.0	1.75	1531	0.7	0.55
CdS	2.52	57.0	2.42	2023	0.8	0.77
ZnTe	2.64	63.0	2.27	1568	0.5	0.066
ZnSe	2.45	66.0	2.72	1788	0.8	0.099
ZnS	2.36	73.0	3.75	2103	0.9	0.268

Table 1.4 Bulk modulus B (10^{11} dyn/cm^2), shear modulus C_s (10^{11} dyn/cm^2), linear compressibility C_o (10^{-13} cm^2/dyn), and microhardness H (GPa) for II-VI semiconductors at 300 K

Group II-VI compounds	Zinc blend				Wurzite			
	B	C_s	C_o	H	B	$*C_{o\perp}$	$**C_{o//}$	H
CdTe	4.24	0.830	7.86	0.45- 0.60	-	-	-	-
CdSe	5.31	1.020	6.28	-	5.31	6.50	5.90	0.90
CdS	6.16	1.160	5.41	-	6.27	5.40	5.20	1.21-2.30
ZnTe	5.10	1.540	6.53	0.60 - 0.90	-	-	-	-
ZnSe	6.24	1.750	5.34	1.37 - 1.83	-	-	-	-
ZnS	7.71	1.870	4.33	1.78	7.40	4.50	4.60	1.78

* Along a direction ⊥ c-axis, ** Along a direction // c-axis

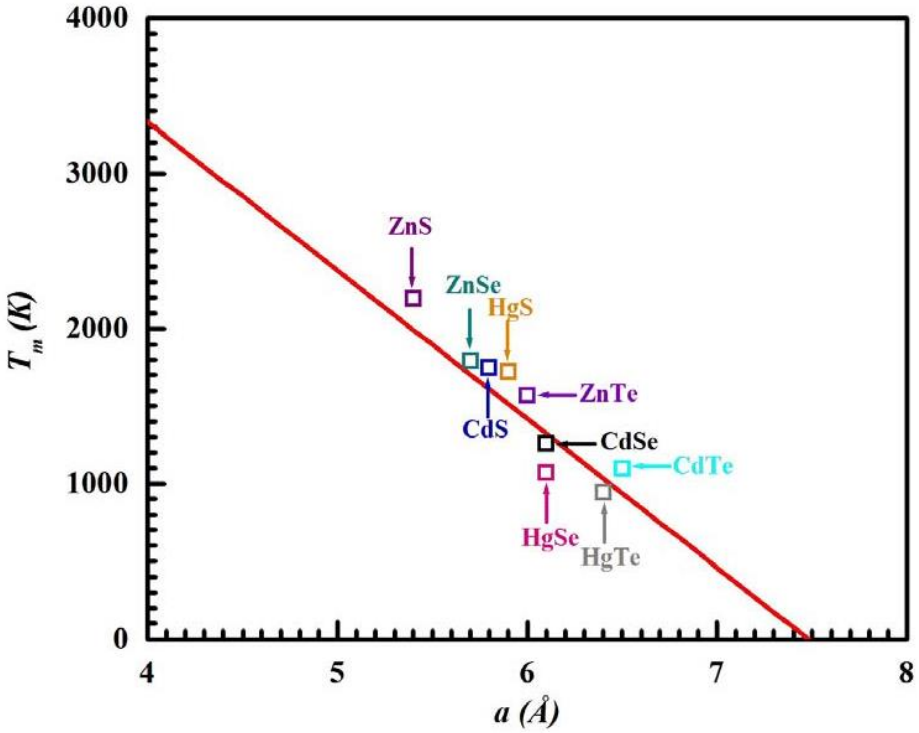

Figure 1.2 Melting point (T_M) versus lattice constant *a* for some II-VI semiconductor compounds

1.3 Elastic Properties

Table 1.4 shows bulk modulus *B*, shear modulus C_s, linear compressibility C_o, and microhardness *H* for some group II-VI semiconductor compounds at T = 300 K [42].

1.4 Thermal Properties

The understanding of the thermal properties of semiconductors over the wide range of temperature are very important for practical uses [42]. Table 1.5 gives the values of some of the essential thermal properties of II-VI semiconductors, such as the specific heat at constant pressure C_p, Debye temperature θ_D, thermal expansion coefficient α_{th}, and thermal conductivity ξ.

Table 1.5 Specific heat C_p, Debye temperature θ_D, thermal expansion coefficient α_{th}, and thermal conductivity ξ of II-VI semiconductors at 300 K

II-VI compounds	C_p (J/g.K)	θ_D (K)	α_{th} (10^{-6} K^{-1})	ξ (W/cm-K)
CdTe	0.211	44	4.67	0.075
CdSe	0.281	135	2.76	0.090
CdS	0.328	310	2.77	0.200
ZnTe	0.258	260	8.33	0.180
ZnSe	0.360	340	6.71	0.190
ZnS	0.486	351	2.49	0.270

1.5 Optical Properties

The band gap (E_g) dependence on temperature is mainly due to the thermal dilation of the lattice and the temperature dependent electron-phonon interaction [43]. The band gap E_g of semiconductor depends on the temperature T and can be described by the formula:

$$E_g(T) = E_g(0) - \frac{\alpha_c T^2}{\beta_c + T} \tag{1.2}$$

where T is in K, and α_c and β_c are constants. At high temperatures (T >> β_c), equation (1.2) reads:

$$E_g(T) = E_g(0) - \alpha_c T \text{ and } \frac{dE_g}{dT} = -\alpha_c \tag{1.3}$$

Table 1.6 shows the temperature coefficient of band gap energy α_c for some II-VI semiconductors. It also lists the free exciton binding energy (E_1) and the photoluminescence (PL) transition energies. Table 1.7, however, lists the refractive index, the static and high-frequency dielectric constants, ε_S and ε_∞, for some cubic as well as hexagonal II-VI semiconductors.

Table 1.6 Temperature coefficient of band gap energy α_c, free exciton binding energy (E_1) and photoluminescence (PL) transition energies for group II-VI semiconductors

Group II-VI compounds	α_c (meV/K)	E_1 (meV)	PL (eV)
CdTe	0.460	11.0	1.595 - 1.597
CdSe	0.370	15.0	1.824 - 1.827
CdS	0.386	29.0	2.551 - 2.553
ZnTe	0.630	12.8	2.380 - 2.381
ZnSe	0.670	20.0	2.800 - 2.804
ZnS	0.880	38.0	3.800 - 3.820

Table 1.7 Refractive indices, static and high-frequency dielectric constants, ε_S and ε_∞, of group II-VI semiconductors

II-VI compounds	n_b at λ = 1000 nm	ε_S	ε_∞
CdTe	2.84	10.4	7.10
CdSe	2.55	9.6	6.20
CdS	2.34	9.8	5.40
ZnTe	2.79	9.4	6.90
ZnSe	2.47	8.9	5.90
ZnS	2.29	8.3	5.10

1.6 Electrical Properties

Table 1.8 gives the electron (*e*) and hole (*h*) mobility at 300 K as well as the electron and hole effective mass (m^*/m_o) for II-VI semiconductors [44].

Table 1.8 Electrical properties of II-VI compounds

Group II-VI compounds	Mobility (cm^2/V-s)		Effective Mass (m^*/m_o)	
	e	*h*	*e*	*h*
CdTe	1050	5	0.39	0.72
CdSe	720	75	0.17	1.09
CdS	350	40	0.15	0.79
ZnTe	3.56	50	0.21	0.80
ZnSe	540	28	0.13	0.45
ZnS	165	100	0.11	0.35

1.7 Defects in Solids

The suitability of semiconductor materials for device applications depends largely on crystal perfection and its control. In general, Imperfections and defects are the major limiting factors of any device performance and its reliability. Therefore, the defects in solids become an important area of study. When a defect state is introduced into the band gap of a semiconductor, it can behave in many ways, for example, as a hole or electron trap, a recombination center, or a luminescent center. Definitely, it is well known that defect levels can affect the optical and electrical properties of a material [45].

1.7.1 Defect states in semiconductors

Defect levels are localized electronic states in the solid due to a variety of causes but all leading to a loss of translational symmetry of the crystal lattice. Examples of these are substitutional or interstitial impurities, native defects, dislocations or termination of the lattice at the surface. Weakly bound (shallow) defect states can be predicted using a simple hydrogenic model using the Schrodinger equation [45, 46]:

$$H\psi = E_l\psi \tag{1.4}$$

$$H = H_0 + V \tag{1.5}$$

where H is the Hamiltonian of crystal, H_0 is the perfect crystal Hamiltonian, V is the effective impurity potential centered at the site of the defect, ψ defines the wave functions associated with the defect states in the potential, and E_l gives the energies of these states. Reducing the Schrodinger equation to its hydrogenic form, by assuming the amount of localized charge remaining in the region of the short-range potential is small, leads to the

effective mass theory. The energies E_v of defect levels near the bond edges are given by [45-47]:

$$E_v = \frac{m^* R_y}{n^2 \varepsilon^2} \tag{1.6}$$

where R_y is the Rydberg energy unit defined in term of ground-state of an electron in the for a hydrogen atom, m^* is the electron effective mass, ε is the host's dielectric constant and n is the principal quantum number of the state. This resembles the solution for a hydrogen atom immersed in a uniform dielectric medium. The spatial extent of the defect is given by Bohr radius which is related to the hydrogenic radius $a_r(0)$ by [45-47]:

$$a = \frac{n^2 \varepsilon a_r(0)}{m^*} \tag{1.7}$$

The hydrogenic model has been successful in calculating the properties of shallow donors and acceptors, where the impurity potential is dominated by its long-range Coulomb term. However, for deep levels, strong, short-range interactions become increasingly important. The resultant contraction of the defect wave function and the resulting deviation from the hydrogenic model makes theoretical predictions more difficult [45, 46]. The main significant difference in calculating the properties for deep levels is: unlike shallow defects, it is crucial to know the precise atomic locations; one is often concerned with a change in the charge state such as photoionization or carrier capture, or there may be a geometrical change in the defect. A change in the charge state of the deep level involves a redistribution of localized charge. So, defect calculations are based on self-consistent methods [45-47]. There are two types of self-consistent methods: (a) the molecular cluster method, which uses standard molecular techniques to examine cluster sizes of two order of 5-100 atoms. This has been used in the case of transition metal impurity calculation in II-VI compounds (b) Green's function method, which defines an

operator for the perfect crystal $G(0) = \frac{1}{[E - H(0)]}$. The Schrödinger equation then becomes [46, 47]:

$$[1 - G(E)V]\psi = 0 \tag{1.8}$$

This can be solved by expressing the operator *G(E)* and *V* in a particular representation, reducing to a simple set of algebraic expressions. Both techniques have been used successfully, and rather than taking competing roles, they have been complimentary. Green's function methods avoid possible problems with cluster surfaces although these may be eliminated for the cluster method by a choosing sufficiently large cluster [47-49].

1.7.2 Properties of shallow levels

Shallow and deep levels terms are used for defect states based on the positions of the energy levels within the band gap. Shallow levels have ionization energies comparable to *kT*, and so are generally ≤ 0.25 eV. They can be classified as either donor (positivity charged when ionized), or acceptors (negatively charged when ionized). Since shallow levels are ionized at room temperature, they play the dominant role in the determination of the semiconductor conductivity (*n* or *p*). It has been mentioned that the hydrogenic model can be used to describe the shallow levels produced by a defect; therefore, such levels can be spectroscopically resolved. Low-temperature luminescence has been a widely used experimental technique for the study of shallow levels. The distinction between deep and shallow levels is somewhat arbitrary often corresponding to the experimental method used for their analysis. In the case of trapping effects, they are referred to as deep levels [45].

1.7.3 Properties of deep levels

Deep level defects can enhance the recombination of the excess pairs of electrons and holes, thus the free carrier lifetimes can be drastically reduced by these centers depending on the application [45]. This may or may not be useful: (a) long minority carrier lifetimes are required particularly in electro-optic devices in which photons are generated in, say, a light emitting diode (LED) or in photovoltaic devices. In solar cells, deep levels impurities will influence current collection in three ways: by reducing the minority carrier lifetime; by recombination losses in the deep depletion region; and by modification of the junction electric field under illumination [46, 47]. In general, all these effects may apply and so the deep levels will result in poor solar cell efficiency. (b) Fast switching devices require short but controlled minority carrier lifetimes. Si has long minority carrier lifetimes due to its indirect bandgap structure. To suppress carrier storage, in other words, reduce carrier lifetime, impurities are introduced which give states in the band gap that are sufficiently deep to not contribute carriers in competition with shallow dopants but have large capture cross-section to curtail the lifetime [46-49].

1.8 Literature Review

Vogt *et al.* [50] deposited CdTe films by molecular beam epitaxy. They co-evaporated CdTe with Te to enhance the Te content in the film. The purpose of the deposition was to reduce the work function between CdTe and back contact for the enhancement of solar cell efficiency. It was observed that the work function was decreased by 0.62 eV by incorporation of Te in CdTe films [50].

Reese *et al.* [51] prepared cadmium telluride (CdTe) films by a closed sublimation method. The surface of the films was passivated intrinsically with different methods. It was observed that a Cd-rich surface had much less surface recombination velocity as compared to a Te-rich surface [51].

Heisler *et al.* [52] deposited a layer of CdTe by sublimating CdTe, Cd and Te materials. They prepared Cd-rich, stoichiometric, and Te-rich CdTe layers by controlling the sublimation process of the materials during deposition, and substrate temperature. After that, CdTe-based solar cells were fabricated to observe the effect of concentration on the efficiency of the solar cells. It was noticed that at low substrate temperature, Te-rich CdTe layer had very small efficiency, while Cd-rich CdTe layer showed better efficiency comparable to a CdTe film grown at 300 ˚C [52].

Ueng *et al.* [53] fabricated a p-i-n thin film multilayer CdTe solar cell by electrodeposition. The composition of the prepared films was controlled by adjusting the electrodeposition potential. It was observed that, at different electrodeposition potentials, the deposited films had different elemental composition [53].

Raulo *et al.* [54] prepared CdTe ingots to fabricate x-ray and gamma-ray detectors by traveling heat method. They prepared CdTe ingots of different stoichiometry and observed that a Te-rich detector showed better performance [54].

Dawar *et al.* [55] fabricated CdTe, Cd-rich CdTe, and Te-rich CdTe thin films by thermal evaporation by mixing appropriate amounts of Cd and Te powders as a source material. They observed that the stoichiometric films were highly resistive (resistivity $=10^9$ Ω.cm). It was also observed that the Cd-rich CdTe and Te-rich CdTe films were less resistive and the purpose of this research was to fabricate CdTe solar cell without back

contact. They also annealed the samples in hydrogen, and it was observed that the conductivity was decreased by increasing the gas pressure [55].

Olusola *et al.* [56] had grown n-type and p-type zinc telluride (ZnTe) thin films by intrinsic doping using potentiostat electrodeposition. Cyclic voltammogram had been used to obtain the range of growth voltages to obtain the ZnTe film. At high voltage, Zn-rich ZnTe thin films were formed, and at low growth voltages, Te-rich ZnTe thin films were formed. After that, they fabricated a p-n junction diode, with a device fabrication structure of glass/FTO/n-ZnTe-p-ZnTe/Au. For p-n diode fabrication, glass/FTO used as a back contact, n-ZnTe-p-ZnTe used as a p-n junction and Au used as an upper contact. The fabricated diode had shown a reverse saturation current of 10.0 nA, rectification of 10^2, and barrier height of more than 0.77 eV [56].

Kumar *et al.* [57] fabricated non-stoichiometric cadmium sulfide (CdS) thin films by chemical bath deposition. It was observed that those films which were fabricated under rich sulfur environments showed high photoconductivity. Photoluminescence of the prepared films confirmed that there was a large number of sulfur vacancies present in the films [57].

Ouchtari *et al*. [58] synthesized CdS films on a glass substrate by chemical vapor deposition. They observed the effect on the structural, morphological and optical properties of CdS thin film by controlling the bath temperature (T_b), deposition time (t_o), and [sulfur]/[cadimum] ratio in the solution. Those films which were deposited under optimum conditions (T_b = 75 °C, t_o = 60 min, and [sulfur]/[cadimum] ratio = 2.5) were relatively well crystallized. It was also observed that those films which were sulfur-rich showed 80% transmittance in the visible and in the near infrared regions [58].

Hernandez-como *et al.* [59] fabricated CdS films by pulsed laser deposition at different pressures during deposition. They prepared the CdS films of different stoichiometry by controlling the vapor pressure of the gas during deposition to modify the optical and electrical properties. It was observed that at low deposition pressure, the prepared CdS films were Cd-rich. It was noticed that by increasing the deposition pressure, the [S]/[Cd] ratio approached 1. It was also observed that Cd-rich films showed less transmittance and higher carrier concentration [59].

Ayd *et al.* [60] fabricated quantum dots of cadmium selenide (CdSe) via colloidal chemistry. They observed that the optical and photoluminescence properties of CdSe quantum dots can be successfully controlled by changing the Cd:Se atomic concentration ratio and the temperature of the bath. It was observed that the optical absorption peaks were red shifted by increasing the Cd:Se molar ratio in the solution [60].

Ayele *et al.* [61] synthesized stoichiometric quantum dots of CdSe by using a microwave system. After that, the prepared quantum dots were dissolved into a cadmium acetate dehydrate and Na_2SeSO_3 solutions to grow the Cd-rich CdSe and Se-rich CdSe quantum dots, respectively. In this process, the surface composition of quantum dots of CdSe was changed and the band gap of CdSe quantum dots was engineered by controlling the composition. It was observed that the band gap of quantum dots of CdSe was decreased with a redshift of UV-vis absorption edge and photoluminescence peaks [61].

Philipose *et al.* synthesized nanowires of zinc selenide (ZnSe) [62]. They investigated the effect of band edge transition and deep defects transition peaks by fabricating Zn-rich and Se-rich ZnSe nanowires. It was noticed that the band edge

transition peak was enhanced in Zn-rich ZnSe, nanowires and deep defects peak was enhanced in Se-rich ZnSe nanowires [62].

Morimoto [63] fabricated ZnSe films by metalorganic chemical vapor deposition. They controlled the elemental compositions of Zn and Se elements in the films by adjusting the temperature of the substrate. It was noticed that the electrical properties were highly dependent on the stoichiometry of the film. It was also observed that the stoichiometric film was more resistive compared to the non-stoichiometric films [63].

Dong *et al.* [64] synthesized nanoparticles of zinc sulfide (ZnS) by the hydrothermal method using different Zn/S ratio. They measured the ferromagnetic properties of ZnS nanoparticles which had different stoichiometry. They observed that Zn vacancies were responsible for high magnetization in ZnS nanoparticles. They also observed that S vacancies had non-magnetic behavior, as calculated by a theoretical model [64].

Tsai *et al.* [65] prepared ZnS films by two-stage chemical bath deposition. ZnS is the best candidate for window layer for Cu(In, Ga)Se_2 solar cells. For better performance, the stoichiometry of ZnS film is very important. They observed that the ZnS film prepared by two-stage chemical bath deposition was better stoichiometric compared to single-stage chemical bath deposition [65].

Wang *et al.* [66] synthesized ZnS nanospheres by the hydrothermal method. They mixed the Zn and S powders in NaOH solution and then they added $NaBH_4$ as a reducing agent. It was observed that the S vacancies enhanced the absorption in the visible region. $NaBH_4$ is a reducing agent, so it controls the concentration S vacancies in the ZnS

nanospheres. It was observed that those ZnS films, which had S vacancies, showed better photocatalytic activity [66].

1.9 Thermal Evaporation

Thermal evaporation is a physical vapor deposition technique (PVD) that is used for the preparation of thin films. Thermal evaporation is a very simple technique where the source material is evaporated by resistive heating [67]. For resistive heating of the material, an electrically conductive boat made of tungsten or molybdenum is used. The source material is placed in a deposition chamber, which is evacuated to high vacuum before evaporation is started. Each material has a finite vapor pressure, which increases with increasing temperature. Depending upon their properties, some materials are evaporated before they melt and some evaporate after they melt. Usually, a semiconductor sublimates on heating; however, a metal melts first and then evaporates. If no collisions take place, the molecules of the evaporated material move in straight trajectories from the source to the substrate surface [67]. The evaporated molecules are condensed on the surrounding walls of the chamber and on the substrate surface. High vacuum increases the mean free path of evaporated molecules and decreases the impurities in the films that could be incorporated from the residual gas. For film growth, the temperature of the substrate can be kept at room temperature, however, for getting a better quality of the film, the temperature of the substrate may be increased. The rate of evaporation and substrate temperature play a crucial role in the morphology of the film. A schematic diagram of thermal evaporation is shown in fig. 1.3 [67].

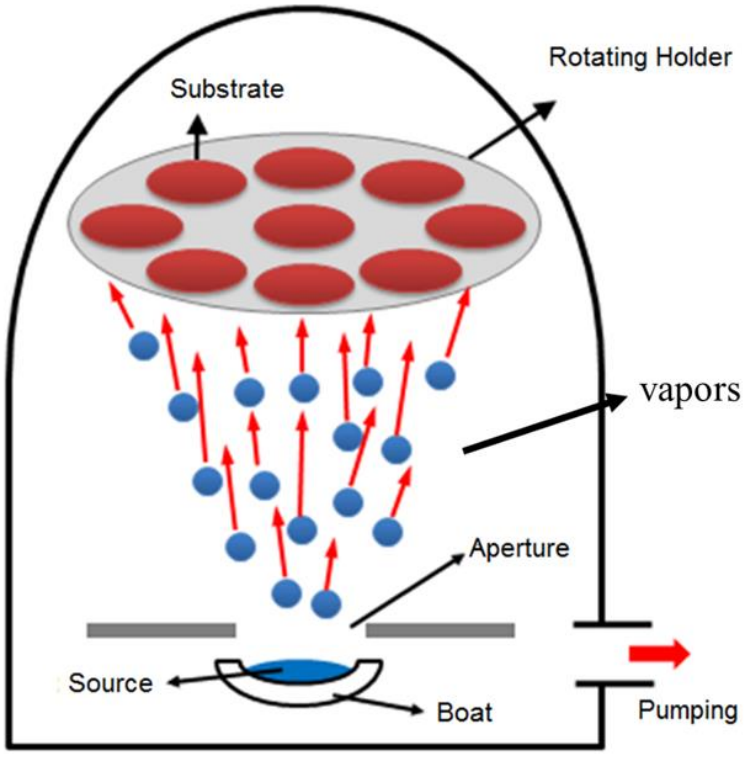

Figure 1.3 Schematic diagram of thermal evaporation

1.10 Dissociation of II-VI compounds

The II-VI compounds dissociate into their constituents during thermal evaporation. The equation of dissociation of II-VI compounds is given as [68, 69]:

$$A^{II}B^{VI}(S) \rightarrow A^{II}(g) + \frac{1}{2}B_2^{VI}(g) \qquad (1.9)$$

$A^{II}B^{VI}(S)$, $A^{II}(g)$, and $B_2^{VI}(g)$ represent the molecule of II-VI compound in the solid phase, an atom of II element in the vapor phase, and a molecule of VI element in the vapor phase, respectively. The existence of molecular species $A^{II}B^{VI}(g)$ in the vapor state is not completely ruled out, but the evidence strongly favors the elemental species [68–

70]. From mass spectroscopic investigations of the vapor species of II and VI elements over II-VI compounds, it appeared that the dominant vapor species of II and VI elements are in the monoatomic and diatomic molecules, respectively [33]. The total pressure (P) over the solid II-VI compound is equal to the sum of the partial pressures of dissociative elements [68].

$$P = P_{II} + P_{VI} = P_{II} + K_e P_{II}^{-2} \tag{1.10}$$

where P_{II} and P_{VI} are the partial pressures of II and VI elements, respectively, and K_e (= $P_{II}^2.P_{VI}$) is the equilibrium constant. At any temperature, there will be a minimum pressure (P_{min}), which corresponds to the condition [70]:

$$P_{II} = 2P_{VI} = 2^{1/3}.K_e^{1/3} \tag{1.11}$$

1.11 Motivation

Thermal evaporation is one of simplest techniques to fabricate high-quality thin films because the evaporation temperature of material and impurity is different. For better performance for photovoltaic devices, the control of defects within the semiconductor is an important factor. For solar cell applications, a preferable semiconductor is one which possesses long carrier lifetime and direct band gap. On the other hand, for fast switching devices, a material is needed which has a short carrier lifetime. To suppress carrier storage, in other words, reduce carrier lifetime, defects levels are introduced within the band gap of the semiconductor that are sufficiently deep and have large capture cross-section to curtail the lifetime of carriers. The II-VI compounds dissociate during evaporation and the elemental composition of II-VI compounds films grown by thermal

evaporation differ from the source material. It is very important to understand the evaporation phenomenon of II-VI compounds and to investigate the factors which are responsible for the change of the stoichiometry of the films from that of the source material. For this purpose, the II-VI compounds films will be deposited at different angles by thermal evaporation to investigate the factors that are responsible for the change of stoichiometry of the films during film growth.

1.12 Problem Statement

The stoichiometry of II-VI compound films prepared by thermal evaporation varies from the source material. The performance of optoelectronic devices fabricated from II-VI compound films or nanostructures depends on their stoichiometry. There is a need to investigate the factors that are responsible for the change of stoichiometry of the II-VI compound films prepared by thermal evaporation.

1.13 Solution

The II-VI compounds dissociate into atoms of II element and molecules of VI element during evaporation. The factors that can effect the stoichiometry will be the vapor pressure or collision during evaporation. We deposited the II-VI compound thin films angularly by thermal evaporation to investigate the factors that will be responsible for the change of stoichiometry.

1.14 Objectives

1. The fabrication of II-VI semiconductors thin films at different angles by thermal evaporation.
2. The elemental analysis of angular-deposited films will be carried out by x-ray energy dispersive spectroscopy and x-ray photoelectron spectroscopy to investigate the factors that are responsible for the change in the stoichiometry of films.
3. The structural and morphological analysis of the films will be carried out by x-ray diffraction and atomic force microscopy, respectively.
4. The electrical properties will be measured by Hall effect and two-probe method.
5. The optical properties of the films will be carried out by spectrophotometry.
6. The photocurrent of the films will be measured.
7. The effect of angular deposition on the properties of the II-VI compound films will be analyzed.

CHAPTER 2

Theoretical Background

2.1 Thermodynamics of Evaporation

The evaporation of a material and then its deposition on any surface to grow a thin film is one of the oldest techniques to fabricate thin films. Here, we begin with a discussion of the simplest one-component system and consider the equilibrium condition for a condensed phase to coexist with a vapor phase. During thin film deposition, two-phase (solid/liquid and vapor) of a material coexist [70-74].

2.1.1 Equilibrium condition for phase transformation in the one-component system

According to Gibbs phase rule, a single component system can exist simultaneously in two phases α and β in equilibrium at a particular temperature and pressure. We shall probe the situation when one phase is in condense (solid/liquid) form with which it is contacted with another phase that exists in vapor form. At equilibrium condition, the temperature (T) and pressure (P) of the system and the surroundings are the same. At equilibrium, the atoms of one phase can transfer to another phase across the boundaries. The equilibrium condition of the transformation of atoms from one phase to another can be determined by the following procedure [73, 74]. The total Gibbs energy is [74]:

$$G = n^{\alpha}G^{\alpha} + n^{\beta}G^{\beta} \tag{2.1}$$

where n^{α} and n^{β} are the number of moles of the α and β phases, respectively, and G^{α} and G^{β} are the Gibbs free energy per mole of the α and β phases, respectively. The total number of moles of an isolated system remains constant.

$$n^{\alpha} + n^{\beta} = \text{constant} \tag{2.2}$$

Therefore,

$$dn^{\alpha} + dn^{\beta} = 0 \tag{2.3}$$

The change in the number of moles of the α phase must be equal to the change in the number of moles of the β phase. The change in Gibbs free energy due to the transfer of a small amount of α phase to β phase at constant pressure and temperature is obtained by taking the differential of equation (2.1) [74-77]:

$$dG = dn^{\alpha}G^{a} + dn^{\beta}G^{\beta} + n^{\alpha}dG^{a} + n^{\beta}dG^{\beta} \tag{2.4}$$

Gibbs energy is an extensive quantity of the system, so according to Gibbs-Duhem relation [78-80]:

$$n^{\alpha}dG^{a} + n^{\beta}dG^{\beta} = 0 \tag{2.5}$$

Therefore, equation (2.4) can be written as:

$$dG = dn^{\alpha}G^{a} - dn^{\alpha}G^{\beta} \tag{2.6}$$

$$dG = (G^{a} - G^{\beta})dn^{\alpha}$$

Under equilibrium condition, the Gibbs energy is stationary, so [81-84]:

$$dG = 0 \tag{2.7}$$

Here, dn^{α} is arbitrary so we can write equation (2.6) in the following form:

$$(G^{a} - G^{\beta}) = 0 \tag{2.8}$$

Or,

$$G^{a} = G^{\beta}$$

Consequentially, when two phases are in equilibrium, the temperature of the system does not vary at a particular pressure. In two-phase one component system, the change in temperature can be possible when one of the phases disappears [80-84].

2.1.2 Clausius-Clapeyron relation

According to the Gibbs phase rule, a one-component system existing in two phases has one degree of freedom. To maintain the equilibrium, the temperature and pressure of the system are changed in a very specific way. The Clausius- Clapyron relation explains the relation between temperature and pressure changes to maintain the equilibrium between the two phases in a one-component system [85-88]. Gibbs free energy depends on the pressure (P) and temperature (T), so the equilibrium condition can be written in the form [85]:

$$G^{a}(T,P) = G^{\beta}(T,P) \tag{2.8}$$

If a plot was drawn between pressure and temperature, the above relation represents a curve as shown in fig. 2.1.

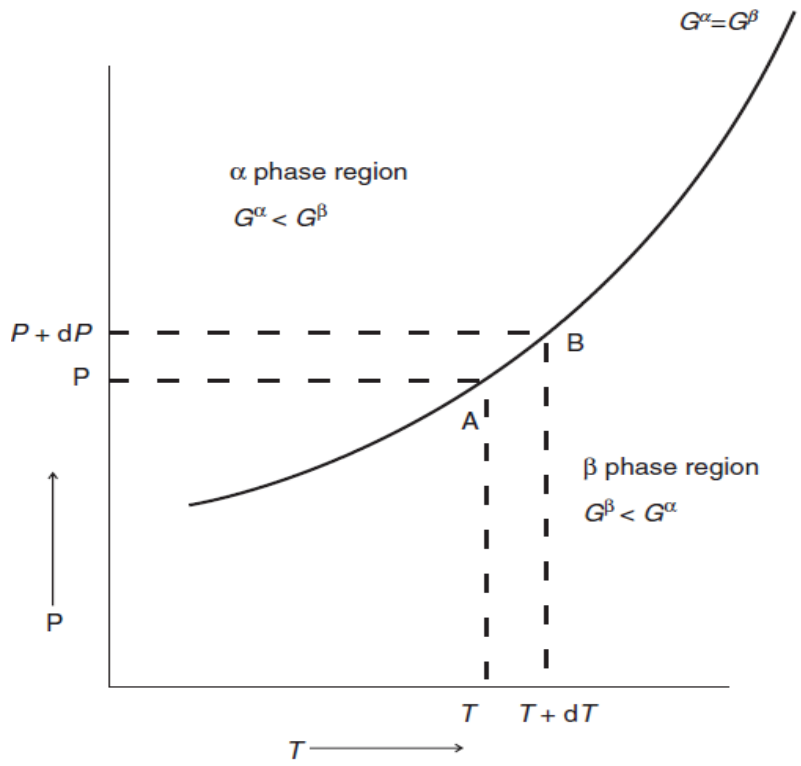

Figure 2.1 Illustration of a relation between temperature versus pressure for a two-phase one-component system at equilibrium

It is clear from fig. 2.1, the α phase is thermodynamically stable above the curve $(G^{a}(T,P) > G^{\beta}(T,P)$ and β phase is stable below the curve $(G^{a}(T,P) > G^{\beta}(T,P)$. The α and β phases are at equilibrium and their Gibbs free energies are equal to each other on the curve. Figure 2.1 also shows that the α phase is stable at low temperature, and the β phase is stable at high temperature. Consider two points along the curve, *A*, and *B*, denoting the equilibrium coexistence of α and β phases. Point *A* corresponds to temperature *T* and pressure *P*, and point *B* corresponds to temperature (*T*+*dT*) and pressure (*P*+*dP*). At equilibrium, the Gibbs free energy of α phase is related to that of β phase as [74, 85]*:*

$$G^{a}(T+dT, P+dP) = G^{\beta}(T+dT, P+dP) \tag{2.9}$$

Subtracting equation (2.9) from equation (2.8), we obtain:

$$dG^{\alpha} = dG^{\beta} \tag{2.10}$$

Using the following thermodynamic relation [91-94]:

$$dG^{\alpha} = V^{\alpha}dP - S^{\alpha}dT = dG^{\beta} = V^{\beta}dP - S^{\beta}dT \tag{2.11}$$

where V is the volume and S is entropy of the system, equation (2.10) can be written in the form:

$$\frac{dP}{dT} = \frac{S^{\beta} - S^{\alpha}}{V^{\beta} - V^{\alpha}} \tag{2.12}$$

$$\frac{dP}{dT} = \frac{\Delta S^{\alpha/\beta}}{\Delta V^{\alpha/\beta}} \tag{2.13}$$

The above equation is known as Clapeyron relation. The enthalpy (H) of a system is related to the change in entropy by the following equation:

$$T(S^{\beta} - S^{\alpha}) = \Delta H^{\alpha/\beta} = H^{\beta}(T,P) - H^{\alpha}(T,P) \tag{2.14}$$

A change in enthalpy $\Delta H^{\alpha/\beta}$ means the system absorbs ($\Delta H^{\alpha/\beta} \geq 0$) or ejects ($\Delta H^{\alpha/\beta} \leq 0$) heat when α and β phases interact with each other. The transformation of α phase to β phase is due to the change of two distinct properties, namely volume and enthalpy. The equation of Clausius-Clapeyron equation is written as [85]:

$$\frac{dP}{dT} = \frac{\Delta H^{\alpha/\beta}}{T\Delta V^{\alpha/\beta}} \tag{2.15}$$

We can simplify equation (2.14) for α phase:

$$\Delta H^{\alpha} = H^{\alpha}(T,P) - H^{0,\alpha}\left(T, P = 1\text{atm}\right) \cong 0$$

$$\Delta S^{\alpha} = S^{\alpha}(T,P) - S^{0,\alpha}(T, P = 1\text{atm}) \cong 0$$

$$\Delta V^{\alpha} = V^{\alpha}(T,P) - V^{0,\alpha}(T,P = 1\text{atm}) \cong 0$$

The superscript zero denotes thermodynamics quantities of the substance in the standard state. The β phase, which is in the vapor phase, obeys the ideal gas law. The enthalpy of β phase depends on the temperature of the gas, and equation (2.14) can be written for β phase as:

$$\Delta H^{\beta} = H^{\beta}(T,P) - H^{0,\beta}(T,P = 1\text{atm}) \cong 0 \qquad (2.16)$$

The entropy of the system in the vapor phase depends on pressure. Therefore, we can write the change in entropy of β phase as [89, 90]:

$$\Delta S^{\beta} = S^{\beta}(T,P) - S^{0,\beta}(T,P = 1\text{atm}) \cong 0 \qquad (2.17)$$

Using the Maxwell relations [91],

$$dS = \left(\frac{\partial S}{\partial P}\right)_T dP = -\left(\frac{\partial V}{\partial T}\right)_p dP = -\frac{R}{P} dP = -Rd(\ln \mathrm{P}) \qquad (2.18)$$

where R is the gas constant, the change in entropy for β phase can be written as [91]:

$$\Delta S^{\beta} = \int_{T,P=1atm}^{T,P} dS = -\int_{P=1atm}^{P=P} -Rd(\ln \mathrm{P}) = -R\ln(P) \qquad (2.19)$$

The change in volume for β phase can be written in the form:

$$\Delta V^{\alpha/\beta} = V^{\beta}(T,P) - V^{\alpha}(T,P) \cong V^{0,\alpha}(T,P = 1\text{atm}) \cong V^{\beta}(T,P) \qquad (2.20)$$

The volume of the solid/liquid phase compared to the volume of the vapor phase is negligible. By substituting the values of entropy change and volume change in equation (2.15), we get the following relation:

$$\frac{dP}{dT} = P\frac{\Delta H^{\alpha/\beta}}{RT^2} \qquad (2.21)$$

$$\frac{d(\ln P)}{dT} = \frac{\Delta H^{\alpha/\beta}}{RT^2}$$

Thus, equation (2.14) can be written as:

$$\Delta H^{\alpha/\beta} = H^{\beta}(T,P) - H^{\alpha}(T,P) \cong H^{0,\alpha}(T, P = 1\text{atm}) - H^{0,\beta}(T, P = 1\text{atm}) = \Delta H^{0,\alpha/\beta}$$

The pressure dependence of change in enthalpy ($\Delta H^{\alpha/\beta}$) is negligible relative to atmospheric pressure. Integrating equation (2.21) shows the dependence of enthalpy difference on temperature. In the simplest approximation, it is assumed that the enthalpy difference is independent of temperature.

$$\ln(\text{P}) = -\frac{\Delta H^{\alpha/\beta}}{RT} + \text{constant} \tag{2.22}$$

A plot of equation (2.22) will yield a straight line between ln(*P*) and 1/*T*. The slope of that equation is equal to $\left(-\frac{\Delta H^{\alpha/\beta}}{R}\right)$, from which, one can determine the enthalpy change of transformation of α and β phases by vapor pressure measurements. For example, the dependence of vapor pressure on the temperature of mercury substance is shown in figure 2.2 [85].

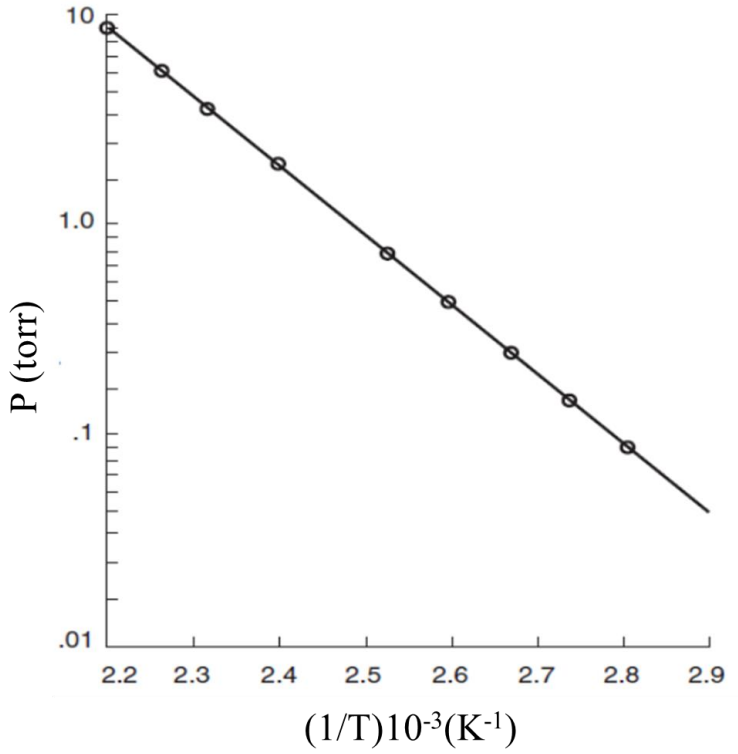

Figure 2.2 Vapor pressure of mercury as a function of temperature at equilibrium

Specific heat data of α and β phases enable us to evaluate the change in enthalpy of each phase with temperature. At fixed pressure, the relation between enthalpy (H) and specific heat (C) can be written according to Kirchhoff's law [90]:

$$d\frac{\Delta H^{\alpha/\beta}}{dT} = \Delta C_P = C_P^{\beta} - C_P^{\alpha} \tag{2.23}$$

Here, we consider the empirical equation of specific heat for each phase [74, 90]:

$$\Delta C_P = \Delta a_1 + \Delta b_1 T + \Delta c_1 T^{-2} \tag{2.24}$$

where,

$$\Delta a_1 = a_1^{\beta} - a_1^{\alpha}\ ,\Delta b_1 = b_1^{\beta} - b_1^{\alpha}\ ,\Delta c_1 = c_1^{\beta} - c_1^{\alpha}$$

In this empirical expression, a_1, b_1, and c_1 are constants. The constant a_1 reflects the value of specific heat at high temperature according to Dulong and Petit law [74, 90]. In the

second term, b_1 is positive and reflects that the specific heat increases by increasing the temperature. The constant c_1 is negative and it reflects the specific heat at low temperature. At low temperature, some vibrations of atoms are frozen out and the specific heat decreased. By inserting equation (2.24) in equation (2.23) and integrating the resultant equation, we get:

$$\Delta H^{\alpha/\beta} = \Delta H_0 + \Delta a_1 T + \frac{1}{2}\Delta b_1 T^2 - \frac{\Delta c_1}{T} \tag{2.25}$$

Putting equation (2.25) into (2.21):

$$d(\ln P) = \frac{\Delta H^{\alpha/\beta} dT}{RT^2}$$

$$= \left[\Delta H_0 + \Delta a_1 T + \frac{1}{2}\Delta b_1 T^2 - \frac{\Delta c_1}{T} \right] \frac{dT}{RT^2}$$

$$= \left[\frac{\Delta H_0}{RT^2} + \frac{\Delta a_1}{RT} + \frac{1}{2}\frac{\Delta b_1}{R} - \frac{\Delta c_1}{RT^3} \right] dT$$

By integration, we get:

$$\ln(P) = \left(-\frac{\Delta H_0}{RT} + \frac{\Delta a_1}{R}\ln T + \frac{1}{2}\frac{\Delta b_1 T}{R} + \frac{1}{2}\frac{\Delta c_1}{RT^2} \right) + I \tag{2.26}$$

Here I is a constant. The plot between In(P) and 1/T based on the above equation is shown in fig. 2.3. It is clear from fig. 2.3, the plot between In(P) and 1/T is not a straight line. The value of the change in enthalpy (ΔH_0) can be measured by two ways: measuring the vapor pressure (P) at different temperatures (T), or can be taken from already published data [85, 90]. The phase diagram of the one-component system is constructed and is shown in figure 2.4. From the already published data, it was noticed that the enthalpy of sublimation of solids is greater than the enthalpy of evaporation of liquids, so the slope of the curve for solid-vapor equilibrium is greater than the slope of

the curve of liquid-vapor equilibrium. There is a small difference in molar volumes of solid and liquid, so the curve of pressure versus temperature is very steep. One-component phase diagram can be divided into three regions. It is clear from the phase diagram, the solid phase is stable at low temperature and high pressure; liquid phase is stable at high temperature and high pressure, and vapor phase is stable at high temperature and low pressure. At each curve, two phases are in equilibrium. The liquid/vapor phase curve ends at a critical point, where the surface energy of the liquid/vapor phase boundary becomes zero and the boundary between liquid and vapor phase vanishes [85, 90].

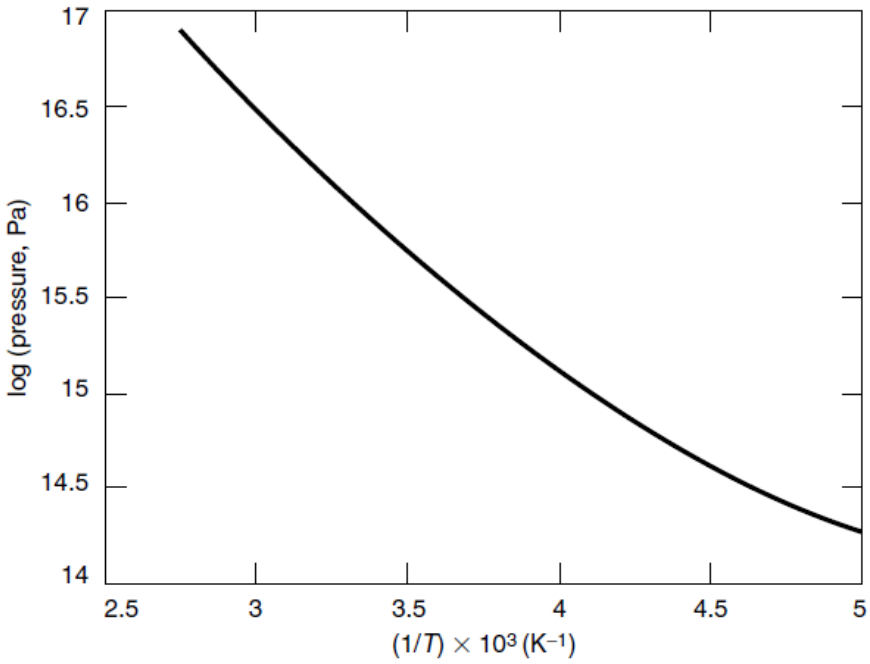

Figure 2.3 Vapor pressure of water as a function of inverse temperature at equilibrium

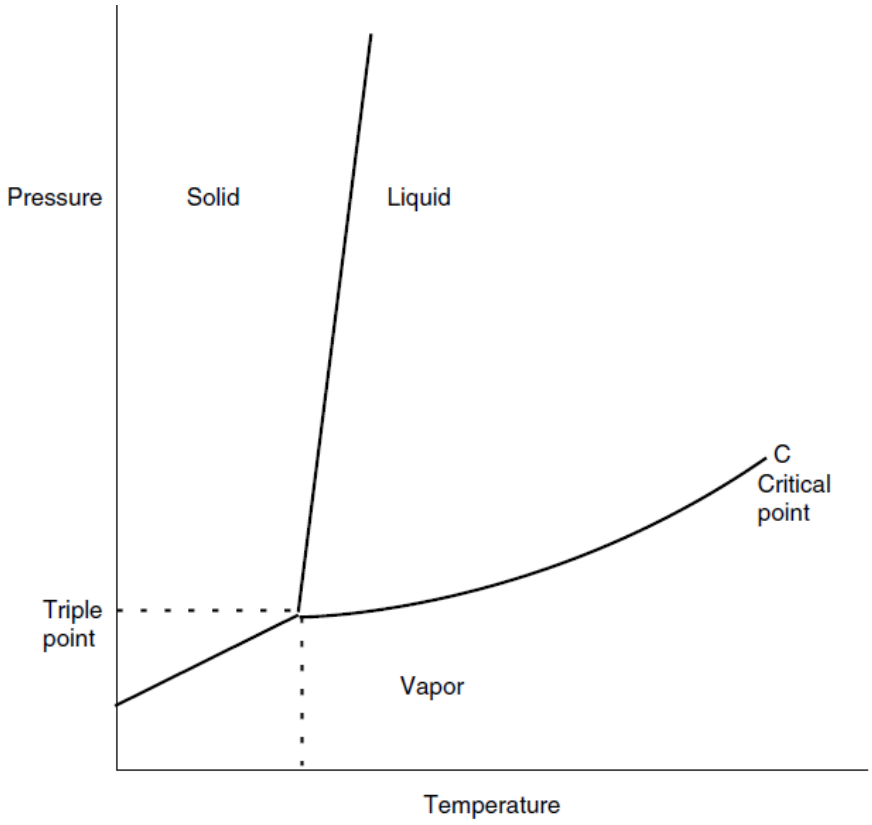

Figure 2.4 One-component phase diagram

At triple point, all the three phases are in equilibrium. It is clear from the one-component phase diagram that if the pressure of the system is below the triple point then the material will sublimate [90]. The one-phase diagram is very useful to know the triple point of a substance to know the vapor pressure of a particular material below that value at which the material is sublimated. The formation of a film by sublimation of a material necessitates avoiding the impurity in the film because the impurities have different vapor pressures. At high vacuum, the material will sublimate to avoid the contamination of material, and the collisions with the atoms of the gaseous phase will decrease, and particles move in a straight line [91-94].

2.2 Mass transport rate and diffusion

Maxwell and Stefan explained the theory of diffusion of multispecies in the gas phase. The Maxwell equation for diffusion of species *A* through species *B* was [69, 95]:

$$dP_A = \alpha_{AB} \frac{\rho_A \rho_B}{M_A M_B} (u_A - u_B) dy \tag{2.27}$$

where P_A is the particle pressure of *A* along a distance *y*, ρ_A, and ρ_B are the densities of species *A* and *B*, M_A and M_B are the molar weights, u_A and u_B are the velocities of the species *A* and *B* in the direction of net diffusion, and α_{AB} is a proportionality constant. Commonly, the rate of diffusion or the mass flux of species *A* in moles per unit time per unit area is [69, 70, 95]:

$$J_A = \frac{u_A \rho_A}{M_A} \tag{2.28}$$

For a multispecies system, the Maxwell equation can be written as [95]:

$$-\frac{dPi}{dy} = \sum_{j=1} r_{ij} (J_i P_j - J_j P_i) \tag{2.29}$$

i= A, B, C……

where $r_{ij} = \alpha_{ij} = RT / D_{ij} P$

Here, D_{ij} is the binary diffusion coefficient. Equation (2.29) holds only when the pressure *P* and temperature *T* remain constant throughout the volume of the system in which the diffusion takes place [68, 95]. II-VI compounds dissociate into their constituents on sublimation. Therefore, two Maxwell equations are needed to be solved. In II-VI compound case, the mass flux of II element and the mass flux of VI element were dependent on each other. Since one of the equations of flux is considered independent because the total pressure (*P*) remains same.

Obviously,

$$J = J_A = 2J_B \tag{2.30}$$

$$J_B = 3\frac{J}{P}P_B - \frac{2}{r_{AB}P}\frac{dP_A}{dy} \tag{2.31}$$

J_A and J_B are the diffusion components, P_A and P_B are the partial vapor pressures, of II and VI elements, respectively. P_A and P_B pressures are related according to the following equations [95]:

$$P_A(y) = \frac{2}{3}P + \left[P_A(L) - \frac{2}{3}P\right]\exp\left[\frac{3}{2}Jr_{AB}(L-y)\right] \tag{2.32}$$

$$P_B(y) = \frac{1}{3}P + \left[P_B(L) - \frac{1}{3}P\right]\exp\left[\frac{3}{2}Jr_{AB}(L-y)\right] \tag{2.33}$$

The total diffusion component J derived from the above equations can be written as:

$$J = \frac{2}{3}\frac{D_{AB}P}{RTL}\ln\frac{P_A(0) - \frac{1}{3}P}{P_A(L) - \frac{1}{3}P} \tag{2.34}$$

$$J = \frac{2}{3}\frac{D_{AB}P}{RTL}\ln\frac{P_B(0) - \frac{1}{3}P}{P_B(L) - \frac{1}{3}P} \tag{2.35}$$

where L denotes the position of the source and 0 denotes the position of the substrate surface. Moreover, consider the flux is moving along y-axis and J is positive along the y-axis. From Eq. (2.34), one can find that when P_A = (2/3)P, or equivalently α (L)= $P_A(L)/P_B(L)$ = *2*, the flux J is infinite, in which case, the mass transport is no longer limited by diffusion or by stoichiometric excess. This condition is also quoted in literature as P_{min} because it corresponds to a minimum in the total pressure [68]. For

example, in the case of ZnSe, the mass transport rate for different α values are shown in fig. 2.5.

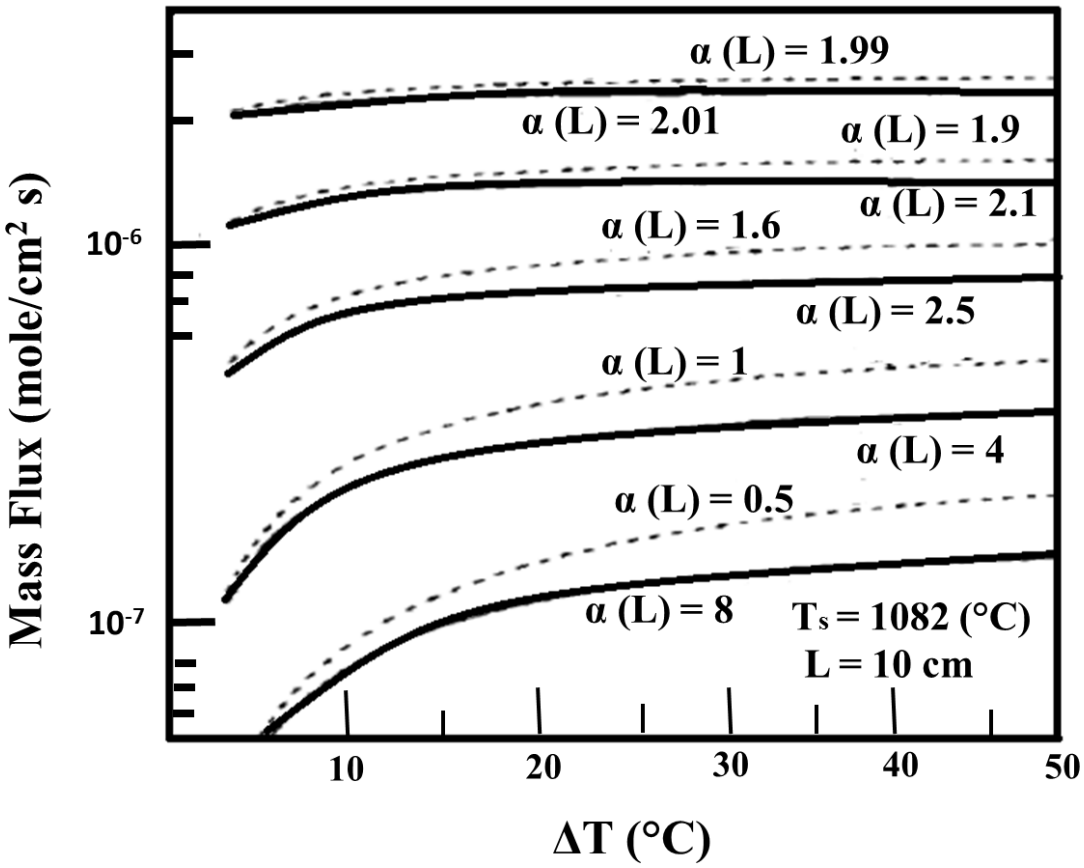

Figure 2.5 Calculated mass flux of ZnSe as a function of ΔT for source temperature (T_s) at 1080 °C and different values of α(L).

It is clear from fig. 2.5 that the mass flux is maximum when the source material is stoichiometric (α (L) = P_{Zn}/P_{Se} = 2), and thus material sublimates congruently. It is also clear from fig. 2.5 that the mass flux decreases as the value of α moves away from 2 [95]. When the source material is non-stoichiometric, then the composition of vapor phase will be different $(\alpha \neq 2)$ from the source material until the source material becomes stoichiometric [95]. Therefore, it is practically impossible to grow a film with desired elemental composition by weighing the constituent elements.

2.3 Collisions during transport

The molecules of a gas collide and exert forces on each other during collisions. In the simplest case, the collisions among the molecules are considered as elastic collisions. The volume of the molecules is negligible compared to the volume of the gas. The deposition of a film by transport of vapors is based on the kinetic theory of gases. The molecules of evaporating materials collide with each other during transport. The important factor of collision phenomena is the mean free path. Let us consider N_1 molecules that collide with each other as they travel. We are interested at any stage in the number of molecules that remain without collisions at any instant (n_w). Consider a molecule that travels an additional distance dx along its path, a collision is likely to occur. It is rational to assume that the number of collisions that occur during additional dx is proportional to both n_w and dx, so the number of molecules those face collision can be removed from n_w:

$$dn_w = \left(-P_b \times n_w\right) dx \tag{2.36}$$

where the negative sign denotes that n_w has decreased and P_b is a constant and represents the collision probability for a gas.

Integrating equation (2.36)

$$\ln n_w = -P_b x + \text{constant} \tag{2.37}$$

Since $n_w=N_1$ at $x=0$

$$n_w = N_1 \exp(-P_b x) \tag{2.38}$$

By putting the values of n_w in equation (2.36), we obtain

$$dn_w = P_b N_1 \exp(-P_b x)\, dx \tag{2.39}$$

The number of molecules that suffer a collision n_c are

$$n_c = N_1 - n_w \tag{2.40}$$

Therefore,

$$dn_c = d(N_1 - n_w) = -dn_w = P_b N_1(-P_b x)dx \tag{2.41}$$

The above equation (2.41) represents the number of molecules with free paths between x and $x+dx$. The average or mean free path is given by λ_f and it can be evaluated by the following expression.

$$\lambda_f = \frac{\int_{n=0}^{N} x dn_c}{\int_{n=0}^{N} dn_c} = \frac{\int_{n=0}^{N} x P_b N_1 \exp(-P_b x)dx}{\int_{n=0}^{N} dn_c} \tag{2.42}$$

$$\lambda_f = \frac{-N_1\left[xe^{-Px} + xe^{-Px}/P_b\right]_0^{\infty}}{N_1} = \left(\frac{1}{P_b}\right)$$

Hence,

$$n_w = N_1 \exp\left(\frac{-x}{\lambda_f}\right)$$

This equation relates the number of molecules that move without collisions with the mean free path λ_f. In high vacuum, the mean free path of the evaporating molecules is increased [97].

2.4 Collision phenomenon between II and VI molecules during evaporation

The II-VI compounds dissociate during thermal evaporation into monatomic II and diatomic VI_2 molecules and transport from source to substrate surface [69]. According to the kinetic theory gases, the atoms of II and VI_2 molecules will collide with

each other during transport. In high vacuum, the dissociative molecules will collide with each other and might deflect at different angles after collisions because of the difference in their masses.

CHAPTER 3

Angular Deposition

3.1 Background

Nanowires and nanorods are the anisotropic nanostructures and have large aspect ratio compared to nanoparticles. The diameter of these nanostructures varies from 1 to 200 nanometers, and length varies up to several micrometers [98-100]. The nanostructures are the building blocks of photonic, nanoelectronic, bioengineering, photovoltaic, and photocatalysis fields. The fabrication of different types of nanostructures with controlled geometry has stimulated research in these fields [98-102]. The nanostructures have unique and fascinating properties such as higher luminescence, superior mechanical properties, and high thermoelectric properties [103, 104]. Homogeneous and stoichiometric nanowires are successfully used as field effect transistors, gas sensors, light emitting diodes, photodetectors, and logic gates [103, 104]. Recently, researchers fabricated the nanostructures with controlled composition to enhance their properties. The controlled composition fabricated nanostructures are known as “superlattice” nanostructures. The superlattice nanostructures enhance the versatility and application of nanoelectronics, photonics, and bioengineering applications [103-105].

One important issue related to nanostructure growth is how to grow the nanostructures in the most effective and controlled way [106, 107]. Therefore, there are four general methods, which are used to grow the nanostructures. These are nanolithography-based method, solution-based method, vapor-based method, and template-based method [106, 107].

The nanolithography-based method is extensively used to construct the sophisticated nanostructures. For the fabrication of different types of nanopatterns, the advanced lithography techniques like x-ray lithography, electron-beam lithography, or proximal lithography were used. Lithography is an expansive technique and the fabrication of nanostructures by lithography is a very slow process. The aspect ratio of nanostructures fabricated by lithography is also limited. Therefore, this technique is not appropriate for the fabrication of nanostructures at large scale [108-110].

The solution-based process was also commonly used for the fabrication of nanostructures. In this process, a mixed solvent with a known metal precursor and a suitable crystal regulating agent were placed in an autoclave at a high pressure and temperature. This process is also complicated and needs a deep knowledge of chemical reactions. The prepared nanostructures from this process usually contain some unwanted elements like nitrogen and chlorine because of the use of different solvents and catalysts [111, 112].

The vapor-based method is also used to grow the nanostructures of different materials. In this process, the material vapors react in the presence of a suitable catalyst to grow the nanostructures. For this method, a specific catalyst is required for a particular material, and relatively high growth temperature is required [113].

Template-based method, in general, is used to grow the anisotropic nonporous materials. The templates of different types such as anodized alumina, block copolymer membranes, polycarbonate membranes etc., serve as host. The nano-templates are filled with sol-gel solution, or vapor, to make the desired nanopatterns. The products may be removed from the templates by moving the host matrix [114-116].

Various types of nanostructures can be fabricated based on the process mentioned above. However, there are still many challenges to fabricate the controlled geometry of nanostructures by a given method [106-117].

3.2 Fabrication of nanostructures by angular deposition

Recently, different types of nanostructured films were fabricated by angular deposition. To grow nanostructures by angular deposition, the commonly used techniques like e-beam evaporation, sputtering, thermal evaporation, laser deposition were used. The simple modification of these techniques enables us to grow the different types of nanostructured films. In an angular deposition, the growth of the nanostructured films was due to shadowing effect that was raised by oblique angles [117, 118]. The angular deposition has several advantages in term of controlling the growth of the nanostructures:

1. Naturally columnar structures are formed.
2. The density and porosity of the thin film can be controlled.
3. There is no limit on materials selection because the growth process is physical vapor deposition.
4. The alignment of nanostructures can be controlled due to the shadowing effect.
5. It has an ability to grow the three-dimensional nanostructures.

There are two types of angular deposition methods, which are used to grow nanostructures [118-121].

(i) Oblique angle deposition

(ii) Glancing angle deposition

3.2.1 Oblique angle deposition

In oblique angle deposition, the flux of vapors arrives on the substrate surface at non-normal angle γ that produce an inclined columnar structure on the substrate surface. In oblique angle deposition, the substrate does not rotate during deposition. In this geometry, only columnar structures are formed. The schematic diagram of oblique angle deposition is shown in fig. 3.1 [122, 123].

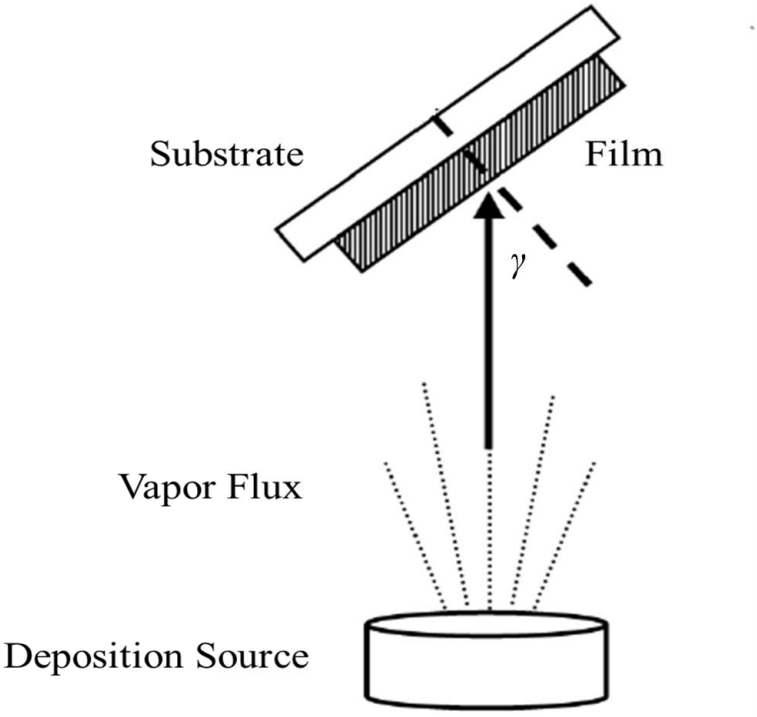

Figure 3.1 Schematic diagram of oblique angle deposition

Assume that the incoming flux has an angle γ with the normal to the surface and treat it as a vector quantity$\vec{F}$. The quantity $\vec{F}$ can be resolved into two components as shown in fig. 3.2.

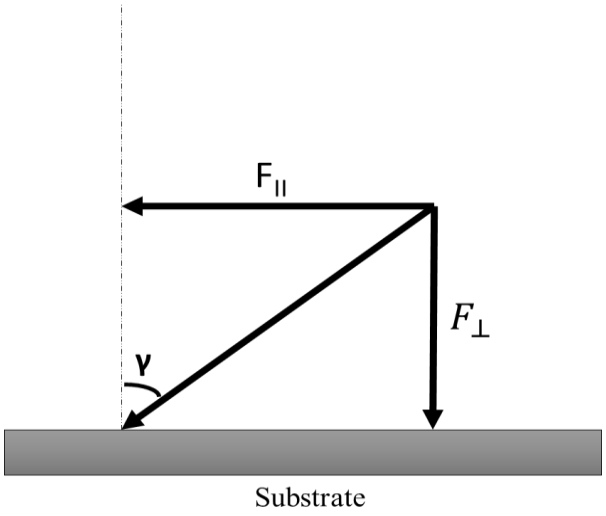

Figure 3.2 The incoming flux F decompose into their components, $F_{\perp}$ is perpendicular to the substrate surface, and $F_{\parallel}$ is flux parallel to the substrate

The incoming flux has two components, a horizontal component ($F_{\parallel} = F\cos\gamma$) and a vertical component ($F_{\perp} = F\cos\gamma$). During the film deposition, initially, the incoming atoms will grow islands on the substrate surface as shown in in figure 3.3.

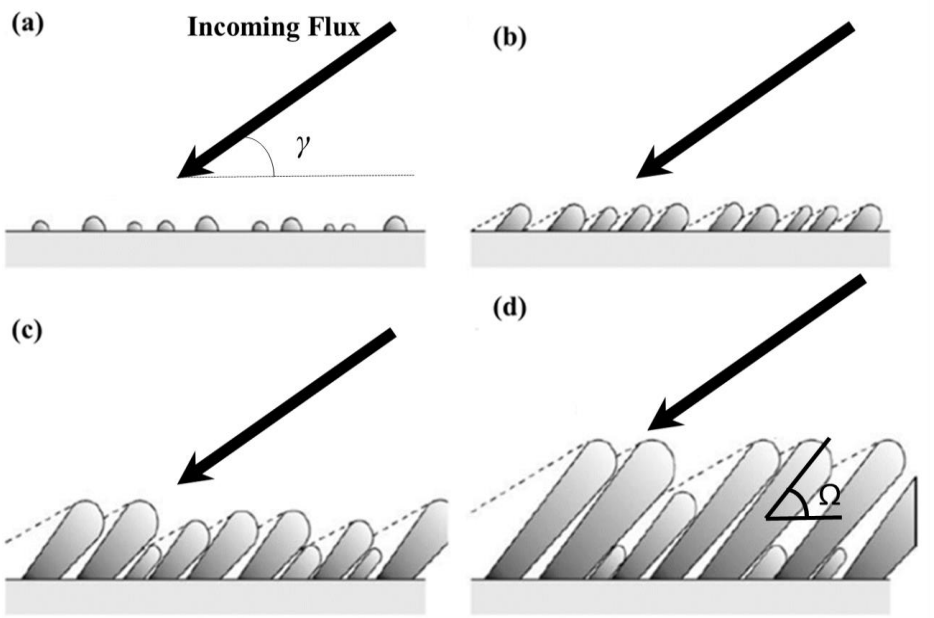

Figure 3.3 Schematic view of oblique angular deposition growth: (a) initial arrival of vapor flux at angle *γ*, creating a random distribution of nuclei; (b) nuclei growth casting shadows across the substrate; (c) columns growth, partially shadowing of small neighbors; (d) columns growth at oblique angle *γ*, completely shadowing of large columns and some columns become extinct

As the deposition proceeds, the initially nucleated islands act as shadow centers. Therefore, all the tall islands will receive more atoms as compared to the shadowed ones. This process will lead a nanocolumnar structure. Clearly, the lateral component $F_{\square}$ is the source of shadowing effect. At a particular incident angle of flux with respect to the normal of the substrate, the grown nanocolumns have a tilting angle **Ω** with respect to the normal of the substrate surface. The tilting angle **Ω** of nanocolumns depend on the incident angle of impinging flux. Figure 3.4 shows the cross-sectional SEM images of Si films, which were grown at different incident angles [124]. Cross-sectional SEM images showed that at 0˚, the deposited film was uniform and continuous; at 30˚, the small columns start to grow; at 60˚, the columns become prominent; and at 80˚, the columns structure was more obvious [124].

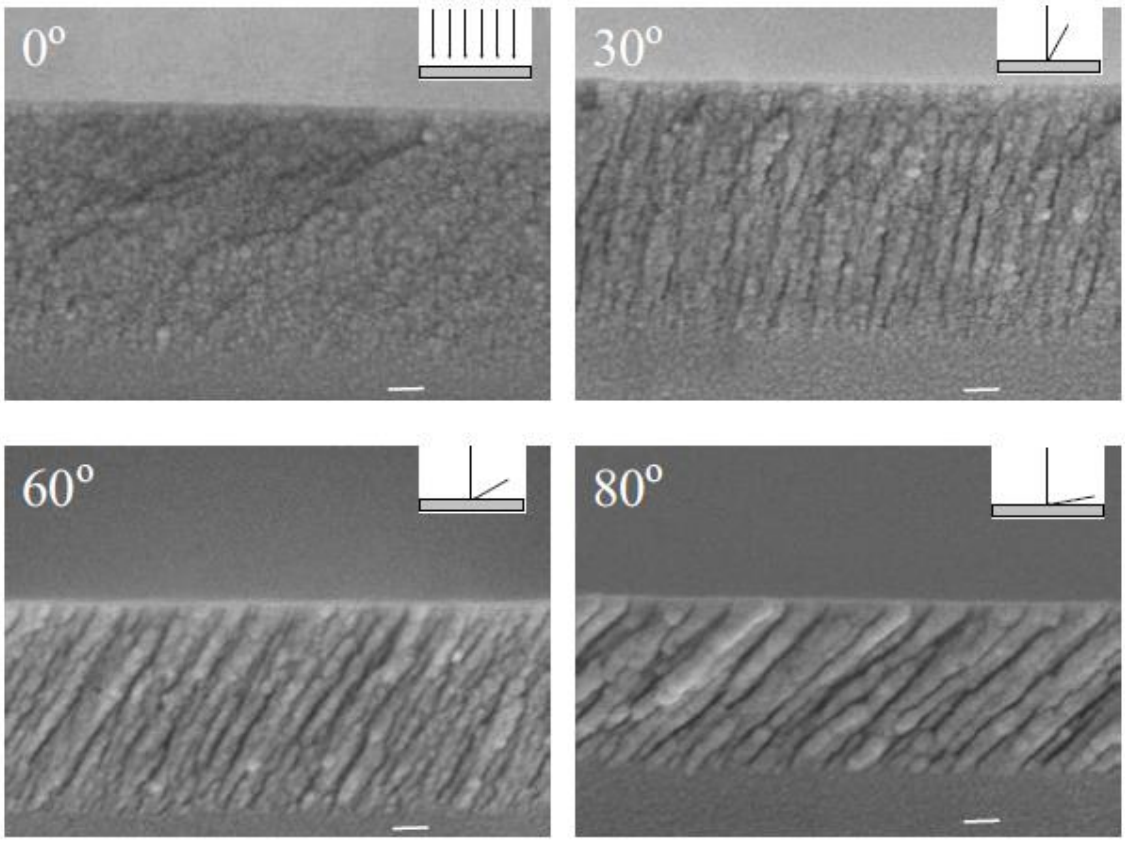

Figure 3.4 Cross-sectional SEM images of silicon films deposited at different incident angles

In general, the columns tilt angle Ω is less than the incident angle γ. The dependence of tilt angle Ω of columns on the incident angle can be written by Tait relation [124]:

$$\Omega = \gamma - \sin^{-1}\left(\frac{1-\cos\gamma}{2}\right) \tag{3.1}$$

3.2.2 Glancing Angle Deposition

In oblique angle deposition, the nanocolumnar films were generated and can be treated as one kind of nanostructure. The preferred tilting angle Ω introduces the anisotropy in the film, which is not desirable in most of the cases [28]. For better control of structure and orientation of nanostructures, glancing angle deposition technique was

developed. The schematic diagram of glancing angle deposition is shown in fig. 3.5. The basic setup of glancing angle deposition is the same as that of oblique angle deposition. The main difference is the substrate is attached with tow motors, one controls the incident angle of the incoming flux and the other controls the azimuthal rotation of the substrate. In glancing angle deposition, the degree of freedom of deposition is increased, and hence, the deposition can be done by only changing the azimuthal rotation of substrate at a fixed incident angle or by changing both the azimuthal rotation and the incident angle [128].

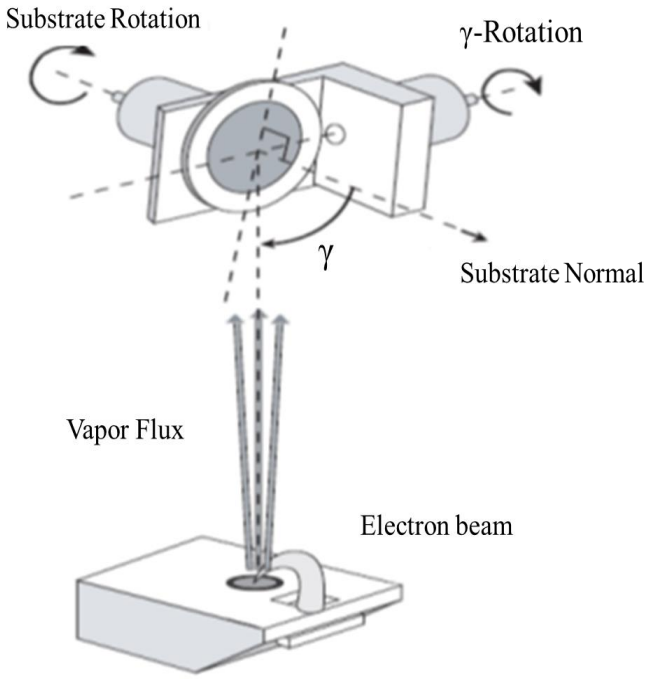

Figure 3.5 Glancing angle deposition set up

By the combination of the two rotations of the substrate as well as deposition rate, the nanostructures can be sculptured in S-shaped, C-shaped, matchsticks, zig zag shape, vertical, and helical columns [126, 127]. Cross-sectional SEM images of different types of microstructures of Si prepared by glancing angle deposition are shown in fig. 3.6 [128].

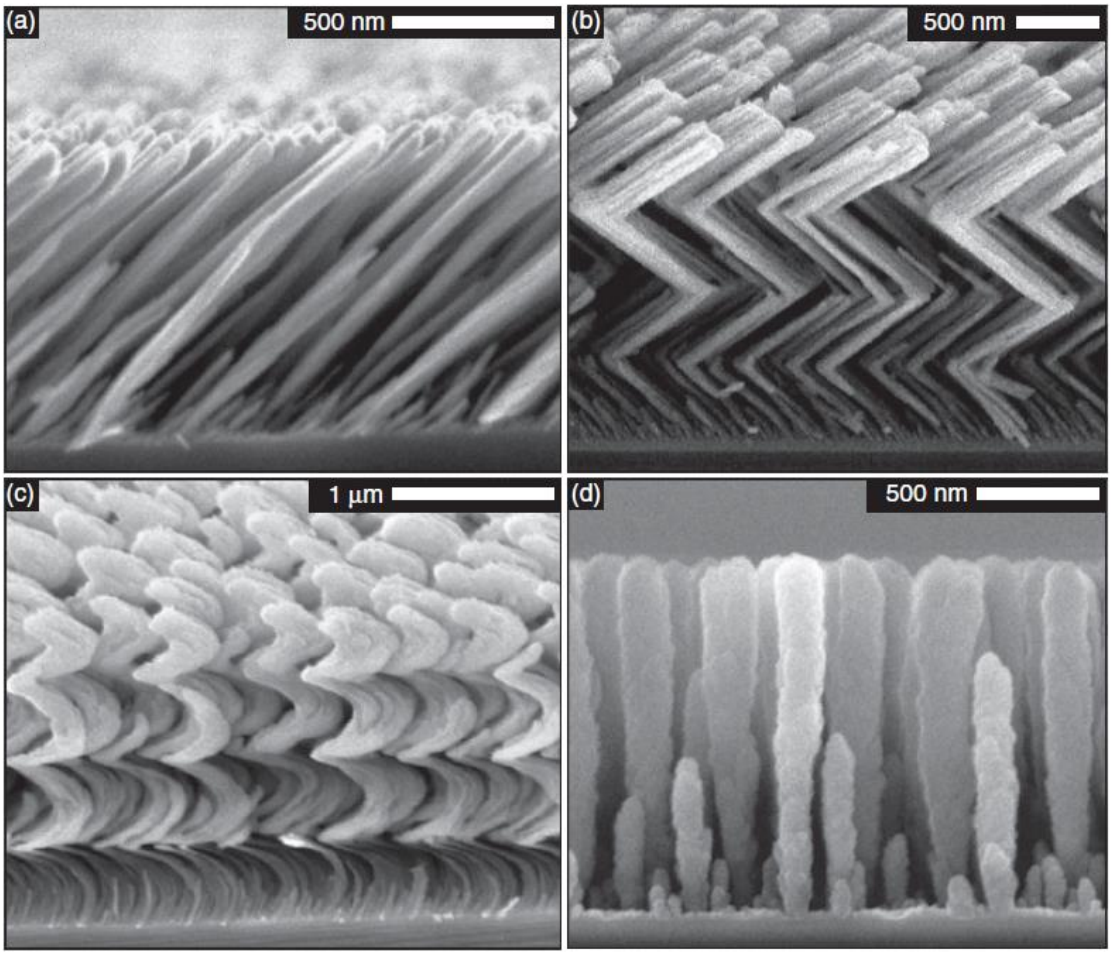

Figure 3.6 Different type of microstructures of Si prepared by glancing angle deposition

3.3 Requirements for angular deposition

3.3.1 Pressure requirement

For angular deposition, shadowing of incoming flux is a critical point. As a result, the evaporated molecules should have a large average free path compared to the dimensions of the chamber of the system. For a typical system, the distance between the source and substrate should by larger than 30 cm, and a vacuum pressure of the chamber $\approx 10^{-3}$ mbar is required.

3.3.2 Vapor source

Different vapor sources have been used for angular deposition, including pulsed laser deposition, thermal evaporation, electron-beam evaporation, sputtering, and co-sputtering. Some materials, which were deposited by angular deposition using different vapor sources, are summarized in Table 3.1 [117].

Table 3.1 summary of the materials and vapor sources used

Material	Deposition method	Material	Deposition method
Aluminum	Thermal, e-beam	WO_3	Sputter, thermal
Chromium	Thermal, sputter	Y_2O_3: Eu	e-beam
Cobalt	e-beam, thermal	$Zr_{65}Al_{7.5}Cu_{27.5}$	e-beam
Germanium	e-beam	ZrO_2	e-beam
Tantalum	e-beam, sputter	Alq_3	Thermal
Al_2O_3	e-beam	C_{60}	Thermal
CeO_2	e-beam	CuPc	Thermal
Carbon	PLD	Parylene C	Nozzle
ITO	e-beam	Pentacene	Thermal
MgF_2	e-beam	PPX	Nozzle
SiO	e-beam	Znq_2	Thermal
Nb_2O_5	e-beam	Acrylates	Spin-coating
SiO_2	e-beam	Copper	Electroplating
TiO_2	e-beam	Nickel	Electroplating

e-beam: electron beam; PLD: pulsed-laser deposition

3.3.3 Substrate Motion

For angular deposition, the substrate should move to any orientation between (0, 0) and (π/2, 0). This can be accomplished by attaching two motors to the substrate. One

motor can be used to control the incident angle of vapor flux and the second can be used to control the rotation of substrate about its axis of rotation [117, 128].

3.3.4 Monitoring requirements

For the fabrication of high quality nanostructures by angular deposition, the control of the rate of vapor flux is very important. The deposition rate is defined as the increase of film thickness per unit time at (0, 0) orientation of the substrate. Crystal thickness monitor was used to monitor the deposition rate of vapor flux. In an angular deposition, the substrate does not have (0, 0) orientation. Therefore, the crystal thickness monitor should by aligned along the substrate surface before deposition to get the accurate deposition rate [117].

3.4 Density of Film

As a result of angular deposition, the columnar-structured films were grown based on the shadowing effect. Because of the shadowing effect, the porosity of the films was increased that resulted in the decrease of film density. The density of the film depends on the angle of vapor flux with respect to the normal to the substrate surface. The dependence of density on the incident angle was described by the following equation [117].

$$\rho = \rho_0 \frac{2\cos\gamma}{1+\cos\gamma} \tag{3.2}$$

ρ is the density of film that was deposited at any angle, ρ_0 is the density of film that was deposited at 0˚. It was clear from the above equation that the density of the film was

decreased by increasing the deposition angle because of the increase in porosity due to shadowing effect.

3.5 Proposed equations of film density of the angular deposited II-VI compound

Most of the materials, like metals and metal oxides, do not dissociate by evaporation. The film density of the angular deposited non-dissociative material is a function of incident angle. II-VI compounds dissociate during evaporation and the stoichiometry of the deposited films various from that of the source material. The deposited films will be II (metal) element rich or VI (chalcogen) element rich, which will effect the density of the film because the density of II or VI elements differs from the density of the II-VI compound. The density of the angular deposited II-VI compound film will not only depend on the incident angle but also on the density and concentration of the rich element (II or VI). The proposed equations for angular deposited II-VI film are given below:

If the film is chalcogen-rich then the film density will be:

$$\rho = \rho_0 \left(\frac{2\cos\gamma}{1+\cos\gamma}\right) * \left(\frac{\varphi_{VI}}{\varphi_{II-VI}} * \frac{X_{VI}}{X_{II}}\right) \tag{3.3}$$

If the film is metal-rich then film density will be:

$$\rho = \rho_0 \left(\frac{2\cos\gamma}{1+\cos\gamma}\right) * \left(\frac{\varphi_{II}}{\varphi_{II-VI}} * \frac{X_{II}}{X_{VI}}\right) \tag{3.4}$$

where $\varphi_{II,}$ φ_{VI} and $\varphi_{II\text{-}VI}$ are the densities of II element, VI element, and II-VI compound, respectively. X_{II} and X_{VI} are the concentrations of II and VI elements in the films, respectively.

CHAPTER 4

Experimental Techniques and Experimental Procedure

4.1 Energy Dispersive X-ray Spectroscopy

X-ray spectroscopy is a technique that uses the characteristic x-rays of materials to identify the elements and determine their elemental compositions. In this technique, a high-energy electron beam irradiates the sample and the atoms of the sample emit the characteristic x-rays [129, 130]. The interaction of the electron beam with the sample is shown in fig. 4.1

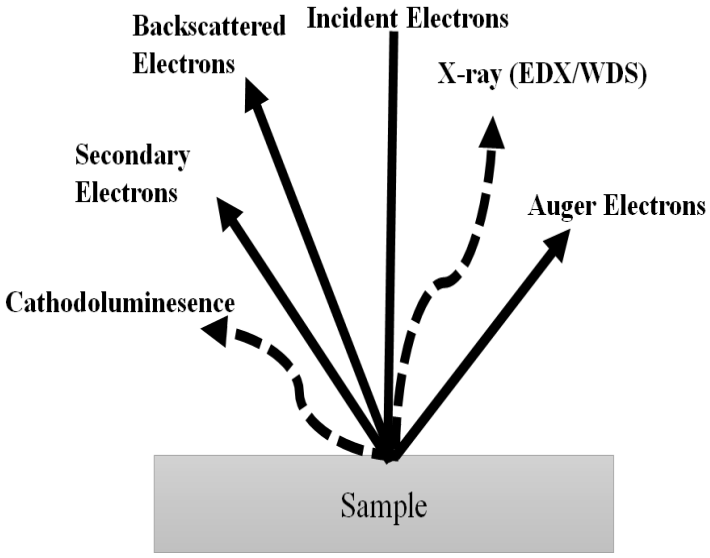

Figure 4.1 Schematic illustrations of the principal results of the interaction of an electron beam with a sample

From the characteristic x-ray emitted from the sample atoms, chemical elements can be identified using two techniques: (i) energy dispersive x-ray spectroscopy (EDX), and (ii) wavelength dispersive x-ray spectroscopy (WDX). In EDX analysis, the energy and the intensity of the emitted x-ray are analyzed in a manner that identifies the

elements and their respective concentrations in the analyzed region of the specimen. The most commonly used instruments for this analysis are electron microscopes equipped with EDX detectors. In electron microscopes, the energetic electron beam generate the characteristic x-rays from the specimen atoms. EDX detector uses these characteristic x-rays to examine the chemical composition on a microscopic scale [129, 130]. When a high energetic electron beam hits the atoms of the specimen, it ejects electrons from the core levels of the atoms and creates vacancies. To fill these vacancies, the electrons of the upper shell jump to lower shells and emit the characteristics x-rays. The illustration of this phenomenon is shown in fig. 4.2.

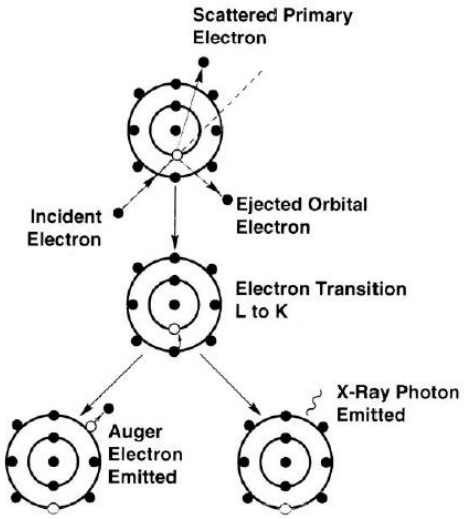

Figure 4.2 X-ray and Auger electron emission through electron transition resulting from ejected k-shell electrons

Each element has unique orbital transition energies or atomic energy levels. Therefore, electron transitions between any two shells result in the release of x-ray photoemission with an energy unique to that element. The chemical composition can be found by integrating the area under the intensity peak. EDX analysis provides a plot of intensity or x-ray counts vs. its energy [131].

4.2 X-ray photoelectron spectroscopy

X-ray photoelectron spectroscopy (XPS) is a surface and chemical analysis technique in which a sample is irradiated with an x-ray beam, and the energies of the resulting photoelectrons are measured. The working of XPS technique is based on the photoelectric effect. A high energetic x-ray beam is incident on a material and the electrons of the core levels of the atoms of the sample are ejected. The kinetic energies of the ejected electrons are measured by using an electron spectrometer [132, 133]. By using the law of conservation of energy, the binding energy of the ejected electrons is calculated:

$$h\nu = E_B + E_k + \phi_{spec} \tag{4.1}$$

where $h\nu$ is the energy of incident x-ray, E_B represents the binding energy of the photoelectron, and it is characteristic of the orbitals from where the electrons are ejected, E_k is the kinetic energy of the ejected photoelectron, and ϕ_{spec} is the work function of the spectrometer. The photoelectric effect is illustrated schematically in fig. 4.3 [134].

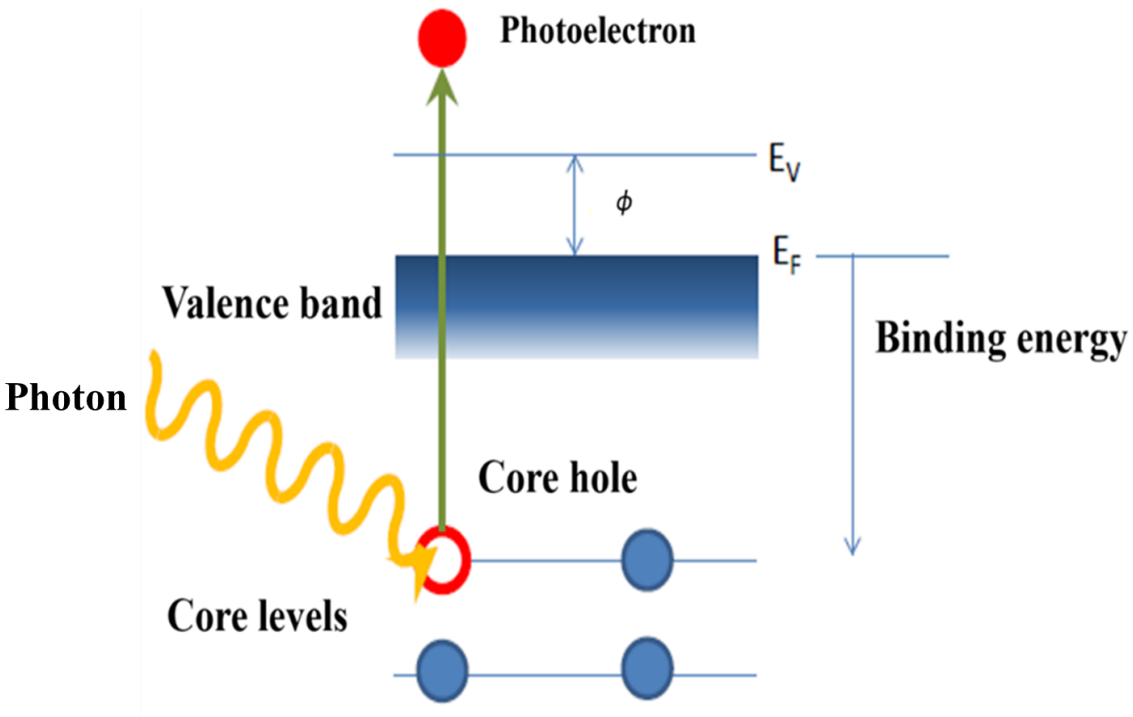

Figure 4.3 Illustration of the photoelectric effect

The study of kinetic energies of the ejected photoelectrons provides a lot of knowledge about the material. XPS can identify all elements except hydrogen and helium. Elemental recognition can be accomplished by chemical oxidation state, chemical shift, and surrounding environment of a particular atom. XPS imaging and angle-resolved XPS provide information about spatial atomic distribution and variation in composition near the surface [132-135]. The graphical representation of XPS is shown in fig. 4.4. It is clear from the graphical representation that the kinetic energy (E_k) of the ejected electron is directly related to the binding energy (E_B) of the orbitals of the specimen, and it is also noticed that the kinetic energy of the ejected electron does not depend on the work function (ϕ_{sample}) of the specimen. It depends on the work function

(ϕ_{spec}) of spectrometer that is a constant for a particular XPS setup and it acts as a reference point [136-139].

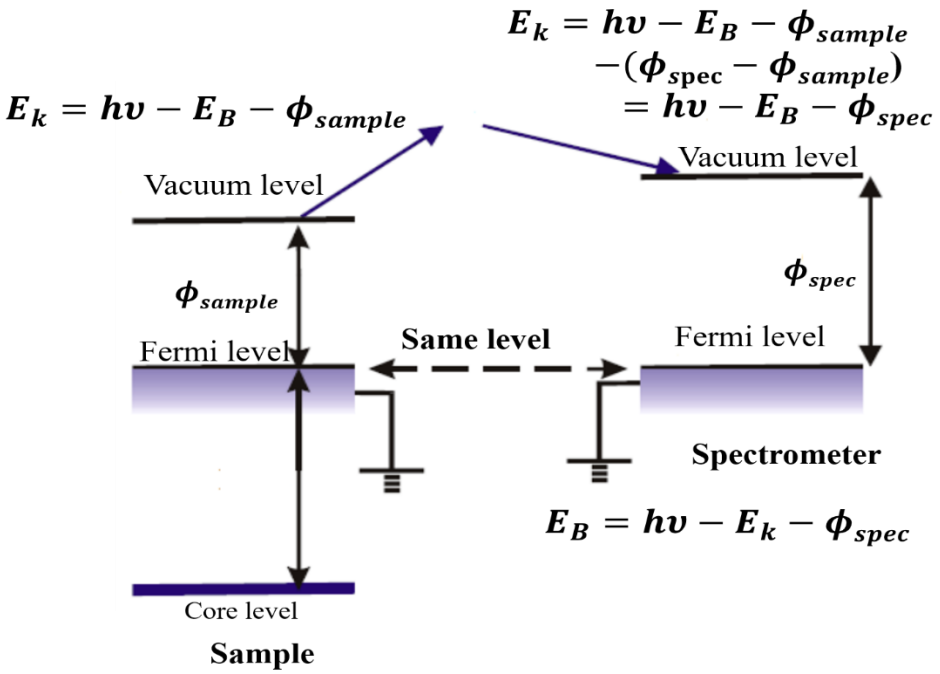

Figure 4.4 Graphical representation of XPS setup

4.3 X-ray Diffraction

X-ray diffraction (XRD) is a widely used technique for the characterization of the structure of a material. It can be used for both the liquid and the solid phase of a material. The basic principle of this technique lies on the interaction of x-rays with the atoms of a material. Each material has a different crystal structure due to the arrangement of atoms in it. When x-rays interact with these atoms, they diffract and create a unique diffraction pattern. This diffraction pattern can be used as a finger print to identify the material [140, 141]. The diffraction phenomenon is governed by Bragg's law. It states that constructive interference will occur if the path difference of two rays, interacting with the atoms of the

lattice planes, is an integral multiple of their wavelength. Constructive interference in a certain direction and the production of diffracted x-rays is governed by the Bragg's equation:

$$2d_i \sin\theta = m\lambda_x \tag{4.2}$$

where d_i is lattice spacing, λ_x is the wavelength of x-rays and m is the order of maxima. The basic diagram of diffraction in Bragg's law is shown in fig. 4.5 [140, 141]. With the help of x-ray diffraction, several interesting properties of the material can be analyzed using the diffraction pattern. These include the phase of the sample (amorphous or crystalline), structure of the sample (how atoms are arranged in the sample), defects, strain, and dislocation.

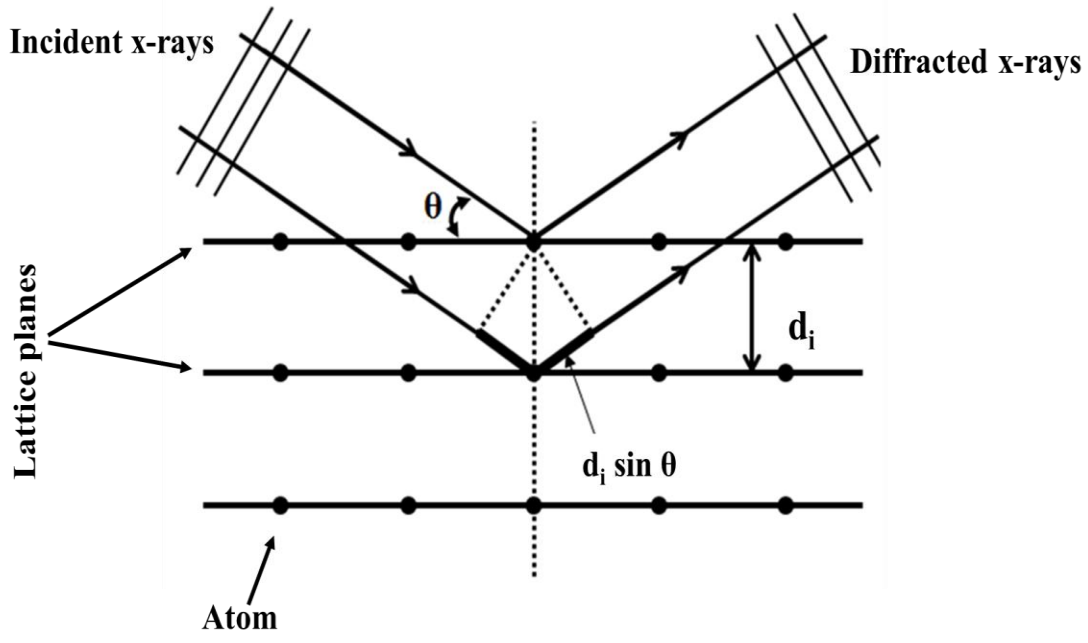

Figure 4.5 Schematic diagram of Bragg's condition of x-ray diffraction

4.4 Atomic Force Microscopy

Atomic force microscopy (AFM) is a surface analysis technique which is used to investigate the surface morphology of a sample. The basic principle used in AFM is Hook's law, which measures the force between the sample and a sharp tip fixed at the end of a cantilever. The cantilever, operating in the raster scan mode, moves over the surface of the sample and bends as a result of the attractive force between the surface and the tip. In order to monitor the bending of the cantilever, an optical lever technique is employed. The basic diagram of an atomic force microscope is shown in fig. 4.6 [142]. A laser light is continuously reflected from the cantilever and recorded by a position sensitive detector. As the cantilever bends, due to the force felt by the sharp tip, a change in the reflection of light occurs. This change in reflection is further analyzed to calculate the force between the sample and the tip, and in this way, the surface morphology of the sample is obtained. There are two modes associated with AFM. These include contact and tapping modes. In the contact mode, the tip remains continuously in contact with the surface of the sample. For the scanning of soft and rather mobilized materials, the tapping mode is preferred. Here, the tip remains oscillating with a certain resonant frequency and interacts with the sample during its oscillations. The information which can be extracted from a sample by employing AFM includes the lateral grain size, nature of the surface (granular, columnar or flat), and surface roughness [143, 144].

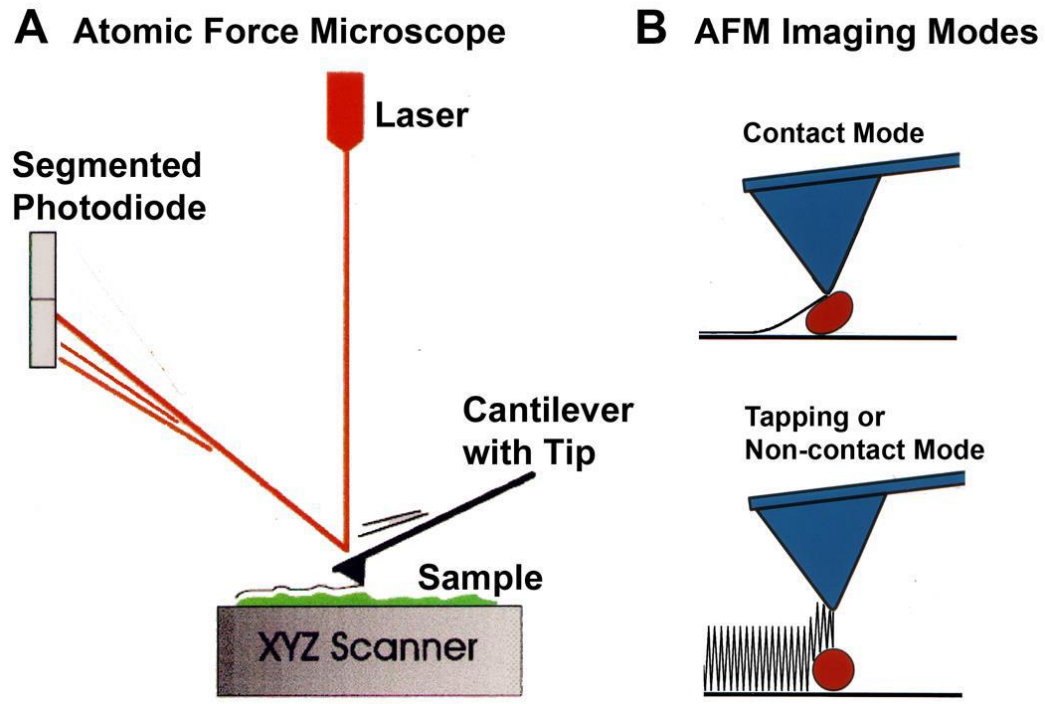

Figure 4.6 Working principle of atomic force microscopy

4.5 Spectrophotometry

Spectrophotometry is a method to measure the optical properties of a sample like transmittance, reflectance, and absorbance. The basic principle of a spectrophotometer lies in the fact that each material can absorb, transmit or reflect light up to a certain wavelength. When light passes through a sample, its intensity changes. The incident and emergent intensities are then related to each other to obtain the optical properties of the sample. There are two basic modes under which a spectrophotometer can be operated. These include transmittance/ absorbance mode and the reflectance mode [145, 146]. The transmittance (T_{trans}) can be calculated by the ratio of the fraction of light which transmits through the sample (I_t) to the initial intensity I_o incident on the sample:

$$T_{trans} = \frac{I_t}{I_0} \tag{4.3}$$

Reflectance is defined as the ratio of the fraction of light I, which reflects from the surface of the sample to the initial intensity I_o incident on the material. There are lots of information that can be extracted from the knowledge of transmittance, absorbance, and reflectance. Typical examples include the composition of the material that can be found from the Beer Lambart's law once the absorbance is known, the thickness of the sample, and optical parameters like refractive index, extinction coefficient, dielectric function, and band gap [145-147]. A schematic diagram of a double beam spectrophotometer is shown in fig. 4.7.

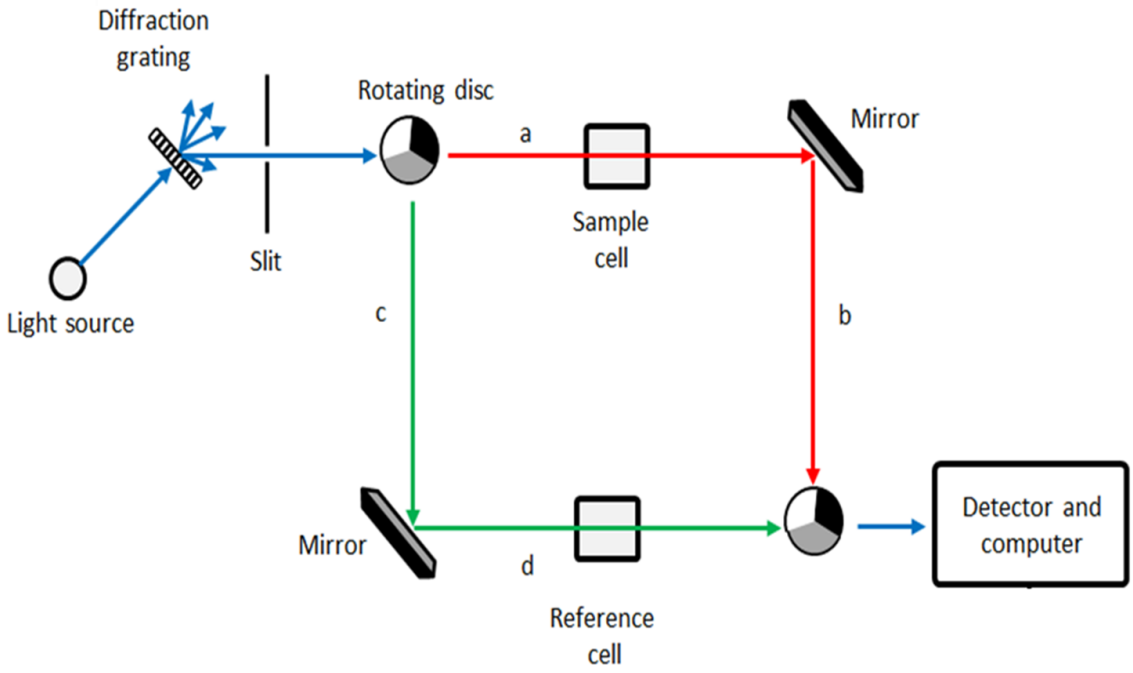

Figure 4.7 Schematic diagram of a double beam spectrophotometer

4.6 Photocurrent Measurement

The photocurrent of a semiconductor describes its conversion capability of optical light into electrical current. The photocurrent is an important property of a material that explains how efficient is it for the fabrication of photovoltaic devices. The current-

voltage curves of a material enable us to measure the photocurrent of a material. When excess electrons and holes are generated within the semiconductor, the conductivity of the semiconductor is increased. The generated electrons and holes within the semiconductor are separated by an external electric field (E_e) and a current will be produced [148]. For this purpose, ohmic contacts at each end of the semiconductor are deposited to collect the current. A schematic diagram of a photoconductor is shown in fig. 4.8.

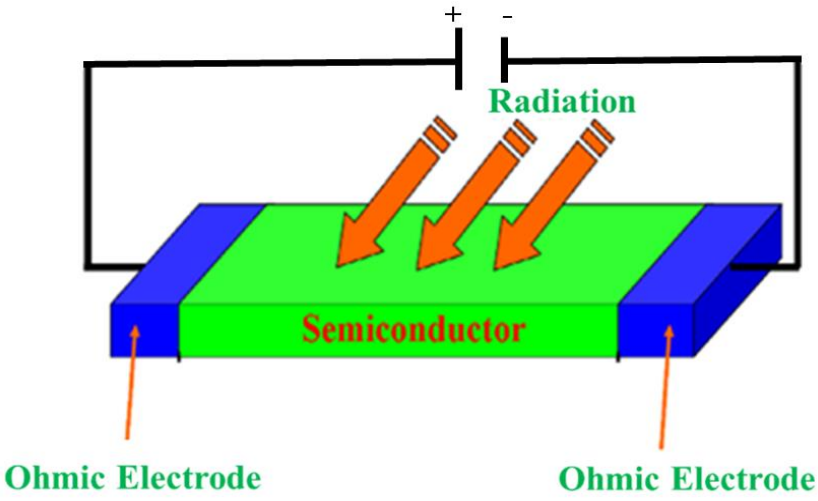

Figure 4.8 A schematic diagram of a photoconductor

The conductivity σ_0 of a semiconductor can be written as:

$$\sigma_0 = e\left(\mu_n n_0 + \mu_p p_0\right) \tag{4.4}$$

where μ_n and μ_p are the mobilities of electrons and holes, n_0 and p_0 are the electron and hole concentrations, respectively. If excess carriers are generated under light, the conductivity becomes

$$\sigma_0 = e\left[\mu_n(n_0 + \delta n) + \mu_p(p_0 + \delta \mathrm{p})\right] \tag{4.5}$$

where, δn and δp are the excess electron and hole concentrations, respectively. Due to charge neutrality in the semiconductor, the excess number of holes is equal to the excess number of electrons. In steady state, the excess carrier concentration is given by $\delta p = G_L \tau_p$ where G_L is the generation rate of the excess carrier ($cm^{-3}s^{-1}$) and τ_p is the lifetime of minority carriers. Equation (4.5) can be rewritten as:

$$\sigma = e\left(\mu_n n_0 + \mu_p p_0\right) + e\left(\delta p\right)\left(\mu_n + \mu_p\right) \tag{4.6}$$

The increase in conductivity due to optical excitation is known as photoconductivity. The photoconductivity can be written as

$$\Delta\sigma = e\left(\delta p\right)\left(\mu_n + \mu_p\right) \tag{4.7}$$

An electric field is applied across the semiconductor which produces a current. The current density can be written as [148]:

$$J_c = (J_0 + J_L) = (\sigma_0 + \Delta\sigma)E_e \tag{4.8}$$

where J_0 is the current density of the semiconductor prior to optical excitation, J_L is the photocurrent density, J_c is the total current density, E_e is the electric filed. If the electrons and holes are generated uniformly in the semiconductor, then the photocurrent can be written as

$$I_{photo} = J_L.A = \Delta\sigma.A.E_e = e\left(G_L\tau_p\right)\left(\mu_n + \mu_p\right)A.E_e \tag{4.9}$$

where A is the cross-sectional area of the device. It is clear from equation (4.9) that the photocurrent is directly proportional to the excess carrier generation rate, which depends on the incident photon flux [148. 149].

4.7 Experimental Procedure

CdTe, CdSe, CdS, ZnTe, ZnSe, and ZnS thin films were deposited on unheated fused silica and tantalum substrates at angles of 0˚, 20˚, 40˚, 60˚ and 80˚ by thermal evaporation. The schematic diagram of angular deposition is shown in fig. 4.9.

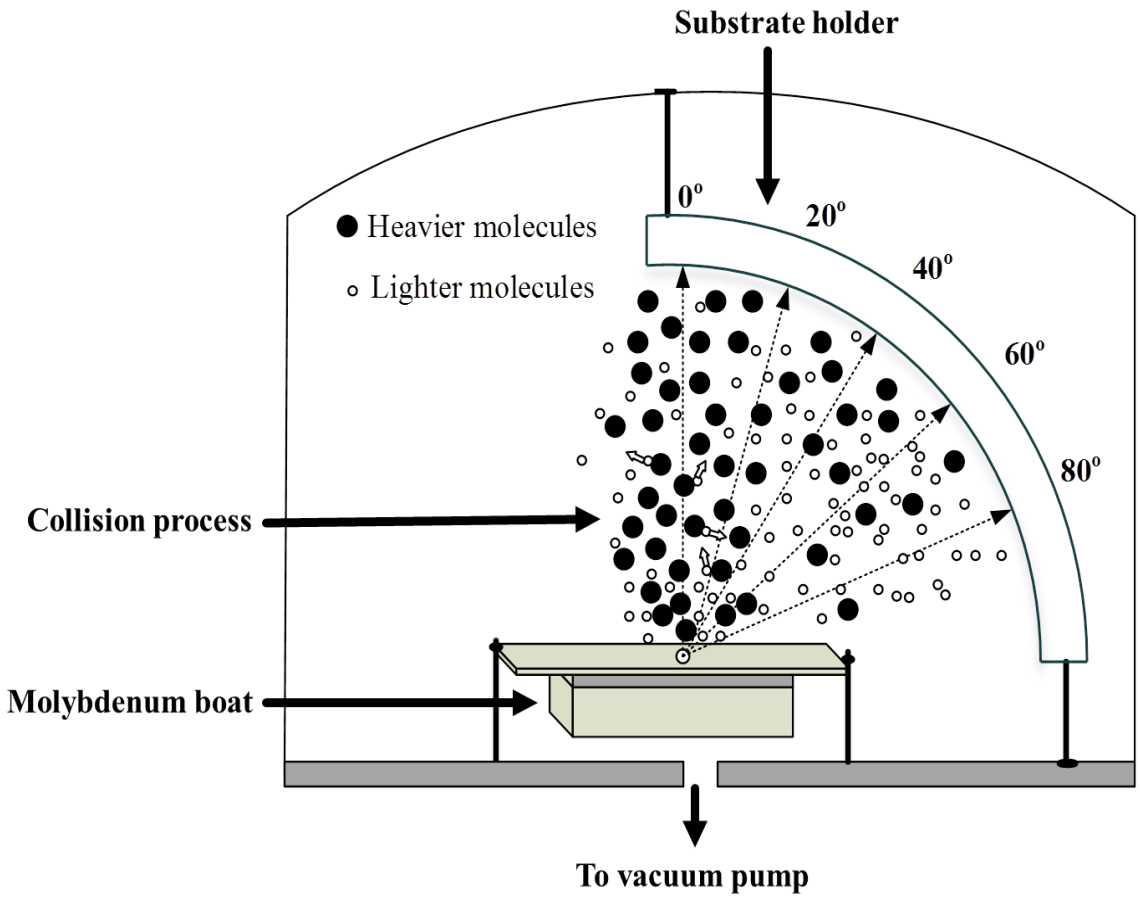

Figure 4.9 Schematic diagram of angular deposition of II-VI compound thin films

The angular deposited II-VI compounds thin films were labled according to their angles and are listed in table 4.1.

Table 4.1 Labels of angular deposited CdTe, CdSe, CdS, ZnTe, ZnSe, and ZnS films

Angle (θ)	CdTe	CdSe	CdS	ZnTe	ZnSe	ZnS
0˚	CdTe-0˚	CdSe-0˚	CdS-0˚	ZnTe-0˚	ZnSe-0˚	ZnS-0˚
20˚	CdTe-20˚	CdSe-20˚	CdS-20˚	ZnTe-20˚	ZnSe-20˚	ZnS-20˚
40˚	CdTe-40˚	CdSe-40˚	CdS-40˚	ZnTe-40˚	ZnSe-40˚	ZnS-40˚
60˚	CdTe-60˚	CdSe-60˚	CdS-60˚	ZnTe-60˚	ZnSe-60˚	ZnS-60˚
80˚	CdTe-80˚	CdSe-80˚	CdS-80˚	ZnTe-80˚	ZnSe-80˚	ZnS-80˚

The source materials were II-VI compound powder (Sigma-Aldrich 99.99% purity) and were evaporated from a molybdenum boat. The thermal evaporation was carried out in a Leybold L560 unit at a base pressure of 9×10^{-6} mbar. The radial distance between the substrate holder and the molybdenum boat was 35 cm. The evaporation rate was set to 7 Å/s and the thickness of the film fixed to be 500 nm. Both the evaporation rate and the thickness of the films were monitored using a quartz crystal thickness monitor. The substrates were cleaned prior deposition by sonication using ethanol, followed by isopropanol and then dried in an oven for 30 minutes. The chemical composition of the films was studied by x-ray energy dispersive spectroscopy (EDX) performed in a JEOL JSM-6610 scanning electron microscope (SEM) equipped with an EDX spectrometer, which has a Sapphire detecting unit. X-ray photoelectron spectroscopy (XPS) was done in a Thermo Scientific Escalab 250Xi spectrometer equipped with a monochromatic Al $K\alpha$ (1486.6 eV) x-ray source, which has a resolution of 1 eV. XPS depth profiles were obtained by a sequence of 180-s ion etching followed by XPS measurement to measure

the relative atomic concentration along the thickness. Etching used a 2-keV Ar^+ ion beam on a 1-mm^2 area of the surface. During XPS analysis, the chamber pressure was 5×10^{-9} mbar. To minimize the electrostatic charging of the samples, the films deposited on the tantalum substrates were used for the XPS analysis. The structural properties were studied by x-ray diffraction using a Rigaku Ultima IV diffractometer with Cu $K\alpha$ (1.5406 Å) radiation. The surface morphology of the films was examined using an atomic force microscope (Veeco Innova diSPM) that was working in tapping mode and the surface of the films was probed with antimony-doped silicon tip that had a radius 10 nm and oscillated at its resonant frequency of 300 kHz. The electrical properties were measured by a two-probe method and van der pauw geometry (Ecopia HMS 3000). In two-probe method, two gold contacts (100 nm) were deposited on the films to make Ohmic contacts with semiconductor films and then the known currents were passed through the films to measure their resistance using a Keithley 6517B electrometer. After that, the resistivities of the films were calculated using the resistance and the dimensions (length, width, and thickness) of the films. The optical properties were measured by a Jasco V-570 double beam spectrophotometer, which is capable of operating from ultra violet to near infrared regions. The photocurrent of all the films was determined by measuring their current-voltage characteristics under dark and light illumination using the two probe technique. A Keithley 238 source meter and a xenon lamp with a light illumination intensity of 150 W were used as the photoelectrical analysis system.

CHAPTER 5

Chemical Analysis

In this chapter, the chemical properties of II-VI compound films are presented.

5.1 EDX Analysis

Energy dispersive spectroscopy was used to measure the atomic concentration of II and VI elements in the films. Figure 5.1 represents the EDX spectra of the CdTe films. It is clear from fig. 5.1 that the peak intensity of Te peak relative to Cd decreased by increasing the angle from 0˚ to 80˚.

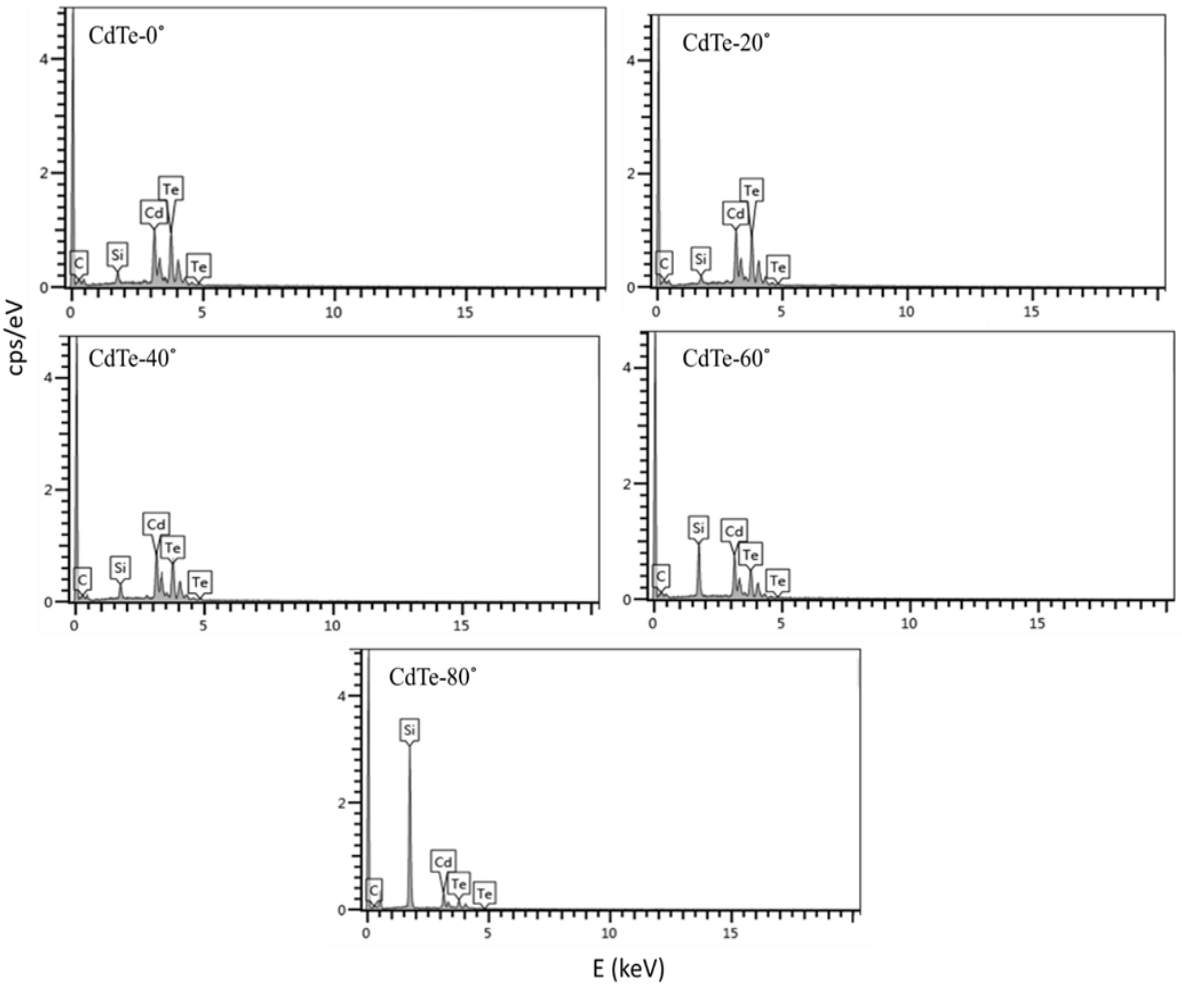

Figure 5.1 EDX spectra of CdTe films

EDX results showed that at lower angles (0˚ and 20˚), the deposited films were Te-rich; at 40˚, the deposited film was nearly stoichiometric; and at higher angles (60˚ and 80˚), the deposited films were Cd-rich. The change in the elemental compositions of the films is due to the collisions between the atoms of Cd and molecules of Te_2 during evaporation according to the kinetic theory of gases [70, 95]. The atomic mass of Cd is 112.41 u and the molecular mass of Te_2 is 255.2 u. During the collision, the heavier molecules (Te_2) deflect less and deposit more at lower angles (0˚ and 20˚); while Cd atoms are lighter than Te_2 molecules, they deflect more during the collision and deposit more at higher

angles (60˚ and 80˚). The change in the atomic concentrations of Cd and Te elements in the films by changing the angle from 0˚ to 80˚ is shown in fig. 5.2.

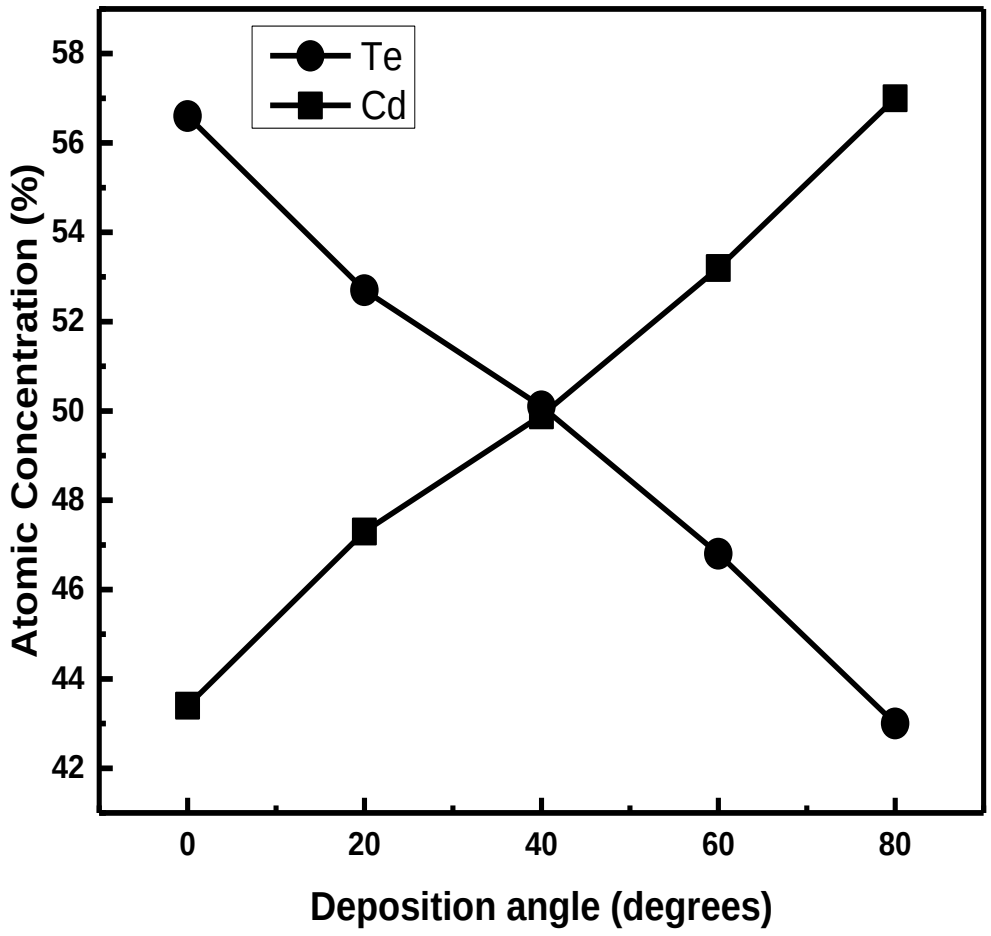

Figure 5.2 Atomic concentration of Cd and Te elements in CdTe films

Figure 5.3 represents the EDX spectra of CdSe films. It was observed that at lower angles (0˚ and 20˚), the deposited CdSe films were Se-rich; at 40˚, the deposited film was nearly stoichiometric; and at higher angles (60˚ and 80˚), the deposited films were Cd-rich.

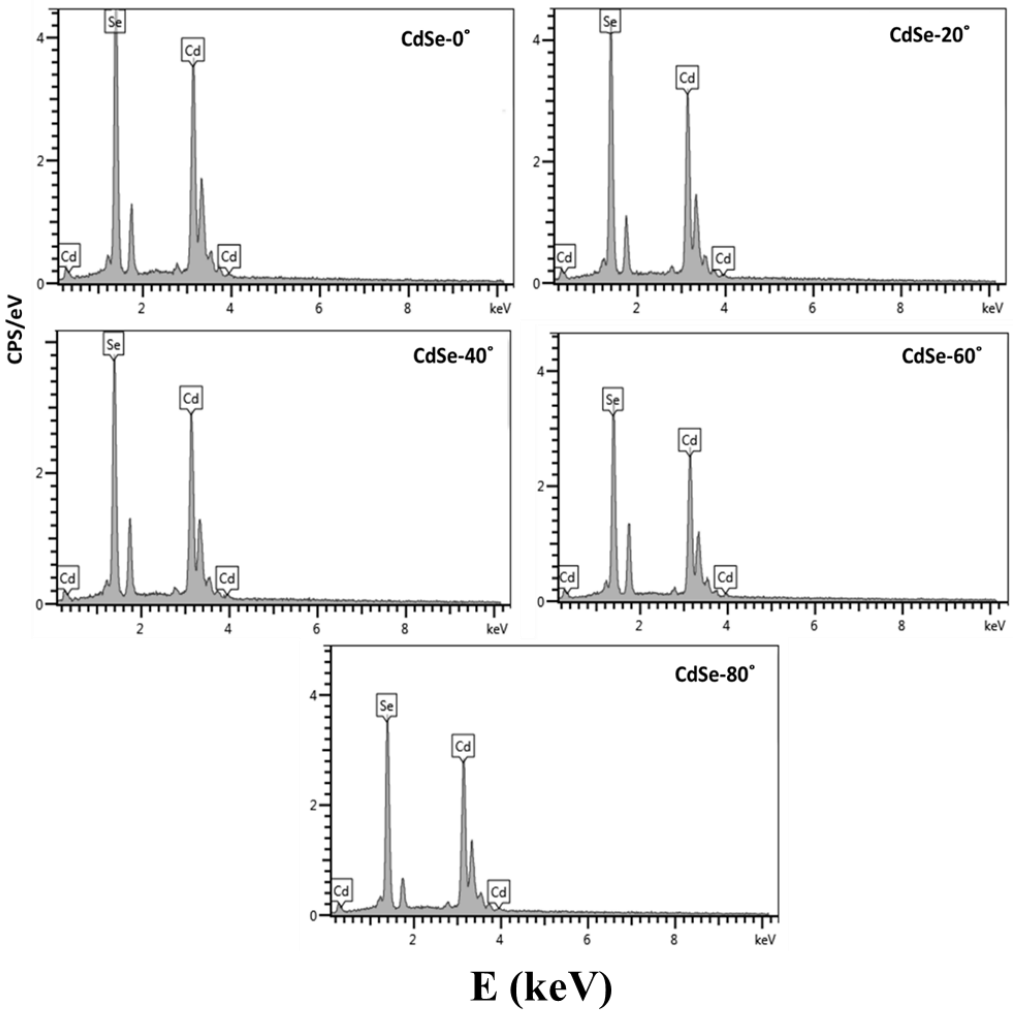

Figure 5.3 EDX analysis of CdSe films

The change in the atomic concentrations of Cd and Se elements in the films by changing the angles from 0˚ to 80˚ is shown in fig. 5.4. Because of the high molecular mass of Se_2 (157.92 u) compared to that of Cd (112.41 u), the molecules of Se_2 suffer less deflection

in collisions with Cd atoms during the transport. This causes lower angles (0˚ and 20˚) deposited films to be enriched with Se. On the other hand, the high deflection of Cd atoms during collisions results in an increase of the concentration of cadmium in the films deposited at higher angles (60˚ and 80˚). It was also noticed that the change in atomic concentration of CdSe by changing the deposition angle was small compared to that of CdTe. This is because of the fact that the difference between the atomic mass of Cd and molecular mass of Se_2 is small as compared to the difference between the atomic mass of Cd and molecular mass of Te_2.

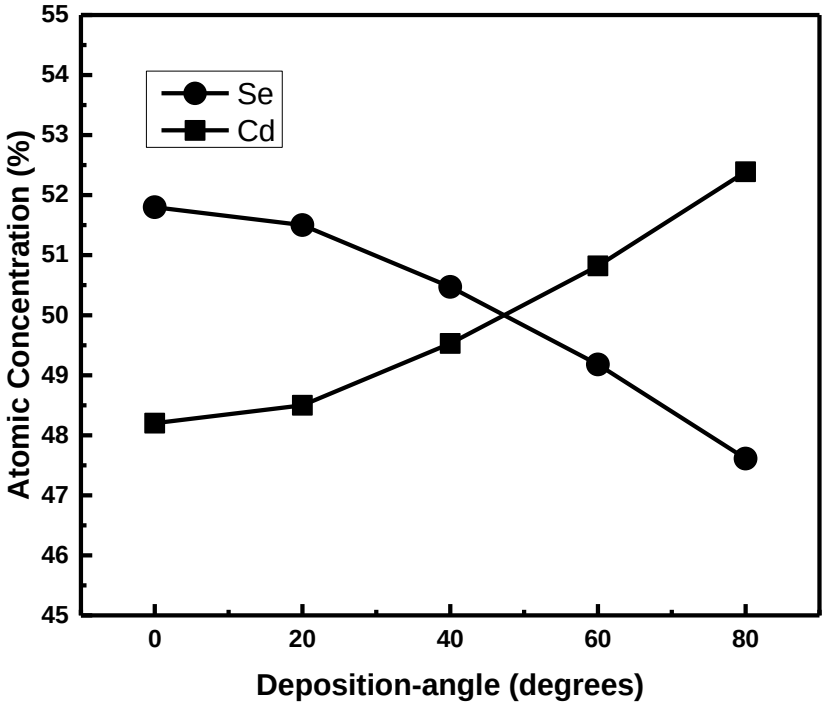

Figure 5.4 Atomic concentration of Cd and Se in CdSe films

Figure 5.5 represents the EDX spectra of CdS films. It was observed that at 0˚, 20˚ and 40˚, the deposited films were Cd-rich; and at 60˚ and 80˚, the deposited films

were S-rich. It is clear from fig. 5.5 that the peak intensity of S relative to Cd increased by changing the deposition angle from 0˚ to 80˚.

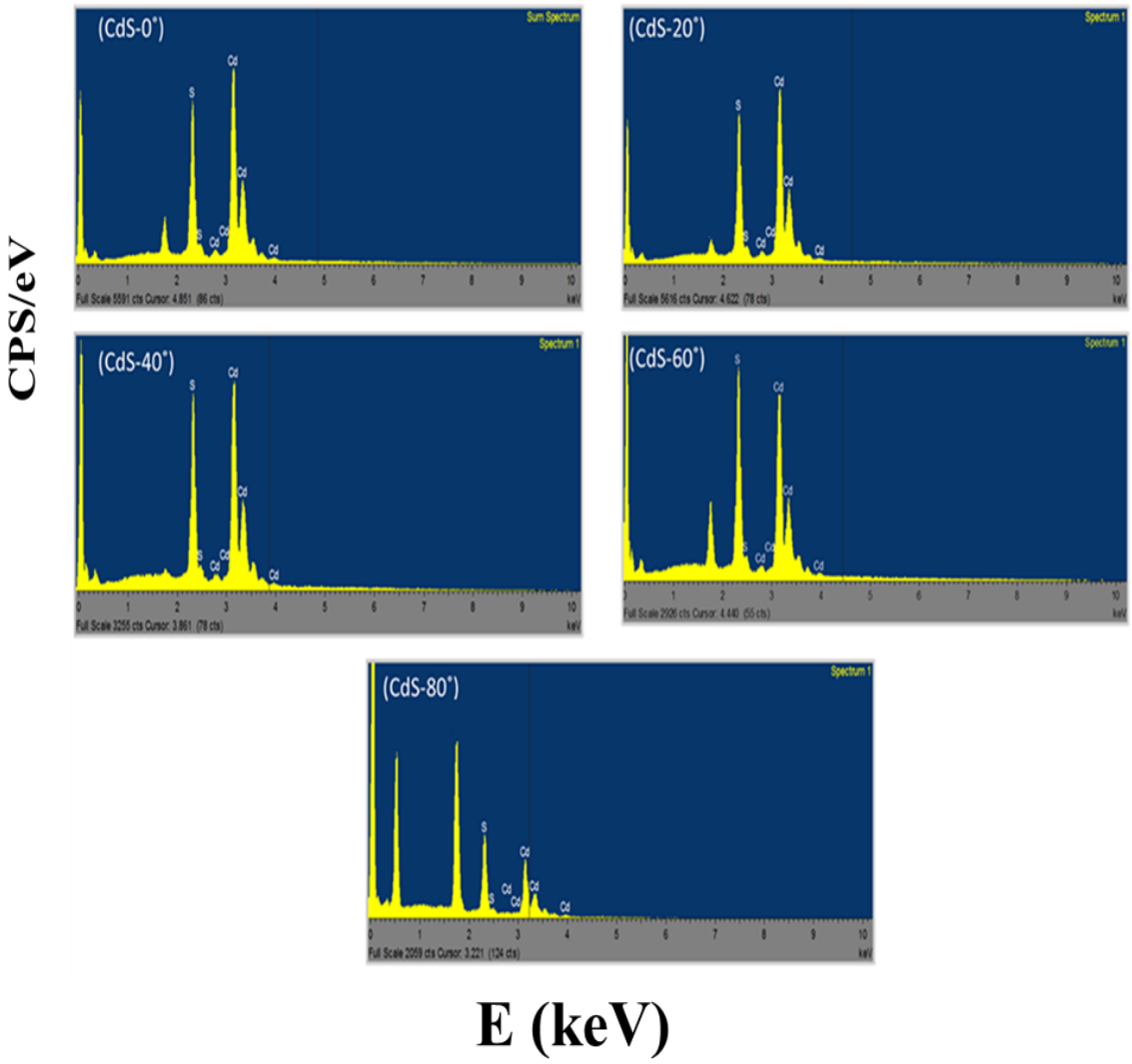

Figure 5.5 EDX analysis of CdS films

The atomic concentrations of Cd and S in the films are shown in fig. 5.6. In CdTe and CdSe cases, the chalcogen (Te or Se) was deposited more at lower angles, and metallic Cd was deposited more at higher angles. However, in CdS, metallic Cd was deposited more at lower angles and chalcogen S was deposited more at higher angles. This was because Cd atoms (atomic mass = 112.41 u) are heavier than S_2 molecules

(molecular mass = 64.13 u). Cd atoms were deposited more at lower angles because they deflect less during collisions with S_2 molecules, while S_2 molecules scattered more at higher angles because S_2 molecules are lighter compared to Cd atoms.

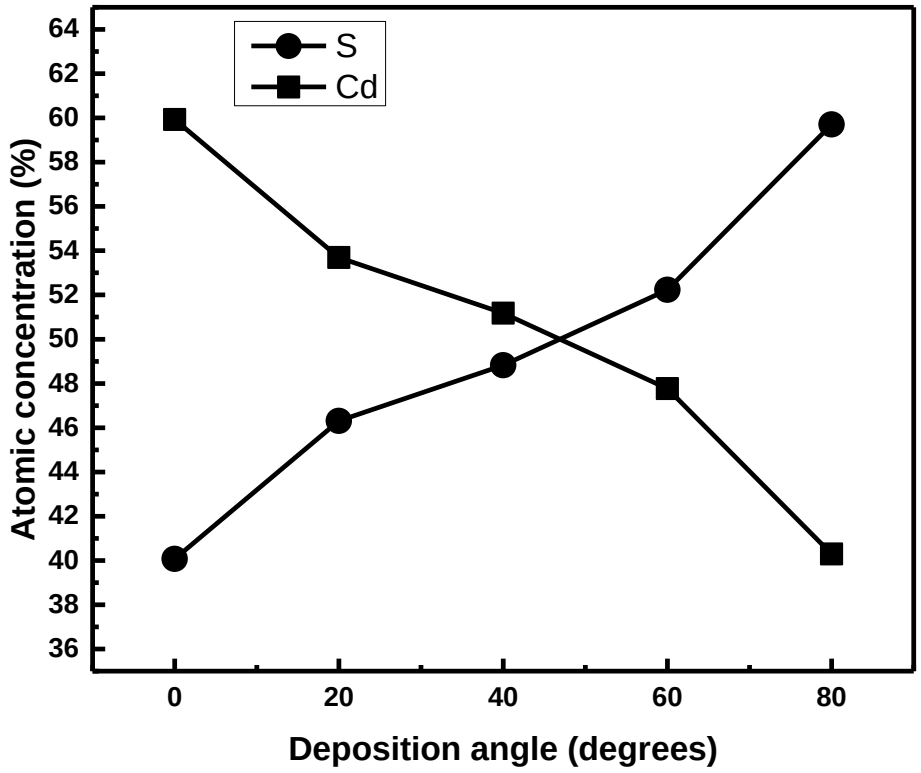

Figure 5.6 Atomic concentration of Cd and S in CdS films

Figure 5.7 represents the EDX spectra of ZnTe films deposited at different angles. It was observed that at lower angles (0˚ and 20˚), the deposited films were Te-rich; at 40˚, the deposited film was nearly stoichiometric, and at higher angles (60˚ and 80˚), the deposited films were Zn-rich. It is clear from fig. 5.7 that the peak intensity of Te relative to Zn decreased by increasing the angle from 0˚ to 80˚.

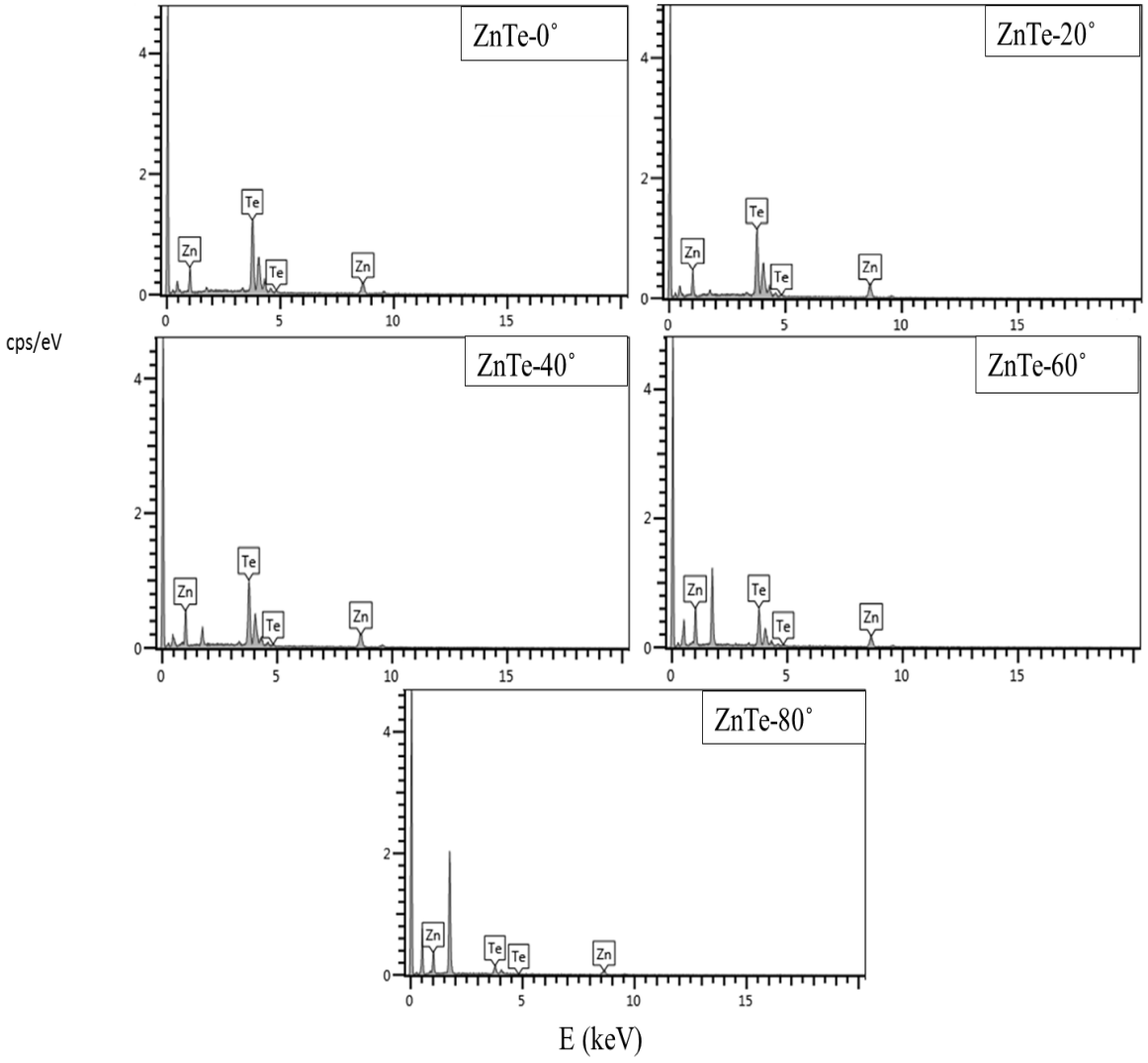

Figure 5.7 EDX spectra of ZnTe films deposited at different angles

The change in the elemental compositions of Zn and Te in the films is shown in fig. 5.8. The change in elemental concentration of ZnTe films was due to the difference of masses of Te_2 molecules and Zn atoms. The heavier Te_2 molecules (molecular mass = 225.2 u) deflect less during the collision and deposited more at lower angles, while lighter Zn atoms (atomic mass = 65.38 u) deflect more during the collision and deposited more at higher angles.

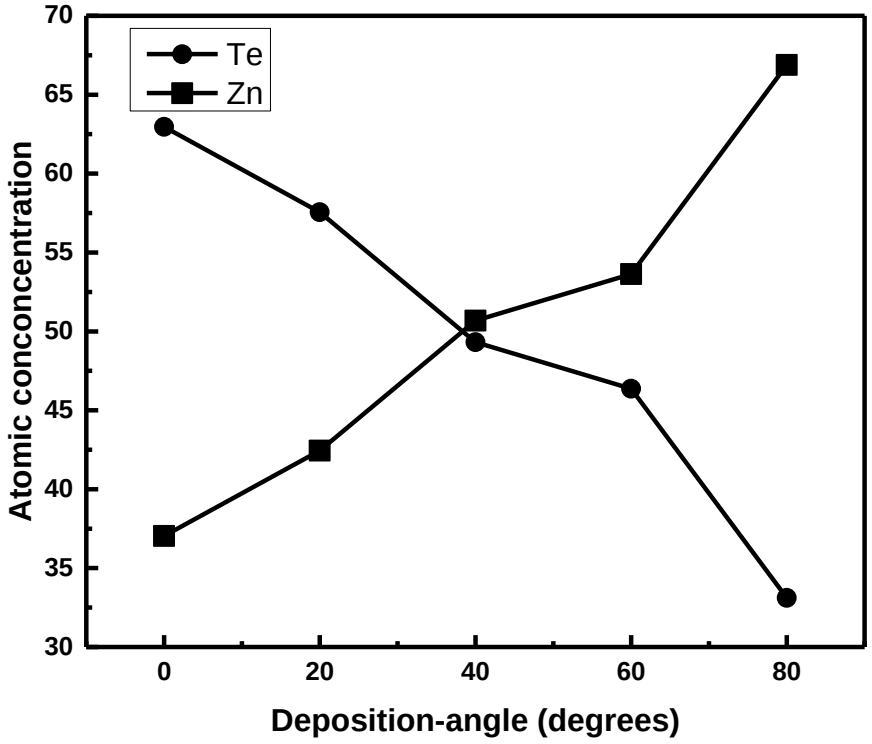

Figure 5.8 Atomic concentrations of Zn and Te in ZnTe films

Figure 5.9 represents the EDX analysis of ZnSe films. It is clear from fig. 5.9 that the peak intensity of Se relative to Zn was decreased by increasing deposition angle from 0˚ to 80˚.

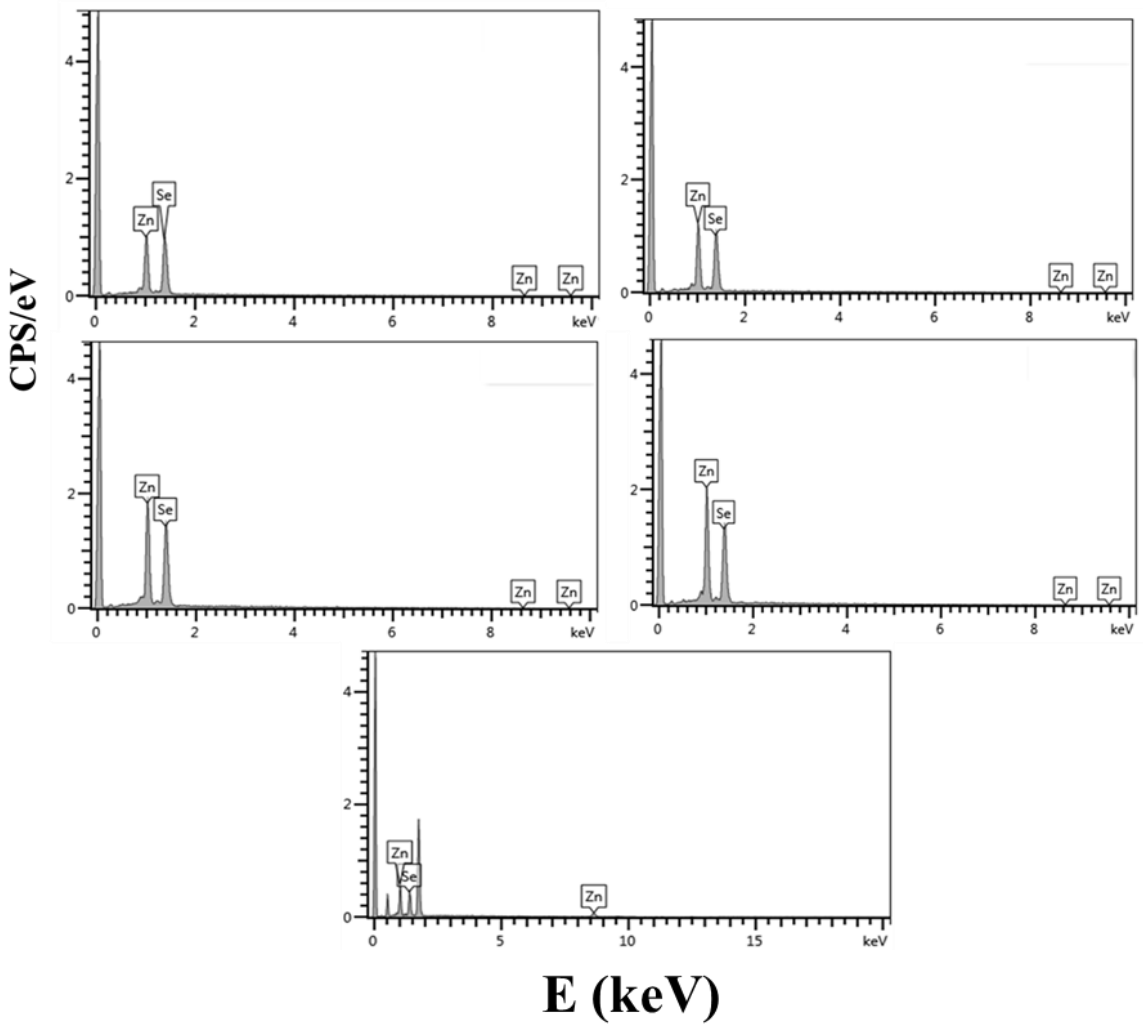

Figure 5.9 EDX analysis of ZnSe films

EDX analysis showed that at lower angles (0 and 20˚), the deposited films were Se-rich; at 40˚, the deposited film was nearly stoichiometric; and at higher angles (60˚ and 80˚), the deposited films were Zn-rich. In ZnSe, like CdTe, CdSe, CdS, and ZnTe, the heavier Se_2 molecules (molecular mass = 157.92 u) deposited more at lower angles and lighter Zn

atoms (atomic mass = 65.38 u) deposited more at higher angles. The atomic concentrations of Zn and Se in the films is illustrated in fig. 5.10.

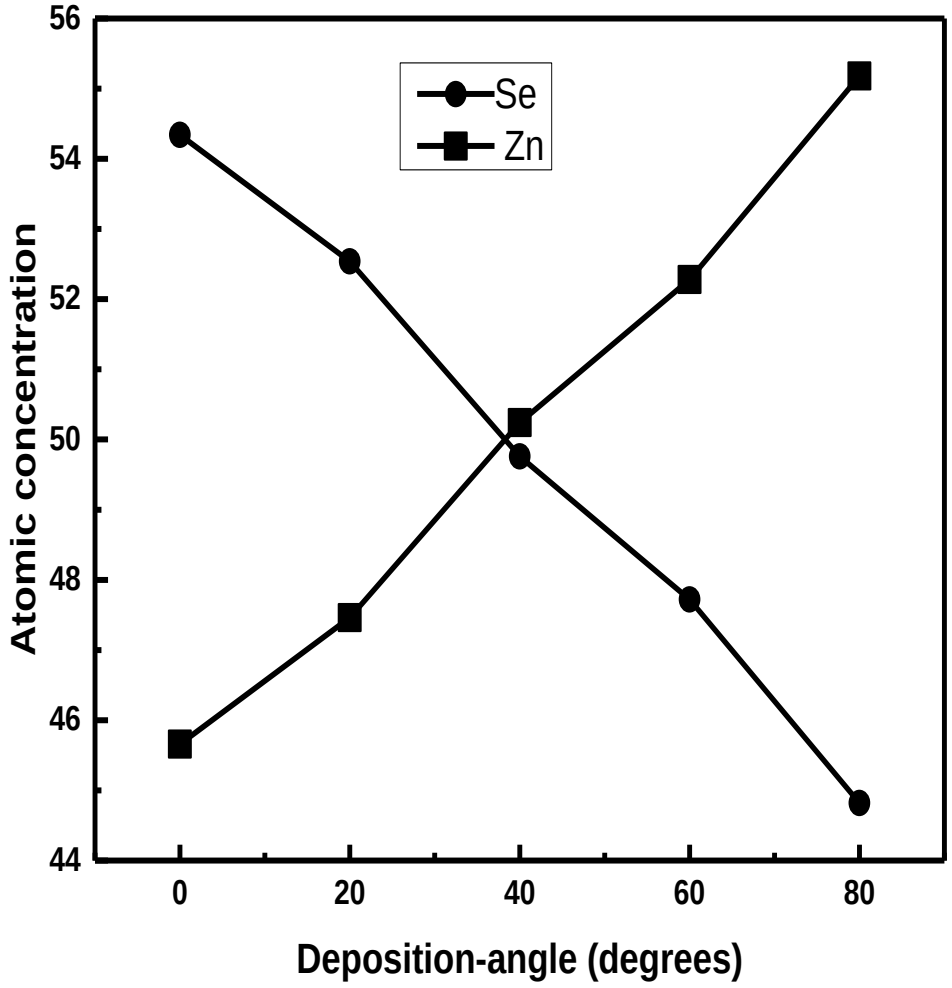

Figure 5.10 Atomic concentrations of Se and Zn in ZnSe films

Figure 5.11 represents the EDX analysis of ZnS films. It was observed that the peak intensity of Zn relative to the S was almost same.

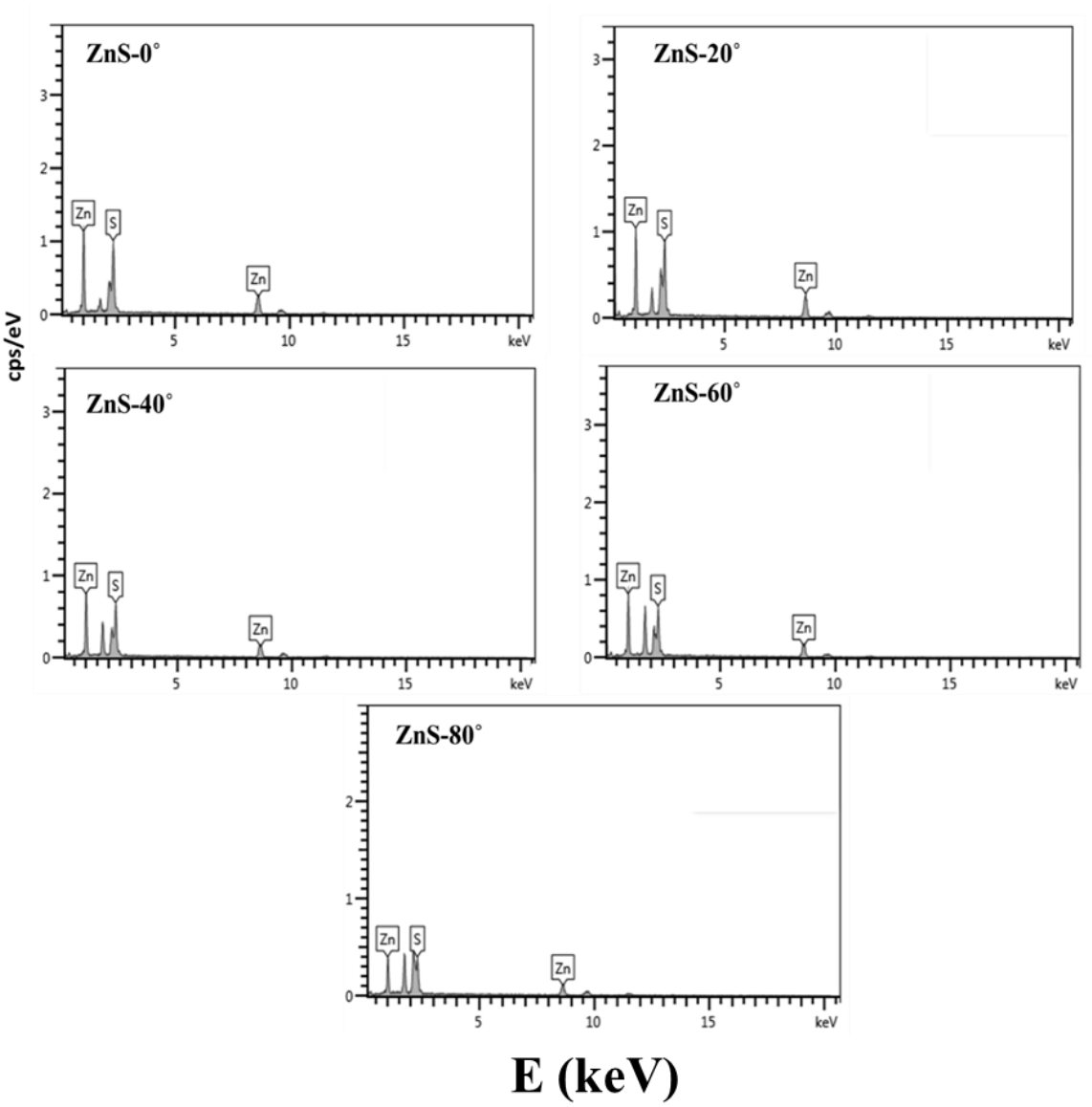

Figure 5.11 EDX analysis of ZnS films

EDX analysis showed that angular deposited ZnS films are nearly stoichiometric. This was because the molecular mass of S_2 molecule (64.13 u) and the atomic mass of Zn atom (65.38 u) are almost same. Therefore, the probability of deflection of Zn atoms and S_2 molecules after the collision is the same, which results in the stoichiometric films at different angles. The atomic concentrations of Zn and S in the ZnS films were shown in fig. 5.12.

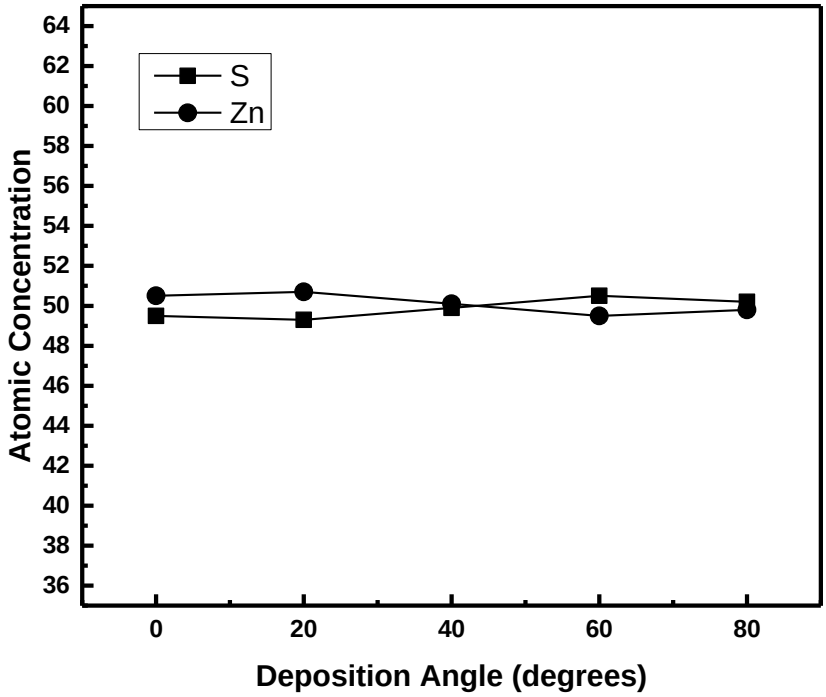

Figure 5.12 Atomic concentration of Zn and S in ZnS films

5.2 XPS Analysis

The chemical states and spatial distribution of the II and VI elements throughout the thickness of the II-VI compound films were obtained by XPS.

Figure 5.13 represents the XPS survey spectrum of a CdTe film deposited at 0˚. It was observed that all peaks were related to Cd and Te elements, and no impurity peak was observed in the spectrum. It was indicated that the fabricated films were highly pure by thermal evaporation. It was because the evaporation temperature of impurity and the evaporation temperature of source material are different. It is an advantage of thermal evaporation over other deposition techniques like chemical vapor deposition where the background impurities are incorporated into the fabricated films.

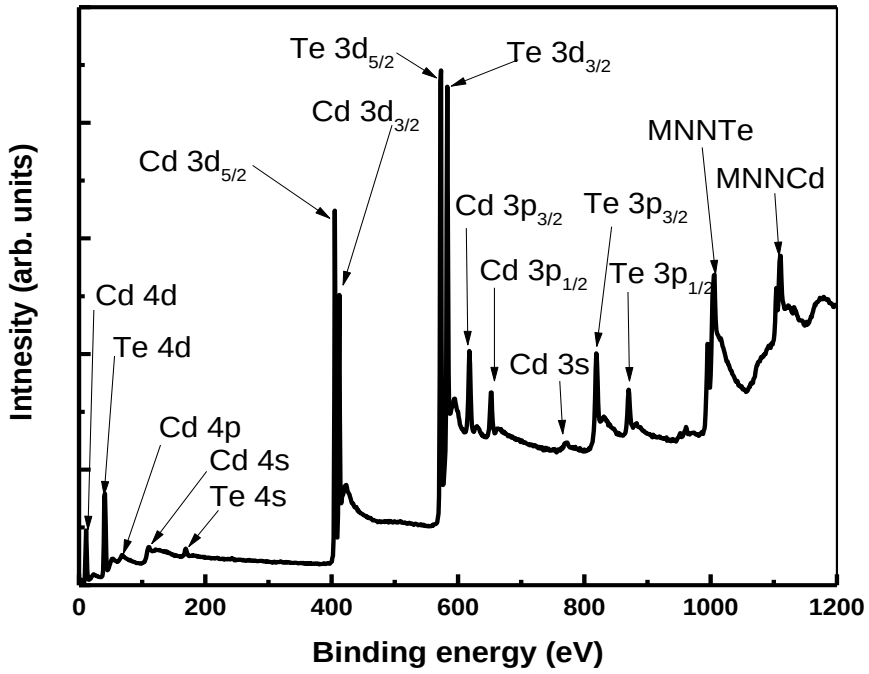

Figure 5.13 XPS survey of a CdTe film deposited at 0˚

Figure 5.14 shows high-resolution XPS spectra of Cd and Te peaks of a CdTe film deposited at 0˚. It was observed that the Cd $3d_{5/2}$ and the Cd $3d_{3/2}$ peaks lied at binding energies of 405.2 eV and 412.0 eV, respectively, and were similar to the values reported in the literature [150]. Similarly, XPS peaks of Te $3d_{5/2}$ and Te $3d_{3/2}$ lied at binding energies 572.6 eV and 583.2 eV, respectively, and were similar to the values reported in the literature [151,152].

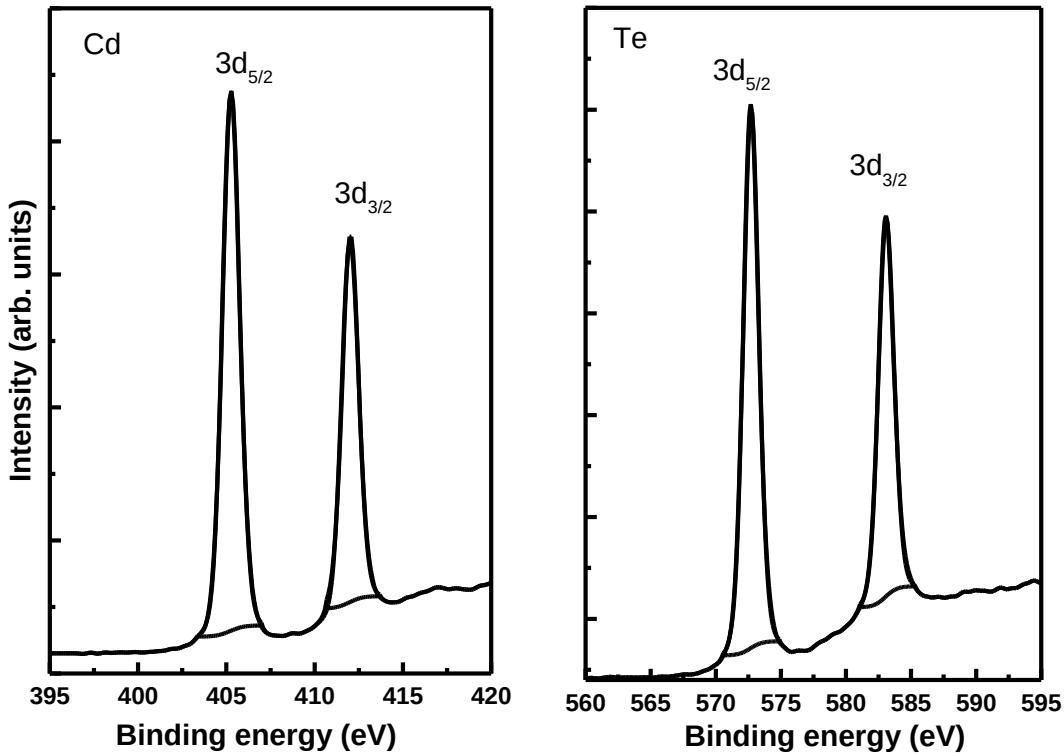

Figure 5.14 XPS spectra Cd 3d and Te 3d peaks of a CdTe thin film deposited at 0°

The areas of the Cd and Te peaks are directely propertional to the atomic concentrations of Cd and Te within the film. Therefore, the areas of Cd $3d_{5/2}$ and Te $3d_{5/2}$ peaks were measured and normalized to measure the relative intensity of elements. For this purpose, the depth profile of the films was done to evaluate the relative intensity of elements throughout the thickness of the films. Depth profile shows that the relative intensity along the depth remains same as it was on the surface of the film. This indicates that the vapor compositions of Cd and Te throughout the film deposition remained the same. Figure 5.15 shows the relative intensity of the Cd $3d_{5/2}$ and Te $3d_{5/2}$ peaks throughout the film thickness. It was observed that the relative intensity of Cd increased

by increasing the deposition angle while the relative intensity of Te element decreased by increasing the deposition angle. These results are consistent with EDX results.

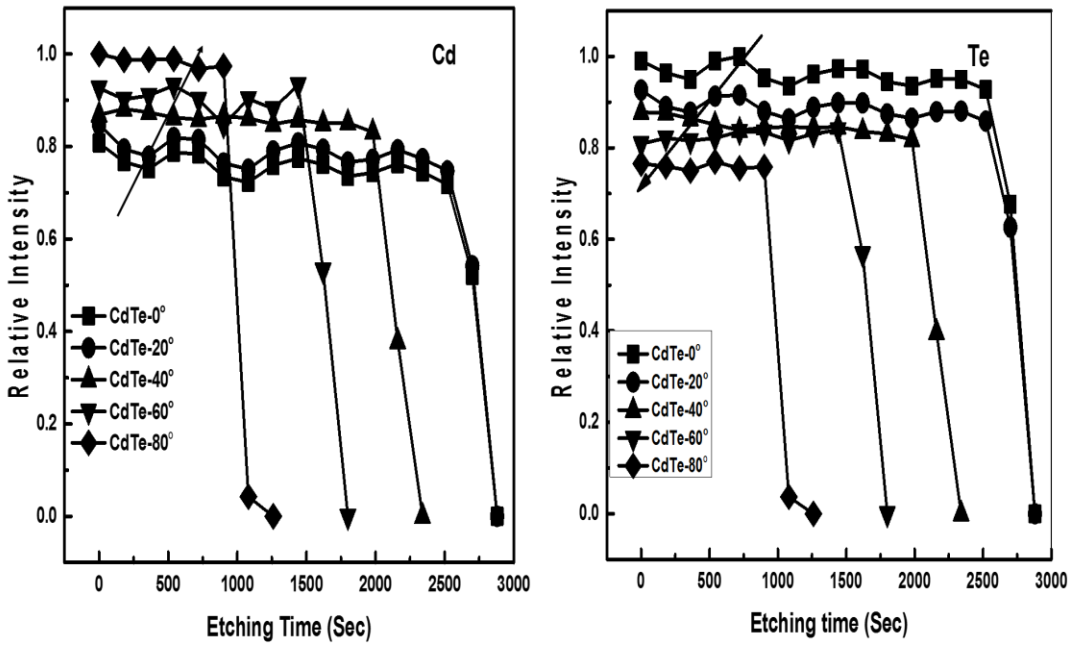

Figure 5.15 Spatial distribution of the Cd and Te throughout the thicknesses of the films as obtained by XPS depth profiling

Figure 5.16 shows high-resolution XPS spectra of Cd and Se peaks of a CdSe film that was deposited at 0˚. It was observed that the Cd $3d_{5/2}$ and Cd $3d_{3/2}$ peaks lied at binding energies of 405.2 eV and 411.8 eV, respectively, and were similar to the values reported in the literature [153]. Similarly, XPS peaks of Se $3d_{5/2}$ and Se $3d_{3/2}$ lied at binding energies 53.9 eV and 54.8 eV, respectively and were similar to the values reported in the literature [153].

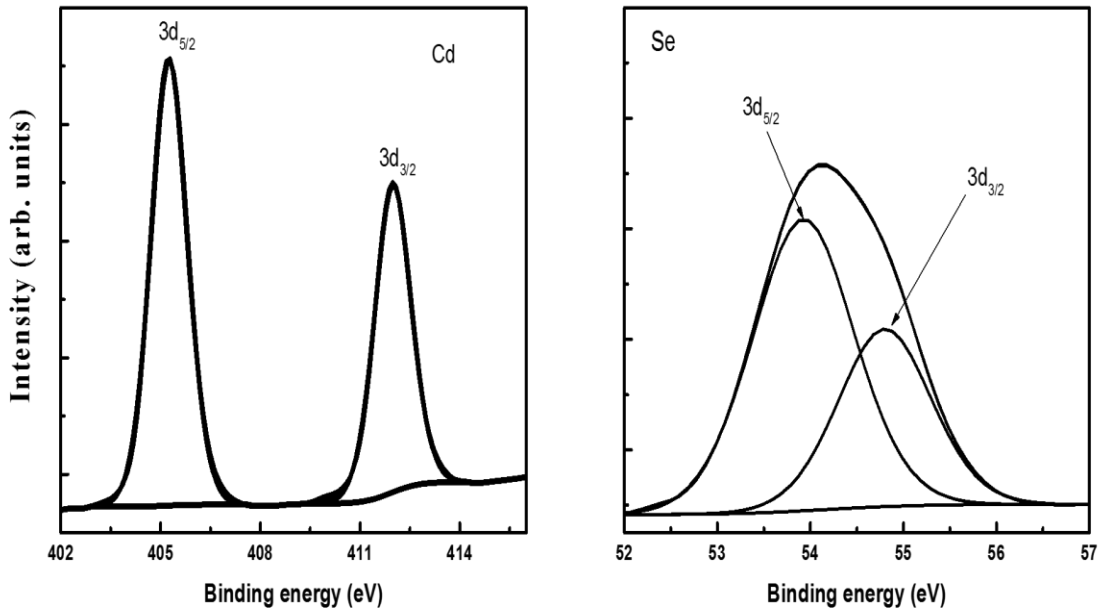

Figure 5.16 XPS spectra Cd 3d and Se 3d peaks of a CdSe thin film deposited at 0˚

Figure 5.17 represents the spatial distribution of the Cd and Se elements throughout the thickness of the films as obtained by XPS depth profiling. It was observed that the relative intensity of Se was decreased and the relative intensity of Cd was increased by increasing the deposition angle from 0˚ to 80˚ because the atomic concentration of Se was decreased and the atomic concentration of Cd was increased by increasing the angle from 0˚ to 80˚. It was also noticed that the atomic concentrations of Cd and Se along the film depth almost remained the same as it was near the surface of the film. This indicates that the vapor composition of Cd and Se during film deposition also remained the same throughout the deposition.

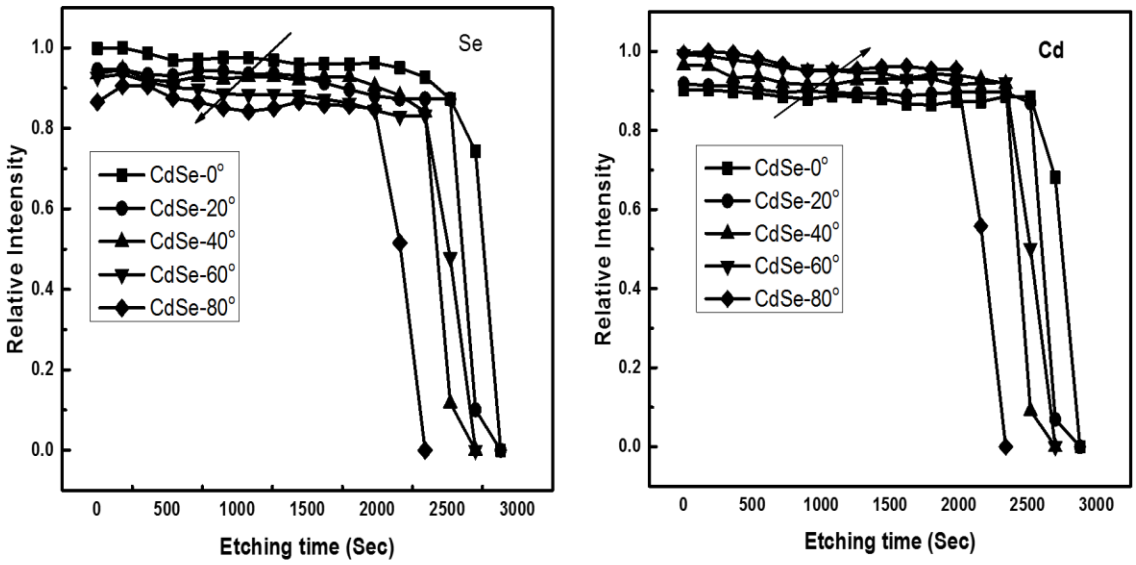

Figure 5.17 Spatial distributions of the Cd and Se throughout the thicknesses of the CdSe films as obtained by XPS depth profiling

Figure 5.18 shows high-resolution XPS spectra of Cd and S peaks of a CdS film that was deposited at 0˚. It was observed that the Cd $3d_{5/2}$ and Cd $3d_{3/2}$ peaks lied at binding energies 405.2 eV and 411.8 eV, respectively, and XPS peaks of S $2p_{3/2}$ and S $2p_{1/2}$ lied at binding energies 162.0 eV and 163.1 eV, respectively and were similar to the values reported in the literature [154, 155]

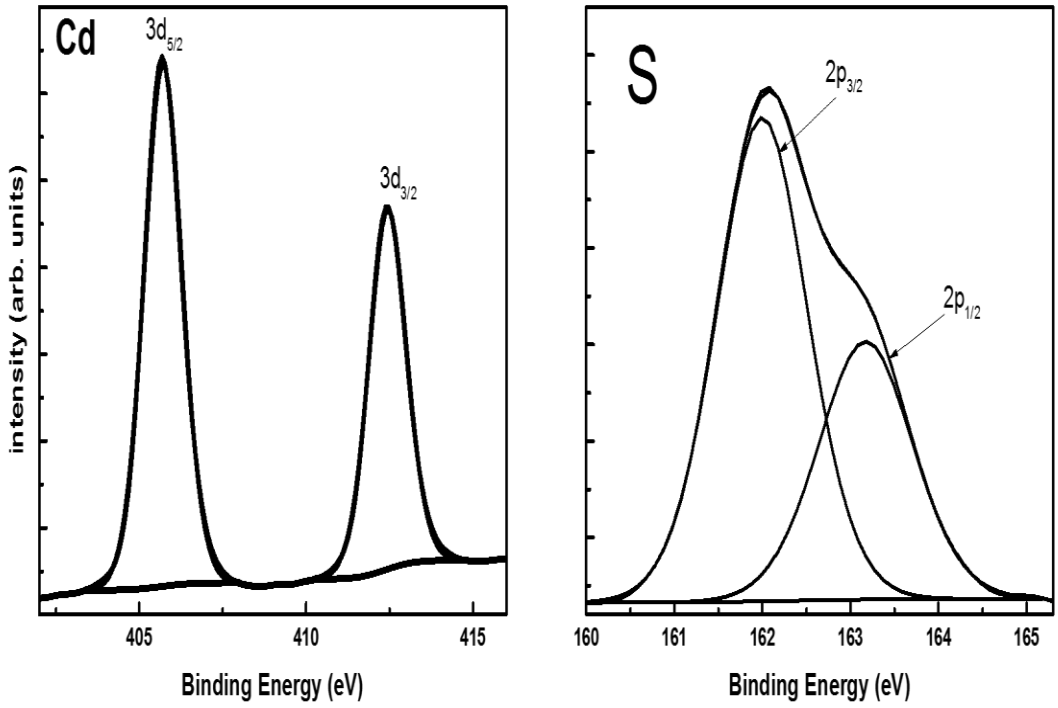

Figure 5.18 XPS analysis of Cd 3d and S 2p peaks of a CdS film deposited at 0˚

Figure 5.19 represents the spatial distribution of the Cd and S elements throughout the thickness of the films as obtained by XPS depth profiling. It was observed that the relative intensity of Cd was decreased and the relative intensity of S was increased by increasing the deposition angle from 0˚ to 80˚. This indicates that atomic concentration of Cd was decreased and the atomic concentration of S was increased by increasing the deposition angle from 0˚ to 80˚. It was also noticed that the concentrations of Cd and S elements throughout the film remained the same as it was on the surface, which indicates that the vapor composition during film growth remains same throughout the deposition. The small variation in relative intensities of Cd and S along the film might be due to the change in density due to angular deposition.

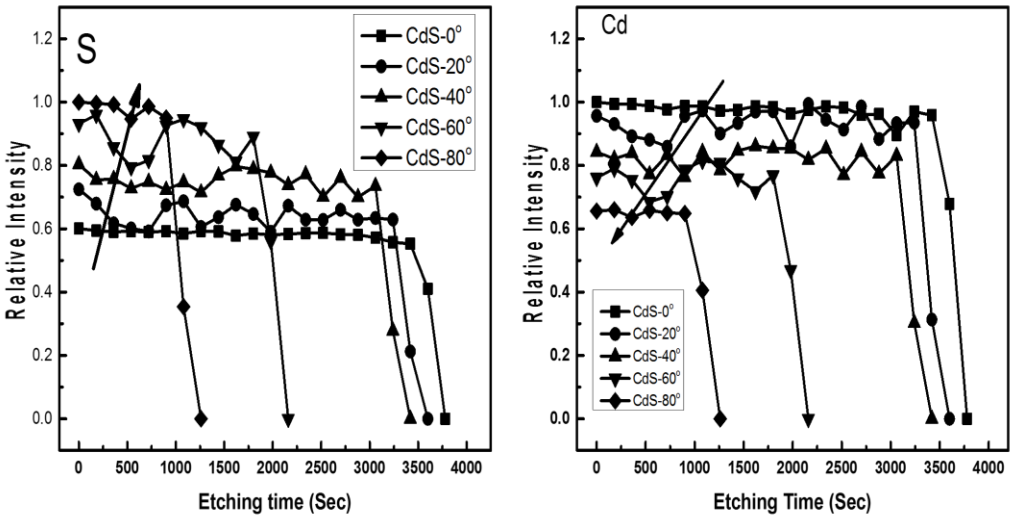

Figure 5.19 Spatial distributions of the Cd and S throughout the thicknesses of the CdS films as obtained by XPS depth profiling

Figure 5.20 shows high-resolution XPS spectra Zn and Te of a ZnTe thin film deposited at 0˚. It was observed that the Zn $2p_{3/2}$ and Zn $2p_{1/2}$ peaks lied at binding energies 1020.9 eV and 1045.1 eV, respectively and XPS spectra of Te $3p_{5/2}$ and Te $3p_{3/2}$ lied at binding energies 570.8 eV and 581.6 eV, respectively. The binding energies of Zn and Te peaks were similar to the values reported in the literature [156, 157].

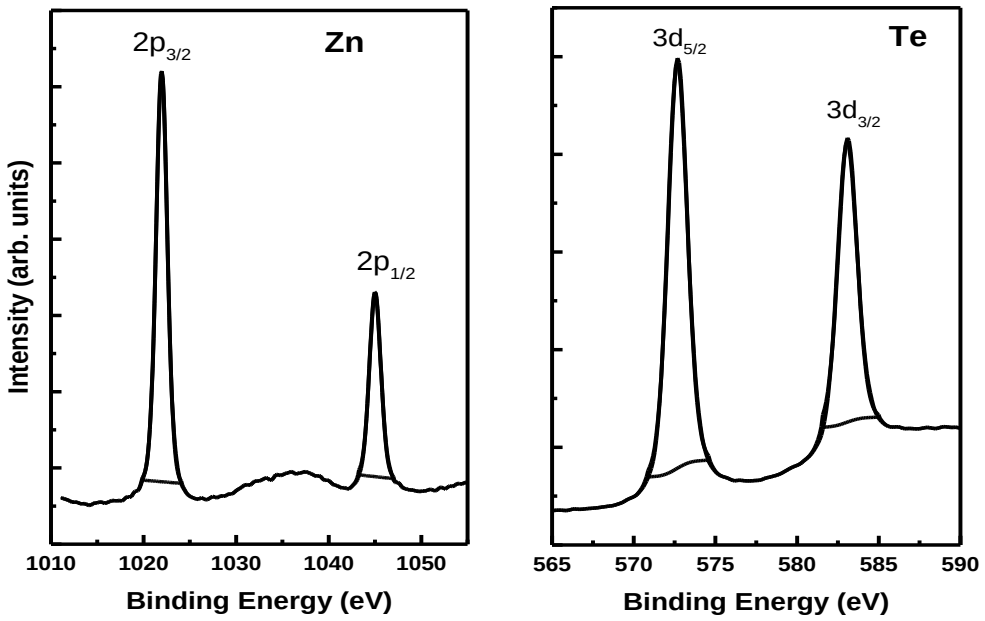

Figure 5.20 XPS spectra Zn 2p and Te 3d peaks of a ZnTe thin film deposited at 0˚

Figure 5.21 represents the spatial distribution of Zn and Te elements throughout the thickness of the films as obtained by XPS depth profiling. It was observed that the relative intensity Te was decreased and the relative intensity of Zn was increased by increasing the deposition angle from 0˚ to 80˚. It was noticed that relative intensities of Zn and Te throughout the films did not remain the same. This reveals that initially, the vapor pressure of Zn was greater than that of Te, and the vapors were rich in Zn. Afterward, the vapor pressures of Zn and Te become $P_{Zn} = 2P_{Te}$ to hold the sublimation process based on the condition of sublimation of II-VI compounds [68].

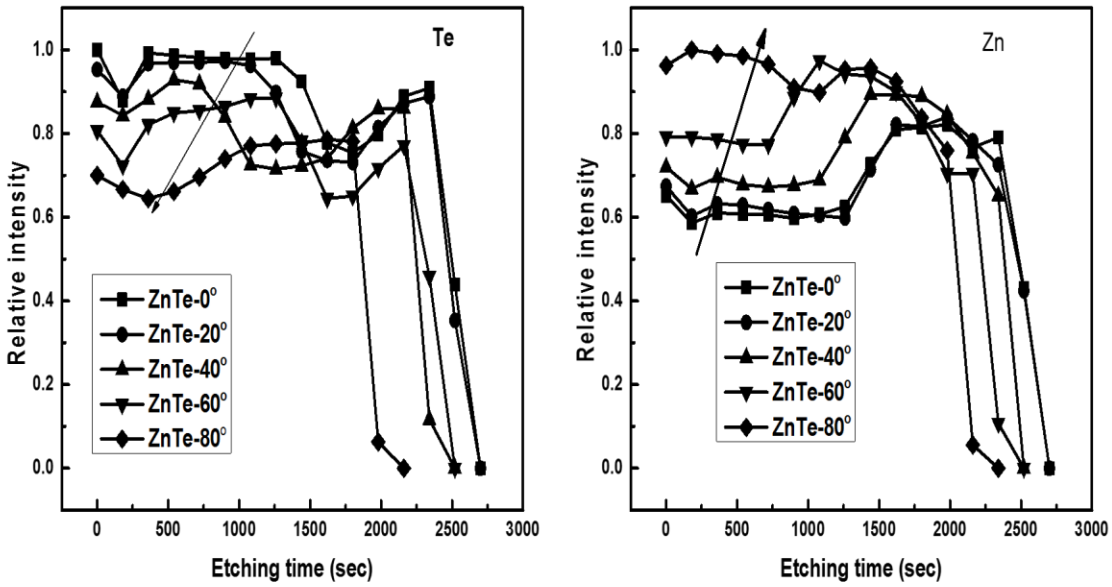

Figure 5.21 Spatial distribution of Zn and Te elements throughout the thickness of the ZnTe films as obtained by XPS depth profiling

Figure 5.22 represents high-resolution XPS spectra of Zn and Se peaks of a ZnSe film deposited at 0˚. It was observed that the Zn $2p_{3/2}$ and Zn $2p_{1/2}$ peaks lied at binding energies of 1021.8 eV and 1045.1 eV, respectively, and were similar to the values reported in the literature [158]. Similarly, XPS peaks of Se $3d_{5/2}$ and Se $3d_{3/2}$ lied at binding energies of 53.9 eV and 55.8 eV, respectively and was similar to the values reported in the literature [158].

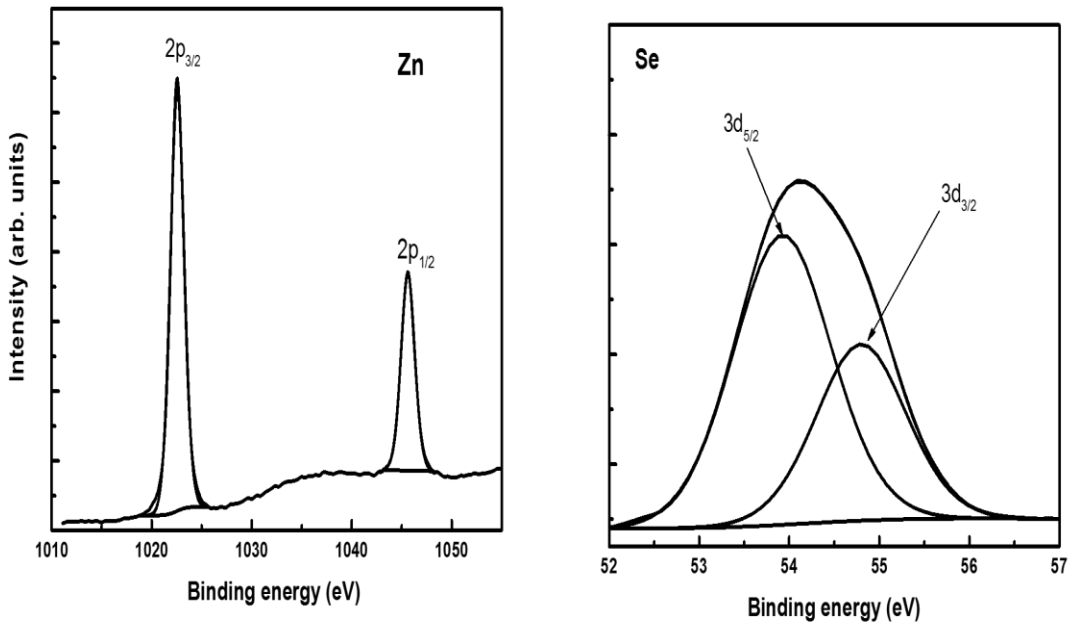

Figure 5.22 XPS spectra Zn 3d and Se 3d peaks of a ZnSe thin film deposited at 0˚

Figure 5.23 shows the spatial distribution of the elements throughout the thickness of the films as obtained by XPS depth profiling. It was observed that the relative intensity of Zn was increased and the relative intensity of Se was decreased by increasing the deposition angle from 0˚ to 80˚. The depth profiles indicate that the Zn and Se concentration almost remained the same as it was near the surface. This indicates that the vapor concentrations of Zn and Se remained the same throughout the film deposition.

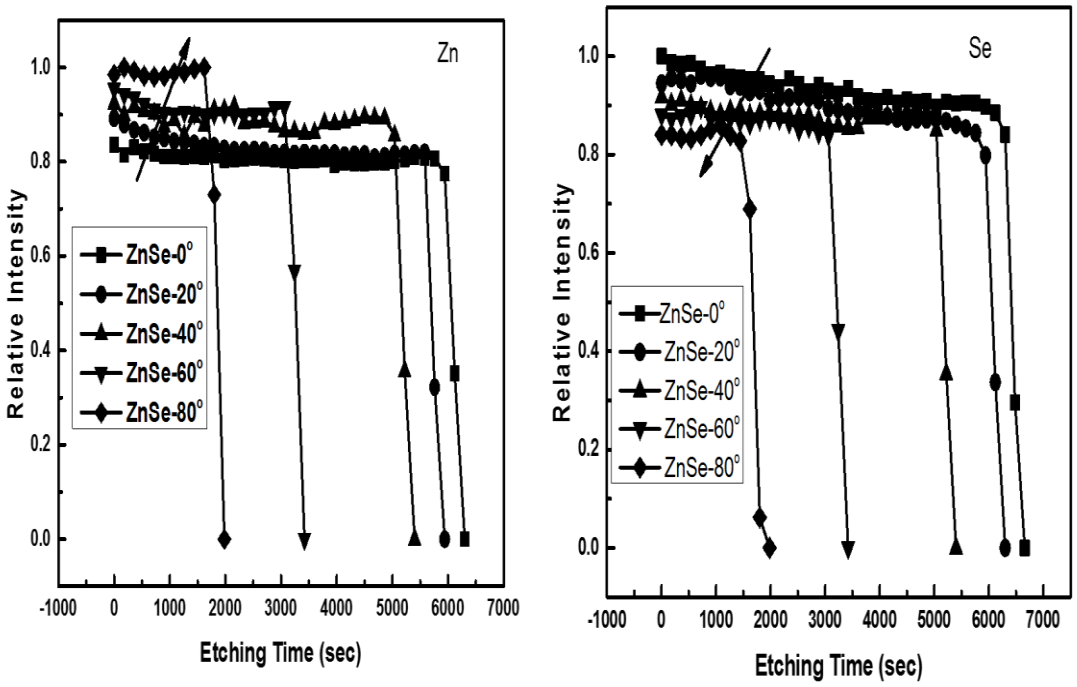

Figure 5.23 Spatial distribution of Zn and Se elements throughout the thickness of the ZnSe films as obtained by XPS depth profiling

Figure 5.24 represents high-resolution of XPS spectra of Zn and S of a ZnS film deposited at 0˚. It was observed that the Zn $2p_{3/2}$ and Zn $2p_{1/2}$ peaks lied at binding energies of 1021.8 eV and 1045.1 eV, respectively, and were similar to the values reported in the literature [159]. Similarly, S $2p_{3/2}$ and S $2p_{1/2}$ XPS peaks lied at binding energies of 162.5 eV and 163.8 eV respectively and were similar to the values reported in the literature [159].

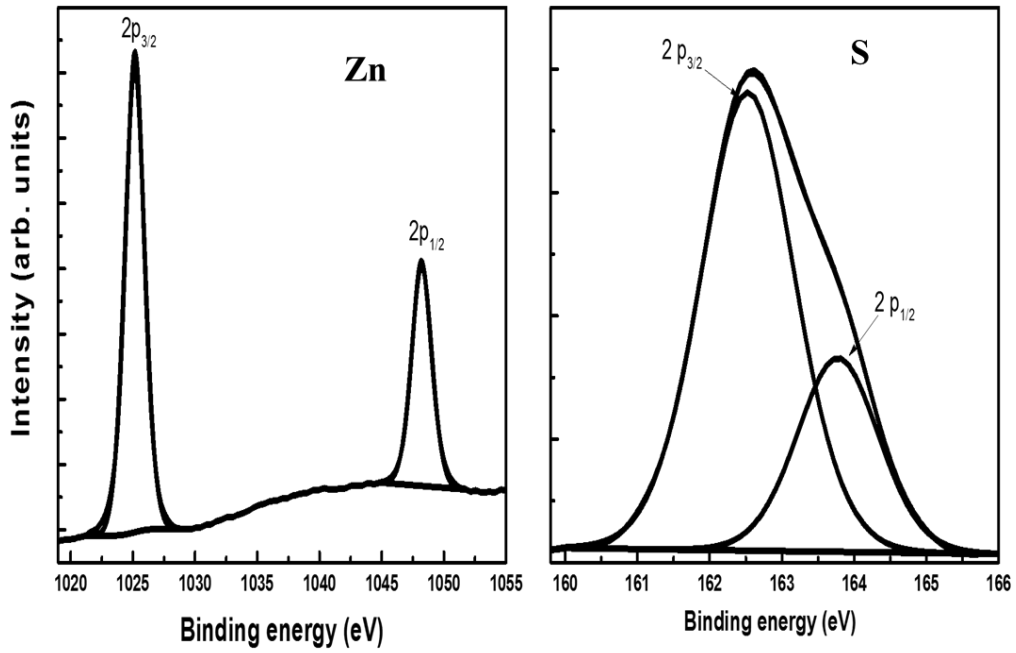

Figure 5.24 XPS spectra Zn 2p and S 2p peaks of a ZnS thin film deposited at 0˚

Figure 5.25 represents the spatial distribution of the Zn and S elements throughout the thickness of the films as obtained by XPS depth profiling. It was observed that the relative intensities of Zn and S almost remained the same by increasing the deposition angle from 0˚ to 80˚. This indicates that all angular deposited ZnS films had the same elemental composition and these results were consistent with EDX analysis.

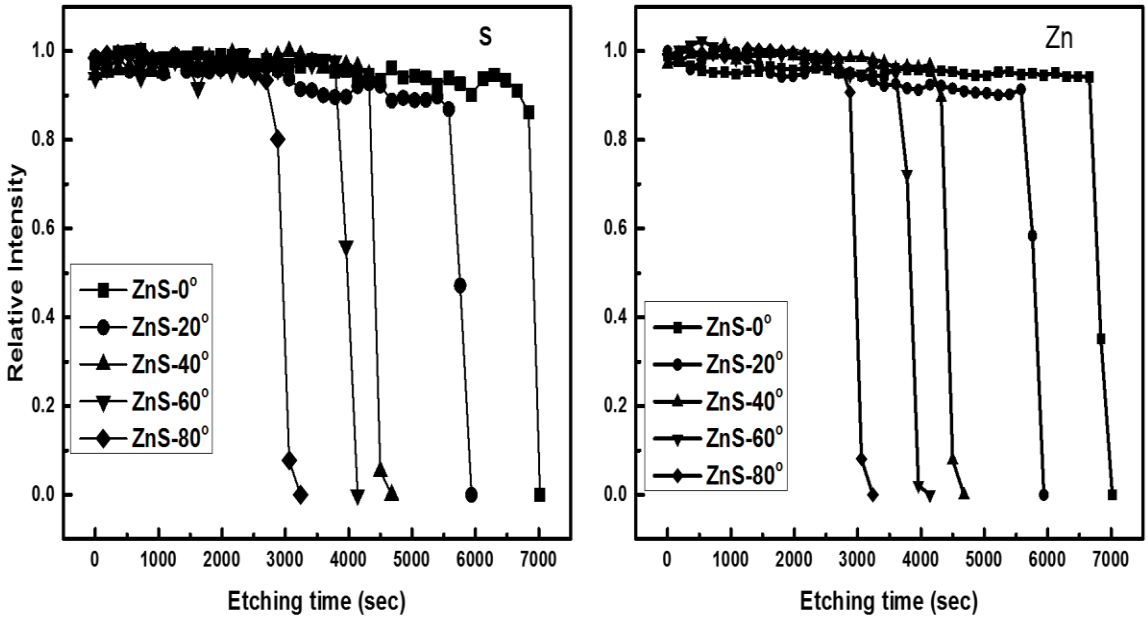

Figure 5.25 Spatial distributions of the Zn and S elements throughout the thicknesses of the ZnS films as obtained by XPS depth profiling

CHAPTER 6

Structural and Morphological Properties

6.1 Structural Properties

X-ray diffraction was used to investigate the structural properties of the angular-deposited II-VI compound films

Figure 6.1 depicts the XRD patterns of CdTe films. All CdTe films showed three peaks (111), (220) and (311) which were characteristic of polycrystalline cubic CdTe (JCPDS data card #15-0770) [160]. The dominant peak in all the XRD patterns was (111), signifies that the films had a preferred orientation in the (111) direction. It was observed that CdTe-0˚ and CdTe-20˚ films showed a (110) peak marked with an asterisk at 22.70˚ that belongs to Te element. This peak indicates that these films were Te-rich.

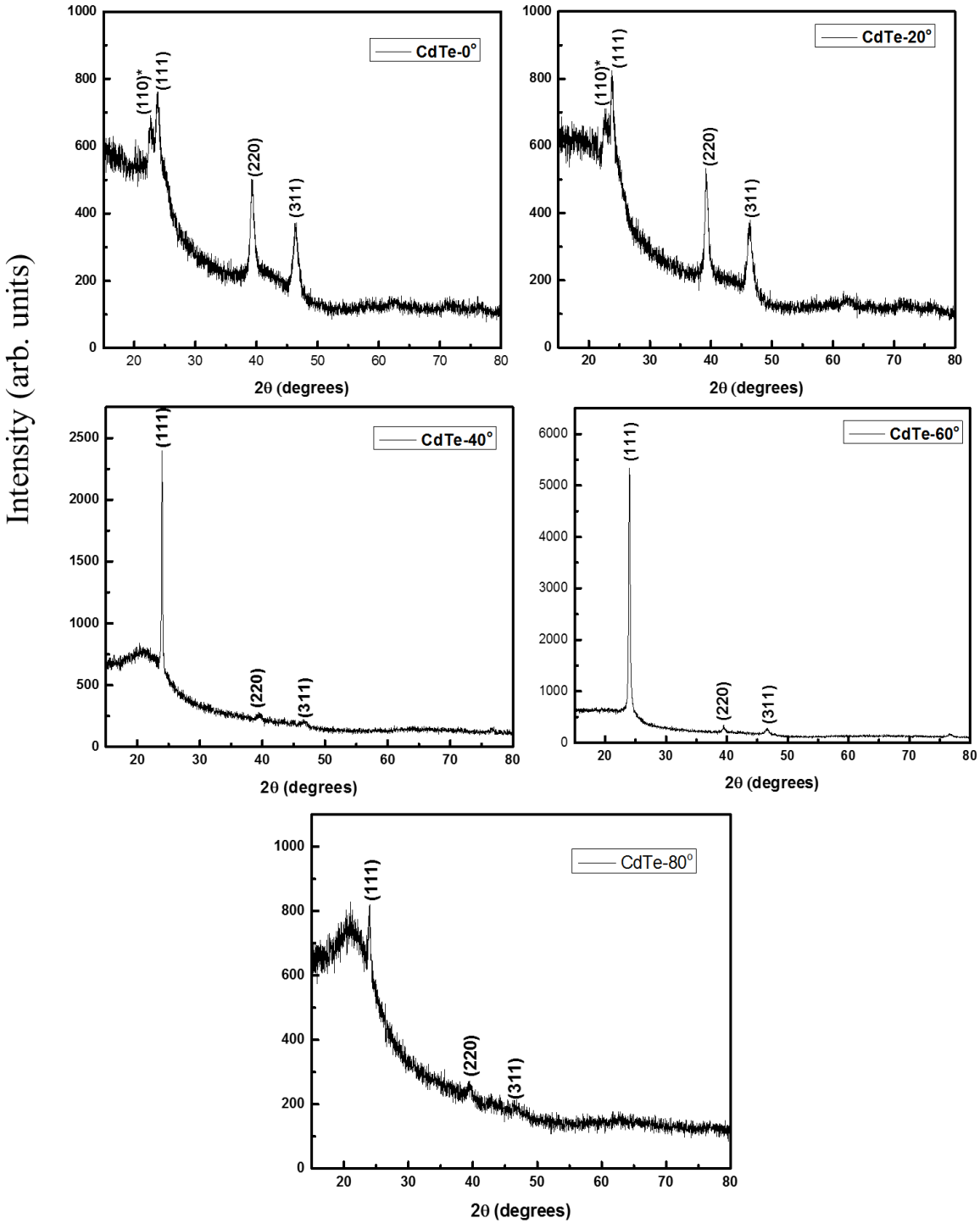

Figure 6.1 XRD patterns of CdTe films

It was noticed that the peak intensity was increased by increasing the metallic Cd content in the films. The peak intensity of CdTe-80˚ film was small because of its small thickness [25]. The values of the crystallite size of the films were calculated by Sherrer's formula, given as [161, 62]:

$$t_s = \frac{K_x \lambda_x}{B \cos\theta} \tag{6.1}$$

where t_s is the crystallite size, B is the full width at half maximum (FWHM) of the dominant peak, K_x = 0.94 is the Sherrer constant, λ_x = 1.5406 Å is the wavelength of x-rays, and θ represents the position of the dominant peak. The calculated values of crystallite size are listed in table 6.1.

Figure 6.2 depicts the XRD patterns of CdSe films. All CdSe films showed a peak 2θ = 26.4˚ corresponding to (002) plane, which was characteristic of a single crystal CdSe (JCPDS card no. 01-077-2307) [163]. It was observed that the (002) peak intensity was increased with the increase of metallic Cd content in the films. However, the peak intensity of the film deposited at 80˚ was less because of small thickness. The values of crystallite sizes of CdSe films were calculated using equation (6.1) and are listed in Table 6.1.

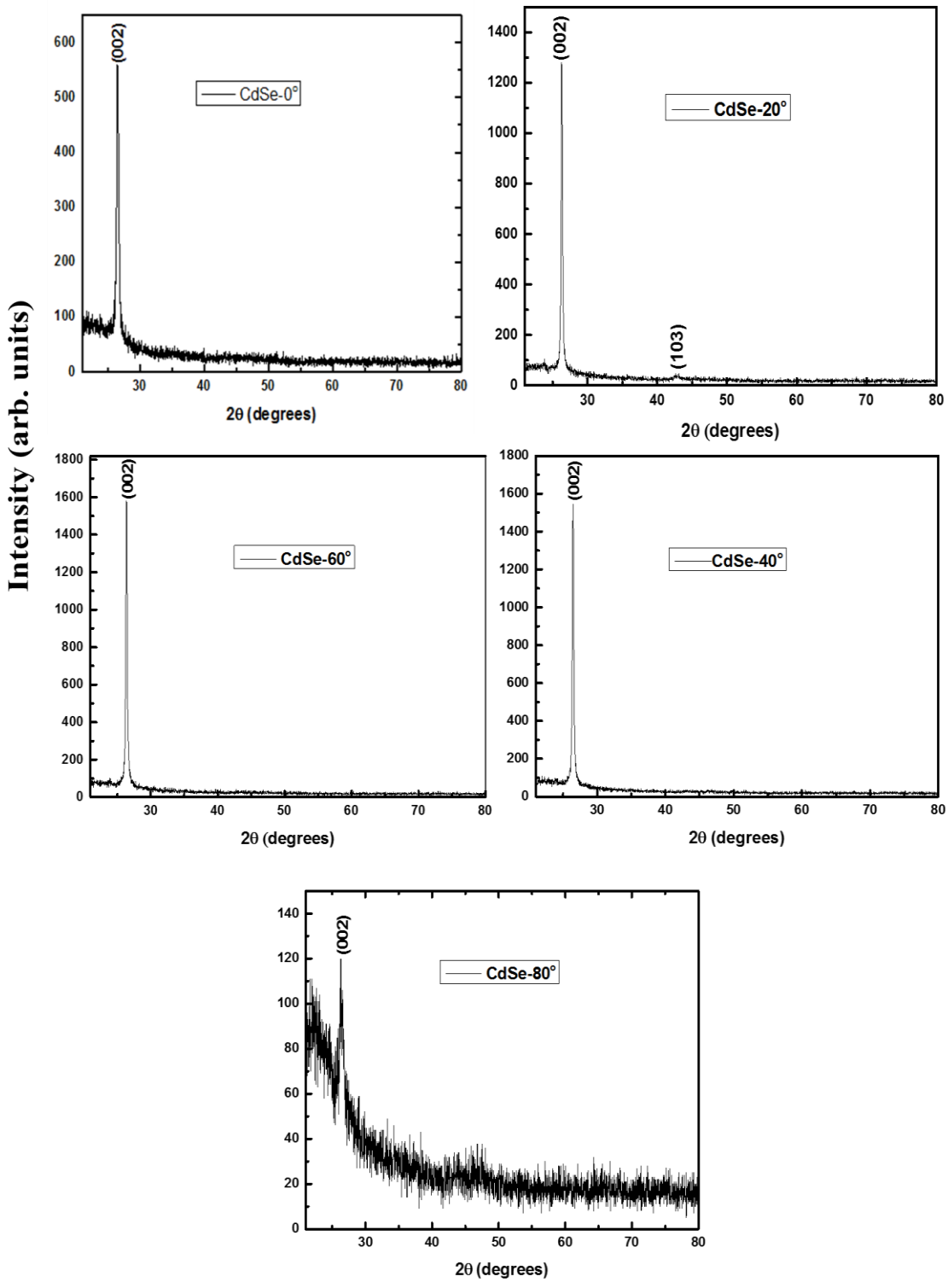

Figure 6.2 XRD patterns of CdSe films

Figure 6.3 shows the XRD patterns of CdS films. All XRD patterns showed a (111) peak at $2\theta = 26.63^{\circ}$, which were characteristic of a single crystal CdS (JCPDS card No. 10-0454) [164]. The (111) peak signifies that the films had a preferred orientation along (111) plane. It was observed that the (111) peak intensity was decreased by decreasing the metallic Cd content in the films. The values of crystallite size of the films were calculated using equation (6.1) and are listed in Table 6.1.

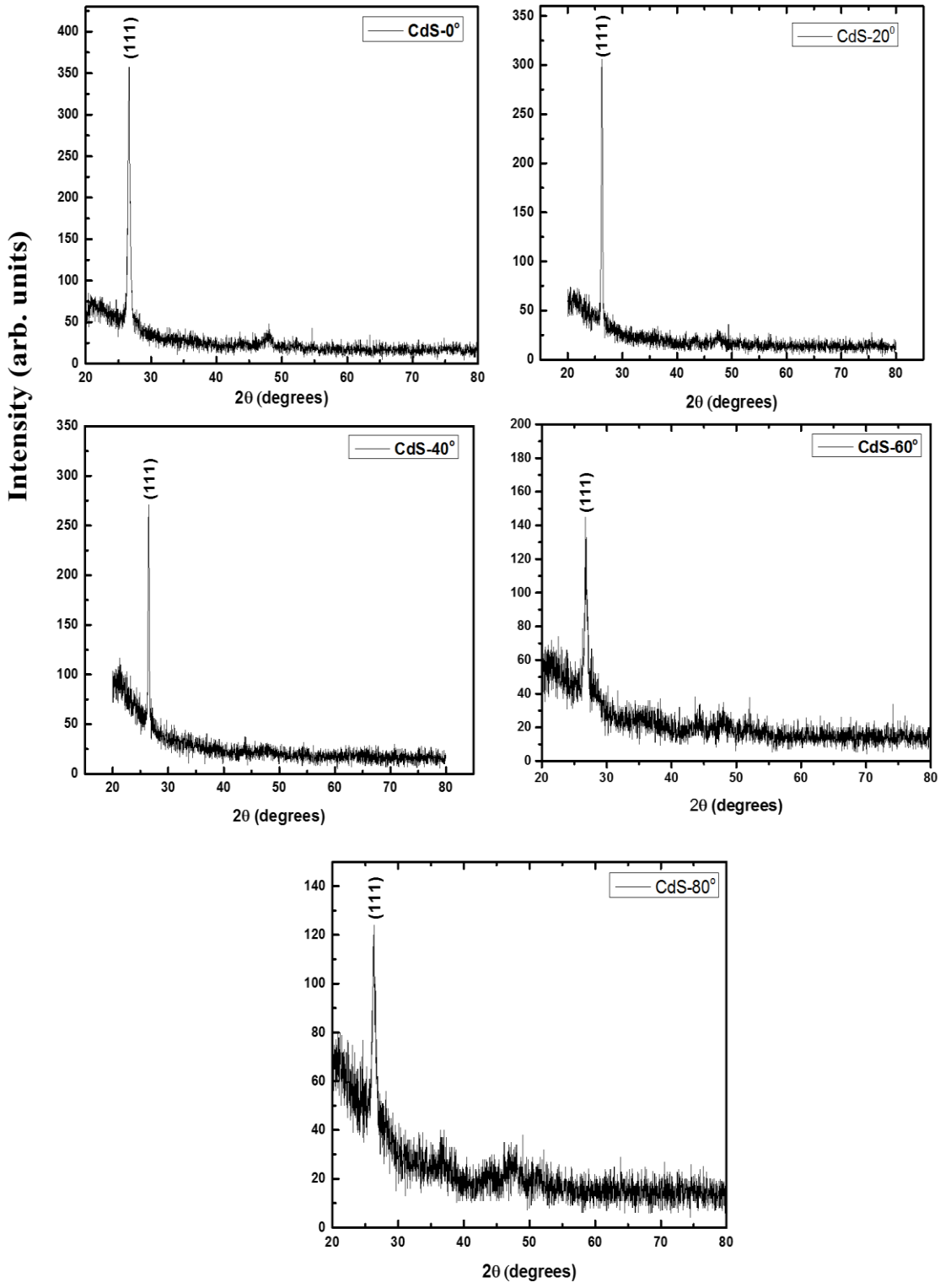

Figure 6.3 XRD patterns of CdS films

Figure 6.4 shows the XRD patterns of the ZnTe films. All films showed three peaks at 2θ = 25.53˚, 41.93˚, and 49.68˚ corresponding to (111), (202), and (311) planes, which are characteristic of polycrystalline ZnTe (JCPDS data card #96-900-8859) [165]. The dominant peak in all the XRD patterns was (111), signifies that the films had a preferred orientation in the (111) direction. It was observed that ZnTe-0˚ and ZnTe-20˚ films showed a (310) peak marked with an asterisk at 2θ = 36.30˚ that belongs to Te element because these films were Te-rich (JCPDS data card #96-153-3531) [166]. The values of crystallite size of the films were calculated using equation (6.1) and are listed in Table 6.1.

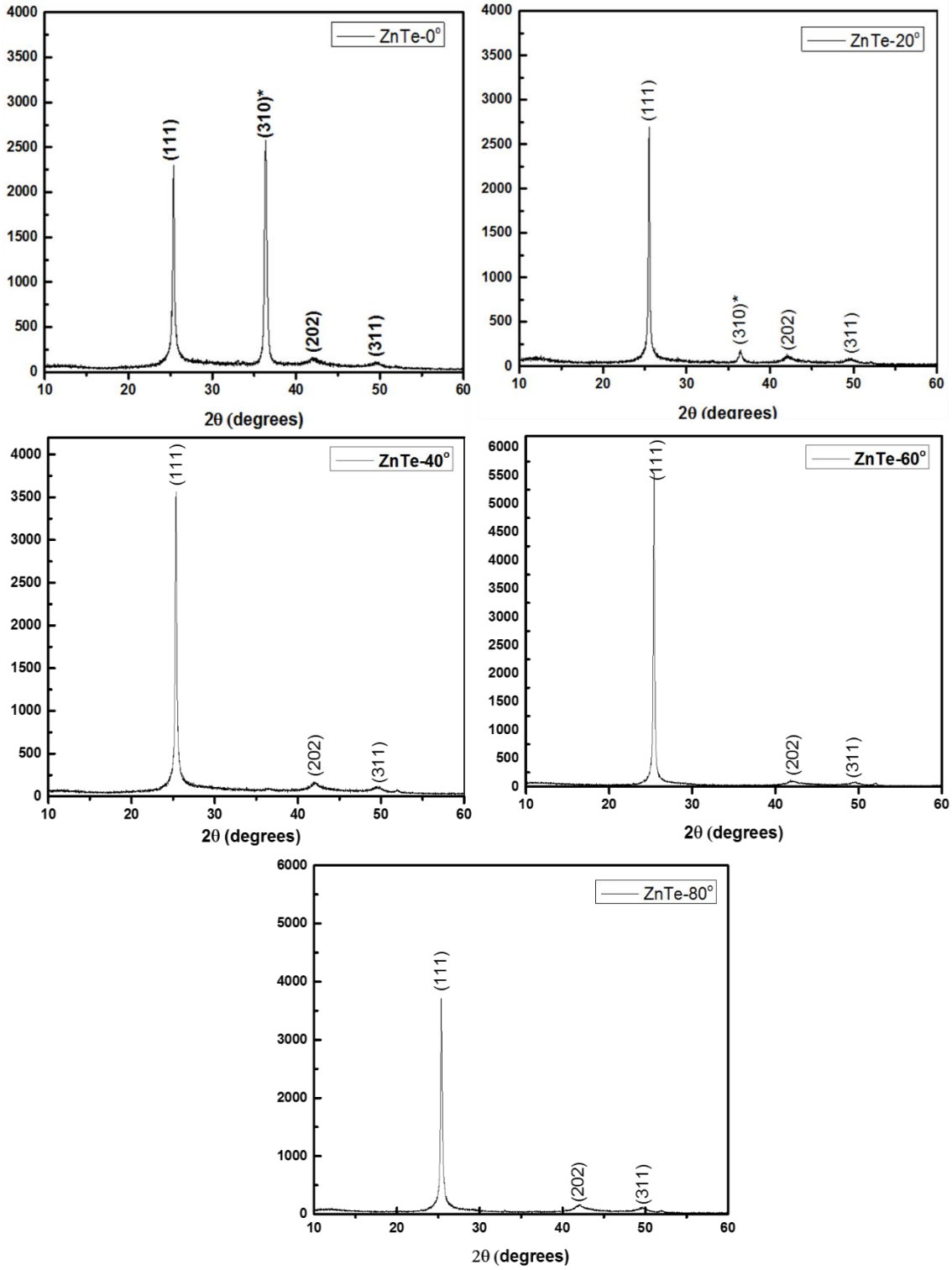

Figure 6.4 XRD patterns of ZnTe films

Figure 6.5 showed the XRD patterns of ZnSe films. XRD pattern of ZnSe films showed that films are polycrystalline (JCPDS card No. 80-002) [167]. The dominant peak in all the XRD patterns was (111), signifying that the films had a preferred orientation in the (111) direction. It was observed that the intensity of (111) peak increased by increasing the metallic Zn content in the films. The values of crystallite size of ZnSe film were measured using equation (6.1) and are listed in Table 6.1.

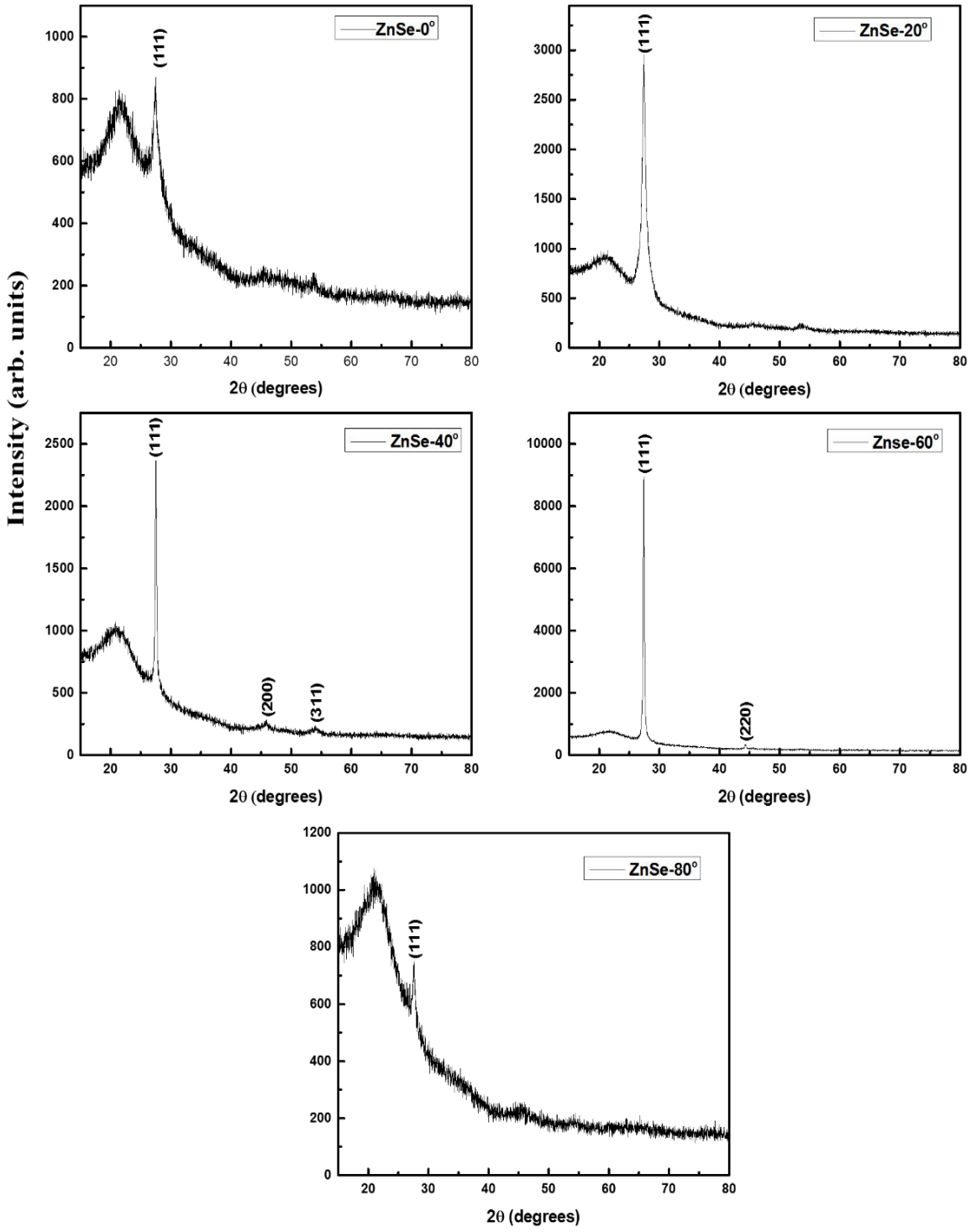

Figure 6.5 XRD patterns of ZnSe films

Figure 6.6 shows the XRD patterns of ZnS films. All ZnS films showed two peaks at $2\theta = 29.08^{\circ}$ and 48.13° corresponding to (002) and (110) planes, which were characteristic of polycrystalline ZnS (JCPDS: 00-065-0309) [168]. The dominant peak in all the XRD patterns was (110), signifies that the films had a preferred orientation in the (110) direction**.** It was observed that the peak intensities decreased by increasing the deposition angle because the decrease of thickness. The crystallite sizes of all the films are calculated using equation (6.1) and are listed in Table 6.1

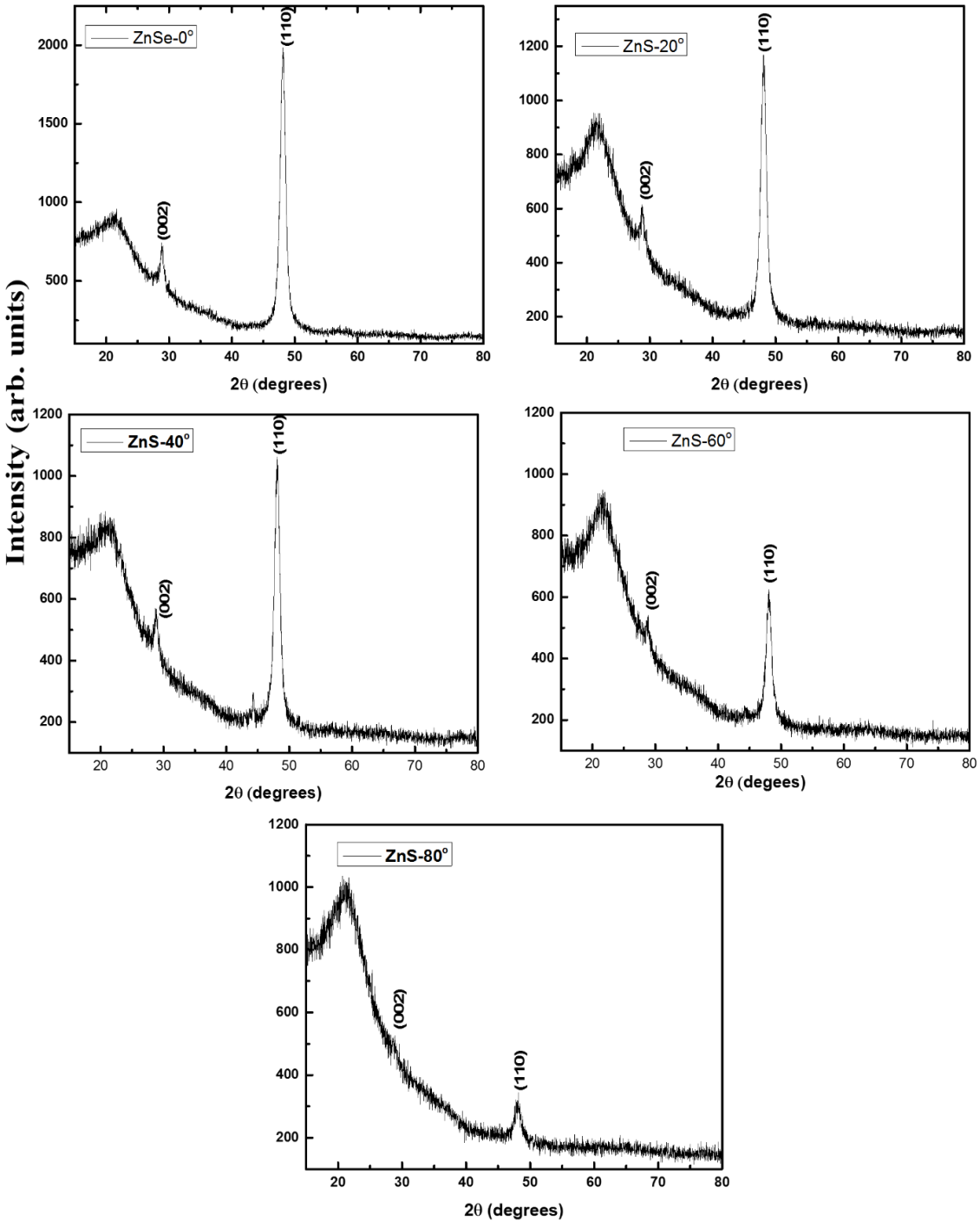

Figure 6.6 XRD patterns of ZnS films

XRD analysis of angular-deposited II-VI compound films shows that all films were polycrystalline because it is the property of II-VI compounds. It was also observed that the crystallite size is also dependent on the deposition angle. In thin film deposition, the lattice strain is induced during growth and affects the crystallite size. The change in crystallite size might be due to lattice strain that was induced during film growth [169].

Table 6.1 Values of crystallite size (t_s) of II-VI compound films

Sample	t_s *(nm)*
CdTe-0˚	5.9
CdTe-20˚	10.2
CdTe-40˚	29.7
CdTe-60˚	41.0
CdTe-80˚	12.9
CdSe-0˚	25.1
CdSe-20˚	31.7
CdSe-40˚	32.9
CdSe-60˚	34.0
CdSe-80˚	21.5
CdS-0˚	38.1
CdS-20˚	34.0
CdS-40˚	21.9
CdS-60˚	15.9
CdS-80˚	13.9
ZnTe-0˚	27.9
ZnTe-20˚	32.8
ZnTe-40˚	37.5
ZnTe-60˚	38.5
ZnTe-80˚	30.8
ZnSe-0˚	9.4
ZnSe-20˚	11.3
ZnSe-40˚	28.7
ZnSe-60˚	31.3
ZnSe-80˚	21.2
ZnS-0˚	8.3
ZnS-20˚	8.1
ZnS-40˚	7.8
ZnS-60˚	7.7
ZnS-80˚	7.3

6.2 Morphological Properties

Atomic force microscopy (AFM) was used to study the surface morphology, film growth mode, and the statistical analysis of AFM images provided the root-mean-square surface roughness (R_{rms}). The surface scan area of 2×2 μm^2 was taken to account for this purpose. Two-dimensional (2D) AFM images of CdTe, CdSe, CdS, ZnTe, ZnSe, and ZnS thin films are shown in figs. 6.7, 6.9, 6.11, 6.13, 6.15, and 6.17, respectively. Three-dimensional (3D) AFM images of CdTe, CdSe, CdS, ZnTe, ZnSe, and ZnS thin films are shown in figs. 6.8, 6.10, 6.12, 6.14, and 6.18, respectively. Two-dimensional AFM images of CdTe, CdSe, CdS, ZnTe, and ZnSe films show well-defined grains on the surfaces and two-dimensional AFM images of ZnS films did not show grains on the surface. It is clear from the two-dimensional AFM images that the surfaces had some voids and it could be due to the fact that the substrates were not rotating during deposition. Three-dimensional images of II-VI compound films showed a columnar structure which became more well defined by increasing the deposition angle. It was also noticed that the surface roughness of II-VI compound films was increased by increasing the deposition angle from 0˚ to 80˚. The increase of surface roughness was due to shadowing effect raised by oblique angle [170, 171]. The values of surface roughness are listed in Table 6.2

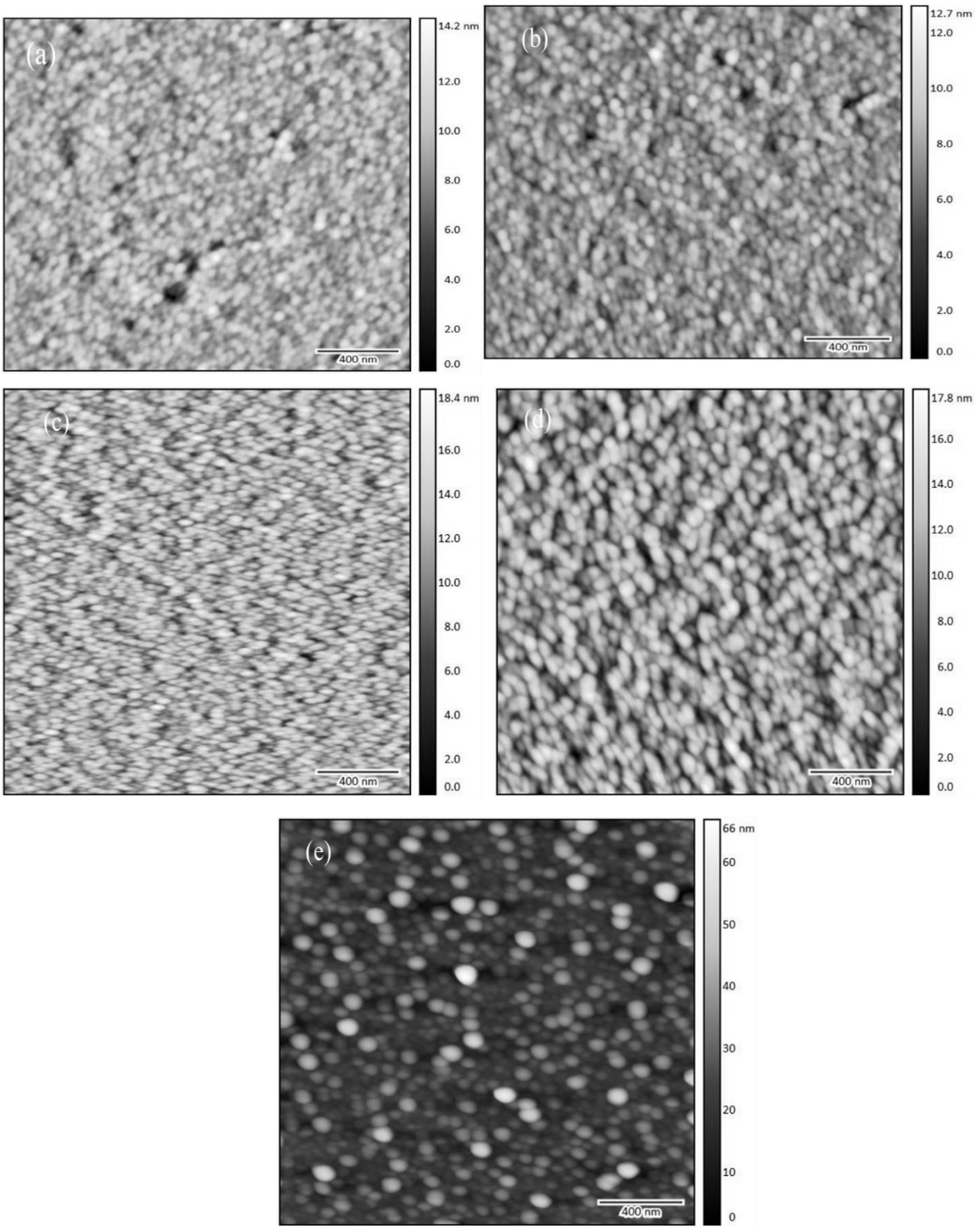

Figure 6.7 2D AFM images of (a) CdTe-0˚, (b) CdTe-20˚, (c) CdTe-40˚, (d) CdTe-60˚, and (e) CdTe-80˚ films

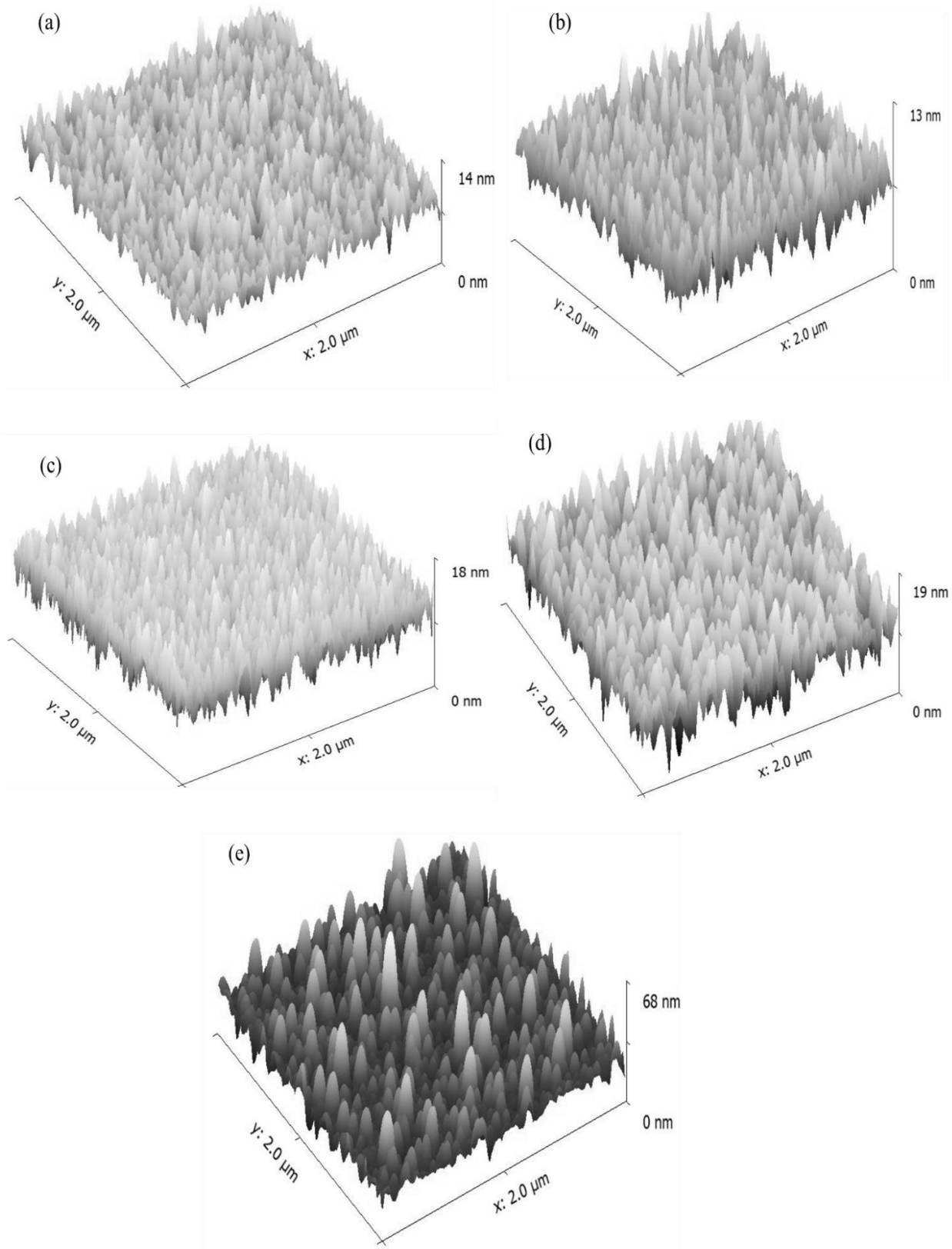

Figure 6.8 3D AFM images of (a) CdTe-0˚, (b) CdTe-20˚, (c) CdTe-40˚, (d) CdTe-60˚, and (e) CdTe-80˚ films

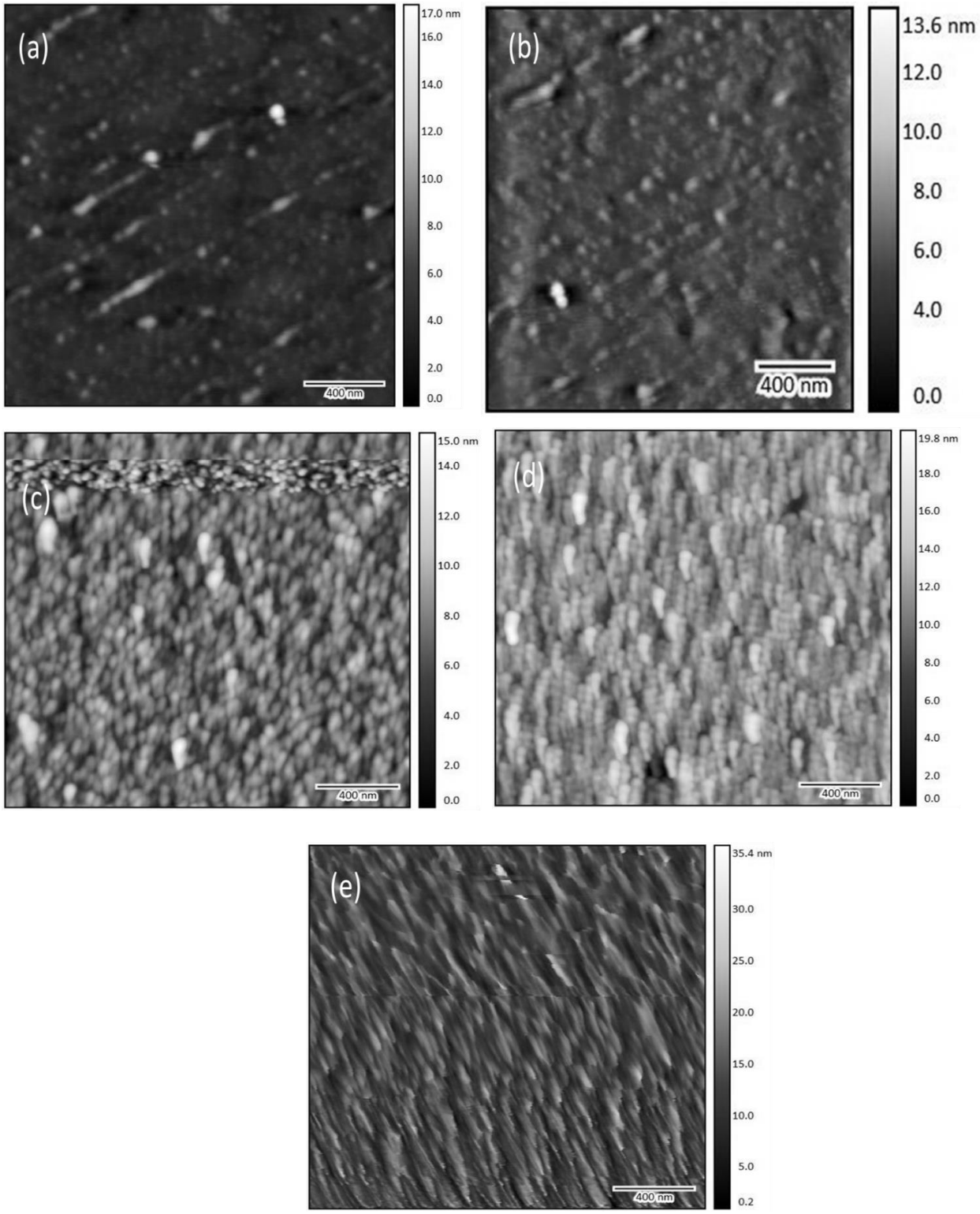

Figure 6.9 2D AFM images of (a) CdSe-0˚, (b) CdSe-20˚, (c) CdSe-40˚, (d) CdSe-60˚, and (e) CdSe-80˚ films

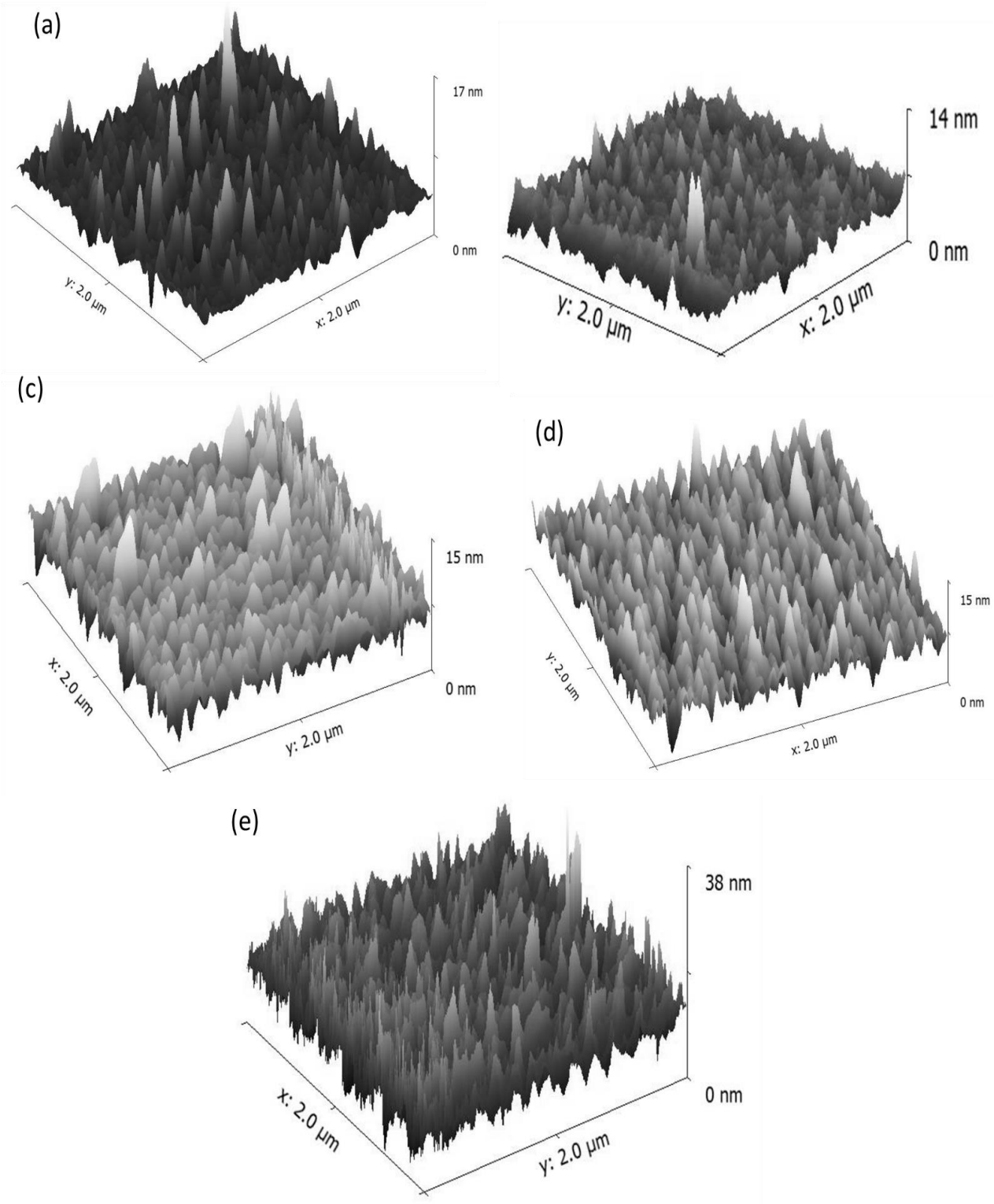

Figure 6.10 3D AFM images of (a) CdSe-0˚, (b) CdSe-20˚, (c) CdSe-40˚, (d) CdSe-60˚, and (e) CdSe-80˚ films

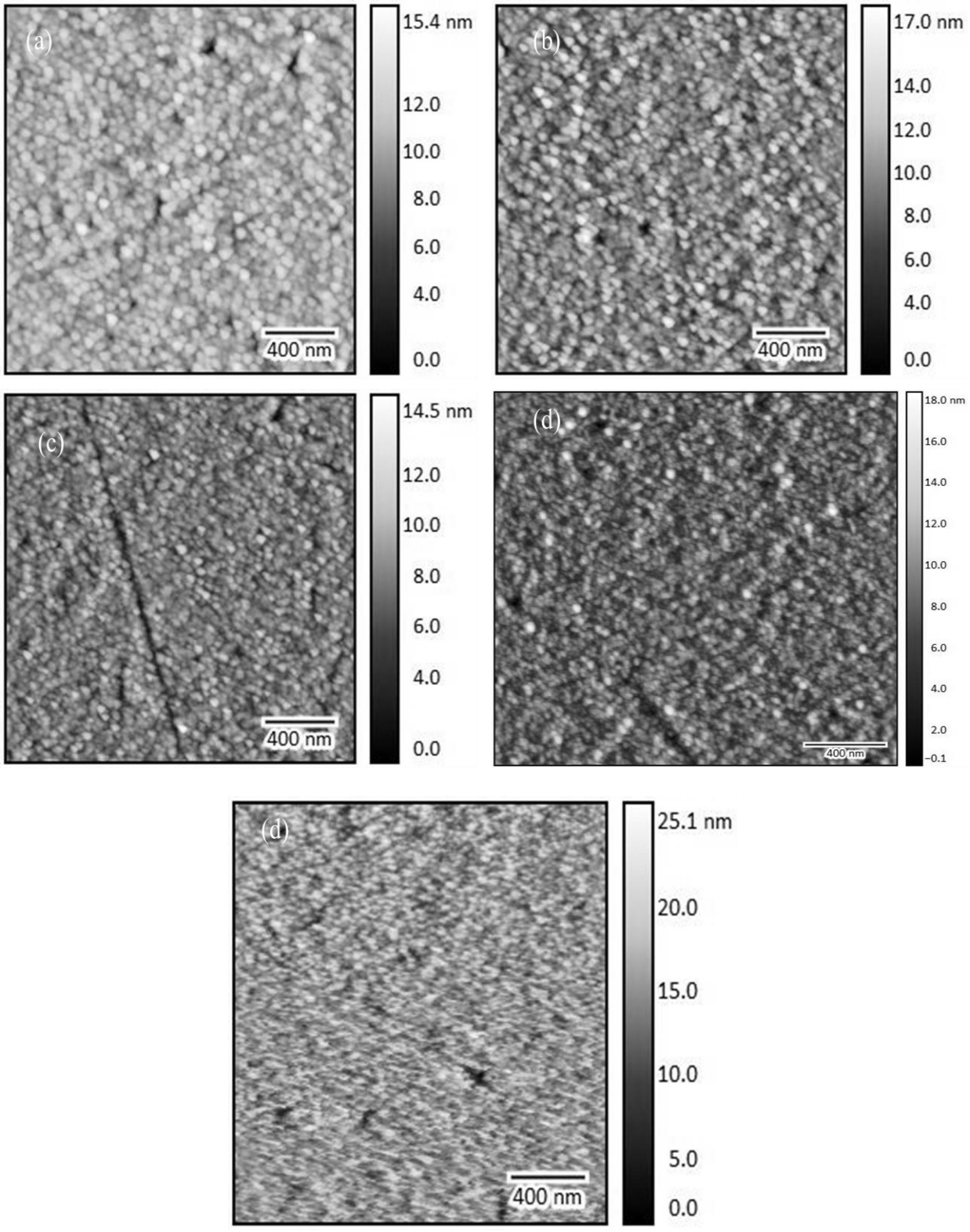

Figure 6.11 2D AFM images of (a) CdS-0˚, (b) CdS-20˚, (c) CdS-40˚, (d) CdS-60˚, and (e) CdS-80˚ films

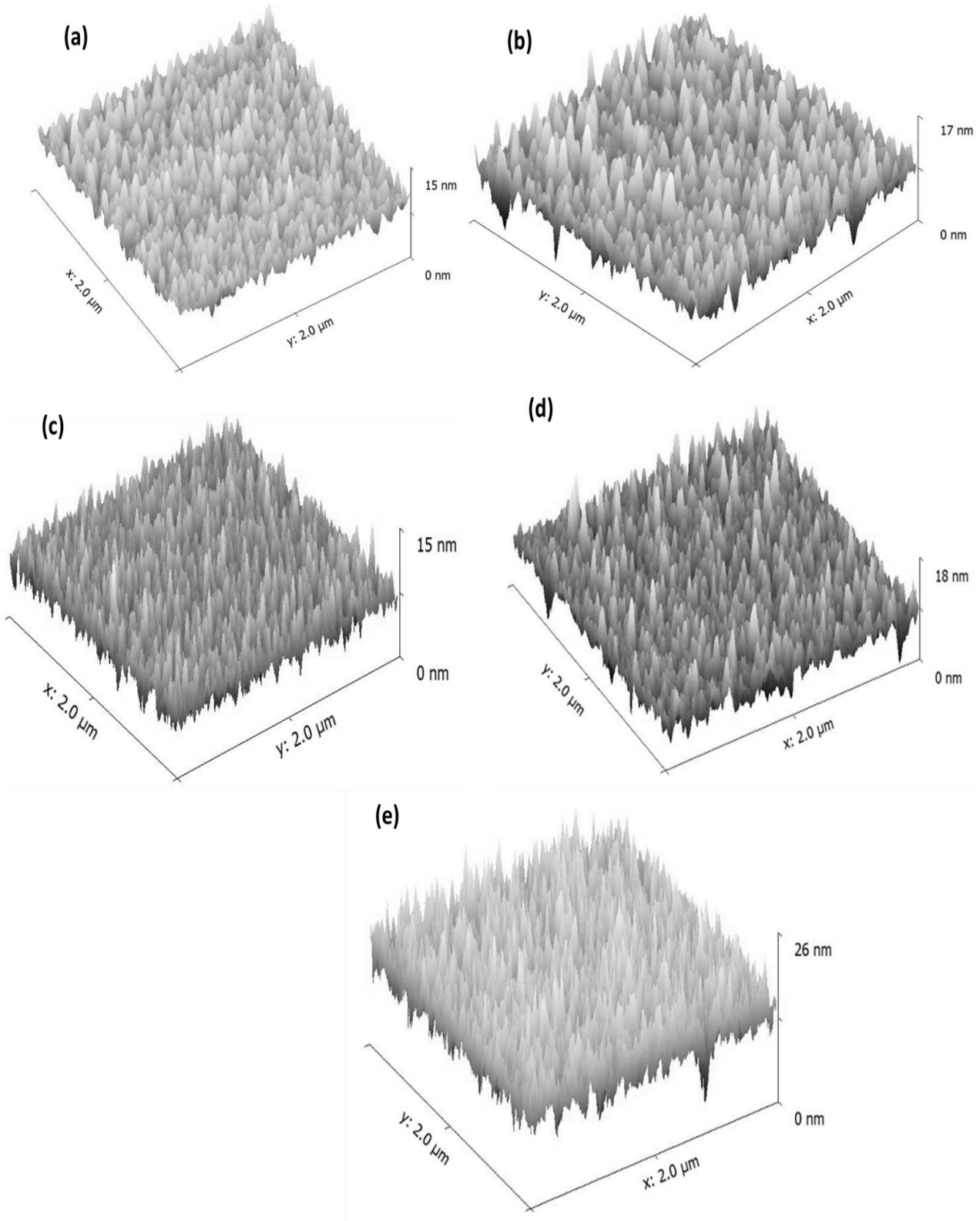

Figure 6.12 3D AFM images of (a) CdS-0˚, (b) CdS-20˚, (c) CdS-40˚, (d) CdS-60˚, and (e) CdS-80˚ films

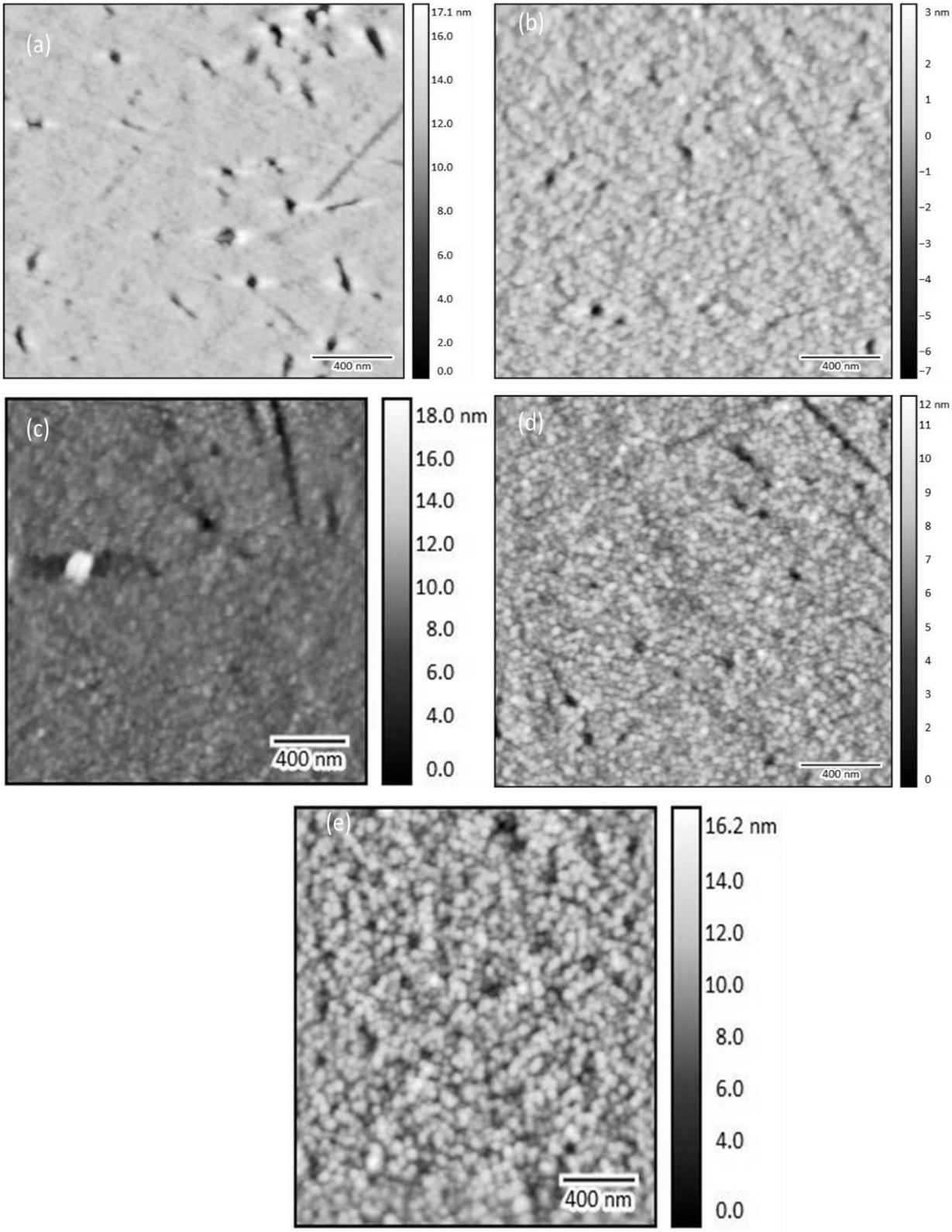

Figure 6.13 2D AFM images of (a) ZnTe-0˚, (b) ZnTe-20˚, (c) ZnTe-40˚, (d) ZnTe-60˚, and (e) ZnTe-80˚ films

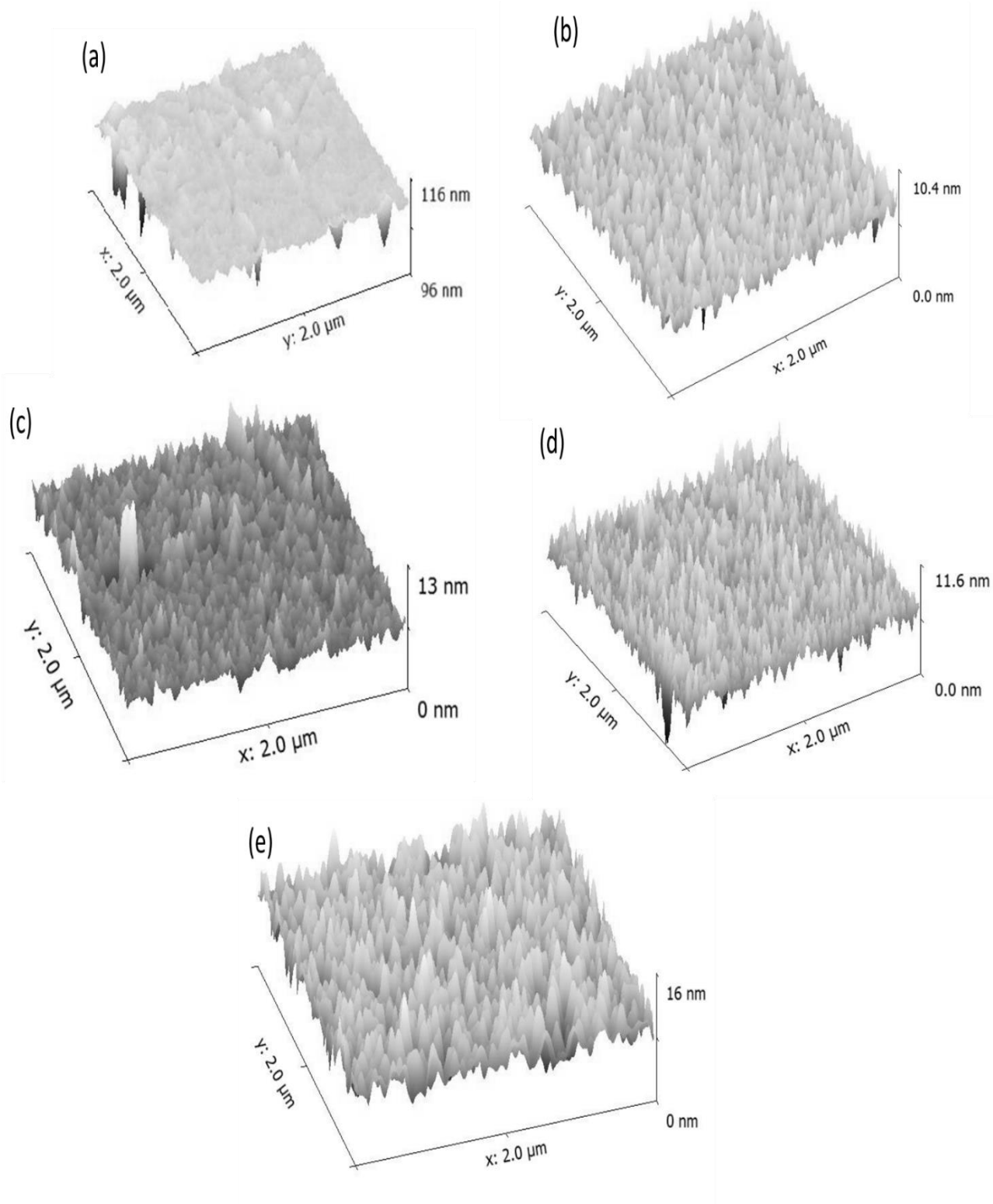

Figure 6.14 3D AFM images of (a) ZnTe-0˚, (b) ZnTe-20˚, (c) ZnTe-40˚, (d) ZnTe-60˚, and (e) ZnTe-80˚ films

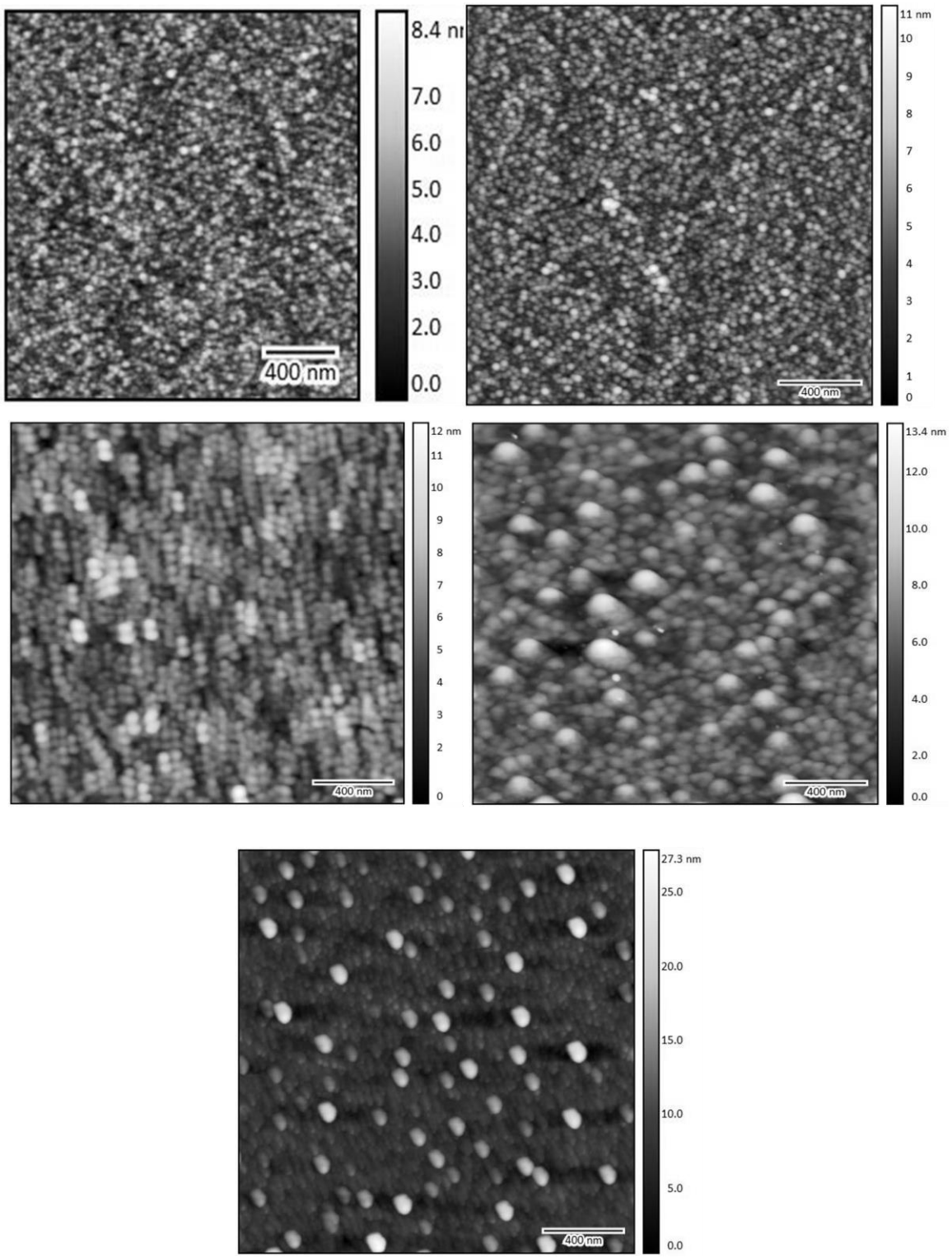

Figure 6.15 2D AFM images of (a) ZnSe-0˚, (b) ZnSe-20˚, (c) ZnSe-40˚, (d) ZnSe-60˚, and (e) ZnSe-80˚ films

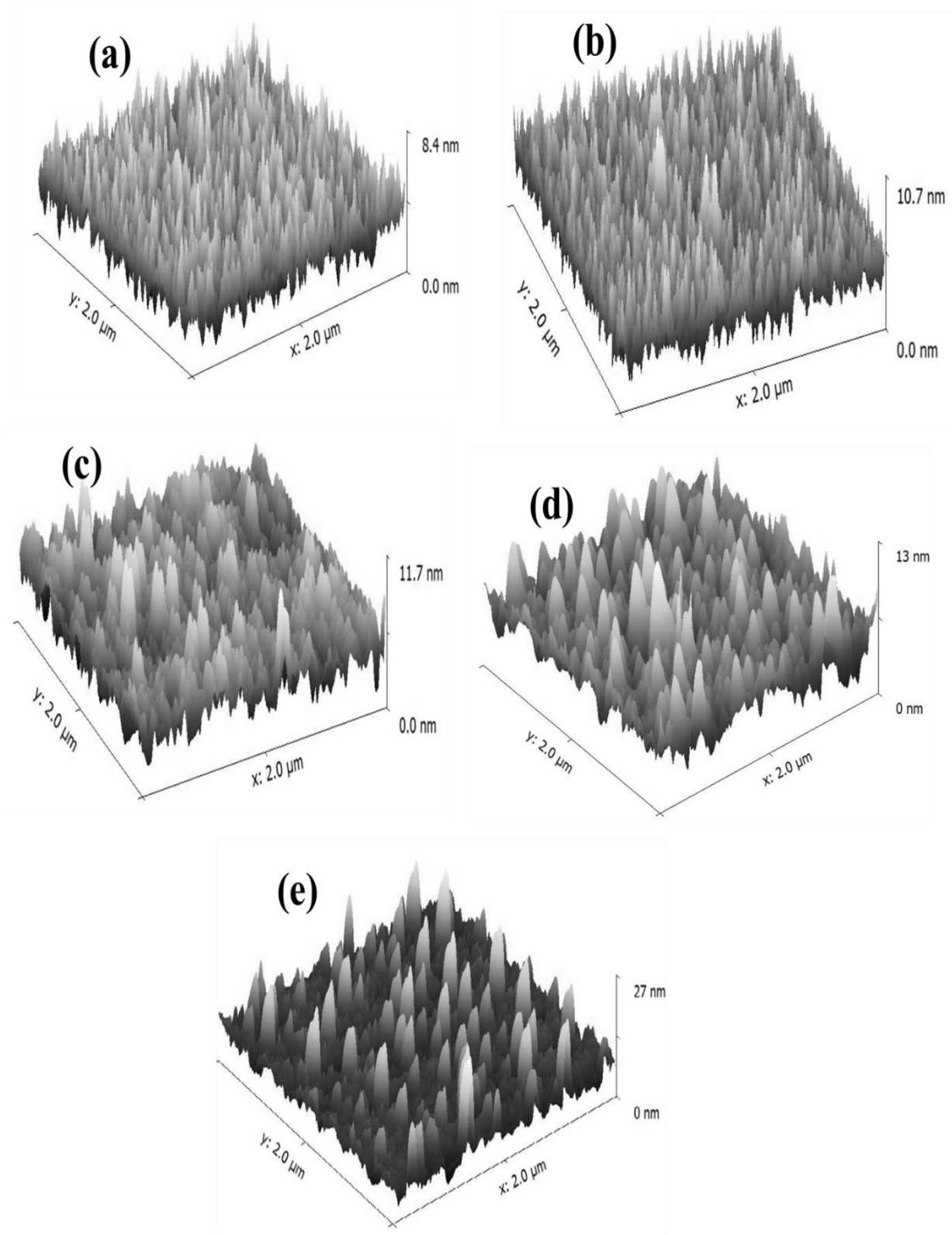

Figure 6.16 3D AFM images of (a) ZnSe-0˚, (b) ZnSe-20˚, (c) ZnSe-40˚, (d) ZnSe-60˚, and (e) ZnSe-80˚ films

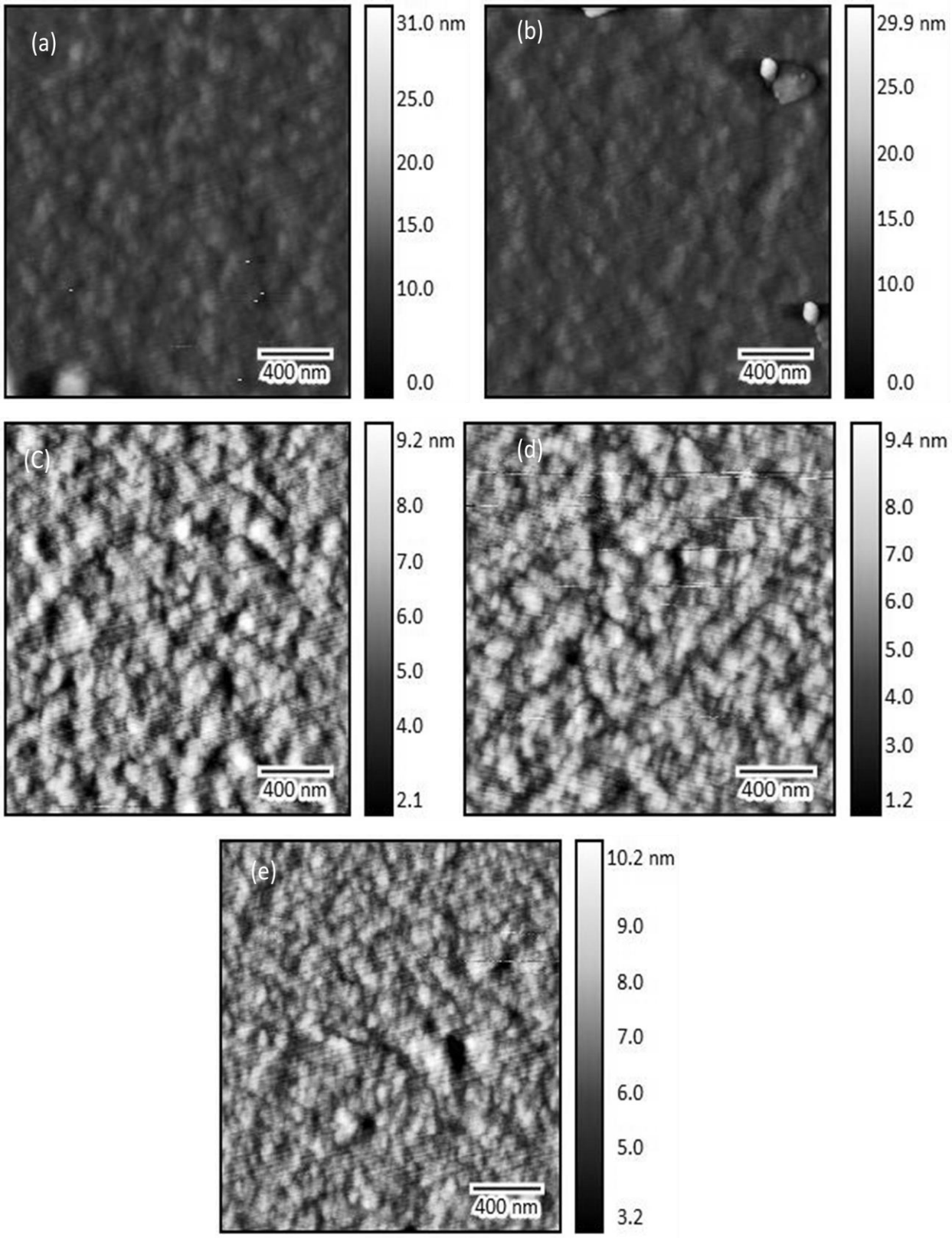

Figure 6.17 2D AFM images of (a) ZnS-0˚, (b) ZnS-20˚, (c) ZnS-40˚, (d) ZnS-60˚, and (e) ZnS-80˚ films

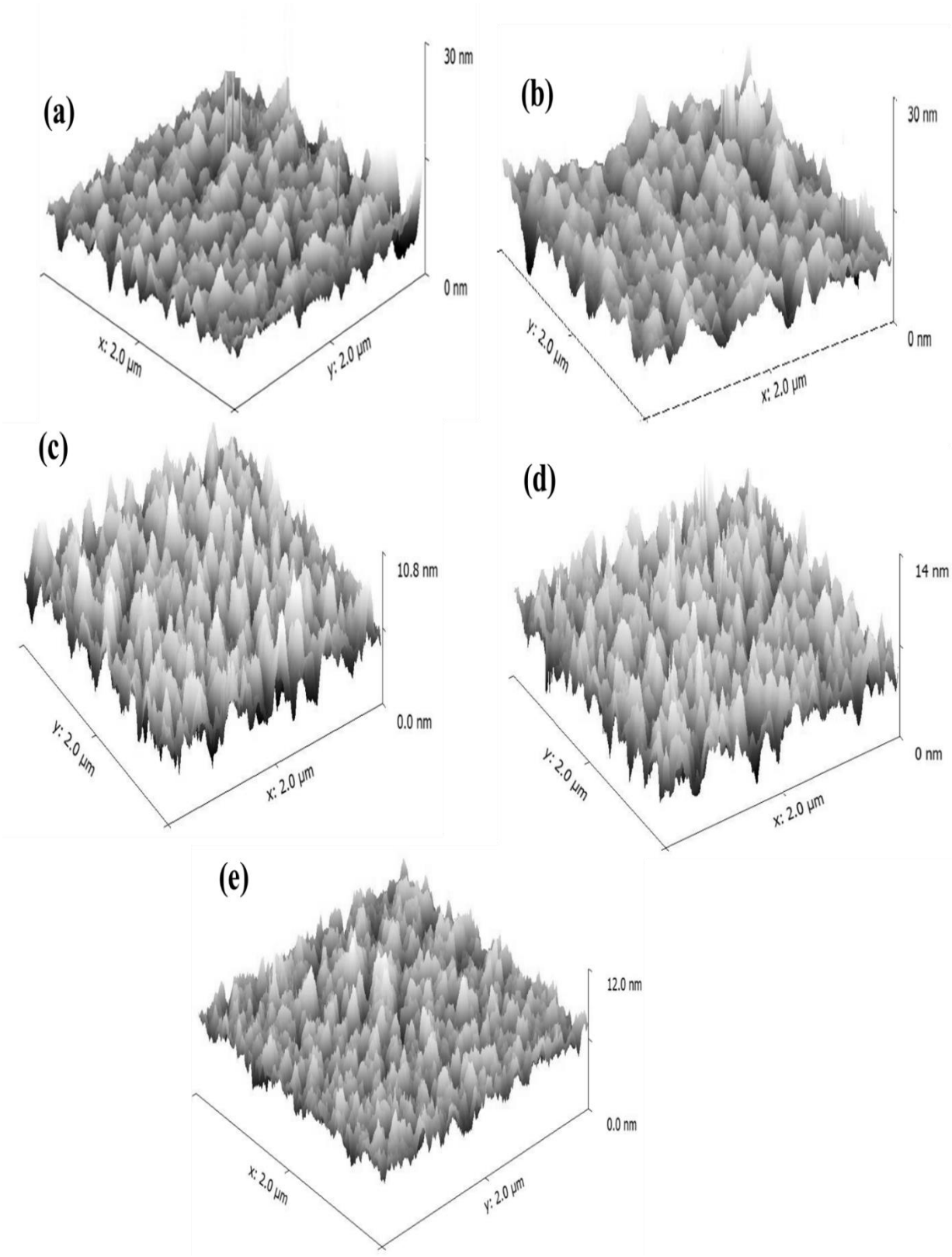

Figure 6.18 3D images of (a) ZnS-0˚, (b) ZnS-20˚, (c) ZnS-40˚, (d) ZnS-60˚, and (e) ZnS-80˚ films

Table 6.2 Values of surface roughness (R_{rms}) of II-VI compound films

Sample	R_{rms} (nm)
CdTe-0˚	1.2
CdTe-20˚	1.3
CdTe-40˚	2.1
CdTe-60˚	2.5
CdTe-80˚	6.7
CdSe-0˚	1.0
CdSe-20˚	1.2
CdSe-40˚	1.5
CdSe-60˚	1.6
CdSe-80˚	3.2
CdS-0˚	1.2
CdS-20˚	1.3
CdS-40˚	1.7
CdS-60˚	1.9
CdS-80˚	3.1
ZnTe-0˚	0.8
ZnTe-20˚	0.9
ZnTe-40˚	1.0
ZnTe-60˚	1.4
ZnTe-80˚	2.8
ZnSe-0˚	1.0
ZnSe-20˚	1.2
ZnSe-40˚	1.7
ZnSe-60˚	2.8
ZnSe-80˚	5.6
ZnS-0˚	8.4
ZnS-20˚	9.0
ZnS-40˚	12.5
ZnS-60˚	11.6
ZnS-80˚	15.1

CHAPTER 7

Optical Properties

In this chapter, the optical properties of angular deposited II-VI compound films are presented.

7.1 Transmittance and Reflectance

The transmittance and reflectance spectra of II-VI compound films were measured by spectrophotometry. Figures 7.1 (a), 7.2 (a), 7.3 (a), 7.4 (a), 7.5 (a), and 7.6 (a) represent the transmittance spectra of CdTe, CdSe, CdS, ZnTe, ZnSe, and ZnS films, respectively. Figures 7.1 (b), 7.2 (b), 7.3 (b), 7.4 (b), 7.5 (b), and 7.6 (b) represent the reflectance spectra of CdTe, CdSe, CdS, ZnTe, ZnSe, and ZnS films, respectively. The transmittance and reflectance spectra of CdTe, CdSe, ZnTe, and ZnSe films showed that at higher angles (60˚ and 80˚) deposited films had less transmittance and high reflectance compared to lower angles (0˚, 20˚, and 40˚) deposited films. The transmittance and reflectance spectra of CdS films showed that at lower angles (0˚, 20˚, and 40˚) deposited films had less transmittance and high reflectance compared to higher angles (60˚ and 80˚) deposited films. The transmittance spectra of ZnS films showed that angular deposited ZnS films were transparent in the visible and the near infrared (NIR) regions. It was observed that the transmittances of angular deposited ZnS films were the same. Reflectance spectra of angular-deposited ZnS films showed that reflectance of all films was also the same. It was noticed that those films, which had less transmittance and high reflectance were metal (Cd or Zn) rich. Like other metals, Cd and Zn metals are also

reflective materials and high content of Cd or Zn in the film increased the reflectance of the film and hence decreased its transmittance [172, 173]. The transmittance and reflectance of angular deposited ZnS films were the same because these films were nearly stoichiometric. It was noticed that the transmittance and reflectance of II-VI compound films were dependent on the stoichiometry of the films.

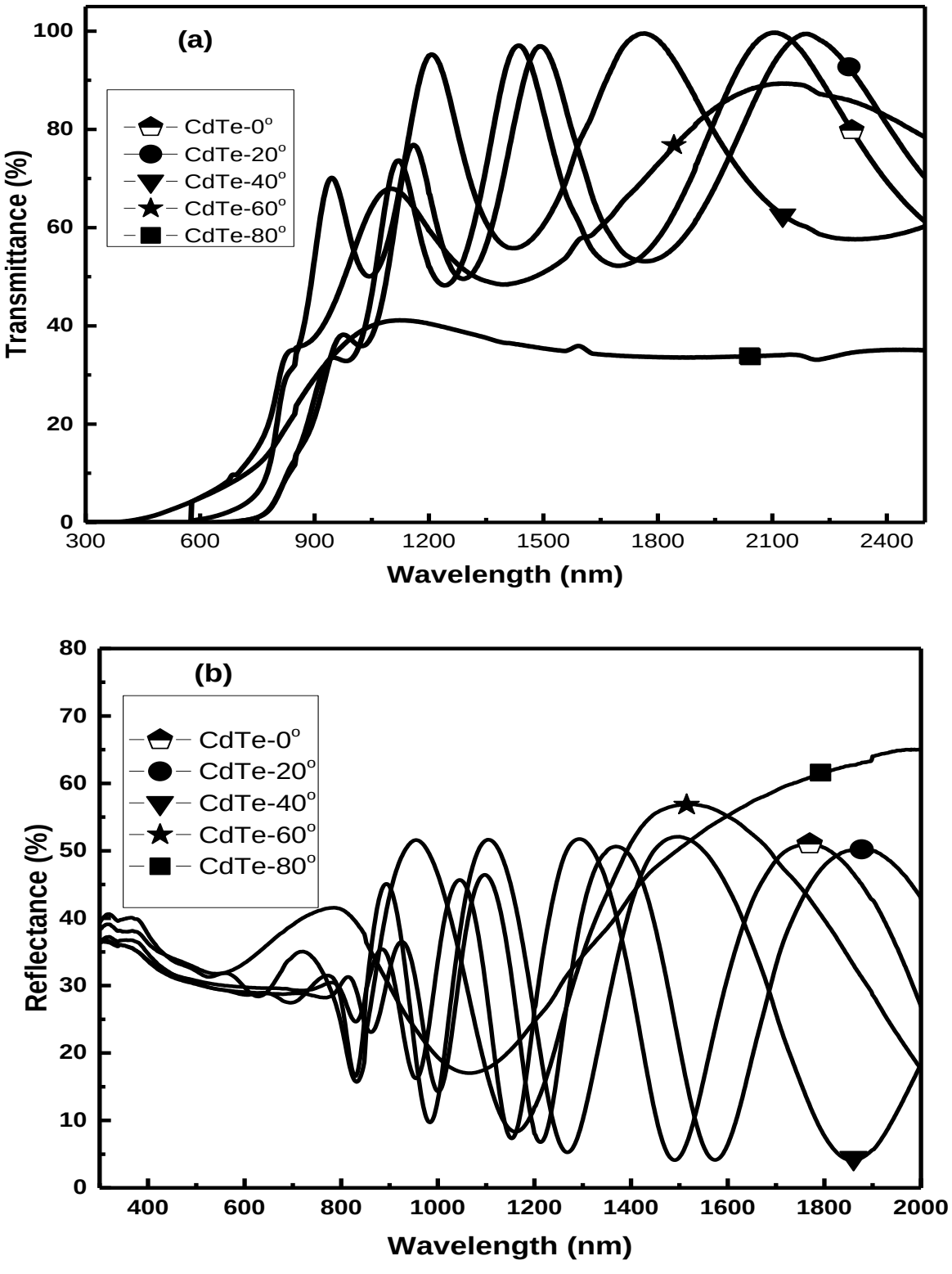

Figure 7.1 (a) Transmittance and (b) Reflectance spectra of CdTe films

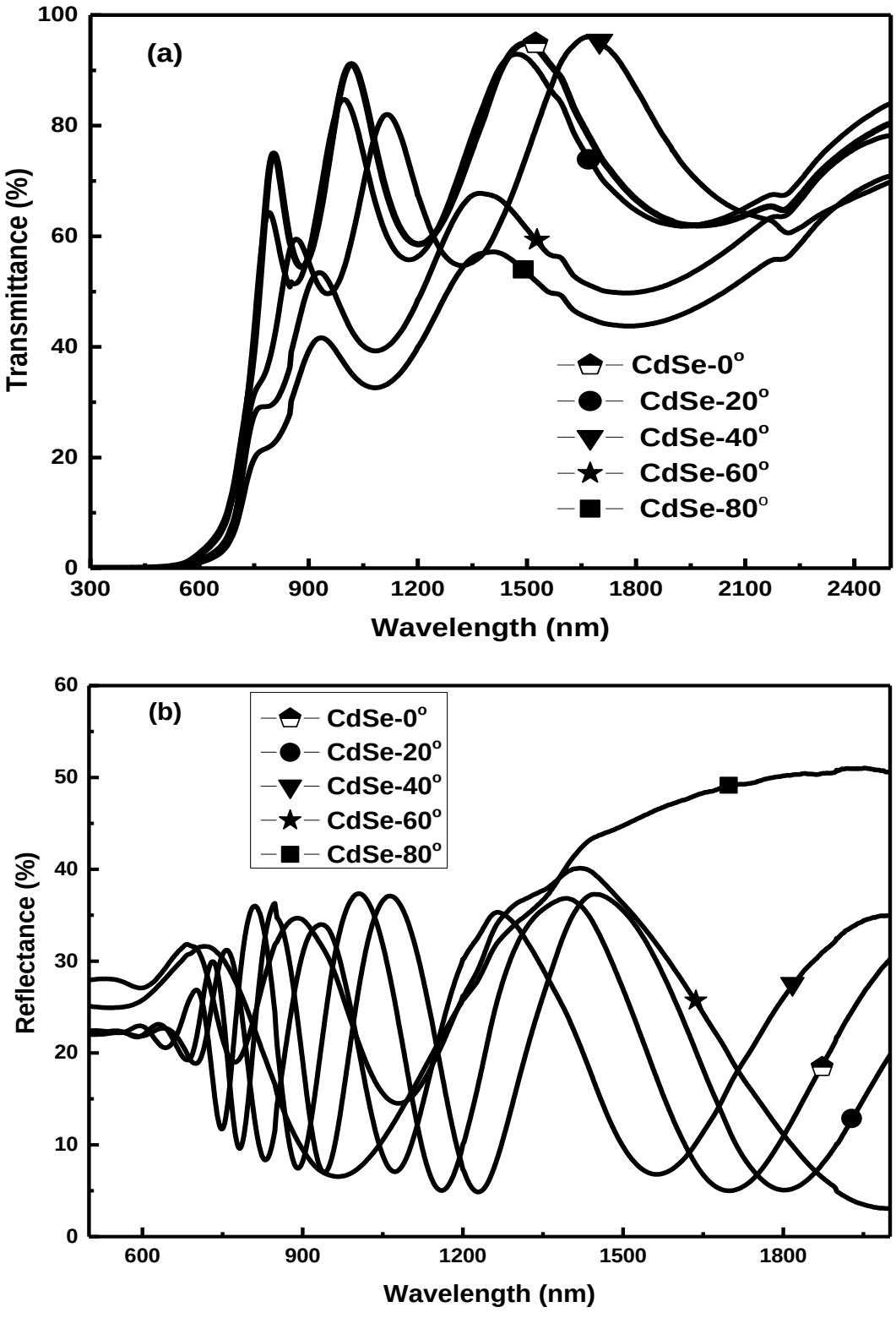

Figure 7.2 (a) Transmittance and (b) Reflectance spectra of CdSe films

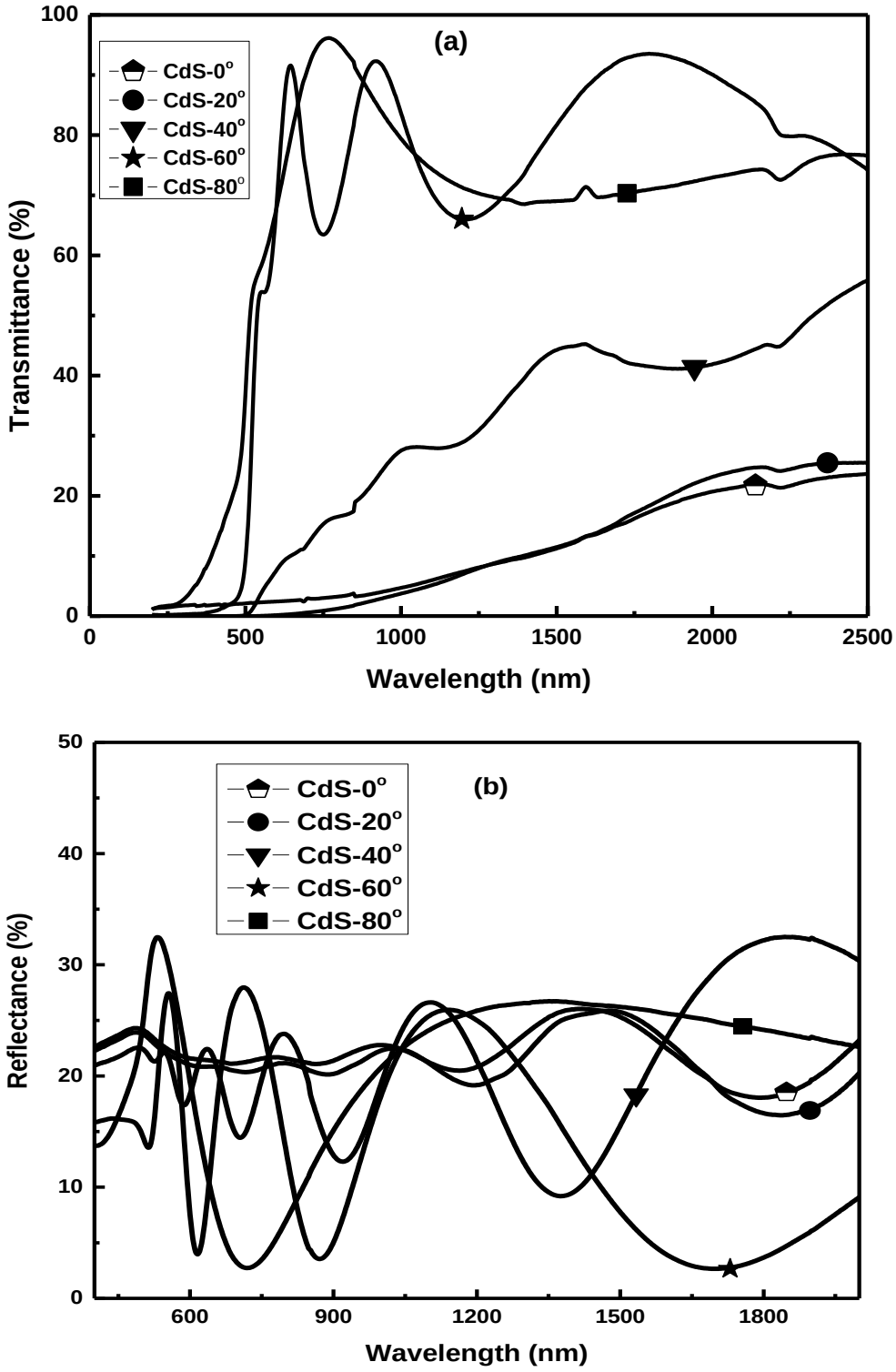

Figure 7.3 (a) Transmittance and (b) Reflectance spectra of CdS films

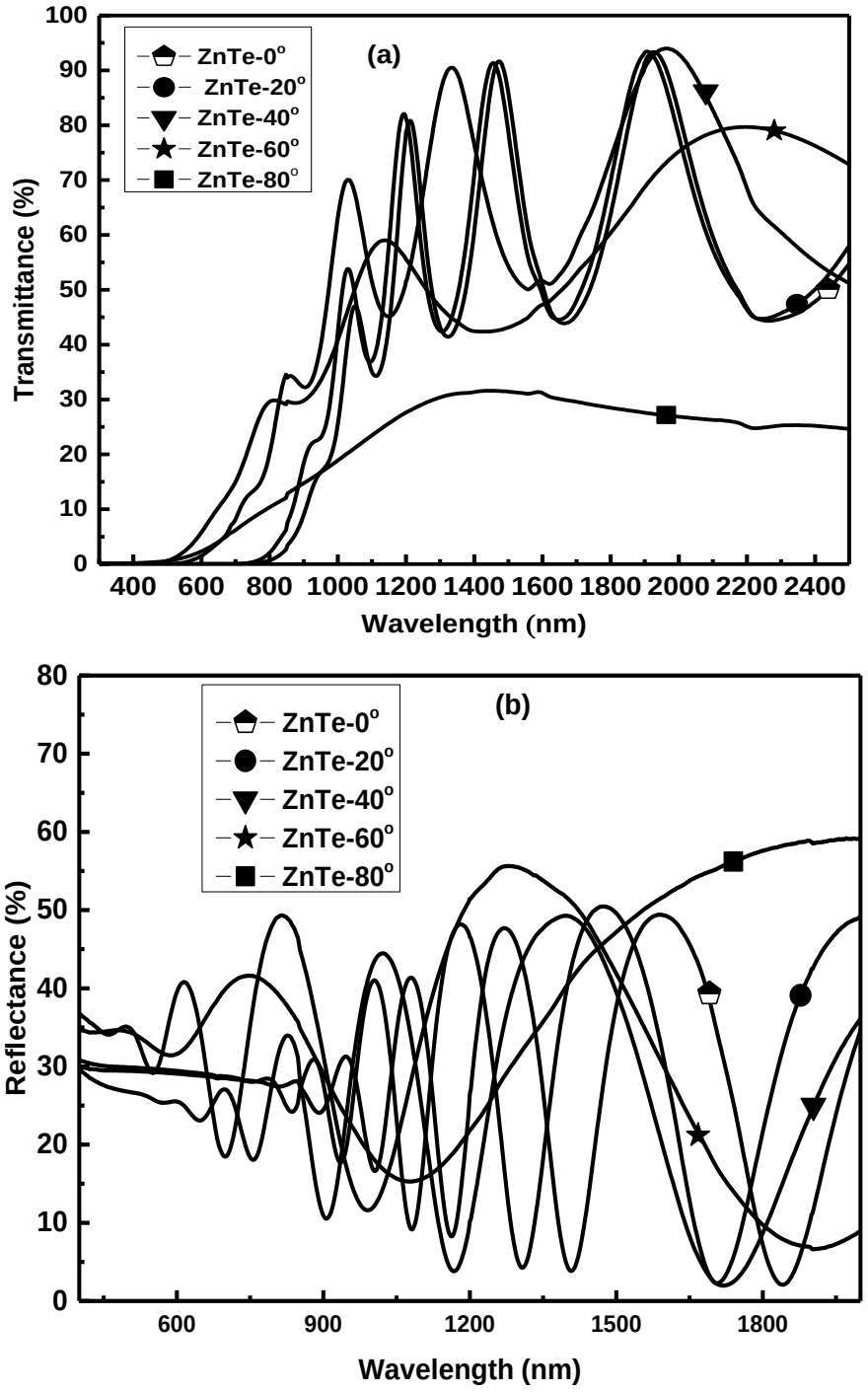

Figure 7.4 (a) Transmittance and (b) Reflectance spectra of ZnTe films

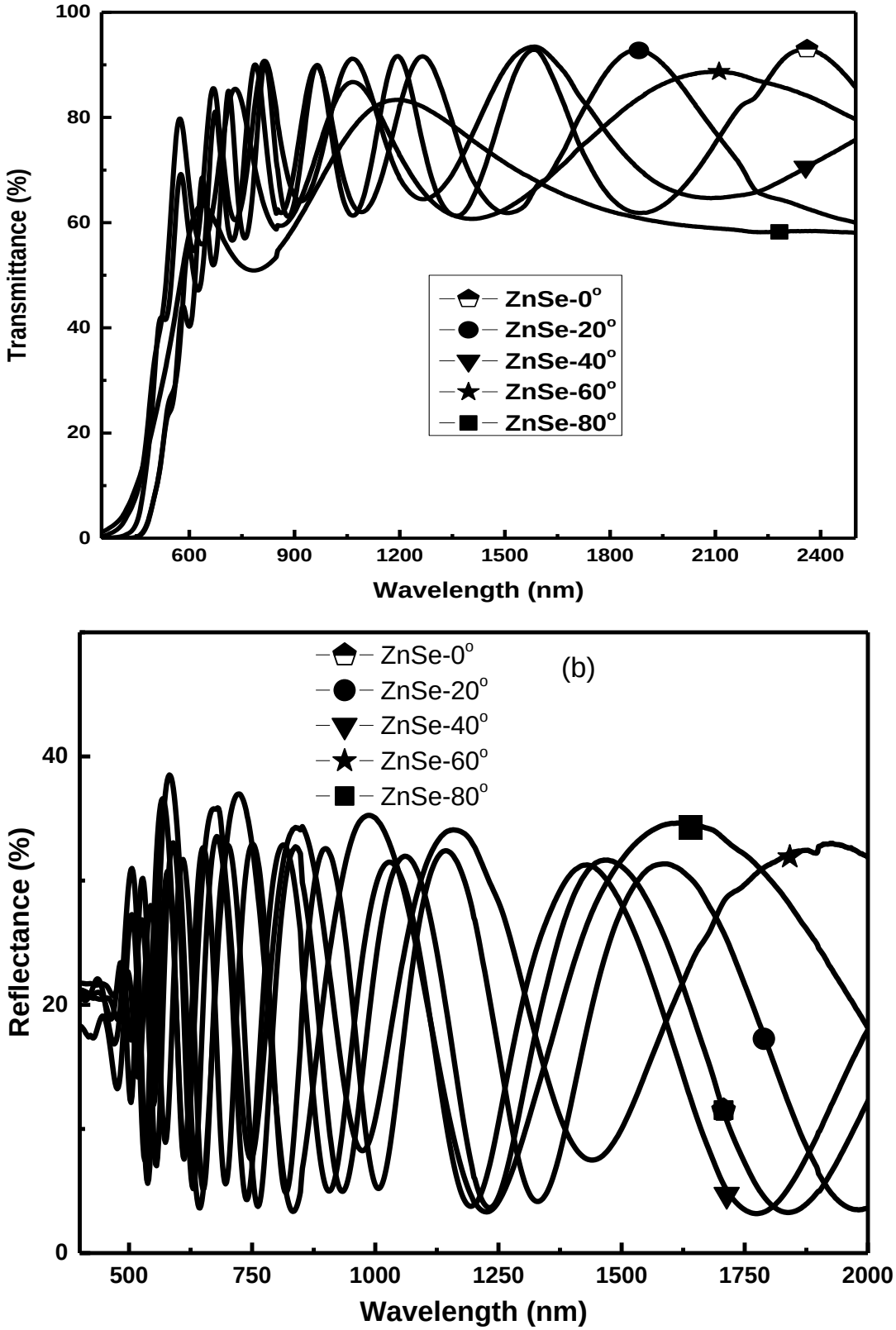

Figure 7.5 (a) Transmittance and (b) Reflectance spectra of ZnSe films

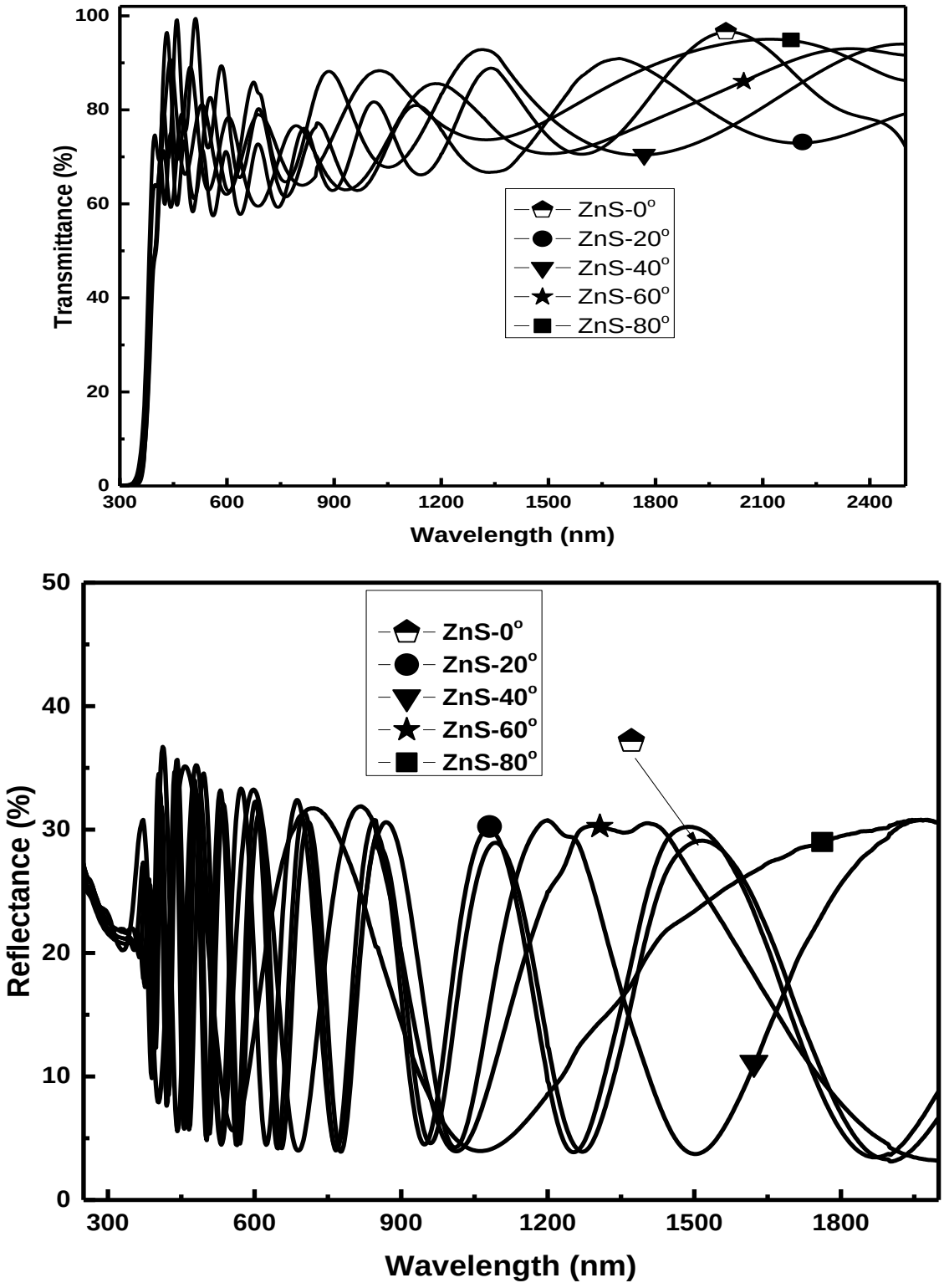

Figure 7.6 (a) Transmittance and (b) Reflectance spectra of ZnS films

7.2 Calculation of band gap

The optical spectra of the II-VI compound films were used to determine the bandgaps (E_g). For band gap determination, the thickness of film was needed. The thicknesses of the films were calculated optically using the following relation:

$$d = \frac{\lambda_{\max} \times \lambda_{\min}}{4n_f \left|\lambda_{\max} - \lambda_{\min}\right|} \tag{7.1}$$

where λ_{max} is the wavelength corresponding to a maximum in transmittance, λ_{min} is the wavelength corresponding to the adjacent minimum, and n_f is the refractive index of the film and it is estimated using the empirical relation:

$$n_f = 4.22 - 2.94T_{tran-\min} \tag{7.2}$$

The optical absorption coefficient (α_c) can be determined from measurements of transmittance (T_{trans}) and reflectance (R_{ref}) using following relations [174, 175]:

$$T_{trans} \cong (1 - R_{ref}^2)e^{-\alpha_c d} \tag{7.3a}$$

$$\alpha_c = \frac{1}{d}\ln\left[\frac{(1 - R_{ref}^2)}{T_{trans}}\right] \tag{7.4b}$$

The optical band gap of the films was determined using the following equation [174]:

$$(\alpha_c E)^{1/z} = \beta_c (E - E_g) \tag{7.5}$$

where β_c is a constant, E is the photon energy, and z is power factor of the transition mode, which depends on the nature of the material. II-VI compounds have direct band gaps, thus thus z = 2 [162, 175]. Figures 7.7-7.12 represent the plots of $(\alpha E)^2$ as a function of photon energy of CdTe, CdSe, CdS, ZnTe, ZnSe and ZnS films, respectively. The extrapolation of the linear portion gives the band gap values of the films, which are

listed in Table 7.1. It was observed that the band gap values were dependent on the stoichiometry of the films. In case of CdTe, CdSe, ZnTe, ZnSe, it was noticed that the band gaps of the non-stoichiometric films were small compared to the nearly stoichiometric films. The small band gaps of the non-stoichiometric films could be due to the presence of defect states within the band gaps. The deviation from stoichiometry creates interstitial and deep defect states within the band gaps [171-177]. It was reported that in Te-rich CdTe film and Te-rich ZnTe film, the favorable Cd (V_{Cd}) and Zn (V_{Zn}) vacancies defects were present within the band gap, respectively, and they lied above the valence band [178, 179]. It was also reported that in Cd-rich CdTe and Zn-rich ZnTe films, the Cd and Zn interstitial donor defects were present within the band gap, respectively, and they lied below the conduction band [178, 180]. The change in band gaps was due to the presence of donor interstitial defects (Cd or Zn) or vacancies defects (V_{Cd} or V_{Zn}). The estimated band gaps of nearly stoichiometric CdTe-40˚, CdSe-40˚, and ZnTe-40˚ films were 1.50 eV, 2.25 eV, and 2.36 eV, respectively, which were close to the values reported in the literature [181, 182]. The estimated band gaps of CdS-0˚, CdS-20˚, and CdS-40˚ films are 1.85 eV, 2.00 eV, and 2.25 eV, respectively, which were less compared to the expected band gap (2.42 eV) of CdS. CdS-0˚, CdS-20˚, and CdS-40˚ films were Cd-rich films and Cd interstitial site defects could be responsible for small band gap [178]. The estimated values of the band gap of S-rich films (CdS-60˚ and CdS-80˚) were 2.44 eV and 2.50 eV, which were greater than the expected value (2.42 eV). The increase in band gap values could be due to the large band gap values of the sulfur element (2.44 eV) compared to the band gap CdS. In case of ZnS, it was noticed that the band gap values varied from 3.39 eV to 3.46 eV by increasing the deposition angle from

0˚ to 80˚. The large deviation in the band gap of ZnS films was not observed because all angular-deposited ZnS films were nearly stoichiometric. The small increase in band gap was due to a decrease in the film thickness [183]. The calculated values of the band gap, along with the thickness of II-VI compound films are listed in Table 7.1.

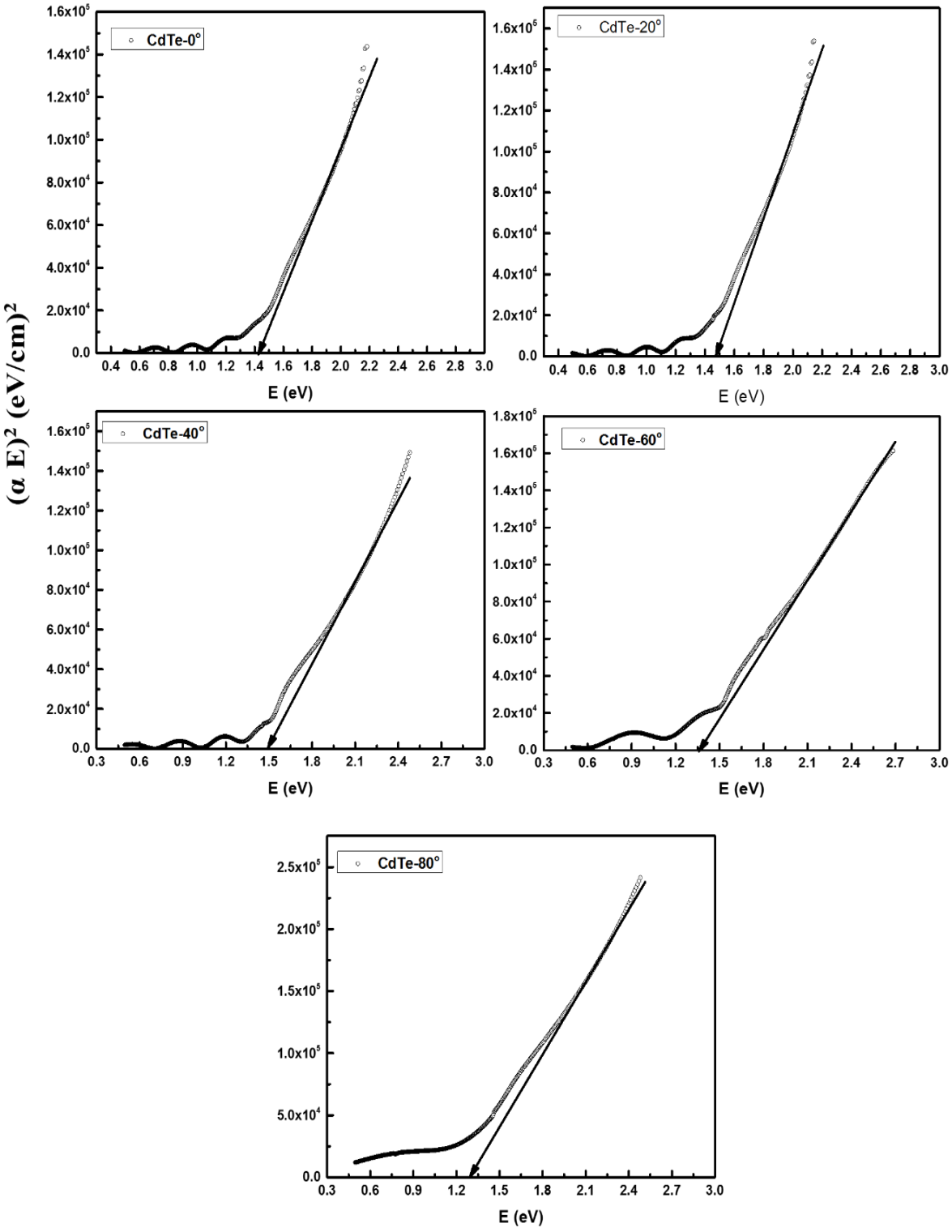

Figure 7.7 Tauc Plots of CdTe films

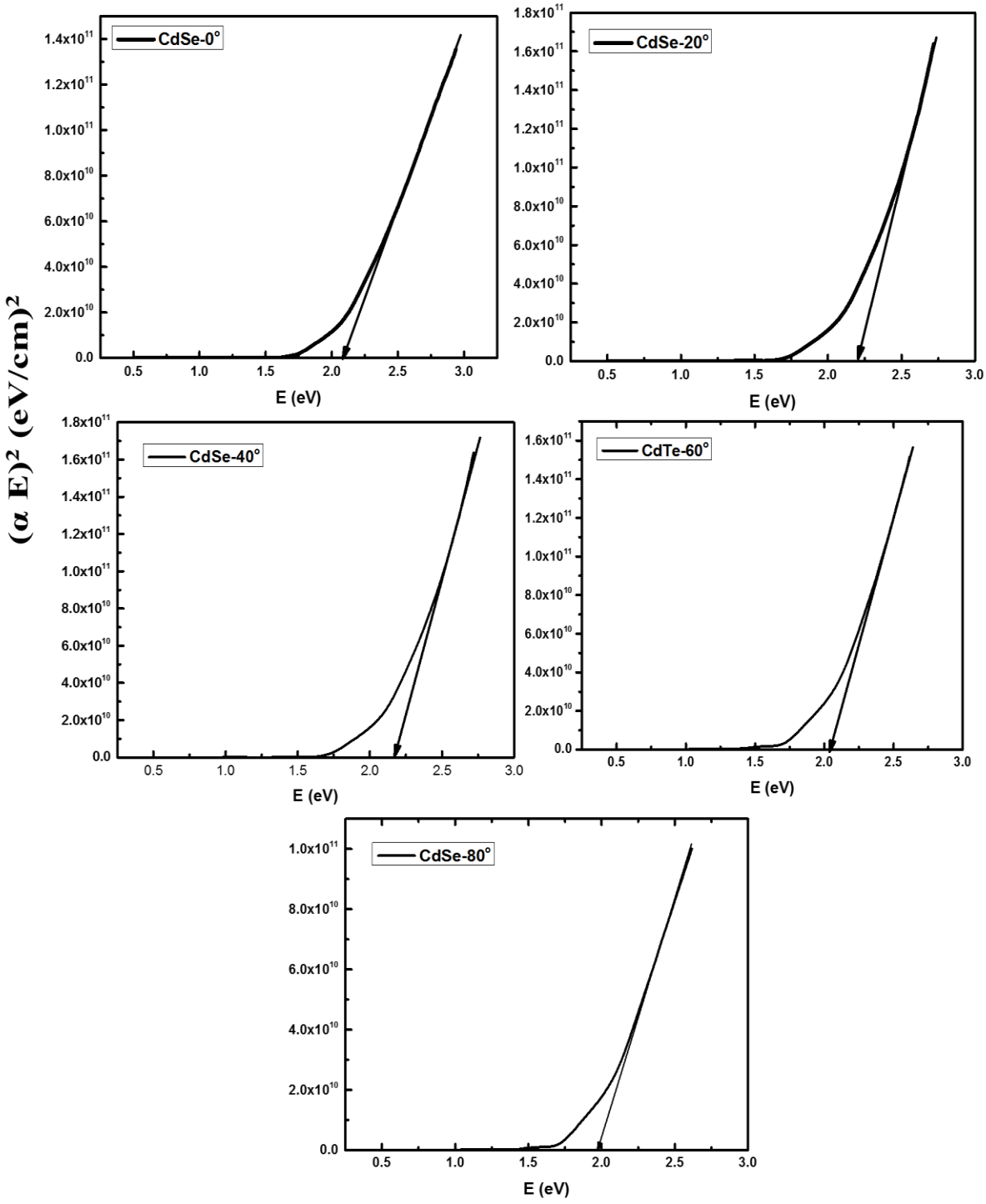

Figure 7.8 Tauc Plots of CdSe films

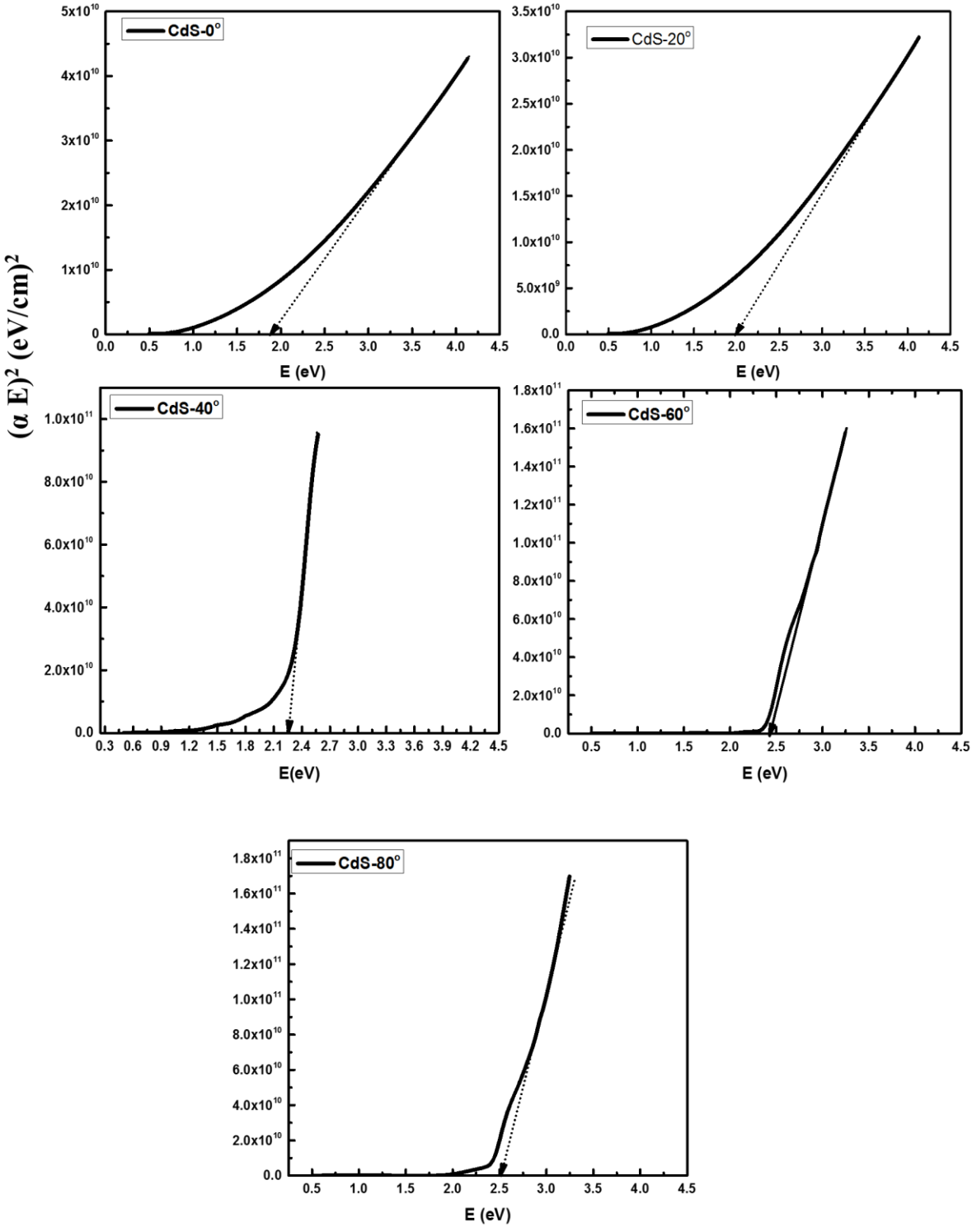

Figure 7.9 Tauc Plots of CdS films

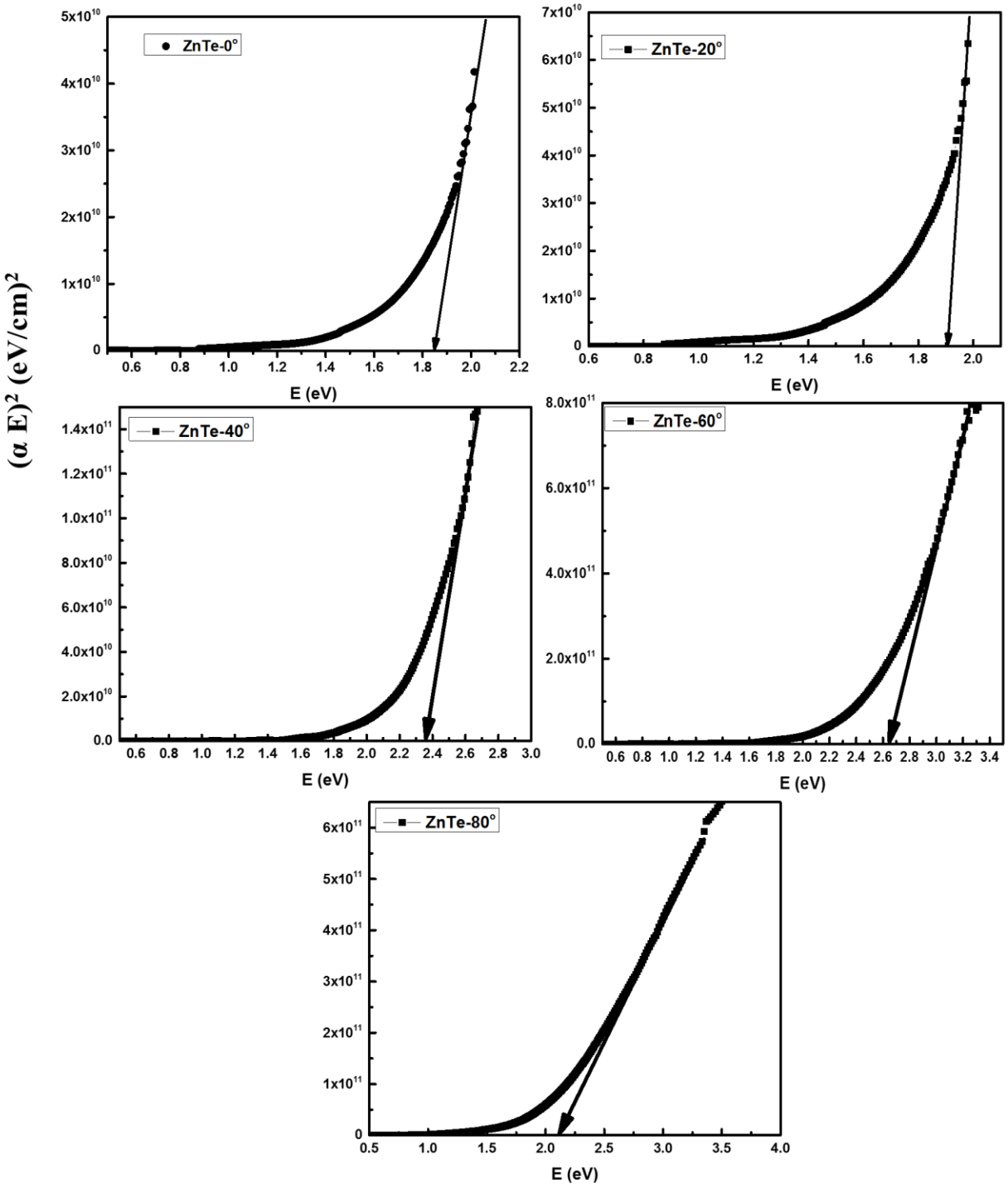

Figure 7.10 Tauc Plots of ZnTe films

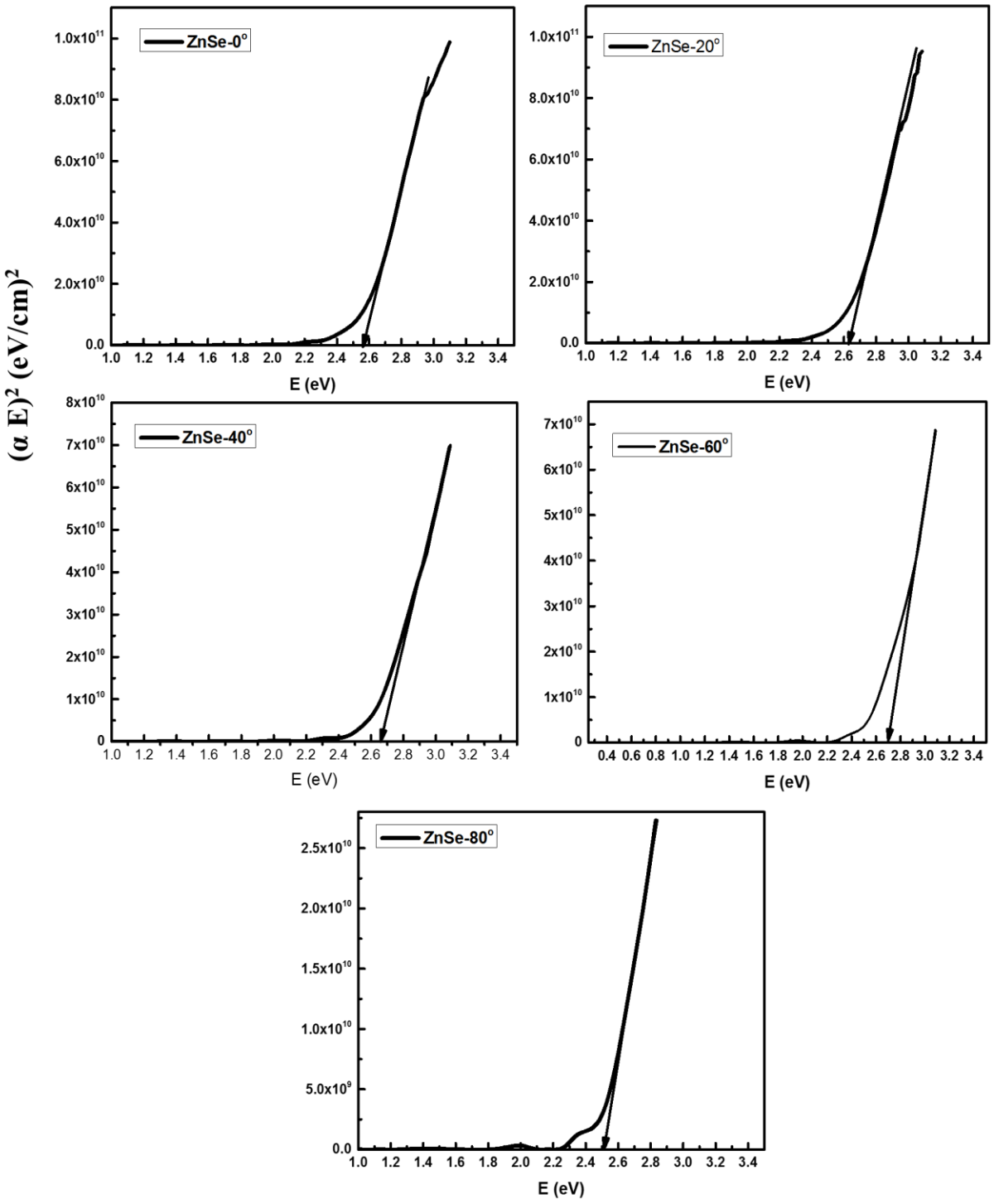

Figure 7.11 Tauc Plots of ZnSe films

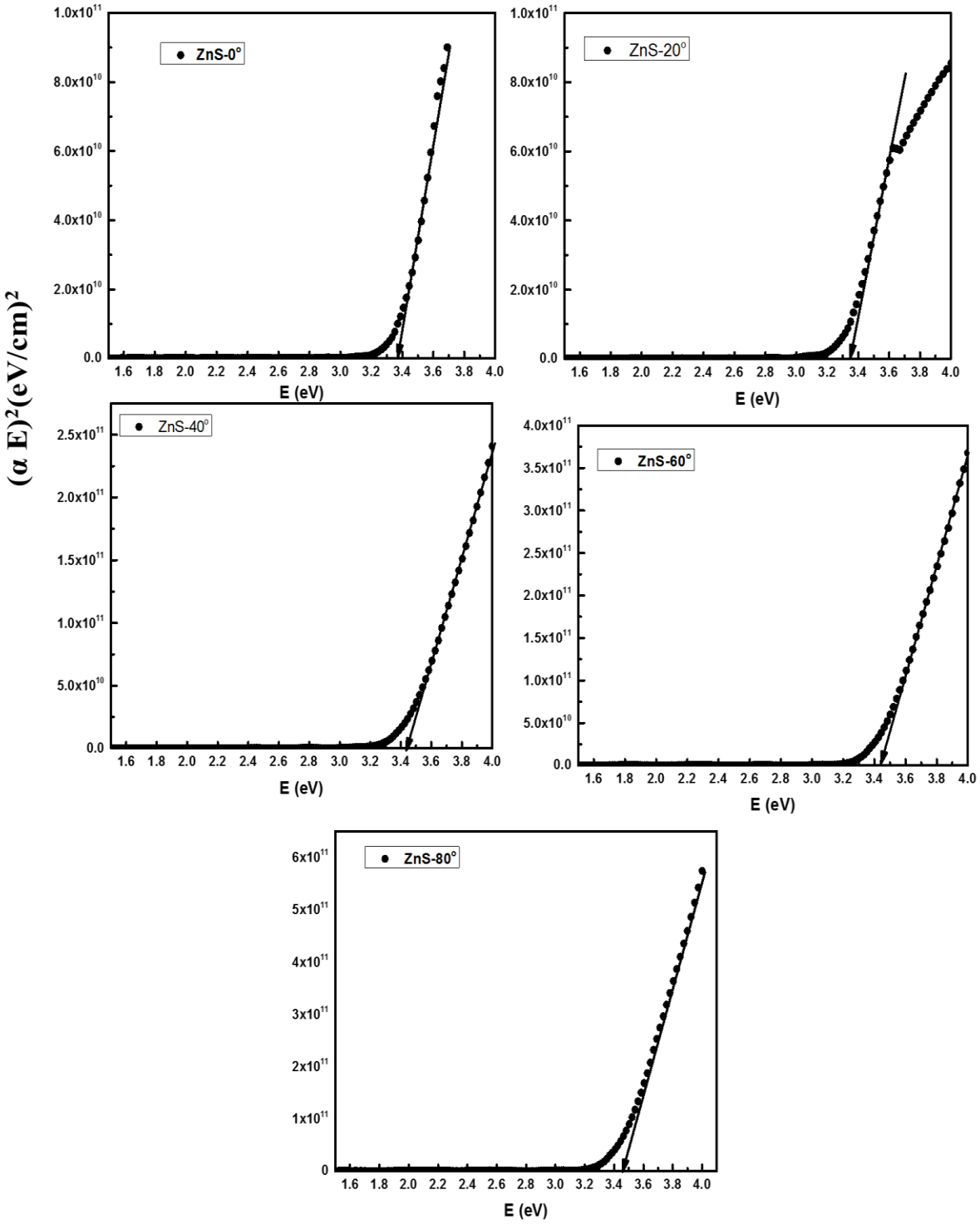

Figure 7.12 Tauc plots of ZnS films

Table 7.1 Values of film thickness (d) and band gaps (E_g)

Sample	d (nm)	E_g (eV)
CdTe-0°	850	1.44
CdTe-20°	804	1.48
CdTe-40°	703	1.50
CdTe-60°	520	1.36
CdTe-80°	337	1.28
CdSe-0°	647	2.12
CdSe-20°	644	2.23
CdSe-40°	611	2.24
CdSe-60°	420	2.08
CdSe-80°	229	2.00
CdS-0°	930	1.85
CdS-20°	780	2.00
CdS-40°	634	2.25
CdS-60°	430	2.44
CdS-80°	196	2.50
ZnTe-0°	994	1.85
ZnTe-20°	986	1.90
ZnTe-40°	740	2.36
ZnTe-60°	442	2.65
ZnTe-80°	144	2.15
ZnSe-0°	1073	2.58
ZnSe-20°	863	2.61
ZnSe-40°	736	2.62
ZnSe-60°	489	2.70
ZnSe-80°	270	2.50
ZnS-0°	1011	3.39
ZnS-20°	850	3.38
ZnS-40°	688	3.43
ZnS-60°	572	3.44
ZnS-80°	495	3.46

7.3 Relative density of angular-deposited II-VI compound films

The relative density of a film can be estimated using the Lorentz-Lorenz relation [184, 185]

$$\frac{\rho_f}{\rho_b} = \frac{(n_f^2 - 1)(n_b^2 + 2)}{(n_f^2 + 2)(n_b^2 - 1)} \tag{7.6}$$

where ρ_f and ρ_b represent the densities of the film and bulk material, respectively. n_f, and n_b represent the refractive indices of the film and bulk material, respectively. The film density of an angular deposited film relative to the film density that was deposited at 0˚ is given as [117]:

$$\rho_f = \rho_{f0} \frac{2\cos\gamma}{1+\cos\gamma} \tag{7.7}$$

ρ_f is the density of the film deposited at any angle (γ), ρf_0 is the density of the film deposited at 0˚. It was clear from the equation that the density of the film was decreased by increasing the deposition angle because of the increase of porosity due to shadowing effect. II-VI compounds dissociate during evaporation and the stoichiometry of the film deviates from the source material. Therefore, the density of a II-VI compound film will be affected by the elemental composition of the film. The density of the angular deposited II-VI compound film will not only depend on incident angle but also on the density and concentration of the rich element. The proposed equations for angular deposited II-VI film are given below:

If the film is chalcogen-rich, then the film density will be:

$$\rho_f = \rho_{f0}\left(\frac{2\cos\gamma}{1+\cos\gamma}\right) * \left(\frac{\varphi_{VI}}{\varphi_{II-VI}} * \frac{X_{VI}}{X_{II}}\right) \tag{7.8}$$

Where φ_{VI}, $\varphi_{II\text{-}VI}$, are the densities of II element and II-VI compound, respectively, X_{II}, and X_{VI} are the elemental concentrations of II and VI elements within the film.

If the film is metal-rich, then film density will be:

$$\rho_f = \rho_{f0}\left(\frac{2\cos\gamma}{1+\cos\gamma}\right)*\left(\frac{\varphi_{II}}{\varphi_{II-VI}}*\frac{X_{II}}{X_{IV}}\right) \quad (7.9)$$

The relative densities of angular deposited II-VI compound films were calculated using equation (7.6). The values of refractive index of II-VI compound films were dependent on $T_{tran\text{-}min}$ and calculated using equation (7.2). The $T_{tran\text{-}min}$ values were measured from the absolute transmittance spectra of the II-VI compound films.

The values of $T_{tran\text{-}min}$ corresponding to their wavelengths, refractive index of CdTe thin film (n_f), refractive index of bulk CdTe (n_b) [186], and relative density (ρ_f/ρ_b) are listed in table 7.2. The refractive index values of bulk CdTe material is taken from reference 186.

Table 7.2 Values of $T_{trans\text{-}min}$ corresponding to their wavelengths, refractive index of CdTe thin film (n_f), refractive index of bulk CdTe (n_b), and relative density (ρ_f/ρ_b)

Sample	Wavelength (nm)	$T_{trans\text{-}min}$	n_f	n_b	ρ_f/ρ_b
CdTe-0˚	1686	0.52	2.69	2.72	0.99
CdTe-20˚	1772	0.53	2.66	2.72	0.98
CdTe-40˚	1415	0.57	2.57	2.74	0.95
CdTe-60˚	1402	0.48	2.81	2.75	1.01
CdTe-80˚	1889	0.33	3.45	2.71	1.12

It is clear from Table 7.2 that the relative density was not decreased by increasing the deposition angle as expected for angular deposition according to equation (7.6). This indicates that the relative density of CdTe also depends on the stoichiometry of the film. The densities of Te, CdTe, and Cd are 6.24 g/cm^3, 5.85 g/cm^3, and 8.69 g/cm^3, respectively. It was observed that the relative densities of Te-rich (CdTe-0˚ and CdTe-20˚) films were high compared to the relative density of nearly stoichiometric (CdTe-40˚) because the density of Te (density = 6.24 g/cm^3) is higher than the CdTe compound

(density = 5.85 g/cm^3). The high content of Te in CdTe-0˚ and CdTe-20˚ films increased the density of the films. It was also observed that the relative densities of Cd-rich (CdTe-60˚ and CdTe-80˚) films were high compared to the relative densities of the nearly stoichiometric (CdTe-40˚) film and the Te-rich (CdTe-0˚ and CdTe-20˚) films because the density of Cd element is higher than the CdTe compound and Te element.

The values of $T_{tran\text{-}min}$ corresponding to their wavelengths, refractive index of CdSe thin film (n_f), refractive index of bulk CdSe (n_b) [187], and relative density (ρ_f/ρ_b) are listed in table 7.3. The refractive index values of bulk CdSe material is taken from reference 187.

Table 7.3 Values of $T_{trans\text{-}min}$ corresponding to their wavelengths, refractive index of CdSe thin film (n_f), refractive index of bulk CdSe (n_b), and relative density (ρ_f/ρ_b)

Sample	Wavelength (nm)	$T_{trans\text{-}min}$	n_f	n_b	ρ_f/ρ_b
CdSe-0˚	1194	0.59	2.49	2.53	0.98
CdSe-20˚	1169	0.56	2.58	2.54	1.01
CdSe-40˚	1322	0.55	2.60	2.52	1.02
CdSe-60˚	1082	0.39	3.07	2.55	1.13
CdSe-80˚	1092	0.32	3.27	2.55	1.18

It is clear from Table 7.3 that the relative density of CdSe films was increased by increasing the deposition angle. According to equation (7.6), the relative density should be decreased as the disposition angle increased because of shadowing effect but it was increased by increasing the deposition angle. This indicates that the relative density of the film depends on the stoichiometry of the film. The densities of Se element, CdSe compound, and Cd element are 4.82 g/cm^3, 5.82 g/cm^3, and 8.69 g/cm^3, respectively. EDX analysis of angular deposited CdSe films showed that CdSe-0˚ and CdSe-20˚ were Se-rich; CdSe-40˚ film was nearly stoichiometric, and CdSe-60˚ and CdSe-80˚ films were

Cd-rich. The increase in relative density by increasing the deposition angle was because the densities of CdSe compound and Cd element were greater than Se element.

The values of $T_{tran\text{-}min}$ corresponding to their wavelengths, refractive index of CdS thin film (n_f), refractive index of bulk CdS (n_b) [188], and relative density (ρ_f/ρ_b) are listed in table 7.4. The refractive index values of bulk CdS material is taken from reference 188.

Table 7.4 Values of $T_{trans\text{-}min}$ corresponding to their wavelengths, refractive index of CdS thin film (n_f), refractive index of bulk CdS (n_b), and relative density (ρ_f/ρ_b)

Sample	Wavelength (nm)	T_{min}	n_f	n_b	ρ_f/ρ_b
CdS-0˚	1386	0.09	3.96	2.31	1.40
CdS-20˚	1386	0.10	3.93	2.31	1.40
CdS-40˚	1114	0.27	3.43	2.33	1.31
CdS-60˚	1205	0.66	2.28	2.32	0.98
CdS-80˚	1394	0.70	2.16	2.30	0.93

It is clear from Table 7.4 that the relativity density of CdS film decreased by increasing the deposition angle. It was noticed that the relative densities of CdS-0˚, CdS-20˚, and CdS-40˚ are 1.40, 1.40, and 1.31, respectively and these values were much greater than the maximum expected value of 1. This indicates that the relative density was highly dependent on the stoichiometry of the film. CdS-0˚, CdS-20˚, and CdS-40˚ films were rich in Cd and their relative densities were greater compared to the relative densities of CdS-80˚, CdS-80˚ films because the density of Cd element (density = 8.69 g/cm^3) is greater than the CdS compound (density = 4.82 g/cm^3) and S element (2.07 g/cm^3).

The values of $T_{tran\text{-}min}$ corresponding to their wavelengths, refractive index of ZnTe thin film (n_f), refractive index of bulk ZnTe (n_b) [186], and relative density (ρ_f/ρ_b)

are listed in table 7.5. The refractive index values of bulk ZnTe material is taken from reference 186.

Table 7.5 Values of $T_{trans\text{-}min}$ corresponding to their wavelengths, refractive index of ZnTe thin film (n_f), refractive index of bulk ZnTe (n_b), and relative density (ρ_f/ρ_b)

Sample	Wavelength (nm)	$T_{trans\text{-}min}$	n_f	n_b	ρ_f/ρ_b
ZnTe-0˚	1663	0.44	2.93	2.73	1.05
ZnTe-20˚	1645	0.45	2.90	2.73	1.04
ZnTe-40˚	1577	0.51	2.72	2.73	0.99
ZnTe-60˚	1427	0.42	2.99	2.74	1.06
ZnTe-80˚	2261	0.26	3.46	2.71	1.15

It was observed that the relative densities of Te-rich (ZnTe-0˚ and ZnTe-20˚) and Zn-rich (ZnTe-60˚ and ZmTe-80˚) films were greater compared to the relative density of nearly stoichiometric (ZnTe-40˚) film because the densities of Te (6.24 g/cm^3) and Zn (7.14 g/cm^3) elements are greater than ZnTe compound (5.90 g/cm^3). It was also noticed that the relative densities of Zn-rich films were greater than the Te-rich films because the density of Zn element is greater than the density of Te element.

The values of $T_{tran\text{-}min}$ corresponding to their wavelengths, refractive index of ZnSe thin film (n_f), refractive index of bulk ZnSe (n_b) [186], and relative density (ρ_f/ρ_b) are listed in table 7.6. The refractive index values of bulk ZnSe material is taken from reference 186.

Table 7.6 Values of $T_{trans\text{-}min}$ corresponding to their wavelengths, refractive index of ZnSe thin film (n_f), refractive index of bulk ZnSe (n_b), and relative density (ρ_f/ρ_b)

Sample	Wavelength (nm)	$T_{trans\text{-}min}$	n_f	n_b	ρ_f/ρ_b
ZnSe-0˚	1016	0.61	2.42	2.48	0.98
ZnSe-20˚	1087	0.62	2.39	2.47	0.97
ZnSe-40˚	1264	0.64	2.34	2.45	0.95
ZnSe-60˚	1405	0.60	2.45	2.45	0.99
ZnSe-80˚	2239	0.58	3.51	2.43	1.03

It was observed that the relative densities of Zn-rich (ZnSe-60˚ and Zn80˚) films were high compared to Se rich (ZnSe-0˚ and ZnSe-20˚) and the nearly stoichiometric (ZnSe-40˚) films because the density of Zn element (density = 7.14 g/cm^3) is higher than the Se element (density = 4.82 g/cm^3) and ZnSe compound (5.27 g/cm^3). It was also noticed that the relative density of the nearly stoichiometric ZnSe-40˚ film is less compared to the relative densities of ZnSe-0˚ and ZnSe-20˚ but the density of ZnSe compound (5.27 g/cm^3) is greater than the Se element (density = 4.82 g/cm^3). The change in elemental composition of ZnSe films was small. The effect of Se content was small compared to the effect of deposition angle (γ). Therefore, the films deposited at lower angles (0˚ and 20˚) showed high relative density compared to a film that was deposited at 40˚ because the porosity of the film increased at higher angle due to shadowing effect.

The values of $T_{tran\text{-}min}$ corresponding to their wavelengths, refractive index of ZnS thin film (n_f), refractive index of bulk ZnS (n_b) [187], and relative density (ρ_f/ρ_b) are listed in table 7.7. The refractive index values of bulk ZnS material is taken from reference 187.

Table 7.7 Values of $T_{trans\text{-}min}$ corresponding to their wavelengths, refractive index of ZnS thin film (n_f), refractive index of bulk ZnS (n_b), and relative density (ρ_f/ρ_b)

Sample	Wavelength (nm)	$T_{trans\text{-}min}$	n_f	n_b	ρ_f/ρ_b
ZnS-0˚	1144	0.66	2.28	2.28	0.99
ZnS-20˚	1335	0.67	2.25	2.28	0.98
ZnS-40˚	1761	0.70	2.16	2.27	0.95
ZnS-60˚	1504	0.71	2.13	2.27	0.93
ZnS-80˚	1325	0.74	2.05	2.78	0.89

It was observed that the relative density of ZnS film decreased by increasing the angle from 0˚ to 80˚. Angular deposited ZnS films were nearly stoichiometric so, the relative density of ZnS films only depends on the deposition angle (γ). The density of ZnS film was decreased by increasing the deposition angle because the porosity of the film was

increased due to shadowing effect raised by angular deposition and hence the density of the film was decreased.

CHAPTER 8

Electrical and Photocurrent Properties

In this chapter, the electrical and photocurrent properties of angular-deposited II-VI compound films are discussed.

8.1 Electrical Properties

The electrical properties of angular deposited II-VI compound films were determined by Hall effect measurements and two-probe method. CdTe-60˚, CdTe-80˚, CdSe-60˚, CdSe-80˚, CdS-0˚, CdS-20˚, CdS-40˚, ZnTe-60˚, and ZnTe-80˚ films were less resistive, and their electrical properties were determined by Hall effect measurements. CdTeTe-0˚, CdTe-20˚, CdTe-40˚, CdSe-0˚, CdSe-20˚, CdSe-40˚, CdS-60˚, and CdS-80˚, ZnTe-40˚, ZnSe-0˚, ZnSe-20˚, ZnSe-40˚, ZnSe-60˚, ZnSe-80˚, ZnS-0˚, ZnS-20˚, ZnS-40˚, ZnS-60˚, and ZnS-80˚ were highly resistive and their electrical properties cannot be measured by Hall effect. Therefore, the resistivities of these films were measured by the two-probe method. CdTe-60˚, CdTe-80˚, CdSe-60˚, CdSe-80˚, CdS-0˚, CdS-40˚, and CdS-60˚ films showed less resistivity because these films were metal Cd rich. It was reported in the literature that in Cd rich CdTe, CdSe, CdS films, the interstitial Cd defects are present within the band gap. These defects are shallow donor defects that lie just below the conduction band [178, 179]. The decrease in resistivity of Cd-rich films is due to the presence of these defects. Similarly, in Zn-rich ZnTe films, the presence of Zn shallow donor defects within the band gap is responsible for the decrease in resistivity. It was noticed that the nearly stoichiometric films (CdTe-40˚, CdSe-40˚, ZnTe-40˚, and ZnSe-

40˚) were more resistive compared to metal rich or chalcogen (S, Se, or Te) rich films. It was due to the presence of less defects in the nearly stoichiometric films. In chalcogen (S, Se, or Te) rich films, the Cd or Zn vacancies are the most favorable defects and these defects lie above the valence band [180, 189]. These defects make the films p-type semiconductor and are responsible for the decrease in resistivity [189, 190]. It was also noticed that chalcongen (S, Se, or Te) rich films were more resistive compared to metal (Cd or Zn) rich film because Cd or Zn vacancies are deep level defects while Cd or Zn interstitial defects are shallow donors [189, 191]. It was observed that angular deposited ZnS films were highly resistive and no significant change in resistivity was observed because all ZnS films were nearly stoichiometric. A small increase in resistivity was observed by increasing the deposition angle and it could be due to decreased crystallinity. The measured values of resistivity (ρ_e) and carrier concentration (N) of II-VI compound films are listed in Table 8.

Table 8.1 Values of resistivity (ρ_e) and carrier concentration (N) of II-VI compound films

Sample	ρ_e (Ω.cm)	N (cm^{-3})
CdTe-0°	4.2×10^{7}	----------
CdTe-20°	5.1×10^{7}	----------
CdTe-40°	3.1×10^{8}	----------
CdTe-60°	1.6×10^{4}	2.2×10^{13}
CdTe-80°	4.8×10^{2}	4.8×10^{16}
CdSe-0°	3.6×10^{5}	----------
CdSe-20°	7.1×10^{5}	----------
CdSe-40°	2.1×10^{6}	----------
CdSe-60°	5.6×10^{-2}	2.7×10^{18}
CdSe-80°	3.6×10^{-2}	5.1×10^{18}
CdS-0°	2.7×10^{-1}	3.9×10^{18}
CdS-20°	3.6×10^{-1}	1.4×10^{18}
CdS-40°	8.1	2.6×10^{16}
CdS-60°	3.7×10^{3}	----------
CdS-80°	7.2×10^{5}	----------
ZnTe-0°	3.2×10^{5}	----------
ZnTe-20°	6.3×10^{5}	----------
ZnTe-40°	6.0×10^{6}	----------
ZnTe-60°	4.4×10^{3}	7.1×10^{13}
ZnTe-80°	3.84	1.9×10^{19}
ZnSe-0°	1.9×10^{3}	----------
ZnSe-20°	4.1×10^{3}	----------
ZnSe-40°	3.1×10^{4}	----------
ZnSe-60°	3.9×10^{3}	----------
ZnSe-80°	9.6×10^{2}	----------
ZnS-0°	1.6×10^{8}	----------
ZnS-20°	1.7×10^{8}	----------
ZnS-40°	2.8×10^{8}	----------
ZnS-60°	5.4×10^{8}	----------
ZnS-80°	7.1×10^{8}	----------

8.2 Photocurrent properties

The photocurrent of II-VI compound films was measured by plotting their current-voltage curves under dark and undar light conditions. For this purpose, two Au contacts (100 nm) were deposited on the films to make ohmic contact with semiconductors for the collection of charge carriers. Figure 8.1-8.6 represent the current-voltage characteristics of the films under dark and under light conditions, respectively. It was observed that CdTe, CdSe, CdS, ZnTe, and ZnSe films showed linear current-voltage curves. It was observed that Cd-rich and Zn-rich films (CdTe-60˚, CdTe-80˚, CdSe-60˚, CdSe-80˚, CdS-0˚, CdS-20˚, and CdS-40˚, ZnTe-0˚, and ZnTe-40˚) showed high dark current because of the high conductivity of these films. The high conductivity was due to high metallic Cd or Zn contents in these films. It was observed that the photocurrent response was highly dependent on the elemental composition of the films. Current-voltage curves showed that nearly stoichiometric films had better photocurrent response compared to non-stoichiometric films. The doping and defects in the semiconductor decreased the mobility and carrier lifetime of charge carriers in the semiconductor [148, 149]. The photocurrent response of a semiconductor is dependent on the mobility and carrier lifetime of the charge carrier in the semiconductor [148, 175]. In metal (Cd or Zn) rich or chalcogen (Te, Se, or S) rich films, the additional metal (Cd or Zn) or chalcogen (Te, Se, or S) atoms in the films reside at interstitial sites within the crystal. These interstitial defects deteriorate the mobility and carrier lifetime of the charge carriers, and thus the photocurrent of the non-stoichiometric films was less compared to the nearly stoichiometric films. It was also observed that the current-voltage curves of ZnS films were not linear, which indicates that the junction between Au and ZnS is non-ohmic. It was because the band gap of ZnS

is large. It was also noticed that photocurrent of metal (Cd or Zn) rich films was less compared chalcogen (S, Se, or Te) rich films because metal (Cd or Zn) content in the film increased the reflectance of the film and it decreased the light absorption within the films. The photocurrent responses (P_r) of CdTe, CdSe, CdS, ZnTe, and ZnSe films were measured at 5 V using the following relation [192].

$$P_r = \frac{I_{photo} - I_{dark}}{I_{dark}} \tag{8.1}$$

where I_{dark} and I_{photo} represent the current under dark and under light conditions and P_r represents the photocurrent response. Figures 8-7-8.11 represent the photocurrent response of CdTe, CdSe, CdS, ZnTe, and ZnSe films. It was observed that light response of CdTe-40˚ film was greater than other films because of its high absorption coefficient (~ 10^6 cm^{-1}) [193].

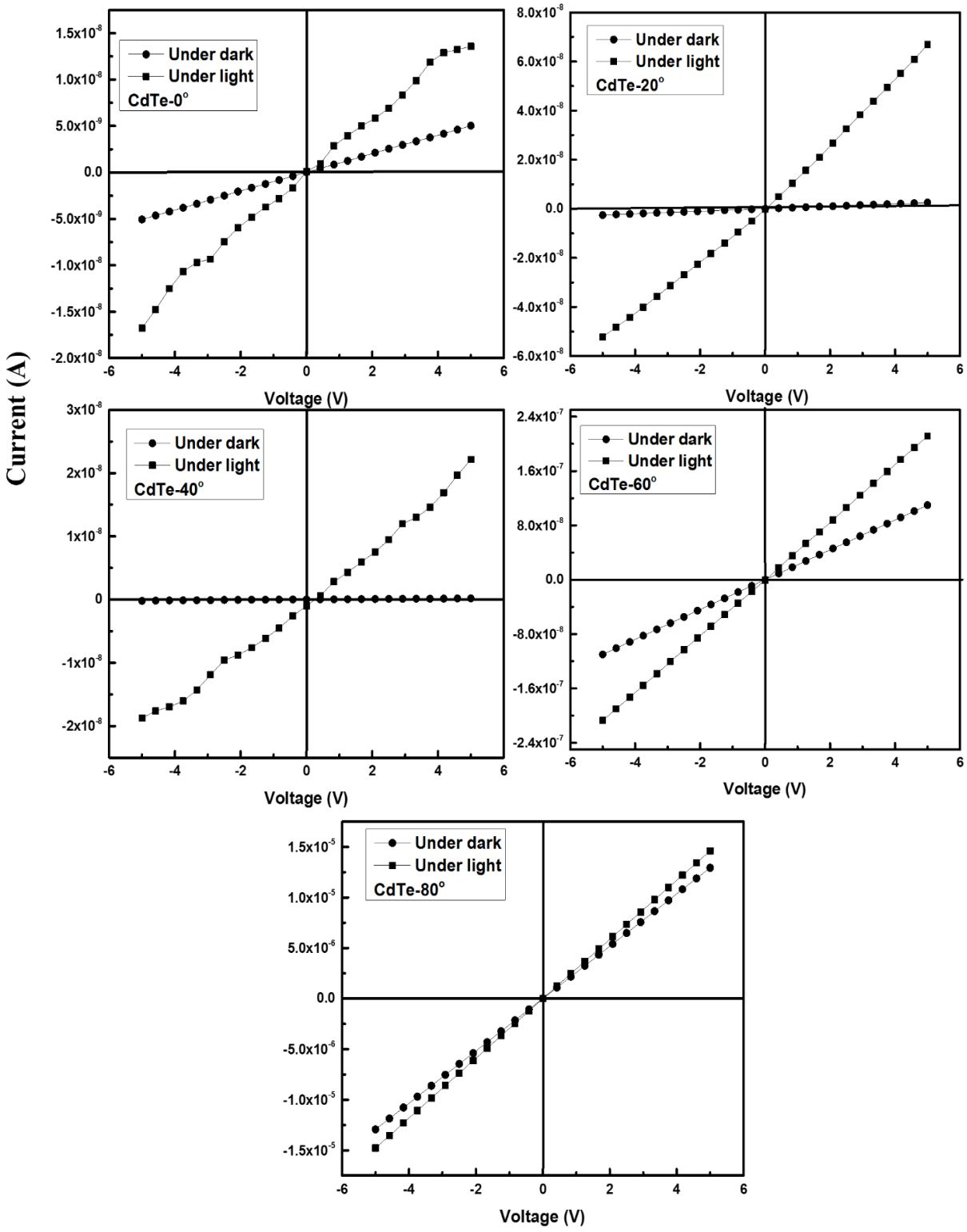

Figure 8.1 Current-voltage curves of CdTe films measured under dark and under light

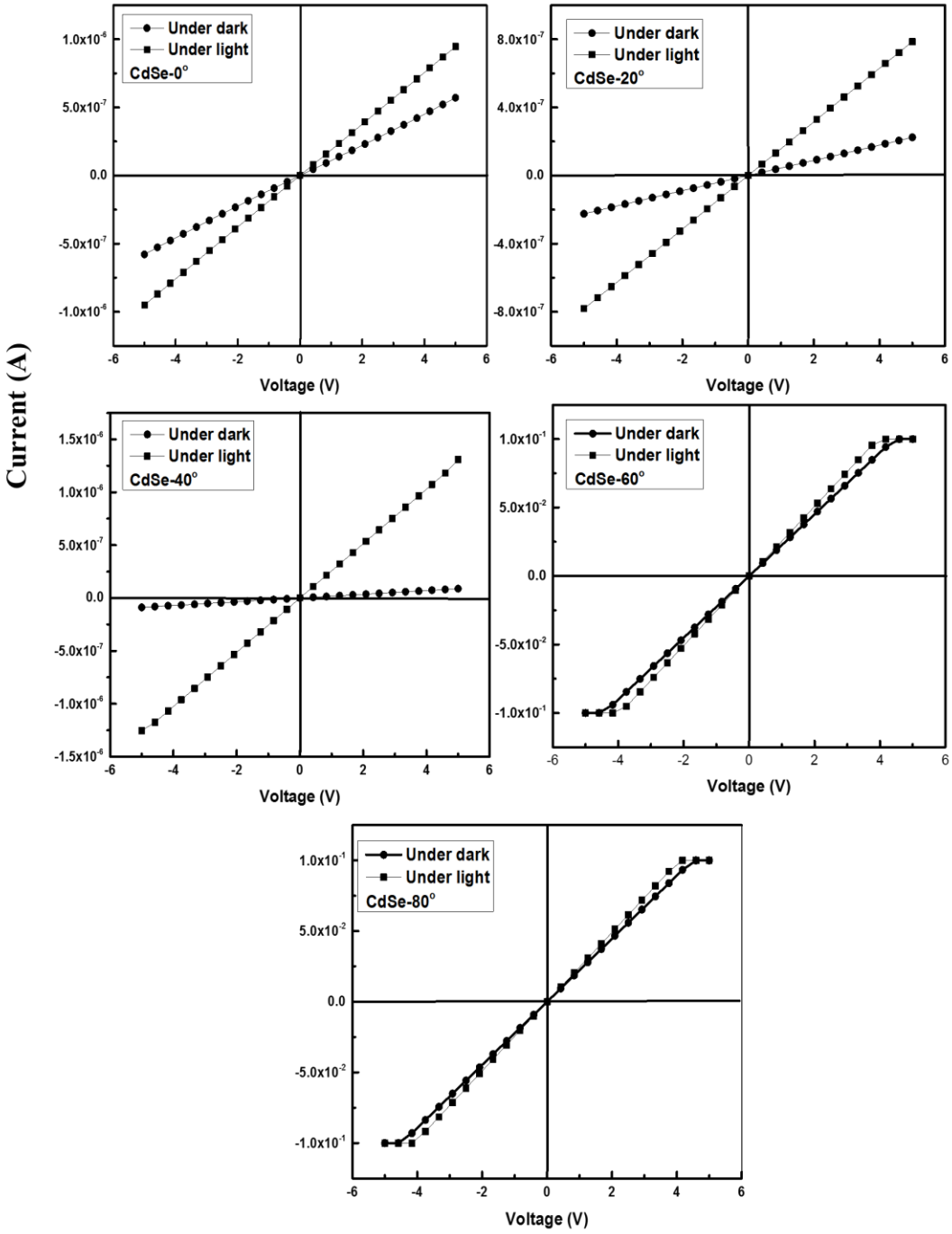

Figure 8.2 Current-voltage curves of CdSe films measured under dark and under light

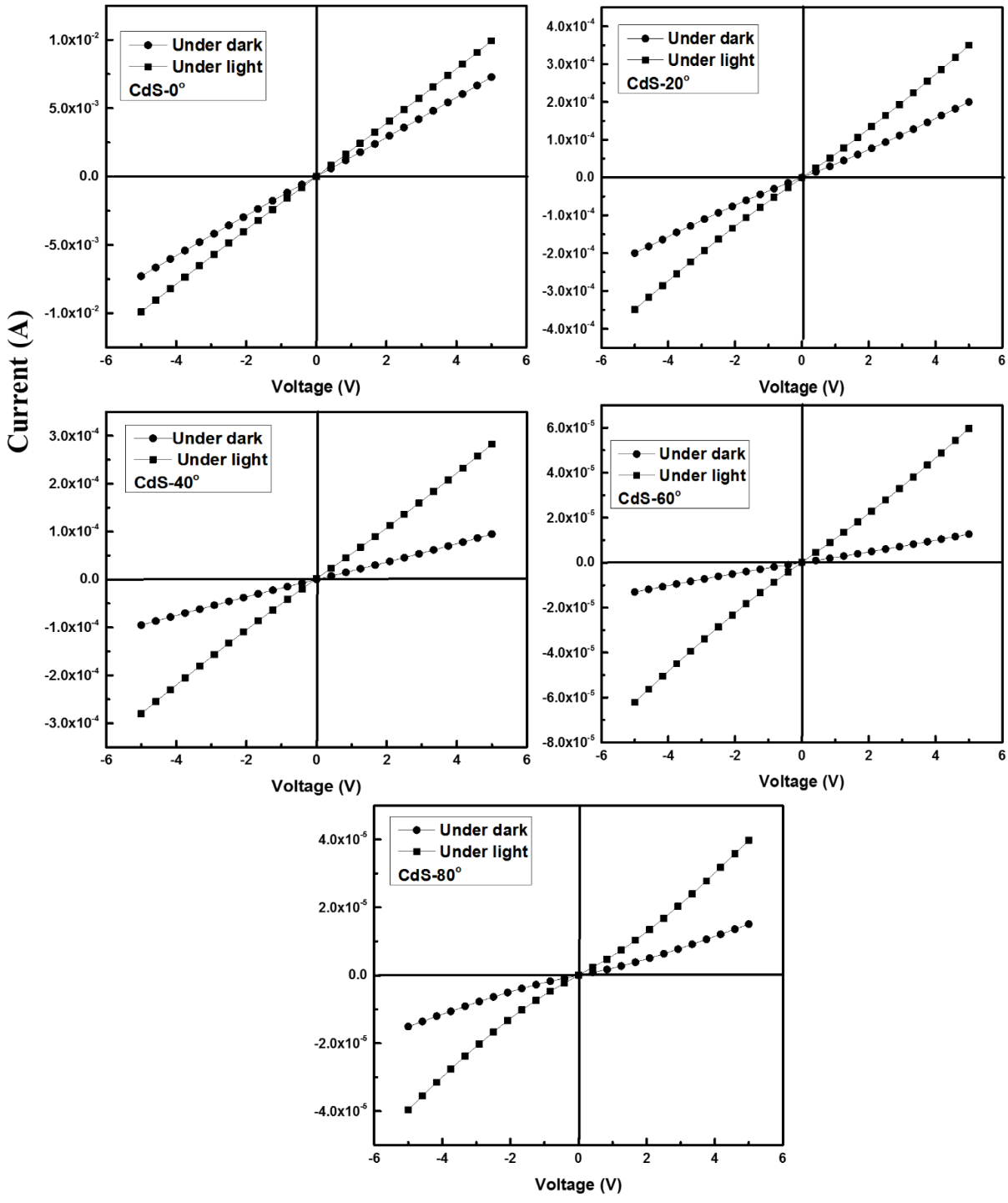

Figure 8.3 Current-voltage curves of CdS films measured under dark and under light

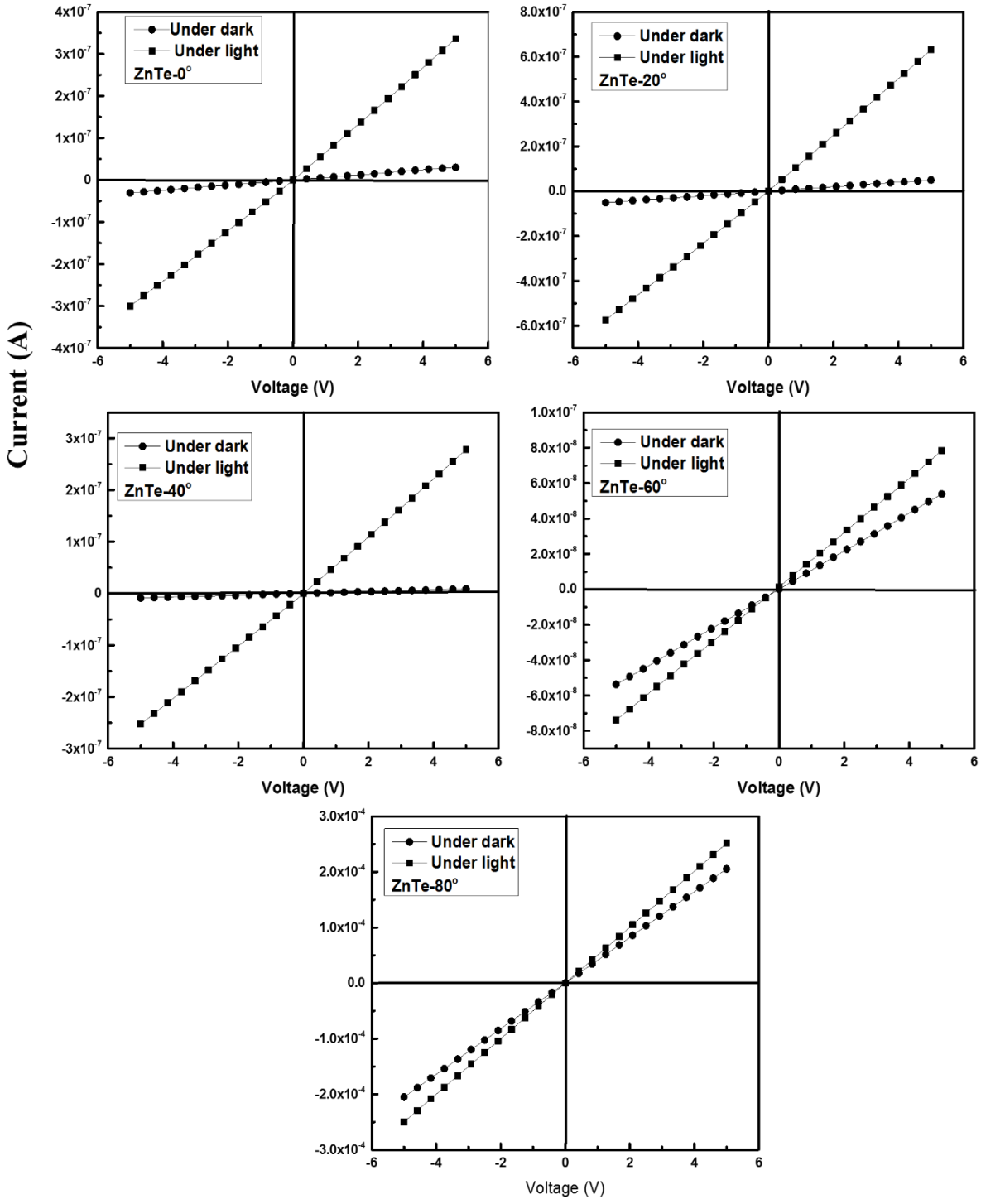

Figure 8.4 Current-voltage curves of ZnTe films measured under dark and under light

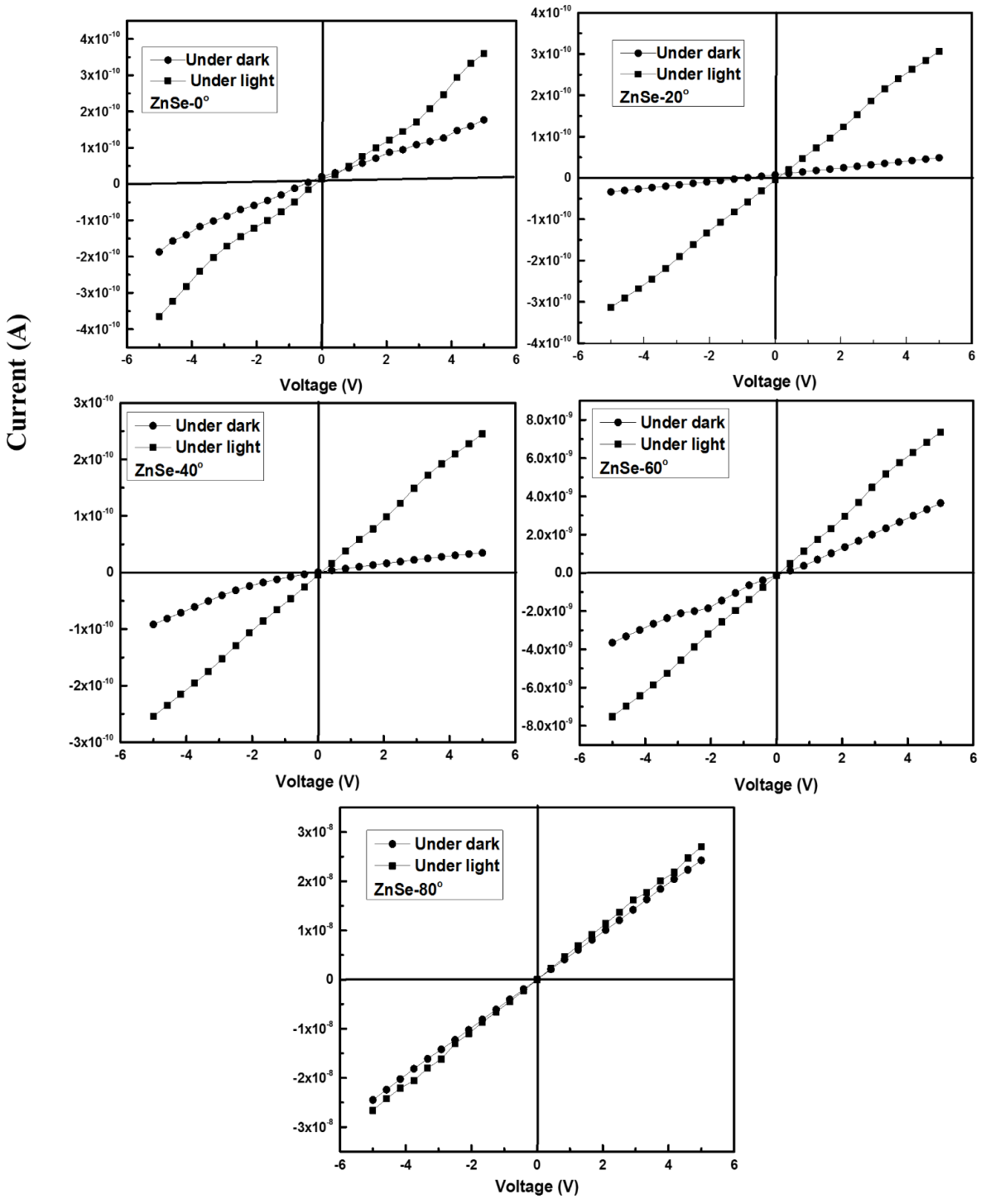

Figure 8.5 Current-voltage curves of ZnSe films measured under dark and under light

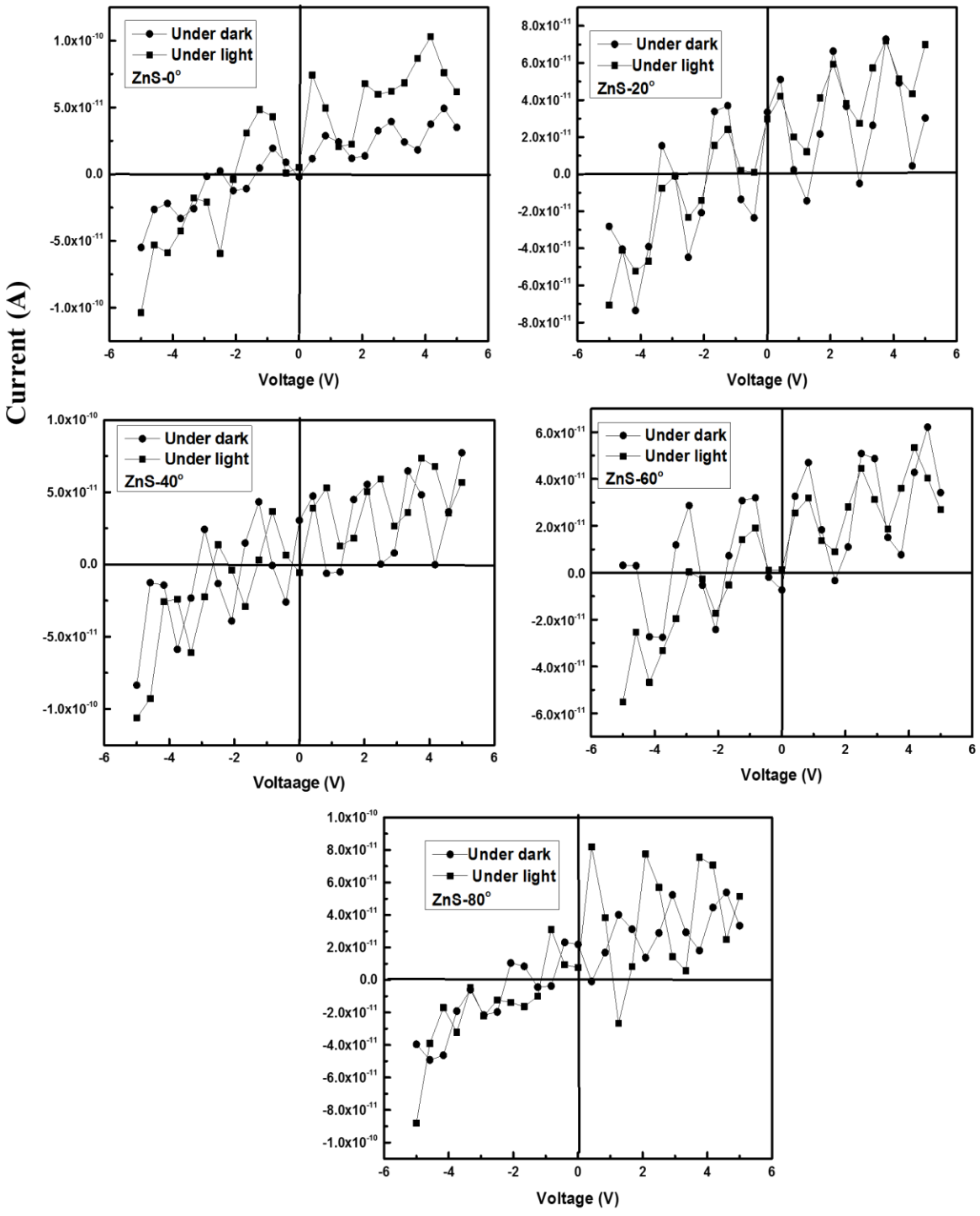

Figure 8.6 Current-voltage curves of ZnS films measured under dark and under light

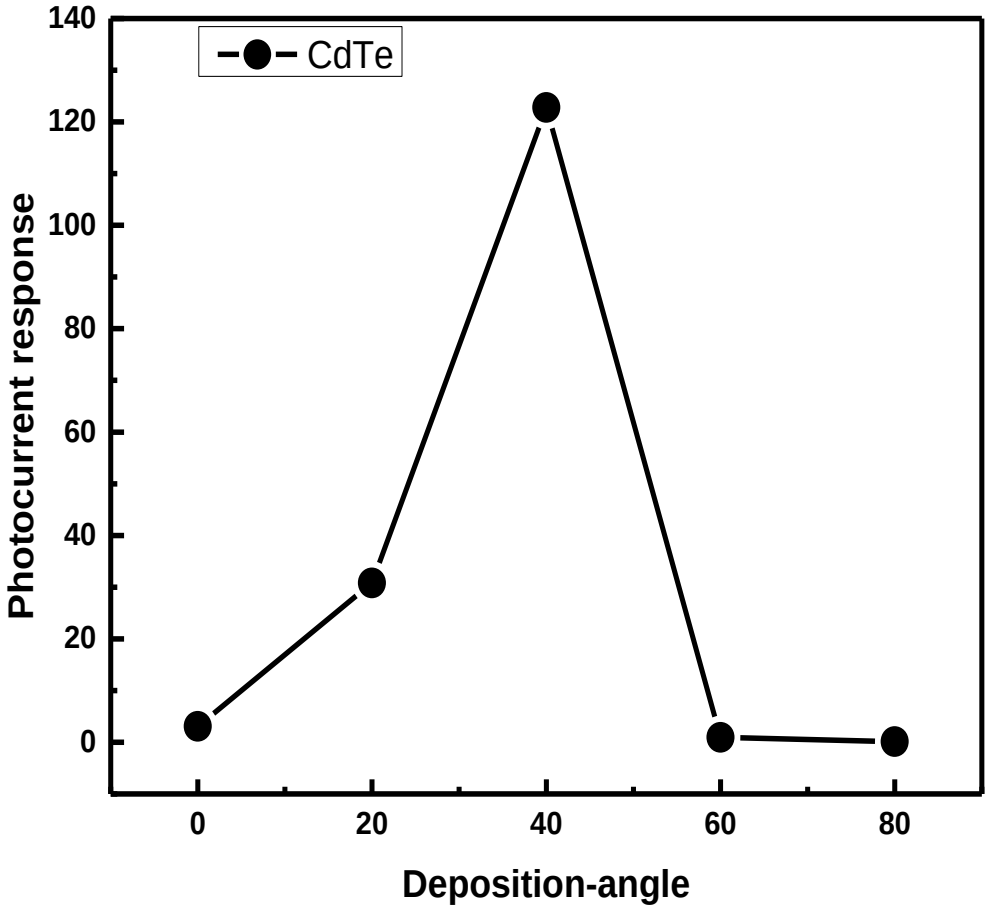

Figure 8.7 Photocurrent response of CdTe films measured at 5 V

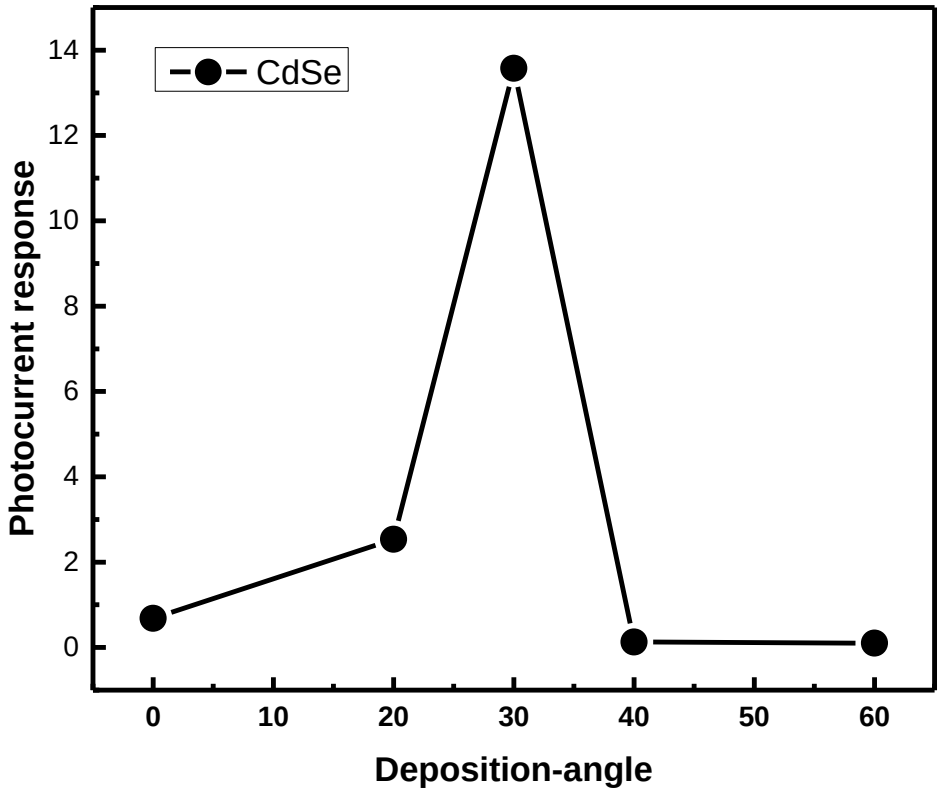

Figure 8.8 Photocurrent response of CdSe films measured at 3.5 V

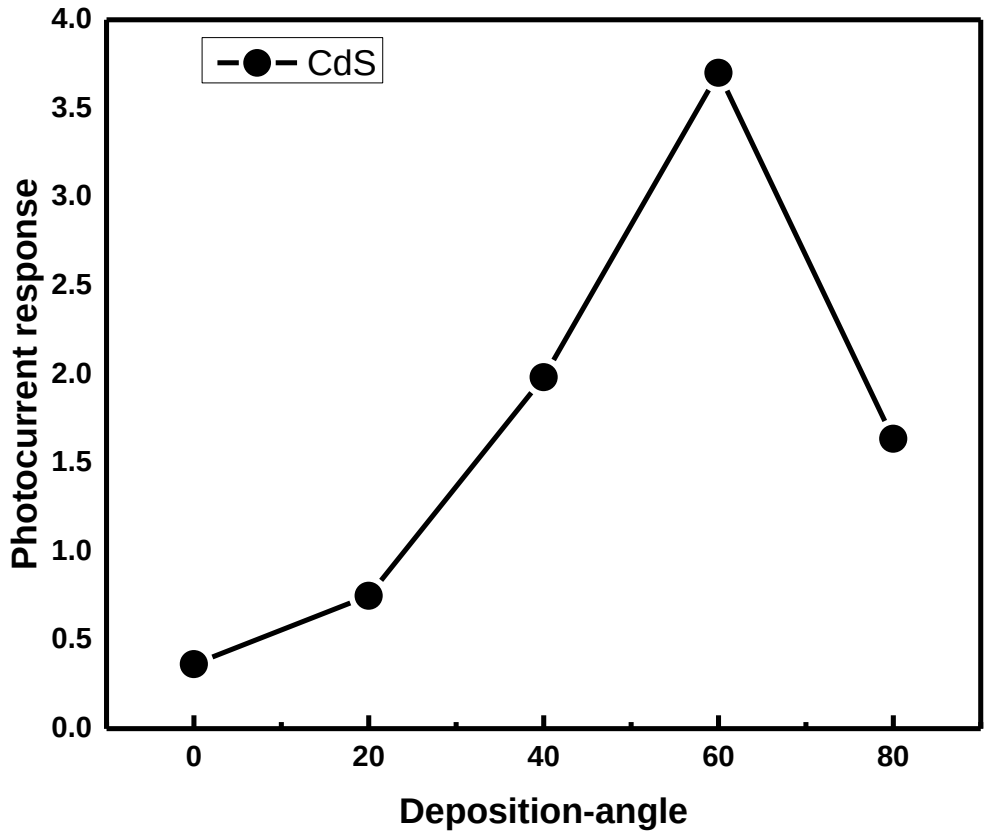

Figure 8.9 Photocurrent response of CdS films measured at 5 V

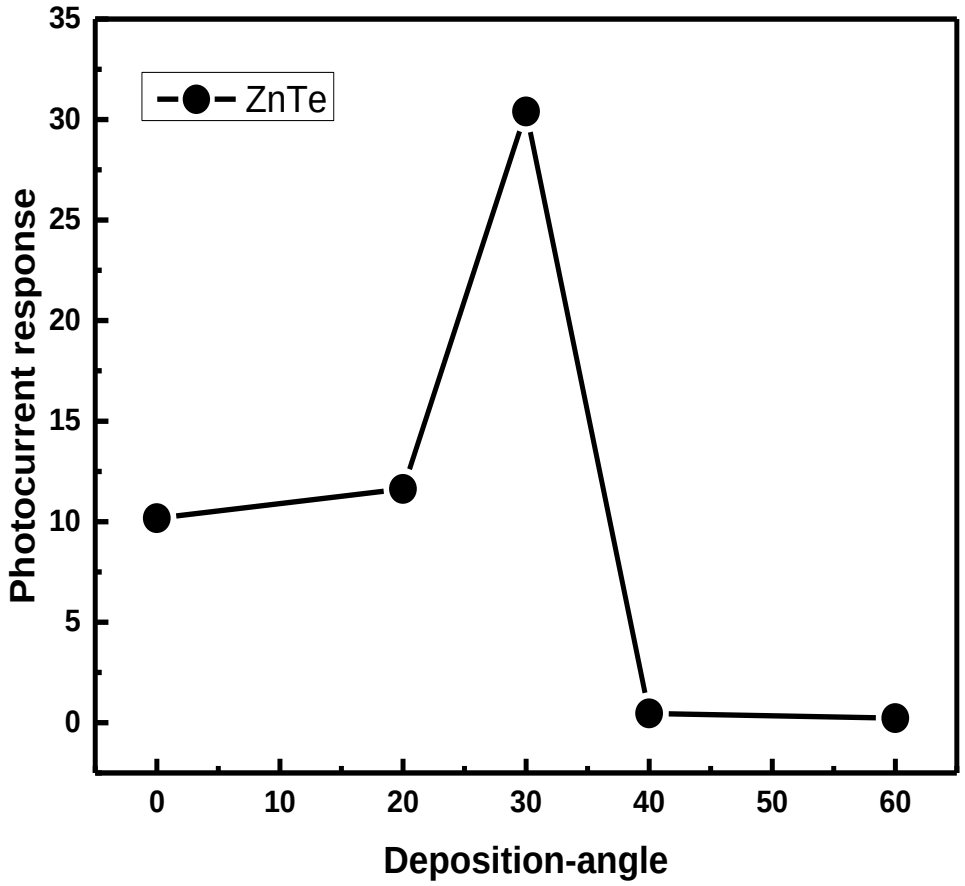

Figure 8.10 Photocurrent response of ZnTe films measured at 5 V

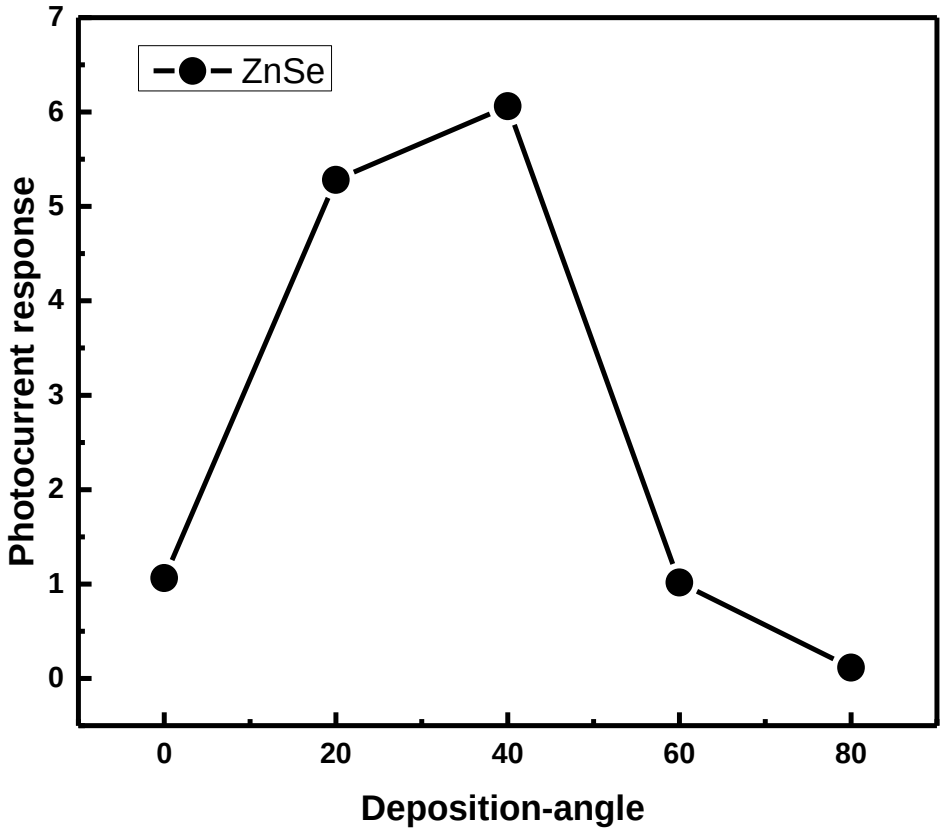

Figure 8.11 Photocurrent response of ZnSe films measured at 5 V

CHAPTER 9

Conclusion

CdTe, CdSe, CdS, ZnTe, ZnSe, and ZnS compound films were deposited at 0˚, 20˚, 40˚, 60˚, and 80˚ by thermal evaporation. The elemental composition of the films was analyzed by EDX and XPS. EDX analysis of CdTe films showed that at lower angles (0˚ and 20˚), the deposited films were Te-rich; at 40˚, the deposited film was nearly stoichiometric; and at higher angles (60˚ and 80˚), the deposited films were Cd-rich. XPS analysis of CdTe films also showed that the relative intensity of Te was decreased and the relative intensity of Cd was increased by increasing the deposition angle from 0˚ to 80˚. EDX analysis of CdSe films showed that at lower angles (0˚ and 20˚), the deposited films were Se-rich; at 40˚, the deposited film was nearly stoichiometric; and at higher angles (60˚ and 80˚), the deposited films were Se-rich. XPS analysis of CdSe films showed that the relative intensity of Se element was decreased and the relative intensity of Cd element was increased by increasing the deposition angle from 0˚ to 80˚. In case of CdS, EDX analysis showed that at lower angles (0˚, 20˚, and 40˚), the deposited films were Cd-rich; and at higher angles (60˚, and 80˚), the deposited films were S-rich. XPS analysis of CdS films showed that the relative intensity of Cd decreased and the relative intensity of S increased by increasing the deposition angle from 0˚ to 80˚. EDX analysis of ZnTe films showed that at lower angles (0˚ and 20˚), the deposited films were Te-rich; at 40˚, the deposited film was nearly stoichiometric; at higher angles (60˚, and 80˚), the deposited films were Zn-rich. XPS analysis of ZnTe films showed that the relative intensity of Te was decreased and the relative intensity of Zn was increased by increasing the deposition

angle from 0˚ to 80˚. EDX analysis of ZnSe films showed that at lower angles (0˚ and 20˚), the deposited films were Se rich; at 40˚, the deposited film was nearly stoichiometric film; and at higher angles (60˚ and 80˚), the deposited films were Zn rich. XPS analysis of ZnSe films showed that relative intensity of Se was decreased and the relative intensity of Zn was increased by increasing the deposition angle from 0˚ to 80˚. EDX analysis of ZnS films showed that all angular deposited films were nearly stoichiometric. XPS analysis of ZnS films showed that the relative intensity of S and the relative intensity of Zn were the same by increasing the deposition angle from 0˚ to 80˚. XPS depth profiles showed that the spatial distribution of II and VI elements in the II-VI compound films throughout the thickness. XPS depth profile analysis showed that the spatial distributions of Cd and Te elements in CdTe films, Cd and Se elements in CdSe films, Cd and S elements in CdS films, Zn and Se elements in ZnSe films, and Zn and S elements in ZnS films throughout the thickness of the films were the same as they were near the surfaces of the films. This indicates that the vapor composition of elements throughout the film deposition remained same. XPS depth profile of ZnTe films showed that the spatial distribution of Zn and Te elements throughout the thickness of the films were not the same as it was near the surface of the films. It was noticed that the relative intensity of Zn is greater than Te near the surface of the substrate and it indicates that vapor composition was rich with Zn content when the evaporation was started. Based on EDX and XPS results, it was noticed that the heavier molecules were deposited more at lower angles and lighter molecules deposited more at higher angles. This indicates that collision is the major factor that is responsible for the change of stoichiometry of the films from the source material. The heavier molecules deflect less during collisions and

deposited more at lower angles and lighter molecules deflect more during collisions and deposited more at higher angles. The effect of angular deposition on the structural, morphological, electrical, optical, and photocurrent properties was also investigated. XRD analysis showed that angular-deposited CdSe and CdS films were single crystal while angular-deposited CdTe, ZnTe, ZnSe, and ZnS films were polycrystalline. XRD patterns of lower angle deposited CdTe and ZnTe films showed at extra peaks $2\theta = 22.70^{\circ}$ and $2\theta = 36.30^{\circ}$, respectively that belong to Te element because these films were Te rich. XRD analysis also showed that crystallite size of angular deposited films was varied by the change the deposition angle. It could be due to the change in lattice strain that was induced during film deposition. AFM images revealed that the surface roughness of the films was increased by increasing the deposition angle from 0° to 80° because shadowing effect raised due to an oblique angle. Hall effect and two-probe method showed that nearly stoichiometric II-VI compound films were more resistive compared to non-stoichiometric films. It was noticed that metal (Cd, or Zn) rich films were less resistive compared to chalcogen (S, Se, Te) rich films because of the presence of shallow donor defects in metal rich films but in chalcogen rich films, Cd vacancies or Zn vacancies were the favorable deep level defects above the valence band. It was observed that the optical properties of angular deposited II-VI compounds were highly dependent on the stoichiometry of the films. It was observed that the transmittance of the metallic (Cd, or Zn) rich films was less compared to nearly stoichiometric and chalcogen (Te, Se, or S) rich films while reflectance of the metallic (Cd, or Zn) rich films was more compared to the nearly stoichiometric and the chalcogen (Te, Se, or S) rich films. It was due to the reflective nature of Cd and Zn. It was observed that the band gap of II-VI

compound films was dependent on the stoichiometry of the films. The band gap of non-stoichiometric films was less compared to nearly stoichiometric films because of the presence of defect states within the band gap. It was noticed that the density of angular-deposited II-VI compound films is not only a function of deposition angle but also depends on the stoichiometry of the films. Current-voltage curves showed that the photocurrent response of the stoichiometric films was better than the non-stoichiometric films because the stoichiometric films possessed less defects and had better mobility and carrier lifetime compared to non-stoichiometric films. It was also observed that the metal-rich films had large dark current because of the high conductivity of these samples. The photocurrent response of CdTe films was high because CdTe has a large absorption coefficient. The properties of the II-VI compounds can be controlled successfully by depositing them at different angles.

Future Recommendations

The elemental composition of II-VI compound films prepared by thermal evaporation was dependent on the deposition angle. Since, the change in elemental composition creates the interstitial and vacancy defects within the film, and it was also observed that the electrical and optical properties of II-VI compound films were highly dependent on the stoichiometry of the films. Therefore, the deep understanding of these defects is needed to investigate the mechanism of the change in the electrical and optical properties of II-VI compound films. For this purpose, II-VI compound films should be characterized future using the scanning tunneling microscopy to study the location of the

defects and low temperature photoluminescence and electroluminescence spectroscopies should be used to investigate the optical transitions related to these defects.

References

[1] S. Kasap, P. Capper, Handbook of Electronic and Photonic Materials, 2nd edtion, Springer, (2017)

[2] Y. Mizuguchi, Recent advances in layered metal chalcogenides as superconductors and thermoelectric materials: Fe-based and Bi-based chalcogenides, The Chemical Record. 16 (2016) 633–651.

[3] E. Fortunato, P. Barquinha, R. Martins, Oxide semiconductor thin-film transistors: A review of recent advances, Advanced Materials. 24 (2012) 2945–2986.

[4] J. Sheng, H. J. Jeong, K. L. Han, T. Hong, J. S. Park, Review of recent advances in flexible oxide semiconductor thin-film transistors, Journal of Information Display. 18 (2017) 159–172.

[5] R. Höll, M. Kling, E. Schroll, Metallogenesis of germanium: A review, Ore Geology Reviews. 30 (2007) 145–180.

[6] D. D. Vaughn, R. E. Schaak, Synthesis, properties and applications of colloidal germanium and germanium-based nanomaterials, Chemical Society. Reviews. 42 (2013) 2861–2879.

[7] Y. Meng, H. U. Ruizhong, X. Huang, J. Gao, Germanium in Magnetite: A Preliminary Review, Acta Geologica Sinica. 91 (2017) 711–726.

[8] P. S. Goley, M. K. Hudait, Germanium based field-effect transistors: Challenges and opportunities, Materials. 7 (2014) 2301–2339.

[9] F. Meillaud, M. Boccard, G. Bugnon, M. Despeisse, S. Ha, F. Haug, M. Stuckelberger, C. Ballif, J. Persoz, J. Schu, Recent advances and remaining challenges in thin film silicon photovoltaic technology, Materials Today. 18 (2015)

378-384.

[10] G. Beaucarne, Silicon thin film solar cells, Advances in Optoelectronics, (2007) 1-12.

[11] R. B. Bergmann, Crystalline Si thin-film solar cells: a review, Applied Physics A, Materials Science & Processing. 69 (1999) 187–194.

[12] J. D. Major, Grain boundaries in CdTe thin film solar cells: a review, Semiconductor Science and Technology. 31 (2016) 93001.

[13] S. Singh, R. Kumar, K. N. Sood, Structural and electrical studies of thermally evaporated nanostructured CdTe thin films, Thin Solid Films. 519 (2010) 1078–1081.

[14] M. R. Gao, Y. F. Xu, J. Jiang, S. H. Yu, Nanostructured metal chalcogenides: synthesis, modification, and applications in energy conversion and storage devices, Chemical Society Reviews. 42 (2013) 2986.

[15] S. L. Li, K. Tsukagoshi, E. Orgiu, P. Samori, Charge transport and mobility engineering in two-dimensional transition metal chalcogenide semiconductors, Chemical Society Review. 45 (2016) 118–151.

[16] A. A. Tedstone, D. J. Lewis, P. O' Brien, Synthesis, properties, and applications of transition metal-doped layered transition metal dichalcogenides, Chemistry of Materials. 28 (2016) 1965–1974.

[17] A. Oliva, Formation of the band gap energy on CdS thin films growth by two different techniques, Thin Solid Films, 391 (2001) 28–35.

[18] A. Romeo et al., Development of thin-film Cu(In,Ga)Se_2 and CdTe solar cells, Progress in Photovoltaics: Research and Applications, 12 (2004) 93–111.

[19] S. Chander and M. S. Dhaka, Optical and structural constants of CdS thin films grown by electron beam vacuum evaporation for solar cells, Thin Solid Films, 638 (2017) 179–188.

[20] B. Pradhan, A. K. Sharma, and A. K. Ray, A simple hybrid inorganic-polymer photodiode, Journal of Physics D: Applied Physics, 42 (2009) 18–22.

[21] K. Ravichandran, N. Nisha Banu, V. Senthamil Selvi, B. Muralidharan, and T. Arun, Rectification of sulphur deficiency defect in CdS based films by introducing a novel modification in the SILAR cyclic process, Journal of Alloys and Compounds, 687 (2016) 402–412.

[22] D. T. Ung, T. K. C. Tran, T. N. Pham, D. N. Nguyen, D. K. Dinh and Q. L. Nguyen, CdTe and CdSe quantum dots: synthesis, characterizations and applications in agriculture, Advances in Natural Sciences: Nanoscience and Nanotechnology, 3 (2012) 043001.

[23] R. Kobayashi, S. Takamatsu, K. Fukushima, K. Kishino, I. Nomura, Investigation of yellow/green II-VI compound semiconductor laser diode structures on InP substrates, Physica Status Solidi (C). 13 (2016) 669–672.

[24] I. Salzmann, G. Heimel, Journal of Electron Spectroscopy and Toward a comprehensive understanding of molecular doping organic semiconductors, Journal of Electron Spectroscopy and Related Phenomena. 204 (2015) 208–222.

[25] J. C. Ho, R. Yerushalmi, Z. A. Jacobson, Z. Fan, R. L. Alley, A. Javey, Controlled nanoscale doping of semiconductors via molecular monolayers, Nature Materials. 7 (2008) 62–67.

[26] J. Zhang, K. Tse, M. Wong, Y. Zhang, J. Zhu, A brief review of co-doping,

Frontiers of Physics, Frontiers of Physics.11 (2016) 117405.

[27] X. Liu, M. T. Swihart, Heavily-doped colloidal semiconductor and metal oxide nanocrystals: an emerging new class of plasmonic nanomaterials, Chemical Society Reviews. 43 (2014) 3908–3920.

[28] U. V. Desnica, Doping limits in II-VI compounds-challenges, problems, and solutions, Progress in Crystal Growth and Characterization of Materials, 36 (1998) 291–357.

[29] M. Afzaal and P. O' Brien, Recent developments in II-VI and III-VI semiconductors and their applications in solar cells, Journal of Materials Chemistry. 16 (2006) 1597–1602.

[30] I. Ch. Avetissov, E. N. Mozhevitina, A. V. Khomyakov, R. I. Avetisov, A. A. Davydov, V. P. Chegnov, O. I. Chegnova and N. V. Zhavoronkov, Homogeneity limits and nonstoichiometry of vapor grown ZnTe and CdTe crystals, CrystEngComm, 17 (2015) 561–568.

[31] A. Kobayashi, O. F. Sankey, and J. D. Dow, Deep energy levels of defects in the wurtzite semiconductors AIN, CdS, CdSe, ZnS, and ZnO, Physical Review B, 28 (1983) 946–956.

[32] R. N. Bhargava, The role of impurities in refined ZnSe and other II-VI semiconductors, Journal of Crystal Growth, 59 (1982) 15–26.

[33] S. Bhunia and D. N. Bose, Crystal growth and applications of II-VI compounds, Pinsa A. 64 (1998) 211–223.

[34] G. D. Watkins, Intrinsic defects in II–VI semiconductors, Journal of Crystal Growth. 159 (1996) 338–344.

[35] A. Ohtomo, M. Kawasaki, T. Koida, K. Masubuchi, H. Koinuma Y. Sakurai, Y. Yoshida T. Yasuda and Y. Segawa, $Mg_xZn_{1-x}O$ as an II-VI widegap semiconductor alloy, Applied Physics Letters. 19 (1998) 2466–2468.

[36] Nikolai Khrisanfovich Abrikosov, V. F. Bankina, L. V. Poretskaya, L. E. Shelimova, E. V. Skudnova, Semiconducting II–VI, IV–VI, and V–VI Compounds, Springer US, 1969.

[37] R. Scheer, H. W. Schock, Design Rules for Heterostructure Solar Cells and Modules, Wiley 2011.

[38] H. E. Ruda, Widegap II-VI compounds for opto-electronic applications, 1st edition, London ; New York : Chapman & Hall, 1992.

[39] M. L. Cohen, J. R. Chelikowsky, Electronic Structure and Optical Properties of Semiconductors, Springer-Verlag, Tokyo, 1998.

[40] L. E. Smart, E. A.Moore, Solid State Chemistry An Introduction, 3rd edition, Taylor & Francis, 2005.

[41] G. Iadonisi, G. Cantele, M.L. Chiofalo, Introduction to Solid State Physics and Crystalline Nanostructures, 1st edition, Springer-Verlag Mailand, 2014.

[42] S. Adach, Properties of Group-IV, III-V and II-VI Semiconductors, John Wiley & Sons, 2005.

[43] Y. Toyozawa, Optical Processes in Solids, Cambridge University Press, 2003.

[44] M. Jain, II-VI Semiconductor Compounds, World Scientific Publishing, 1993.

[45] B. Monemar, H.G. Grimmeiss, Optical characterization of deep energy levels in semiconductors, Progress In Crystal Growth And Characterization. 5 (1982) 47–88.

[46] T. H. Ning, and C. T. Sah, Multivalley Effective-Mass Approximation for Donor States in Silicon. I. Shallow-Level Group-V Impurities, Phvsical Review B, 4 (1971) 3468-3481.

[47] W. Lambrecht, Dopants and Defects in Semiconductors,Taylor and Francis, 2012.

[48] B. Monemar, H.G. Grimmeiss, Optical characterization of deep energy levels in semiconductors, Progress In Crystal Growth And Characterization. 5 (1982) 47–88.

[49] K. Sumino, Defect control in Semiconductors, 1st Edition, Elsevier Science Publishing Company, 1990.

[50] A. Vogt, S. Schutt, K. Frei, M. Fiederle, CdTe layer structures for X-ray and gamma-ray detection directly grown on the Medipix readout-chip by MBE, Journal of Crystal Growth. 477 (2017) 114–117.

[51] M. O. Reese, C. L. Perkins, J. M. Burst, S. Farrell, T. M. Barnes, S. W. Johnston, D. Kuciauskas, T.A. Gessert, W. K. Metzger, Intrinsic surface passivation of CdTe, Journal of Applied Physics. 118 (2015) 155305.

[52] C. Heisler, M. Brückner, F. Lind, C. Kraft, U. Reislöhner, C. Ronning, W. Wesch, CdTe grown under Cd/Te excess at very low temperatures for solar cells, Journal of Applied Physics. 113 (2013) 224504.

[53] H. Y. Ueng, S. Y. Yang, Electrodeposition of stoichiometric CdTe thin film for photovoltaic application, Journal of Renewable and Sustainable Energy. 4 (2012) 011605.

[54] A. Raulo, G. Hennard, M. Sowinska, R.B. James, A. Fauler, M. Fiederle, Te inclusions in large size CdTe THM crystals, IEEE Nuclear Science Symposium

Conference Record. (2012) 4514–4517.

[55] A. L. Dawari, K. V. Ferdinand, C. Jagdish, P. Kumar and P. C. Mathur, Electrical properties of Te-rich, Cd-rich and hydrogen- exposed polycrystalline CdTe thin films, Journal of Physics D: Applied Physics. 16 (1983) 2349-2360.

[56] O. I. O. Olusola, M. L. Madugu, I. M. Dharmadasa, Growth of n-and p-type ZnTe semiconductors by intrinsic doping, Materials Research Innovations. 19 (2015) 497–502.

[57] C. Kiran Kumar, N. Thi, Q. Hoa, S.-G. Yoon, E. T. Kim, J. H. Lee, G. H. Kim, Highly Photoconductive CdS Thin Films Synthesized by Using Chemical Bath Deposition, Journal of the Korean Physical Society. 55 (2009) 284–287.

[58] F. Ouachtari, Influence of Bath Temperature, Deposition Time and S/Cd Ratio on the Structure, Surface Morphology, Chemical Composition and Optical Properties of CdS Thin Films Elaborated by Chemical Bath Deposition, Journal of Modern Physics. 2 (2011) 1073–1082.

[59] N. Hernandez-Como, V. M. Landeros, I. Mejia, F. S. A. Tostado, C. D. Nascimento, G. D. M. Azevedo, C. Krug, M. A. Quevedo-Lopez, Defect control in room temperature deposited cadmium sulfide thin films by pulsed laser deposition, Thin Solid Films. 550 (2014) 665–668.

[60] H. Ayd, M. R. Karim, M. Balaban, and H. Unlu, Colloidal Synthesis And Characterization Of Cdse Quantum Dots : Role Of Cd :Se Molar Ratio And Temperature, International Journal Of Scientific & Technology Research. 5 (2016) 66–70, 2016.

[61] D. W. Ayele, H. M. Chen, W. N. Su, C. J. Pan, L. Y. Chen, H. L. Chou, J. H.

Cheng, B. J. Hwang, J. F. Lee, Controlled synthesis of CdSe quantum dots by a microwave-enhanced process: A green approach for mass production, Chemistry - A European Journal. 17 (2011) 5737–5744.

[62] U. Philipose, T. Xu, S. Yang, P. Sun, H. E. Ruda, Y. Q. Wang, K. L. Kavanagh, Enhancement of band edge luminescence in ZnSe nanowires, Journal of Applied Physics. 100 (2006).

[63] K. Morimoto, Influence of growth temperature on stoichiometry in ZnSe Influence of growth temperature on stoichiometry in ZnSe, Journal of Applied Physics. 66 (2014) 4206-4212.

[64] J. Dong, X. Zeng, C. Wang, W. Xia, X. Zhang, M. Zhou, Ferromagnetic behavior of non-stoichiometric ZnS microspheres with a nanoplate-netted surface, RSC Advances. 7 (2017) 20874–20881.

[65] P. Tsai, I. Pai, H. D. Shieh, Two-Stage Chemical Bath Deposition for Well-Covered and Stoichiometric ZnS Thin Films, Photovoltaic Specialists Conference (PVSC), 2012 38th IEEE. 2 (2011) 1992–1994.

[66] G. Wang, B. Huang, Z. Li, Z. Lou, Z. Wang, Y. Dai, M. Whangbo, Synthesis and characterization of ZnS with controlled amount of S vacancies for photocatalytic H_2 production under visible light, Scientific Reports. 5 (2015) 1–7.

[67] M. Ohring, The Materials Science of Thin Films, Academic Press, Second Edition, Academic Press,1992.

[68] C. H. Su. and Y. G. Sha, Growth of wide band gap II-VI compound semiconductors by physical vapor transport, Current Topics in Crystal Growth Res. 2 (1995) 401-433.

[69] S. Bhunia, D.N. Bose, Crystal growth and applications of II-VI compounds, Pinsa A. 64 (1998) 211–223.

[70] Y. Marfaing, Self-compensation in II-VI compounds, Progress In Crystal Growth And Characterization. 4 (1981) 317–343.

[71] L. I. Maissel and R. Glang, Handbook of Thin Film Technology, McGraw & Hill, USA, 1970.

[72] B. Lewis and J. C. Anderson, Nucleation and Growth of Thin Films, Academic Press, London,1978.

[73] A. Kundt. Ueber die electromagnetische drehung der polarisationsebene des lichtes imeisen. Annalen der Physik, 263:191–202, 1886.

[74] P. K. S. S. Harsha, Principles of Vapor Deposition of Thin Films, First edition, Elsevier, 2006.

[75] G. Plascencia, D. Jaramillo, Basic Thermochemistry in Materials Processing, Springer, 2017.

[76] L. Cemic, D. Jaramillo, Thermodynamics in mineral sciences: an introduction, Springer, 2005.

[77] H. Donald Brooke Jenkins, Chemical Thermodynamics at a Glance, Wiley-Blackwell, 2007.

[78] J. M Smith, H. C. Van Ness, Introduction to Chemical Engineering Thermodynamics, 4th edition, McGraw-Hill, 1987.

[79] K. Stowe, An introduction to thermodynamics and statistical mechanics, Cambridge University Press, 2007.

[80] A. G. Bird, Molecular Gar Dynamics, Oxford University Press, oxford, 1979.

[81] H. Callen, C. Cercignanai, Mathematical methods in Kinetic Theory, Plenum, New York 1969.

[82] S. Chapaman, T.G. Cowling, The Mathematical Theory of Non-Uniform gases, Cambridge University Press, 1970.

[83] J. F. Clarke, M. McChesney, The Dynamics of Real Gases, Butterworths, London, 1964.

[84] S. Dushman, J. M. Lafferty, Scientific Foundation of Vacuum Technique, 2nd edition, John Wiley & Sons, New York, 1962.

[85] D. J. Evans, D. J. Searles, S. R. Williams, Fundamentals of classical statistical thermodynamics: dissipation, relaxation and fluctuation theorems, Wiley-VCH, 2016.

[86] J. M. Lafferty, Foundations of Vacuum Science and Technology, John Wiley & Sons, New York, 1998.

[87] J. A. Walton, The Three Phases of Matter, 2nd edition, Clarendon Press, Oxford, 1983.

[88] B. N. Ro, Fundamentals of Classical and Statistical Thermodynamics, Wiley, 2002.

[89] J. C. Spickermann, Entropies of condensed phases and complex systems: A first principles approach, Springer, 2011.

[90] D. R. Gaskell, Introduction to the Thermodynamics of Materials, Sixth Edition, Taylor & Francis, 2018.

[91] Y. V. C. Rao, Engineering thermodynamics: through examples, Universities Press, 2003.

[92] J. F. O' Hanlon, A User's Guide to Vacuum Technology, 2nd edition, John Wiley & Sons, New York, 1989.

[93] W. F. Sears, An Introduction to Thermodynamics, the Kinetic Theory of Gases, and Statistical Mechanics, Addison-Wesley, Cambridge, 1950.

[94] I. L. Maissel, Glang, Handbook of Thin Film Technology, McGraw-Hill, New York, 1970.

[95] Y. G. Sidorov, S. A. Dvoretsky, M. V. Yakushev, N. N. Mikhailov, V. S. Varavin, V. I. Liberman, Peculiarities of the MBE growth physics and technology of narrow-gap II-VI compounds, Thin Solid Films. 306 (1997) 253–265.

[96] M. Kardar, Statistical Physics of Particles, Cambridge, New york, 2007.

[97] Guggenheim, E. A., Elements of the Kinetic Theory of Gases, Pergamon, New York, 1960.

[98] Y. Imry, Introduction to mesoscopic physics, 2nd Edition. (Oxford University Press, Oxford, 2002).

[99] A. P. Alivisatos, Semiconductor clusters, nanocrystals, and quantum dots. Science 271, 933 (1996).

[100] A. Barranco, A. Borras, A.R. Gonzalez-Elipe, A. Palmero, Perspectives on oblique angle deposition of thin films: From fundamentals to devices, Progress in Materials Science. 76 (2016) 59–153.

[101] K.Y. Lee, L.C. Chen, Y.J. Wu, Effect of Oblique-Angle Sputtered ITO Electrode in $MAPbI_3$ Perovskite Solar Cell Structures, Nanoscale Research Letters. 12 (2017) 4–9.

[102] A. Barranco, A. Borras, A.R. Gonzalez-Elipe, A. Palmero, Perspectives on oblique

angle deposition of thin films: From fundamentals to devices, Progress in Materials Science. 76 (2016) 59–153.

[103] A. Bachtold, P. Hadley, T. Nakanishi, and C. Dekker, Logic circuits with carbon nanotube transistors, Science. 294 (2001) 1317-1320.

[104] V. Derycke, R. Martel, J. Appenzeller, and P. Avouris, Carbon nanotube inter-and intramolecular logic gates, Nano Letters. 1 (2001) 453–456.

[105] Y. Huang, X. F. Duan, Q. Q. Wei, and C. M. Lieber, Directed assembly of one-dimensional nanostructures into functional networks, Science 291 (2001) 630-633.

[106] Y. Zhang and J. Zhu, Synthesis and characterization of several one-dimensional nanomaterials. Micron 33 (2002) 523-534

[107] G. R. Patzke, F. Krumeich, and R. Nesper, Oxidic nanotubes and nanorods – anisotropic modules for a future nanotechnology. Angew. Chem., 41, (2002) 2446–2461.

[108] Y. Xia, J. A. Rogers, K. E. Paul, and G. M. White sides, Unconventional methods for fabricating and patterning nanostructures, Chemical Reviews. 99 (1999) 1823–1848.

[109] Y. Chen and A. Pépin, Nanofabrication: conventional and noncoventional methods, Electrophoresis. 22 (2001) 187–207.

[110] H. T. Soh, K. W. Guarini and C.F. Quate, Scanning Probe Lithography, Kluwer Academic Publishers, Boston, 2001.

[111] T. J. Trentler, K. M. Hickman, S. C. Geol, A. M. Viano, P. C. Gibbons , and W. E. Buhro, Solution-liquid-solid growth of crystalline III-V semiconductors: an analogy to vapor-liquid-solid growth, Science. 270 (1995) 1791-1794.

[112] X. F. Liu, J. H. Zeng, W. X. Zhang, X. C. Yu, Y. T. Qian, J. B. Cao, and W. Q. Zhang, Solvothermal route to Bi3Se4 nanorods at low temperature. Journal of Materials Research. 16 (2001) 3361–3365.

[113] C. M. Lieber, One-dimensional nanostructures: chemistry, physics and applications, Solid State Communications. 107 (1998) 607-616.

[114] C. R. Martin, Nanomaterials a membrane-based synthetic approach, Science. (1994) 1961-1966.

[115] D. Al-Mawlawi, C. Z. Liu, and M. Moskovits, Nanowires formed in anodic oxide nanotemplates. Journal of Materials Research. 9 (1994) 1014-1018.

[116] J. C. Hulteen and C. R. Martin, A general template-based method for the preparation of nanomaterials, Journal of Material Chemistry. 7 (1997) 1075-1087.

[117] Matthew M. Hawkeye, Michael T. Taschuk, Michael J. Brett, Glancing Angle Deposition of Thin Films Engineering the Nanoscale Wiley, 2014.

[118] K. Robbie, M. Brett, Method of depositing shadow sculpted thin films, US Patent 5,866,204 (1999).

[119] B. Dick, M. Brett, Nanofabrication by Glancing Angle Deposition, Encyclopaedia of Nanoscience and Nanotechnology 6 (2004) 703-710.

[120] R. Messier, T. Gehrke, C. Frankel, V. C. Venugopal, W. Otaño, and A. Lakhtakia, Engineered sculptured nematic thin films, Journal of Vacuum Science & Technology A: Vacuum, Surfaces, and Films. 15 (1997)2148.

[121] K. Robbie and M. J. Brett, Sculptured thin films and glancing angle deposition: growth mechanisms and applications. Journal of Vacuum Science & Technology A: Vacuum, Surfaces, and Films 15(1997) 1460.

[122] A. Lisfi and J.C. Lodder, Magnetic domains in Co thin films obliquely sputtered on a polymer substrate, Physical Review B. 63 (2001) 174441174446.

[123] J. M. Nieuwenhuizen and H. B. Haanstra, Microfractography of thin films. Philips Technical Reviews. 27 (1966) 87-91.

[124] R. N. Trait, T. Smy, and M. J. Brett, Modeling and characterization of columnar growth in evaporated-films. Thin Solid Films 226 (1993) 196-201.

[125] A. L. Elias, K. D. Harris, C. W. M. Bastiaansen, D. J. Broer and M. J. Brett, Large-area microfabrication of three-dimensional, helical polymer structures, Journal of Micromechanics and Microengineering. 15 (2005) 49–54.

[126] N. O. Young and J. Kowal, Optically active fluorite films. Nature 183 (1959) 104–105.

[127] D. X. Ye, Y. P. Zhao, G. R. Yang, Y. G. Zhao, G. C. Wang, and T. M. Lu, Manipulating the column tilt angles of nanocolumnar films by glancing angle deposition, Nanotechnology 13 (2002) 615–618.

[128] K. Robbie, G. Beydaghyan, and T. Brown, Ultrahigh vacuum glancing angle deposition system for thin films with controlled three-dimensional nanoscale structure, Review Of Scientific Instruments. 75 (2004) 1089-1097.

[129] V. Valkovic, X-Ray Spectroscopy in Environmental Sciences, 1st edition, CRC press, 1989.

[130] B. Jeroen A. van; Lamberti, Carlo, X-ray absorption and X-ray emission spectroscopy: theory and applications.

[131] D. Shindo, T. Oikawa, Analytical Electron Microscopy for Materials Science, Springer, Tokyo, 2002.

[132] C. D.Wagner, W. M. Riggs, L. E.Davis, J. F. Mulder, Handbook of x-ray photoelectron spectroscopy. Physical Electronics, 1965.

[133] Royston Paynter; XPS theory, John Wiley and Sons, 2000.

[134] N. Winograd, S.W Gaarenstoorm; X-ray Photoelectron Spectroscopy, Physical Methods in Modern Chemical Analysis Volume 2, 1980.

[135] C. R. Brundal, A. D. Baker, Electron Spectroscopy: Theory, Techniques and Applications, Vol. 4 , Academic Press London, 1982.

[136] L. T. Barr, Modern ESCA The Principles and Practice of X-Ray Photoelectron Spectroscopy Boca Raton, CRC Press, 1994.

[137] J. F. Watts, J. Wolstenholme, An Introduction to Surface Analysis by XPS and AES, J. Wiley, New York, 2003.

[138] D. Briggs and J. T. Grant, Surface analysis by Auger and x-ray photoelectron spectroscopy, IM Publications, UK, 2003.

[139] Cvetko, X-ray photelectron spectroscopy University of Ljubljana, Seminar, 2012.

[140] X-RAYS, arsenic, and essie top coat, . https://cantorscience.org.

[141] B. D. Cullity, Elements of X-Ray Diffraction, Addison-Wesley, 1978

[142] K. C. Chang, Y. W. Chiang, C. H. Yang, J. W. Liou, Atomic force microscopy in biology and biomedicine, Tzu Chi Medical Journal. 24 (2012) 162e169.

[143] G. Haugstad, Atomic Force Microscopy: Understanding Basic Modes and Advanced Applications, Wiley, 2012.

[144] P. Eaton, P. West, Atomic Force Microscopy, Oxford University Press, USA, 2010.

[145] B. J. Clark, T. Frost, UV Spectroscopy: Techniques, instrumentation and data handling, Springer, 4th Ed., (1993).

[146] Michael G. Gore, Spectrophotometry and Spectrofluorimetry. A Practical Approach, Oxford University Press, USA, 200.

[147] T. Owen, Fundamentals of UV-visible spectroscopy, Hewlett-Packard, Germany, 1996.

[148] D. A. Neamen, Semiconductor Physics and Devices: Basic Principles. New York: McGraw-Hill, 2003.

[149] G. Zuo, H. Abdalla, M. Kemerink, Impact of doping on the density of states and the mobility in organic semiconductors, Physical Review B. 93 (2016) 235203.

[150] H. Luo, L.G. Ma, W.M. Xie, Z.L. Wei, K.G. Gao, F.M. Zhang, X.S. Wu, Synthesis of CdTe thin films on flexible metal foil by electrodeposition, Applied Physics A: Materials Science and Processing. 122 (2016) 444-450.

[151] P B. J. Kowalski, B. A. Orłowski and J. Ghijsen, XPS study of CdTe(110) surface oxidation process, Surface Science. 412/413 (1998) 544–554.

[152] D. N. Boset, M. S. Hedge, S. Basut and K. C. Mandalf, XPS investigation of CdTe surfaces : effect of Ru modification, Semiconductor Science and Technology. 4 (1989) 866-870.

[153] J. W. Kim, H. S. Shim, S. Ko, U. Jeong, C. L. Lee, W.B. Kim, Thorny CdSe nanotubes via an aqueous anion exchange reaction process and their photoelectrochemical applications, Journal of Materials Chemistry. 22 (2012) 20889.

[154] W. Li, M. Li, S. Xie, T. Zhai, M. Yu, C. Liang, X. Ouyang, X. Lu, H. Li, Y. Tong,

Improving the photoelectrochemical and photocatalytic performance of CdO nanorods with CdS decoration, CrystEngComm. 15 (2013) 4212.

[155] K. Manikandan, C. S. Dilip, P. Mani, and J. J. Prince, "Deposition and Characterization of CdS Nano Thin Film with Complexing Agent Triethanolamine," American Journal of Engineering and Applied Sciences. 8 (2015) 318–327.

[156] E. E. Khawaja, S. M. A. Durrani, A. B. Hallak, M. A. Salim and M. S. Hussain, Density of thin vapour-deposited films of zinc selenide, Journal of Physics D: Applied Physics. 27 (1994) 1008-1013.

[157] H. Kong, J. Yeo, and H. Lee, A Study on the properties of tellurium-oxide thin films based on the variable sputtering gas ratio, Journal of the Korean Physical Society. 66 (2015) 1744–1749.

[158] V. Mittal, N. P. Sessions, J. S. Wilkinson, G. S. Murugan, Optical quality ZnSe films and low loss waveguides on Si substrates for mid-infrared applications, Optical Materials Express. 7 (2017) 712.

[159] J. Dong, X. Zeng, W. Xia, X. Zhang, M. Zhou, C. Wang, Ferromagnetic behavior of non-stoichiometric ZnS microspheres with a nanoplate-netted surface, RSC Advances. 7 (2017) 20874–20881.

[160] A. A. Ojo, I.M. Dharmadasa, Analysis of electrodeposited CdTe thin films grown using cadmium chloride precursor for applications in solar cells, Journal of Materials Science: Materials in Electronics. 28 (2017) 14110–14120.

[161] P. K. K. Kumarasinghe, A. Dissanayake, B. M. K. Pemasiri, B. S. Dassanayake, Thermally evaporated CdTe thin films for solar cell applications: Optimization of

physical properties, Materials Research Bulletin. 96 (2017) 188-195.

[162] S. Chander, M.S. Dhaka, Optimization of physical properties of vacuum evaporated CdTe thin films with the application of thermal treatment for solar cells, Materials Science in Semiconductor Processing. 40 (2015) 708–712.

[163] D. K. Guptaa, M. Vermab, K. B. Sharmab and N. S. Saxenab, Synthesis, characterization and optical properties of CdSe/CdS and CdSe/ZnS core-shell nanoparticles, Indian Journal of Pure & Applied Physics. 55 (2017) 113-121.

[164] K. Tchakpele, J. P. Albert, C. Gout, Study of ideal vacancies in CdS and CdSe in the wurtzite structure, phyaea 117b & 118b (1983) 200-202.

[165] R. W. G. Wyckoff, Crystal Structures, 2nd edition, Interscience Publishers, New York (1963).

[166] M. Takumi, T. Masamitsu, K. Nagata, X-ray structural analysis of the high-pressure phase III of tellurium, Journal of Physics: Condensed Matter, 14 (2002) 10609-10613.

[167] I. T. Zedan, A.A. Azab, E. M. El-Menyawy, Structural, morphological and optical properties of ZnSe quantum dot thin films, Spectrochimica Acta Part A: Molecular and Biomolecular Spectroscopy. 154 (2016) 171–176.

[168] A. Fairbrother, V. Izquierdo-Roca, X. Fontané, M. Ibáñez, A. Cabot, E. Saucedo, A. Pérez-Rodríguez, ZnS grain size effects on near-resonant Raman scattering: optical non-destructive grain size estimation, CrystEngComm. 16 (2014) 4120.

[169] A. R. Bushroa, R. G. Rahbari, H. H. Masjuki, and M. R. Muhamad, “Approximation of crystallite size and microstrain via XRD line broadening analysis in TiSiN thin films,” Vacuum, 86 (2012) 1107–1112.

[170] C. Guo, M. Kong, D. Lin, C. Liu, B. Li, Microstructure-related properties of magnesium fluoride films at 193nm by oblique-angle deposition., Optics Express. 21 (2013) 960–7.

[171] S. S. Garje, J. S. Ritch, D. J. Eisler, M. Afzaal, P. O' Brien, T. Chivers, Chemical vapour deposition of II–VI semiconductor thin films using M [(TeP^{i} Pr_2)$_2$N]$_2$ (M = Cd, Hg) as single-source precursors, Journal of Materials Chemistry. 16 (2006) 966–969.

[172] S. Regan, L. Matwichuk, E. Cloutis, D. Goltz, P. Mann, Potential signatures of heavy metal complexes in lichen reflectance spectra, International Journal of Remote Sensing. 37 (2016) 2621–2640.

[173] M. Zaier, L. Vidal, S. Hajjar-Garreau, L. Balan, Generating highly reflective and conductive metal layers through a light-assisted synthesis and assembling of silver nanoparticles in a polymer matrix, Scientific Reports. 7 (2017) 1–10.

[174] A. S. Hassanien, K.A. Aly, A.A. Akl, Study of optical properties of thermally evaporated ZnSe thin films annealed at different pulsed laser powers, Journal of Alloys and Compounds. 685 (2016) 733–742.

[175] A. Wang, T. Chen, S. Lu, Z. Wu, Y. Li, H. Chen, Y. Wang, "Effects of doping and annealing on properties of ZnO films grown by atomic layer deposition," Nanoscale Research Letters, 75 (2015) 1-10.

[176] P. Y. Su, C. Lee, G. C. Wang, T. M. Lu, I. B. Bhat, CdTe/ZnTe/GaAs heterostructures for single-crystal CdTe solar cells, Journal of Electronic Materials. 43 (2014) 2895–2900.

[177] K. M. Kouchkarov, K. Sopian, M. Y. Sulaiman, H. S. Ullal, T. M. Razykov, N.

Amin, M. Alghoul, B. Ergashev, C.S. Ferekides, Revolutionary novel and low cost CMBD method for fabrication of CdTe absorber layer for use in thin film solar cells Revolutionary novel and low cost CMBD method for fabrication of CdTe absorber layer for use in thin film solar cells, 7857 (2013).

[178] A. Barcz, G. Karczewski, T. Wojtowicz, M. Sadlo, J. Kossut, Channels of Cd diffusion and stoichiometry in CdTe grown by molecular beam epitaxy, American Institute of Physics, 72 (1998) 206.

[179] Y. Xu, H. Liu, Y. He, R. Yang, L. Luo, and W. Jie, Research into the electrical property variation of undoped CdTe and ZnTe crystals grown under Te-rich conditions, Journal of Alloys and Compounds, 612 (2014) 392–397.

[180] V. N. Iodko, Z. A. Ketko, A. K. Belyaeva, and Y. R. Suprun-belevichb, "Radiative recombination in a ZnTe p-n junction," Journal of Crystal Growth, 185 (1998) 1170–1174.

[181] T.M. Razykov, K.M. Kuchkarov, C.S. Ferekides, B.A. Ergashev, R.T. Yuldoshov, N. Mamarasulov, M.A. Zufarov, Characterization of CdTe thin films with different compositions obtained by CMBD for thin film solar cells, Solar Energy. 144 (2017) 411–416.

[182] Q. Gul, M. Zakria, T. M. Khan, A. Mahmood, and A. Iqbal, Effects of Cu incorporation on physical properties of ZnTe thin films deposited by thermal evaporation, Materials Science in Semiconductor Processing, 19 (2014) 17–23.

[183] S. A. aly, Alaa. A. akl, Influence of Film Thickness on Optical Absorption and Energy Gap of Thermally Evaporated $CdS_{0.1}Se_{0.9}$ Thin Films, Chalcogenide Letters, 12 (2015) 489 – 496.

[184] M.F. Al-Kuhaili, M. Saleem, S.M.A. Durrani, Optical properties of iron oxide (α-Fe_2O_3) thin films deposited by the reactive evaporation of iron, Journal of Alloys and compounds, 521 (2012) 178– 182.

[185] O. Stenzel, The Physics of Thin Film Optical Spectra: An Introduction, SpringerVerlag, Berlin Heidelberg, Germany, 2005.

[186] D. T. F. Marple, Refractive index of ZnSe, ZnTe, and CdTe, Journal of Applied Physics. 35 (1964) 539–542.

[187] M. P. Lisitsa , L. F. Gudymenko , V. N. Malinko , S. F. Terekhova, Dispersion of the refractive indices and birefringence of CdSxSe1-x single crystals, Physica. Status Solidi, 31 (1969) 389-399

[188] T. M. Bieniewski and S. J. Czyzak. Refractive indexes of single hexagonal ZnS and CdS crystals, Journal of the Optical Society of America, 53 (1963) 496-497

[189] C. A. Klein. Room-temperature dispersion equations for cubic zinc sulfide, Pllied Optics, 25, 1873-1875 (1986).

[190] F. Smith, A high temperature study of native defects in ZnTe, Journal of Physics and Chemistry of Solids. 32 (1971) 2201–2209.

[191] O. I. Olusola, M. L. Madugu, N. A. Abdul-Manaf, and I. M. Dharmadasa, Growth and characterisation of n- and p-type ZnTe thin films for applications in electronic devices, Current Applied Physics. 16 (2016) 120–130.

[192] L. Zhipeng, Y. Qingfeng, L. Qianrui, Y. Wang, L. Liu, L. Zhang, P. Shilie, L. Qiang, W. Liduo, J. L. Sun, High-Performance Planar-Type Photodetector on (100) Facet of $MAPbI_3$ Single Crystal

[193] K. Shen, Z. Bai, Y. Deng, R. Yang, D. Wang, Q. Li, D. Wang, High efficiency

CdTe solar cells with a through-thickness polycrystalline CdTe thin film, RSC Adv. 6 (2016) 52326–52333.

VITAE

TANVIR HUSSAIN

PhD Physics

Nationality: Pakistani
Date of Birth: 12 Feb, 1987
Marital Status: Single

Hand Phone: +966595116448
E-mail: tanvirhussainssp905@gmail.com
Skype ID: tanvirhussainssp905
Postal Code: 55100

~ Educational Background ~

- **Doctor of Philosophy** Jan 2014 ~ May 2018
  Physics
  Department of Physics, King Fahd University of Petroleum and Minerals, Saudi Arabia
  Obtained CGPA 3.50/4
  Thesis Title: Angular Deposition of II-VI Compounds by Thermal Evaporation
  Advisor: Prof. Mohammad F. Al-Kuhaili
- **Master of Philosophy** Sep 2009 ~ Oct 2011
  Solid State Physics
  Centre of Excellence in Solid State Physics, University of the Punjab, Lahore, Pakistan
  Obtained CGPA 3.37/4
  Thesis Title: Induced Modifications in the Properties of Sr Doped $BiFeO_3$ Multiferroics
  Advisor: Prof. Saadat Anwar Siddiqi.
- **Bachelor of Science (Honours)** Sep 2005 ~ Jun 2009
  Physics
  Department of Physics, University of the Punjab, Lahore, Pakistan
  Obtained CGPA 3.46/4

~Research Skills~

- Sol-gel combustion method
- Chemical vapor deposition
- Thermal evaporation technique

- E-beam evaporation technique
- DC and RF sputtering
- X-ray photoelectron spectroscopy
- X-ray diffraction
- Van der Paw four probe electrical resistivity and Hall effect measurements
- Dielectric constant measurements with LCR Meter
- Spin coater thin films
- UV-vis spectrophotometer
- FTIR Analysis
- Current-Voltage Characteristics
- Vibrating-sample magnetometer
- Atomic Force Microscopy
- Transmission Electron Microscopy
- Scanning Electron Microscopy
- Energy-dispersive x-ray spectroscopy
- Low temperature photoluminescence
- Annealing of samples in vacuum and in different gases
- Photoelectrochemical cell measurements

~ Publications~

- **Tanvir Hussain**, M.F. Al-Kuhaili, S.M.A. Durrani, H.A. Qayyum, "Influence of angle deposition on the properties of ZnTe thin films prepared by thermal evaporation", Ceramics International, Volume 44, June 2018, Pages 10130-10140.
- **Tanvir Hussain**, M.F. Al-Kuhaili, S.M.A. Durrani, H.A. Qayyum, "Effect of collision during vapor transport between Cd and X (X = Te_2, Se_2, or S_2) molecules on the properties of thermally evaporated CdTe, CdSe, and CdS thin films", Results in Physics, Volume 8, March 2018, Pages 988-1000.
- **Tanvir Hussain**, M.F.Al-Kuhaili, S.M.A.Durrani, Ahsanulhaq Qurashi, H.A.Qayyum, "Enhancement in the solar light harvesting ability of tungsten oxide thin films by annealing in vacuum and hydrogen", International Journal of Hydrogen Energy, Volume 42, November, 2017, Pages 28755-28765.
- **Tanvir Hussain**, Saadat A. Siddiqi, Shahid Atiq, and M. S. Awan,"Induced Modifications in the Properties of Sr doped $BiFeO_3$ Multiferroics," Progress in Natural Science: Materials International, Volume 23, Issue 5, October 2013, Pages 487–492.
- H. A. Qayyum, M. F. Al-Kuhaili, S. M. A. Durrani, **Tanvir Hussain**, M. Ikram, Blue shift in the optical transitions of ZnO thin film due to an external electric field, Journal of Physics and Chemistry of Solids, 112 (2018) 94–99.

- H. A. Qayyum, M.F. Al-Kuhaili, S.M.A. Durrani, **Tanvir Hussain**, Determination of band gap of metal oxide thin films using Electromodulation, Under Review, Journal of Alloys and Compounds.
- Noorhana Yahya, Nadeem Nasir, Majid Niaz Akhtar, Muhammad Kashif, **Tanvir Hussain**, Hasnah Mohd Zaid, Afza Shafie, "Electromagnetic Response studies of the Antenna for Deep Target CSEM Environments, PP. 513-522, Pub. Date: December 31, 2012.
- **Tanvir Hussain**, Saadat A. Siddiqi, Shahid Atiq, Saira Riaz and Shahzad Naseem, "Induced Modifications in the Structural, Electrical and Magnetic Properties of Sr-doped $BiFeO_3$ Multiferroics," The 2012 International Conference on Advances in the Material Research on 26-29 August 2012 at COEX in Seoul, Korea.

~ Computer Skills ~

- Proficient in Word, Excel, Access Power Point, Microsoft Visio, Origin software
- Mathematica

~ Short Course ~

- Short Course On Universal Scanning Probe Microscope (USPM), University of Petronas, Malaysia14-15 Nov. 2011
  Instructor: Prof. Komiyama, Institute for Molecular Sciences
- Short Course on Crystallography, Magnetic Materials and Superconductivity, University of Petronas, Malaysia14-15 Nov. 2011
  Instructor: Prof. Gregory Kozlowski, Wright State University Dayton, USA

~ Language Skills ~

- English
- Urdu
- Punjabi

~ Extra Curricular Activities ~

- Playing Cricket, Table tennis, Badminton, and Football.
- Photography.
- Gym.